

LOAN DOCUMENT

| | | | | | | | | | | | | | | | | |
|---|---|---------------------|---|--|----------------------------|--|------------------------------|--|-----------------------------|--|-----|--|--|--|--|--|
| DTIC ACCESSION NUMBER | | LEVEL | PHOTOGRAPH THIS SHEET | <div style="border: 1px solid black; width: 40px; height: 40px; margin: 0 auto; display: flex; align-items: center; justify-content: center;"> 0 </div> | | | | | | | | | | | | |
| | <p style="font-size: 1.5em; margin: 0;"><i>The Journal of the Acoustical Society...</i></p> <p style="margin: 0;">DOCUMENT IDENTIFICATION</p> <p style="margin: 0; font-size: 1.2em;"><i>Oct 94</i></p> | | | | | | | | | | | | | | | |
| | <div style="border: 1px solid black; padding: 5px; margin: 0 auto; width: 80%;"> <p style="margin: 0;">DISTRIBUTION STATEMENT A</p> <p style="margin: 0;">Approved for public release; Distribution Unlimited</p> </div> <p style="margin: 0;">DISTRIBUTION STATEMENT</p> | | | | | | | | | | | | | | | |
| <div style="border: 1px solid black; padding: 2px;"> <p style="margin: 0;"><small>ACCESSION BY</small></p> <table style="width: 100%; border-collapse: collapse;"> <tr> <td style="width: 50%;"><small>NTIS</small></td> <td style="width: 50%;"><small>GRAM</small></td> </tr> <tr> <td><small>DTIC</small></td> <td><small>TRAC</small></td> </tr> <tr> <td><small>UNANNOUNCED</small></td> <td></td> </tr> <tr> <td><small>JUSTIFICATION</small></td> <td></td> </tr> </table> </div> <div style="border: 1px solid black; padding: 2px; margin-top: 5px;"> <p style="margin: 0;"><small>BY</small></p> </div> <div style="border: 1px solid black; padding: 2px; margin-top: 5px;"> <p style="margin: 0;"><small>DISTRIBUTION/</small></p> </div> <div style="border: 1px solid black; padding: 2px; margin-top: 5px;"> <p style="margin: 0;"><small>AVAILABILITY CODES</small></p> <table style="width: 100%; border-collapse: collapse;"> <tr> <td style="width: 50%;"><small>DISTRIBUTION</small></td> <td style="width: 50%;"><small>AVAILABILITY AND/OR SPECIAL</small></td> </tr> <tr> <td style="height: 40px; vertical-align: bottom; font-size: 1.5em;">A-1</td> <td></td> </tr> </table> </div> | <small>NTIS</small> | <small>GRAM</small> | <small>DTIC</small> | <small>TRAC</small> | <small>UNANNOUNCED</small> | | <small>JUSTIFICATION</small> | | <small>DISTRIBUTION</small> | <small>AVAILABILITY AND/OR SPECIAL</small> | A-1 | | <div style="border: 1px solid black; width: 100%; height: 100%;"></div> <p style="text-align: center; margin-top: 10px;">DATE ACCESSIONED</p> | | | |
| <small>NTIS</small> | <small>GRAM</small> | | | | | | | | | | | | | | | |
| <small>DTIC</small> | <small>TRAC</small> | | | | | | | | | | | | | | | |
| <small>UNANNOUNCED</small> | | | | | | | | | | | | | | | | |
| <small>JUSTIFICATION</small> | | | | | | | | | | | | | | | | |
| <small>DISTRIBUTION</small> | <small>AVAILABILITY AND/OR SPECIAL</small> | | | | | | | | | | | | | | | |
| A-1 | | | | | | | | | | | | | | | | |
| <p style="margin: 0;">DISTRIBUTION STAMP</p> | | | <div style="border: 1px solid black; width: 100%; height: 100%;"></div> <p style="text-align: center; margin-top: 10px;">DATE RETURNED</p> | | | | | | | | | | | | | |
| <p style="margin: 0;">DATE RECEIVED IN DTIC</p> | | | <p style="margin: 0;">REGISTERED OR CERTIFIED NUMBER</p> | | | | | | | | | | | | | |
| <p style="margin: 0;">PHOTOGRAPH THIS SHEET AND RETURN TO DTIC-FDAC</p> | | | | | | | | | | | | | | | | |

HANDLE WITH CARE

DTIC QUALITY INSPECTED 1

19980824 088

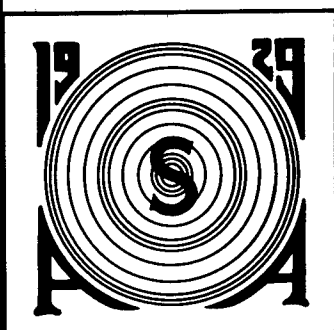
REPORT DOCUMENTATION PAGEForm Approved
OMB No. 074-0188

Public reporting burden for this collection of information is estimated to average 1 hour per response, including the time for reviewing instructions, searching existing data sources, gathering and maintaining the data needed, and completing and reviewing this collection of information. Send comments regarding this burden estimate or any other aspect of this collection of information, including suggestions for reducing this burden to Washington Headquarters Services, Directorate for Information Operations and Reports, 1215 Jefferson Davis Highway, Suite 1204, Arlington, VA 22202-4302, and to the Office of Management and Budget, Paperwork Reduction Project (0704-0188), Washington, DC 20503

| | | | | |
|---|--|---|--|--|
| 1. AGENCY USE ONLY (Leave blank) | | 2. REPORT DATE October 1994 | 3. REPORT TYPE AND DATES COVERED Technical journal, 1994 | |
| 4. TITLE AND SUBTITLE The Journal of the Acoustical Society of America | | | 5. FUNDING NUMBERS N/A | |
| 6. AUTHOR(S) Various | | | | |
| 7. PERFORMING ORGANIZATION NAME(S) AND ADDRESS(ES) Lancaster Press, Inc. Lancaster, PA | | | 8. PERFORMING ORGANIZATION REPORT NUMBER Vo.96(4) October 1994 | |
| 9. SPONSORING / MONITORING AGENCY NAME(S) AND ADDRESS(ES) SERDP 901 North Stuart St. Suite 303 Arlington, VA 22203 | | | 10. SPONSORING / MONITORING AGENCY REPORT NUMBER N/A | |
| 11. SUPPLEMENTARY NOTES Reprinted from The Journal of the Acoustical Society of America, Vol. 96, No. 4, October 1994. No copyright is asserted in the United States under Title 17, U.S. code. The U.S. Government has a royalty-free license to exercise all rights under the copyright claimed herein for Government purposes. All other rights are reserved by the copyright owner. | | | | |
| 12a. DISTRIBUTION / AVAILABILITY STATEMENT Approved for public release: distribution is unlimited | | | 12b. DISTRIBUTION CODE A | |
| 13. ABSTRACT (Maximum 200 Words) This journal contains mainly scientific articles regarding the Heard Island Feasibility Test. This test deals mainly with acoustic transmission through ocean waters. Signals, data, and effects on the behavior of marine mammals are discussed in the various journal articles. | | | | |
| 14. SUBJECT TERMS SERDP, Heard Island Feasibility Test, sound transmission, ocean, marine mammals, behavior, Tasman blockage | | | 15. NUMBER OF PAGES 158 | |
| | | | 16. PRICE CODE N/A | |
| 17. SECURITY CLASSIFICATION OF REPORT unclass | 18. SECURITY CLASSIFICATION OF THIS PAGE unclass | 19. SECURITY CLASSIFICATION OF ABSTRACT unclass | 20. LIMITATION OF ABSTRACT UL | |

NSN 7540-01-280-5500

Standard Form 298 (Rev. 2-89)
Prescribed by ANSI Std. Z39-18
298-102



Reprinted from

THE JOURNAL of the Acoustical Society of America

VOL. 96, NO. 4, OCTOBER 1994

THE HEARD ISLAND PAPERS

| | | |
|--|--|------|
| The Heard Island papers: A contribution to global acoustics | Walter Munk, Arthur Baggeroer | 2327 |
| The Heard Island Feasibility Test | Walter H. Munk, Robert C. Spindel, Arthur Baggeroer, Theodore G. Birdsall | 2330 |
| Signals, signal processing, and general results | Theodore G. Birdsall, Kurt Metzger, Matthew A. Dzieciuch | 2343 |
| Integrated autocorrelation phase at one period lag | Theodore G. Birdsall, Kurt Metzger, Matthew A. Dzieciuch, John Spiesberger | 2353 |
| Comparison of data and model predictions for Heard Island acoustic transmissions | B. Edward McDonald, Michael D. Collins, W. A. Kuperman, Kevin D. Heaney | 2357 |
| Dispersion and repopulation of Heard-Ascension modes | E. C. Shang, Y. Y. Wang, T. M. Georges | 2371 |
| A ray variability analysis of sound transmission from Heard Island to California | Ching-Sang Chiu, Albert J. Semtner, Coenraad M. Ort, James H. Miller, Laura L. Ehret | 2380 |
| Heard Island Feasibility Test: Analysis of Pacific path data obtained with a horizontal line array | Garry J. Heard, N. R. Chapman | 2389 |
| Vertical array receptions of the Heard Island transmissions | Arthur B. Baggeroer, Brian Sperry, Khosrow Lashkari, Ching-Sang Chiu, James H. Miller, Peter N. Mikhalevsky, Keith von der Heydt | 2395 |
| Differential Doppler as a Diagnostic | Matthew Dzieciuch, Walter Munk | 2414 |
| Doppler-inferred launch angles of global acoustic ray paths | Andrew Forbes, Walter Munk | 2425 |
| The Tasman blockage—An acoustic sink for the Heard Island feasibility test? | A. M. G. Forbes | 2428 |
| Reception at Ascension of the Heard Island Feasibility Test transmissions | D. R. Palmer, T. M. Georges, J. J. Wilson, L. D. Weiner, J. A. Paisley, R. Mathiesen, R. R. Pleshek, R. R. Mabe | 2432 |
| Features of the Heard Island signals received at Ascension | T. M. Georges, Linda R. Boden, David R. Palmer | 2441 |
| Observation of the Heard Island signals near the Gulf Stream | Ian A. Fraser, Peter D. Morash | 2448 |
| Heard Island Feasibility Test: Long-range sound transmission from Heard Island to Krylov underwater mountain | S. V. Burenkov, A. N. Gavrilov, A. Y. Uporin, A. V. Furduev | 2458 |
| Heard Island signals through the Agulhas retroflexion region | G. B. Brundrit, L. Krige | 2464 |
| Relative abundance and behavior of marine mammals exposed to transmissions from the Heard Island Feasibility Test | Ann E. Bowles, Mari Smultea, Bernd Würsig, Douglas P. DeMaster, Debra Palka | 2469 |

The Heard Island papers: A contribution to global acoustics

Walter Munk

Scripps Institution of Oceanography, University of California, San Diego, La Jolla, California 92093

Arthur Baggeroer

Departments of Ocean and Electrical Engineering, Massachusetts Institute of Technology, Cambridge, Massachusetts 02139

(Received 19 May 1994; accepted for publication 7 June 1994)

Acoustic transmissions from a low-frequency source near Heard Island in the southern Indian Ocean were monitored at 16 sites worldwide. The results are presented in the following papers. A summary is presented of what has been learned about the dimensions of this new subject: global acoustics.

PACS numbers: 43.30.Qd

The potential for antipodal ocean transmissions was already mentioned by Ewing and Worzel in their paper¹ reporting on the discovery of the ocean sound channel in 1944. In 1960, detonations off Perth, Australia were clearly received by hydrophones on the sound channel axis off Bermuda, nearly halfway around the Earth.² A re-analysis of the Perth-Bermuda transmission³ was presented at an Office of Naval Research lecture in 1988. Following the lecture, the question was asked: "how would you do this experiment today?" and this led directly to the planning of the Heard Island Feasibility Test (HIFT).⁴ An early account of the results has been published.⁵

HIFT is an outgrowth of the Ocean Acoustic Tomography⁶ effort at ever increasing ranges, starting in 1976. Application to ocean basin scale processes⁷ was discussed in 1982. The first very long range phase-coded transmissions were achieved by Spiesberger⁸ in 1987. Still, there was great uncertainty as to whether the electrically driven phase-coded source could be detected at global distances, and whether the signal gain associated with phase-coherent processing could be realized. In this sense HIFT was more of an expedition than an experiment, and the reporting in the following pages reflects the excitement of the adventure.

In late 1992, W. Kuperman, then editor of this *Journal*, suggested that it would be useful to publish within one volume the papers associated with HIFT. Accordingly we have collected the following seventeen papers:

HI 1: W. R. Munk, R. Spindel, A. Baggeroer, and T. Birdsall, "The Heard Island Feasibility Test"

HI 2: T. Birdsall, K. Metzger and M. Dzieciuch, "Signals, signal processing, and general results"

HI 3: T. G. Birdsall, K. Metzger, M. A. Dzieciuch and J. Spiesberger, "Integrated autocorrelation phase at 1 period lag"

HI 4: B. E. McDonald, M. D. Collins, W. A. Kuperman, and K. D. Heaney, "Comparison of data and model predictions for Heard Island acoustic transmissions"

HI 5: E. C. Shang, Y. Y. Wang, and T. M. Georges, "Dispersion and repopulation of Heard-Ascension modes"

HI 6: C.-S. Chiu, A. J. Semtner, C. M. Ort, J. H. Miller, and

L. L. Ehret, "A ray variability analysis of sound transmission from Heard Island to California"

HI 7: G. J. Heard and N. R. Chapman, "Heard Island feasibility test: Analysis of Pacific path data obtained with a horizontal line array"

HI 8: A. B. Baggeroer, B. Sperry, K. Lashkari, C.-S. Chiu, J. H. Miller, P. N. Mikhalevsky and K. von der Heydt, "Vertical array receptions of the Heard Island transmissions"

HI 9: M. Dzieciuch and W. Munk, "Differential doppler as a diagnostic"

HI 10: A. Forbes and W. Munk, "Doppler-inferred launch angles of global acoustic ray paths"

HI 11: A. M. G. Forbes, "The Tasman blockage—An acoustic sink for the Heard Island feasibility test?"

HI 12: D. R. Palmer, T. M. Georges, J. J. Wilson, L. D. Weiner, J. A. Paisley, R. Mathiesen, R. R. Pleshek, and R. R. Mabe, "Reception at Ascension of the Heard Island feasibility test transmissions"

HI 13: T. M. Georges, L. R. Boden and D. R. Palmer, "Features of the Heard Island signals received at Ascension"

HI 14: I. A. Fraser and P. D. Morash, "Observation of the Heard Island signals near the Gulf Stream"

HI 15: S. V. Burenkov, A. N. Gavrilov, A. Y. Uporin, A. V. Furduev, and N. N. Andregev, "Long range sound transmissions from Heard Island to Krylov Underwater Mountain"

HI 16: G. B. Brundrit and L. Krige, "Heard Island signals through the Agulhas retroflexion region"

HI 17: A. E. Bowles, M. Smultea, Bürsig D. P. DeMaster, and D. Palka, "Relative abundance and behavior of marine mammals exposed to transmissions from the Heard Island feasibility test"

The first paper gives an overview of the expedition and reports the major results, drawing freely on the subsequent papers. HI 2 discussed signal processing issues in the face of the enormous uncertainties in *a priori* estimates, and the exceptional phase stability found at all ranges. A special analysis technique reported in HI 3 reveals correlated phase fluctuations over the entire transmitted frequency band. These fluctuations can be traced to minor perturbations in the speed

of the source vessel during the transmission runs. The precise determination of the Doppler *averaged* over a transmission run leads to a number of useful results. Slight differences in the Doppler between early and late ray-like arrivals provide a useful diagnostic tool for ray identification (HI 9). The overall mean Doppler permits a very accurate determination of the geodesic launch angles (relative to the ship's course) which agree very closely with *a priori* calculations of the acoustic paths to Ascension and Christmas Islands (HI 10), but disagree wildly with the expected path through the Tasman Sea to the American west coast (HI 11). Evidently the direct route was blocked by bathymetry, but a relatively weak signal reached the West Coast along an alternate route passing east of New Zealand. In all of the transmissions the source ship CORY CHOUEST had to be underway into the prevailing wind and waves to avoid being broached. Eventually we are striving for transmissions between fixed sources and receivers. The conclusion here is that the motion of the source ship (which we regarded as a necessary evil) has turned into a substantial asset. In the future use of fixed sources, a preliminary stage of moving source geometry is indicated.

Modal propagation models (HI 4, HI 5) indicate strong coupling near sharp oceanic fronts (principally the Antarctic Circumpolar front) and from bathymetric features intruding into the sound channel. The computed results are consistent with the mode-rich arrivals measured with the vertical array at Monterey, California (HI 8). The scattering into neighboring modes and the repopulation of previously dissipated modes are an important and complicating attribute of global acoustics which had not been adequately anticipated. A three-dimensional ray propagation model (HI 6) deals with the influence of mesoscale and seasonal ocean variability.

Horizontal towed arrays provide further information. An array towed off California (HI 12) gave an arrival angle in agreement with the Tasman Sea blockage previously noted (HI 11). Another horizontal array towed across the Gulf Stream gave good signal-to-noise ratios at ranges up to 17 000 km (HI 14). Suspended hydrophones from a Russian vessel in the North Atlantic revealed the ubiquitous amplitude instability and phase stability, the latter being accounted for by the relative motions of source and receiver vessels (HI 15). Finally, a single receiver in the Agulhas retroreflection region off the coast of South Africa illustrates the problems associated with areas of very high spatial variability (HI 16).

The final paper (HI 17) deals with the biological component of HIFT. This program was added at a late planning stage under a protocol that provided for the transmissions to be terminated under certain prescribed circumstances. Observations were restricted to times when winds were weaker than force 8. The biological study was severely limited by the length of period available for the base study prior to the transmissions, and could not, nor was it intended to, provide definitive results. The limited evidence suggests some behavioral changes, but there is no evidence of distress.

The success of the Heard Island Feasibility Test was a necessary (but not sufficient) requirement for the development of Acoustic Thermometry of Ocean Climate (ATOC). Plans are for 195-dB sources at 75-Hz center frequency at

mid-latitude axial depth (1000 m) for ATOC, as compared to 214 dB at 57 Hz and 175-m depth for HIFT. The combined change in source intensity and depth yields a reduction of 34 dB in the intensity within the biologically important surface layers. Given this large reduction and the results of the Heard Island biological reconnaissance, we thought that no further permit difficulties would be encountered. This has not been the case.⁹

ACKNOWLEDGMENTS

We thank Dan Martin and William Kuperman for the initiative leading to the publication of the collected papers; the quality of the papers has been greatly improved by reviewers comments. Ken Rolt has played a major role in the preparation of the papers.

We acknowledge the multi-agency support by ONR, DOE, NSF, and NOAA, with NOAA as the lead agency. But we need to refer to the many individuals without whose help and enthusiasm the HIFT would never have been to sea. Initial encouragement came from Fred Saalfeld (Technical Director, ONR), Adm. Richard Pittenger (Oceanographer of the Navy), and Adm. J. R. (Smoke) Wilson (Chief of Naval Research); it also came from Adm. Craig Dorman, Adm. Dan Wolkensdorfer, Bob Winokur, Art Bisson, Ira Coen, Steve Hollis, Jim Baker, Tom Spence, Eric Hartwig, and Bob Corell. Mel Briscoe, ONR, was largely responsible for coordinating supporting agency activities and we are grateful for his efforts.

The decision to add vertical arrays at Monterey and Bermuda came after the initial planning. David Packard of MBARI and David Hyde of SAIC provided the funding for the two arrays; Ari Patrinos of DOE provided the general support for installation and analysis.

Lee Hunt of the National Academy of Sciences and Bernard Zahuranec of ONR jointly sponsored a lecture series by W. Munk in Europe and India which led to the participation of the R/V SAGAR KANYA of the Indian Institute of Oceanography in Goa. Dr. B. N. Desai, Director of NIO and Dr. C. S. Murthy were instrumental in coordinating the Indian effort. Werner Morawitz of Scripps Institution of Oceanography represented the HIFT aboard the Indian vessel.

Robert Edwards took the observations at Christmas Island; Louise Crossley was in charge of the Mawson Station, Antarctica; Bernard Olivier took the observations off Kerguelen Island on the R/V MARION DUFRESNE; Chris Tindle on HMNZS Tui in the Tasman Sea; Ross Chapman and Gary Heard on the CFAV ENDEAVOUR off California; Nikolai Dubrovsky and V. V. Gavrilov on the AKADEMIK NIKOLAI ANDREEV in the Atlantic, Iwao Nakano on the YOKOSUKA in the Western Pacific; and Leon Krige on the UMZIMKULU in the South Atlantic.

We thank Robert Schlenzig (SAIC), Larry McKinley, and Mel Calderon (NOSC), and the staff of SPAWAR PD-80 for assistance in ensuring that the R/V CORY CHOUEST was available and properly equipped for the voyage. The scientific party aboard the CORY for the HIFT were: George Dworski, Matthew Dzieciuch, Andrew Forbes, and Walter Munk. We thank Captain Russell Bouziga for his cheerful leadership during a long and tiresome journey. Elmer S. Hin-

man, III, of the CORY crew saved one of us (WHM) from falling overboard. William Parris (SAIC) of the technical support staff made a major contribution and we deeply regret his death after the end of the HIFT.

The HIFT could not have been a success without the willing participation of individuals from many organizations and countries. We have tried to note as many as we can recall in the above and we beg the forgiveness of any that have been inadvertently left out. In the latter category are many who appear as authors of papers in this volume. We have left them to speak for themselves.

At a very late stage we were informed by the Marine Mammal Commission that permits would be required. John Knauss, Ned Ostenso, John Carey, William Woodward, and others at NOAA headquarters helped expedite the permit process. With Mel Briscoe playing a leading role and under the guidance of Bill Evans, Doug Demaster, and Bernd Würsig, an international group of marine mammal observers were assembled by Ann Bowles. These included Scott Benson, Chris Burton, John Hunter, Forsyth Kineon, Debbie Palka, Robert Pitman, Lynn Robertson, Richard Howlett, and Mari Smultea. The observers operated aboard the R/V's CORY and AMY CHOUDEST under very trying conditions.

An Australian permit to conduct the HIFT under the Whale Protection Act was also a late requirement. Thanks

are due to Gordon Anderson and Peter Bridgewater (Director) of the Australian National Parks and Wildlife Service for rapidly assessing the application and its attendant objections. The final permit came within 21 hours from start time with a personal message from the Environmental Minister: "Good Luck and Calm Seas." The latter was not to be.

¹M. Ewing, and J. L. Worzel, "Long-range sound transmission," *Geol. Soc. Am. Memoir* 27, Part III, 1-35 (1948).

²R. C. Shockley, J. Northrup, P. G. Hansen, and C. Hartdegen, "SOFAR propagation paths from Australia to Bermuda: Comparison of signal speed algorithms and experiments," *J. Acoust. Soc. Am.* 71, 51-60 (1982).

³W. Munk, W. C. O'Reilly, and J. L. Reid, "Australia-Bermuda sound transmission experiment (1960) revisited," *J. Phys. Oceanogr.* 18, 1876-1898 (1988).

⁴W. Munk and A. M. G. Forbes, "Global ocean warming: An acoustic measure," *J. Phys. Oceanogr.* 19, 1765-1778 (1989).

⁵A. Baggeroer and W. Munk, "The Heard Island feasibility test," *Phys. Today* 45, 22-30 (September 1989).

⁶P. Worcester, B. Cornuelle, and R. Spindel, "A review of ocean acoustic tomography: 1987-1990," *Rev. Geophys. Supp.* 557-570 (1991).

⁷W. Munk and C. Wunsch, "Observing the ocean in the 1990's," *Philos. Trans. R. Soc.* 307, 123-161 (1982).

⁸J. L. Spiesberger, P. J. Bushong, K. Metzger, Jr., and T. G. Birdsall, "Basin-scale tomography: synoptic measurements of a 4000 km length section in the Pacific," *J. Phys. Oceanogr.* 19, 1073-1090 (1989).

⁹J. R. Potter, "ATOC: sound policy or enviro-vandalism? Aspects of a modern media-fueled policy issue," *J. Environ. Devel.* 3(2), 47-62 (1994).

The Heard Island Feasibility Test

Walter H. Munk

Scripps Institution of Oceanography, University of California, San Diego, La Jolla, California 92093

Robert C. Spindel

Applied Physics Laboratory, University of Washington, Seattle, Washington 98105

Arthur Baggeroer

Departments of Ocean and Electrical Engineering, Massachusetts Institute of Technology, Cambridge, Massachusetts 02139

Theodore G. Birdsall

Communications and Signal Processing Laboratory, University of Michigan, Ann Arbor, Michigan 48109-2122

(Received 23 August 1993; revised 20 May 1994; accepted 7 June 1994)

In January 1991, the Heard Island Feasibility Test (HIFT) was carried out to establish the limits of usable, long-range acoustic transmissions. Coded acoustic signals transmitted from a source near Heard Island in the southern Indian Ocean were monitored at 16 sites in the North and South Atlantic, the North and South Pacific, the Indian Ocean, and the Southern Ocean. The question posed by HIFT, whether at such global ranges the signals would permit phase-coherent processing and thus yield favorable signal-to-noise levels, was answered in the affirmative. There was no evidence of distress by the local marine mammal population in response to the acoustic transmissions. HIFT was prerequisite to a program for Acoustic Thermometry of Ocean Climate (ATOC). The principal challenges to such a program are discussed.

PACS numbers: 43.30.Qd

The motivation for the Heard Island Feasibility Test (HIFT) arises from the problem of global warming. The release of CO₂ and other greenhouse gases into the atmosphere produces a disturbance in the radiation balance, leading to an expected increase in global atmospheric temperature. The oceans play a vital role in atmospheric greenhouse warming. They provide for storage of heat and greenhouse gases. Without oceans, the atmosphere would be expected to warm at a rate two to three times the rate with oceans, other factors remaining the same.

Any climatic ocean changes are, of course, of interest in their own right. The thermal and dynamical structure of some coupled atmosphere/ocean models¹ undergo drastic changes, such as a virtual cessation of the thermohaline circulation (buoyancy driven as opposed to wind driven), preventing the ventilation of the deeper layers. This could have a profound impact on marine life.

There is a need for testing model predictions with direct ocean measurements. *Local* measurements of ocean temperature are subject to large variability associated with mesoscale eddies. These are associated with temperature anomalies, positive and negative, on scales of 100 days and 100 km, with magnitudes that are several hundred times the expected yearly rate of ocean greenhouse warming. One needs a method for measuring the *average* temperature over large ocean ranges. This requirement can be met by acoustic thermometry, based on two simple considerations: (i) the travel time of sound between two points is a sensitive indicator of the intervening ocean temperature, and (ii) the ocean is a good propagator of sound and so these points can be very far apart.

To be quantitative, we need to make some assertions concerning oceanic greenhouse warming. One thing is clear: A model of uniform downward diffusion of surface heating is totally inapplicable. The process is one of convection involving horizontal and vertical ocean circulation. All global circulation models (GCMs) predict temperature changes that are not uniform and are structured on gyre and basin scales of order 10 Mm (megameters). For optimum detection of climate variability, the array needs to be gyre-scale resolving and mesoscale suppressing. We envision an array of acoustic sources and receivers with typical spans of 5–10 Mm.

For orientation, take as a typical estimate of greenhouse warming 20 m°C/yr (millidegrees per year) at the ocean-atmosphere boundary, decreasing exponentially to 5 m°C/yr at 1-km depth. (The reader must not interpret this model as representing uniform downward diffusion of heat.) Such an estimate is in line with some computer modeling of greenhouse warming; it requires an incremental heat flux into the oceans of 2 W/m², which is the estimated perturbation of radiative transfer associated with the enhanced greenhouse gases (the associated atmospheric warming requires only 0.03 W/m²). Thermal expansion in this scenario yields a rise in sea level of 2 mm/yr, which is not inconsistent with global tide gauge measurements.

What is the expected acoustic signature? Sound speed increases by 4–5 m/s per °C. Taking +5 m°C/yr at the sound channel axis yields –0.1 s/yr for the travel time over a 10-Mm path. In ocean acoustic tomography travel times are measured to a precision of 1 ms, albeit over 1-Mm ranges. For acoustic thermometry we want to achieve a precision of

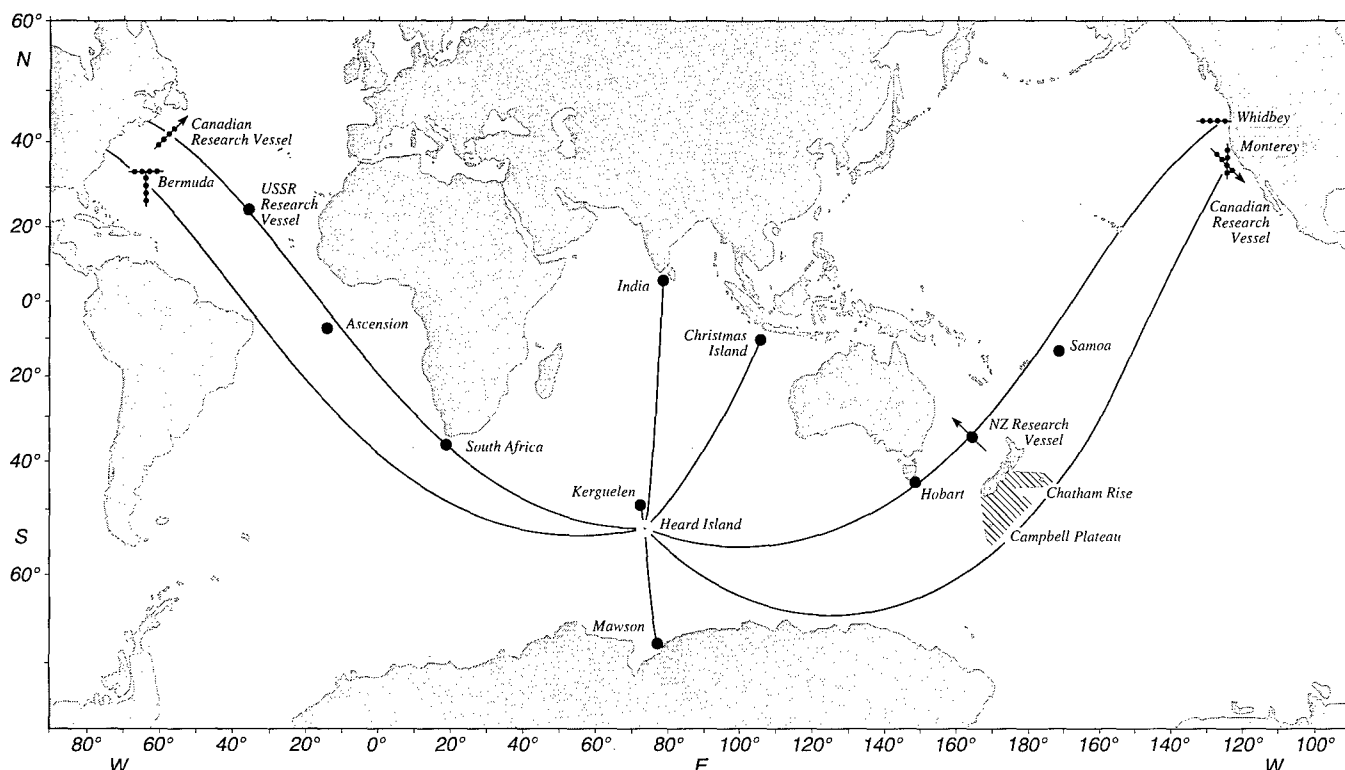


FIG. 1. Ray paths from source to receiver sites are refracted geodesics, i.e., great circles corrected for Earth flattening and horizontal sound speed gradients. The source array was suspended from R/V CORY CHOUEST 50 km southeast of Heard Island. Single dots indicate sites with single receivers. Dots connected by horizontal lines designate horizontal bottom-mounted arrays, vertical lines designate vertical arrays, and slanted lines designate arrays towed in the direction of the arrow. Signals were received at all sites except for the vertical array at Bermuda (which sank) and the Japanese station off Samoa.

10–50 ms, and this sets the required bandwidth and signal-to-noise ratio (SNR).

HIFT tested whether acoustic propagation through the ocean would support travel time measurements to this accuracy. Coded low-frequency acoustic signals were transmitted from a site near Heard Island in the southern Indian Ocean to the 16 receiver sites in the Indian, Atlantic, and Pacific Oceans indicated in Fig. 1. Signals were detected and travel times measured at distances up to 18 Mm.

The proposed acoustic array will, of course, measure the combined greenhouse and ambient climate signals. Their separation constitutes what is perhaps the principal intellectual challenge in this undertaking. Simple frequency and wave-number filtering will not do, as the two signals have overlapping power spectra. But in accordance with ongoing modeling efforts, the spatial structure of the ambient and greenhouse signals are not the same. The separation then depends upon a coordinated modeling and observational effort. It is useful to note that, from an oceanographer's point of view, measurements of the ambient background "noise" are at least as interesting as the detection of greenhouse warming. The understanding of gyre and basin scale variability is perhaps the most challenging problem facing physical oceanographers today. Finally, it is important to emphasize that acoustic thermometry addresses the issue of measuring climatic change (ambient or otherwise) in the oceans; it does not tell us anything about the underlying causes and about the effects on the atmosphere.

I. THE HEARD ISLAND FEASIBILITY TEST

The issues in the HIFT were: can signals generated by currently available acoustic sources be detected at ranges of order 10 Mm, can coded signals be "matched filtered" to measure travel time to better than 0.1 s, and can this be done without harm to local marine life?

It was by no means established *a priori* that these issues could be resolved positively. Uncertainties in surface scattering in the first 5 Mm of RSR (refracted, surface reflected) propagation led to estimates of acoustic propagation loss that differed by 60 dB. Signal coherence and resolvability of paths and/or modes were unknown at these ranges. A successful feasibility test was regarded as the necessary (but not sufficient) prelude for Acoustic Thermometry of Ocean Climate (ATOC).

We were fortunate to obtain from the U.S. Navy the use of powerful low-frequency HLF-4 transducers aboard the R/V CORY CHOUEST. These sources fitted our requirements well except that their operational use was limited to a maximum depth of 300 m. This dictated deployment at high latitude where the SOFAR channel is shallow.

A site near Heard Island (an uninhabited Australian Island discovered in 1853) was found to permit, quite unexpectedly, insonification of both the Atlantic and Pacific Oceans.² The acoustic rays emanating from the source site (Fig. 1) are refracted geodesics; i.e., they are approximately great circles, but they allow for the polar flattening of the Earth and for refraction from horizontal gradients in sound

speed. More precisely, the rays allow for horizontal gradients at the sound axis. This is the proper limit for low acoustic mode numbers at high frequencies. Heaney *et al.*³ have extended the construction to any mode number at any frequency; they also allowed for bathymetric refraction. Both have important consequences that are discussed later.

The initial plan depended entirely on existing U.S. Navy bottom-mounted horizontal receiver arrays at Bermuda and on both coasts of North America. While the planning was underway we received word from oceanographic colleagues in many countries that they were prepared to take receivers to sea to listen to the transmitted signals. The final result was that scientists from nine countries collaborated informally but very effectively using a diverse set of receiving systems.

Very late in the planning stage we were notified by the U.S. National Marine Fisheries Service that permits to "take whales" were required (to "take" is defined to include everything from a slight behavioral response to death. As a consequence the Australian authorities requested that we also file for Australian permits. The principal concern was that the acoustic sources were potentially a threat to marine mammals. By this time ships had been scheduled, and receiving equipment had been shipped to our international partners. Postponement was not an option. The R/V CORY CHOUEST, with Munk and Forbes as chief scientists, sailed from Fremantle, Australia on 9 January 1991 with neither U.S. nor Australian permits. These were received a week and a day, respectively, before the scheduled start of transmissions. A second ship, the R/V AMY CHOUEST, was chartered for the biological observations. Under the leadership of Ann Bowles of Hubbs Sea World, a biological party consisting of three Australian and six American observers was assembled. Clearly the conditions were not ideal for the biological add-on to the experiment. It is preferable to conduct some of the surveys from the air, the least intrusive method, but there is no landing strip within 3 Mm of Heard Island. Baseline measurements and the experiment itself were necessarily short term.⁴

Within these experimental limits there was no indication of any harmful effect on the abundant local marine life, although changes in behavior were observed. The most compelling evidence was the absence of sperm whale sonar "clicks" during the transmission period, but there was no accompanying evidence of mammal distress and none of the behavioral changes observed have been associated with long-term effects. We had agreed on a protocol whereby a transmission would be aborted if any marine mammals were within 1 km of the source ship at transmission start time. There was no such instance.

Our plan was to transmit for 10 days, commencing 0000 Greenwich Mean Time (GMT) 26 January 1991 (Australia Day), on a 1-h-on, 2-h-off schedule. Nine ships and six land based sites were standing by worldwide to receive the signals. R. Spindel at the Applied Physics Laboratory of the University of Washington (APL-UW) coordinated communications. The schedule had been "frozen" and distributed to all receiver sites prior to the experiment, with no changes to be made for equipment malfunctioning, bad weather, or other considerations. This was the right decision; it reduced the

required communication to tolerable levels. As previously stated, there was considerable uncertainty as to whether the signals would be received at the remote stations. The earliest possible responses were from the two arrays with "real time" processors: Bermuda (manned by K. Metzger) and Whidbey Island near Seattle (manned by T. Birdsall). Both transmissions were at ranges of approximately 18 Mm, one westward, the other eastward, nearly half around the Earth with acoustic travel times of $3\frac{1}{2}$ h.

On the day prior to the scheduled start, technicians aboard the R/V CORY CHOUEST requested a routine 5-min checkout of the sources. Three and one-half hours later the CORY received a message via the APL communications center from an excited Metzger at Bermuda describing an early reception at 57 Hz and asking confirmation that it was from the CORY. Soon thereafter, APL-UW reported that Birdsall at Whidbey Island had confirmed a reception in the Pacific. The question about the adequacy of the source level had been answered, and it was not yet Australia Day!

The scheduled transmissions commenced on time, and other stations soon began to report receptions. On 31 January the CORY encountered a gale with 10-m seas. One suspended source was torn loose and went to the bottom. The others were severely damaged. Fortunately, there had been 35 successful transmissions before this untimely termination.

II. SOURCE AND RECEIVERS

The R/V CORY CHOUEST carried ten HLF-4LL acoustic sources (Fig. 2) manufactured by Hydroacoustics, Inc., Rochester, NY, and the specialized handling equipment that enabled them to be deployed in a vertical array through the ship's center well to the depth of 175 m (the local sound channel axis, Fig. 3). Acoustic energy is generated by driving circular faceplates into vibration with hydraulically controlled pistons. The plates resonated at 57 Hz and provided a bandwidth of about 14 Hz. Each source was capable of transmitting a nominal level of 206 dB *re*: 1 μ Pa @ 1 m (3.3 kW acoustic).

A vertical array of ten sources with a 3.81-m spacing (0.15λ at 57 Hz) was used, but only five sources were activated at a time. Overheating of the hydraulic system and possible resonant coupling between sources was a major concern. Indeed, it was not until a November 1990 trial in the Sea of Japan, prior to steaming to Heard Island, that we learned that the sources could be operated continuously for an hour and that five could be operated in parallel, thus providing a maximum transmit level of 220 dB [$206 + 20 \log_{10}(5)$]. *In situ* measurements indicated that source levels of 221 dB were actually obtained.

Receivers at different sites included bottom-mounted hydrophones, either singly or in horizontal arrays, ship-towed horizontal arrays, bottom-moored and ship-suspended vertical arrays, and hydrophones suspended from surface floats (see Table I).

A self-contained receiver and PC-based data processing system was developed to simplify and standardize data acquisition. Sonobuoys, or sonobuoy-like surface floats with hydrophones suspended at the depth of the local sound channel axis, telemetered to ship or shore for recording and pro-

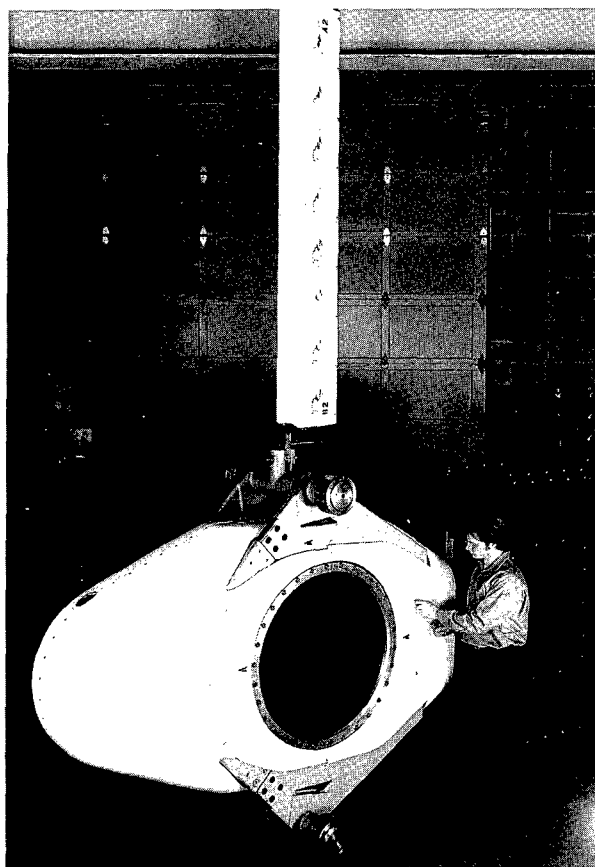


FIG. 2. The HLF-4 acoustic source (courtesy of Hydroacoustics, Inc.). The smooth Fiberglass housing covers most of the transducer mechanical equipment and electrical containers. One of the two exposed circular radiating faces is shown. Ten sources were suspended through the center well of the R/V CORY CHOUEST in a vertical array with 3.81-m element spacing. A maximum of five sources was energized for each hour-long transmission.

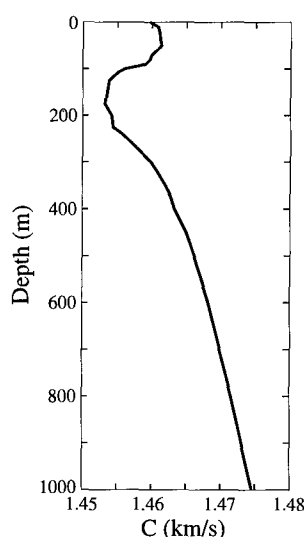


FIG. 3. Sound speed profile at Ascension Island on 26 January 1991. The center of the source array was placed at a depth of 175 m.

TABLE I. Receiving sites for the Heard Island Feasibility Test [surface-suspended systems used a sonobuoy deployment with a radio frequency link; ship-suspended had a cable from the hydrophone(s)].

| Receiving site | Country | Receiver type |
|---------------------------------|--------------------------------|--------------------------------------|
| Ascension Island | U.S.A. (NOAA) | Bottomed, single hydrophone |
| Bermuda | U.S.A. (U. Mich.) | Bottomed, horizontal array |
| Capetown, S.A. | South Africa | Ship-suspended, single hydrophone |
| Christmas Island (Indian Ocean) | Australia | Surface-suspended, single hydrophone |
| Goa, India | India | Surface-suspended, single hydrophone |
| Heard Island (R/V CORY CHOUEST) | Australia | Surface-suspended, single hydrophone |
| Kerguelen Island | France | Surface-suspended, single hydrophone |
| Krylov Seamount (N. Atlantic) | Russia | Ship-suspended, vertical array |
| Mawson Station, Antarctica | Australia | Bottomed, single hydrophone |
| Monterey, California | U.S.A. (MIT, NPS, MBARI, SAIC) | Ship-suspended, vertical array |
| New Zealand | New Zealand | Hydrophones dropped from moving ship |
| Samoa | Japan | Ship-suspended, single hydrophone |
| Tasmania | Australia | Surface-suspended, single hydrophone |
| U.S. East coast (off Cape Cod) | Canada (DREA) | Towed, horizontal array |
| U.S. West coast (off San Diego) | Canada (DREP) | Towed, horizontal array |
| U.S. West coast | U.S.A. (U. Mich.) | Bottomed, horizontal array |

cessing at Mawson, Goa, Kerguelen, Christmas Island, Capetown, Bermuda, Tasmania, New Zealand, the U.S. West Coast, and Ascension Island. Detailed descriptions are given in the appropriate papers in this volume.

Receivers of their own design were used by Soviet investigators anchored off the Krylov Seamount in the North Atlantic⁵ and by Japanese participants near Samoa. Canadian laboratories towed horizontal line arrays off both coasts of North America.^{6,7} A vertical line array was deployed off California.⁸ All arrays used multichannel, digital data acquisition.

III. SIGNALS AND SIGNAL PROCESSING: THE STRATEGY

HIFT signal strategy had to take into account the very large uncertainty in the expected propagation loss, stability, and arrival spread. Path lengths ranged from 1 to 18 Mm.

Receivers ranged from simple sonobuoys to horizontal and vertical arrays with significant array gain. Birdsall *et al.*⁹ developed the signaling strategy, assembled the data, and subjected it to a summary form of frequency domain processing (we refer to their paper for a detailed discussion). The results provide a basis for further analysis by interested investigators.

The frequency of choice was 57 Hz (to avoid confusion with the ubiquitous 50- and 60-Hz power frequencies). The 18-Mm volume attenuation is 5 dB in the Atlantic waters and 3 dB in the Pacific waters (The corresponding Atlantic attenuation at 100 Hz is 19 dB!) Spatial spreading losses were separately examined by three methods using an improved sonar equation, an adiabatic mode propagation model, and a ray/time front propagation model. Each gave a wide spread of answers. What was needed was the intensity of a resolved arrival, either per ray path or per mode, and not the usual CW transmission loss. In the end a compromise between experience and computation yielded an estimate of 135-dB space-time spreading loss at 18 Mm per observable ray or mode.

Surface scattering was a major consideration. For the first few megameters the propagation was along an upward refracting polar channel (RSR) in a region of notoriously high sea states. At 5-Mm ranges, even very low surface scattering losses accumulate; a loss of just 1.2×10^{-2} dB/km accumulates to 60 dB in the polar channel. Ray model losses for the surface interacting rays varied from 2 dB for 10-m/s winds to 60 dB for 20-m/s winds. The conclusion was that very high sea states would kill the signal. A modal analysis by Baggeroer (personal communication) based upon the Kuperman-Ingenito scattering theory¹⁰ raised similar concerns.

Blockage and refraction by islands, seamounts, and ridges were further important considerations. In the final analysis blockage became a question to be answered by the measurements. Horizontal refraction by horizontal gradients in sound speed was a concern since small angular deflections cause large shifts at long ranges.

We chose three types of signals. The first was a simple cw tone at 57 Hz, which allowed detection by the simplest receiving equipment. It had the highest carrier-to-noise ratio of all the HIFT signals. The second signal type was a three-digit M-sequence with 10 carrier cycles per digit and a 45° phase modulation angle. (M-sequences are standard signals long used in tomography and are likely to be the signal of choice for a long-term ocean monitoring program.¹¹) This signal had a period of 0.526 s and a spectral line spacing of 1.9 Hz. It was chosen because it has five principal spectral lines (hence the name "pentalline") with special amplitude properties. The first pair of spectral lines 1.9 Hz from the carrier are roughly 6 dB below the carrier, and the next pair 3.8 Hz from the carrier are about 12 dB below the carrier. This signal allowed a rough estimate of received SNR based only on which lines were present.

The third signal type consisted of four different M-sequences. Their bandwidth and period were sufficient to determine the multipath structure using pulse compression. Each digit consisted of five carrier cycles with sequence du-

urations of 22.4, 44.8, 89.7, and 179.6 s, respectively. We felt that 22.4 s would be sufficient to accommodate the expected time spread in arrival patterns even at the most distant receivers; the longer sequences were insurance.

The requirement was to achieve a 20-dB processed SNR on every significant arrival. This yields a time of arrival precision of one-tenth the nominal resolution of W^{-1} (W is bandwidth), and an insignificant false alarm probability. A basic transmission duration of 1 h was chosen, long enough to provide significant gain, yet short compared to a tidal cycle. On the basis of past experience (though at higher frequencies and shorter ranges) we anticipated being able to achieve 50 s of coherent processing, followed by incoherent processing. These preliminary estimates, made in January 1989, yielded a processed output quality of 10 dB for a single hydrophone at 10 Mm—not good enough. But the far stations had long horizontal arrays that would raise the level by at least 10 dB. An additional gain of 14 dB along the axis could be expected by energizing five sources in parallel, thus achieving well over the 20-dB SNR design goal.

A primary goal was to learn about the phase stability of the recorded arrivals. The signals were designed to give information for integration times as short as 20 s. To our surprise (and delight) we were able to coherently process for up to a half hour at 5 Mm range.

During the 6 days of the test, 35 out of a possible 48 transmissions took place. We refer to Ref. 9 for information on the 16 receiver sites, ranges, and travel times, and on the data acquired at the receiver sites for each of the accomplished 35 transmissions.

IV. RECORDS BY SINGLE RECEIVERS AND FIXED ARRAYS

Some receptions by fixed receivers are presented to give the reader a feel for the quality of the data. More detailed discussions are found in other papers of this volume.

Examples of the three types of signals are shown in Fig. 4. The recorded spectra are nearly perfect replica of the theoretical spectra (apart from the 60-Hz contamination); only the pedestals at the foot of the pentallines give evidence that this is a display derived from measurements. The onset of reception is abrupt, whereas the shutoff lingers suggesting reverberant energy extending beyond the 60-min transmission. This is particularly evident for the M-sequence.

At Ascension Island, 9.2 Mm from the CORY CHOUET, signals were received on single, bottom-mounted hydrophones located at sound channel axis depth (about 800 m) or deeper. These hydrophones are part of the U.S. Air Force's Missile Impact Location System (MILS). SNRs in a 1-Hz band ranged from 19 to 30 dB and averaged about 16 dB (all referenced to a transmit level of 220 dB). Figure 5, based on data taken by Palmer and his collaborators,¹² compares an ideal (simulated) pentalline transmission to an actual reception. Two periods of 0.53 s each are shown. The experimental spectrum was produced by incoherently averaging 500 spectra, each of which was constructed with a 4.49-s data record. Figure 6 from Georges and collaborators¹³ shows matched filtered 255-digit (22.4-s) M-sequence receptions on four hydrophones, taken 24 h apart. For any one hydrophone,

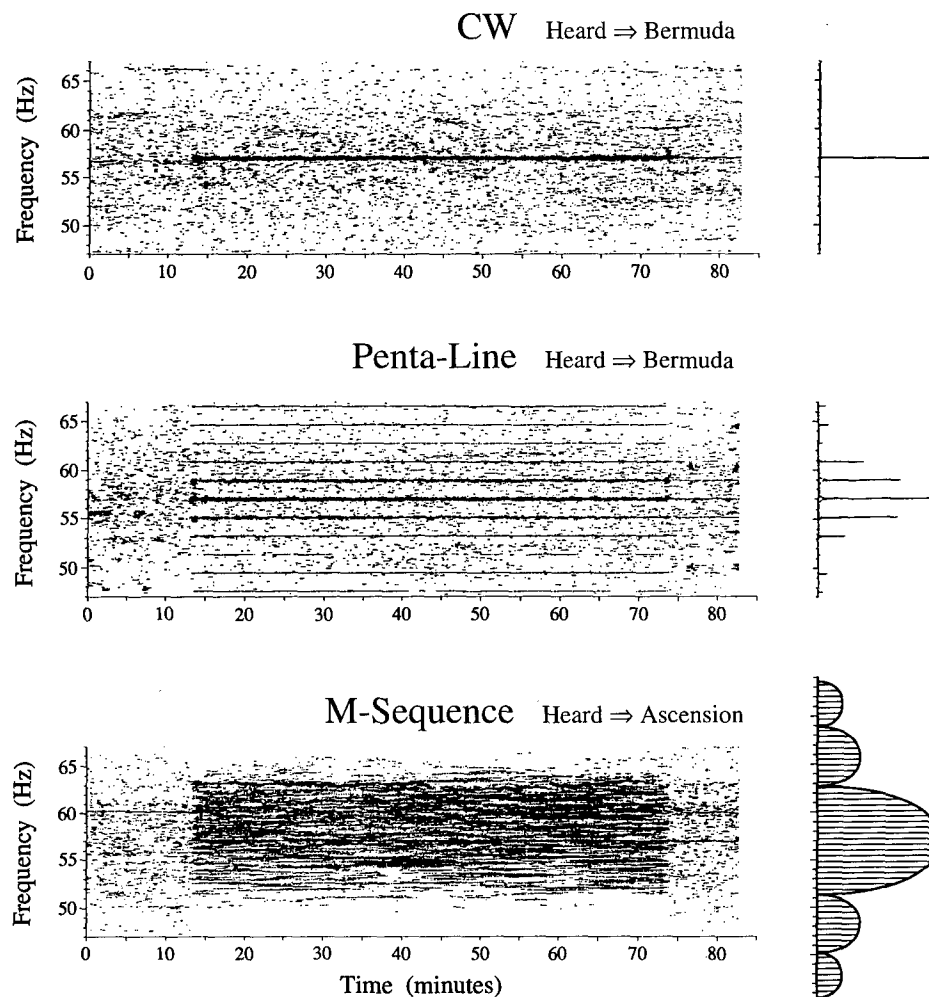


FIG. 4. Three types of HIFT signals as received at Bermuda (range 16 Mm, travel time 2.95 h) and at Ascension Island (9.2 Mm, 1.71 h). Note the 60-Hz interference line for the M-sequence, and the 57-Hz carrier "afterglow" from scattered arrivals. Spectra of the entire 60-min record are shown to the right.

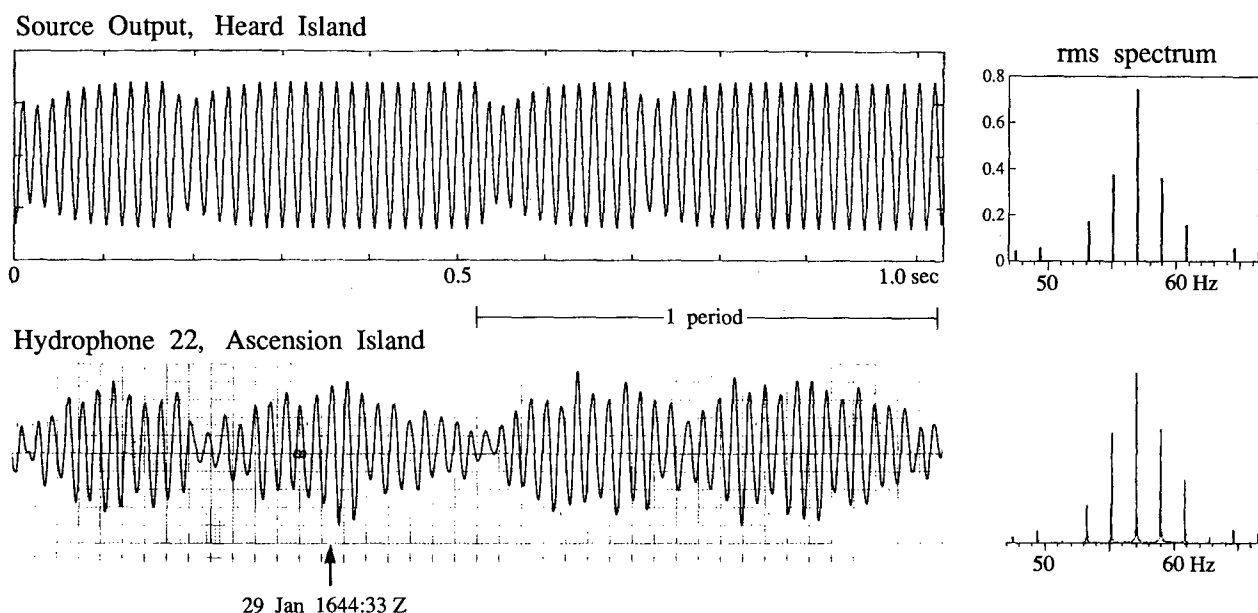


FIG. 5. An example of the pentaline signal in the time domain. Two periods of the 0.53-s sequence are shown. The upper panel shows a simulated signal and its spectrum; the lower panel gives the measured reception and the spectrum computed using 37 min of data.

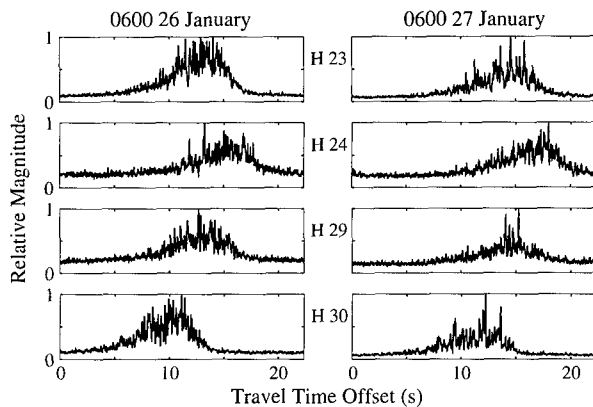


FIG. 6. Arrival pattern at four Ascension hydrophones recorded 24 h apart. Each panel is a 60-min incoherent average of a match-filtered (pulse compressed) 255-digit M-sequence. See Birdsall and collaborators⁹ for details.

the arrival patterns differ from day to day. H23 and H24 are within a few kilometers, yet the arrival patterns from a single transmission differ distinctly. This suggests that the source motion by 3 nautical miles (5.6 km) during a transmission run may contribute significantly to any decorrelation.

Figure 7 shows an interesting display of received signal and out-of-band noise on Krylov Seamount in the Eastern North Atlantic 12.5 Mm and 2.32 acoustic hours from Heard Island,⁵ as function of the number of sources that were transmitting. Another example from this data set (Fig. 8) is the output of a spectrum analyzer during the reception of a pentaline signal. The five spectral lines are clearly visible.

Measurements taken off South Africa,¹⁴ though closer to the source than Ascension, were generally of poorer quality

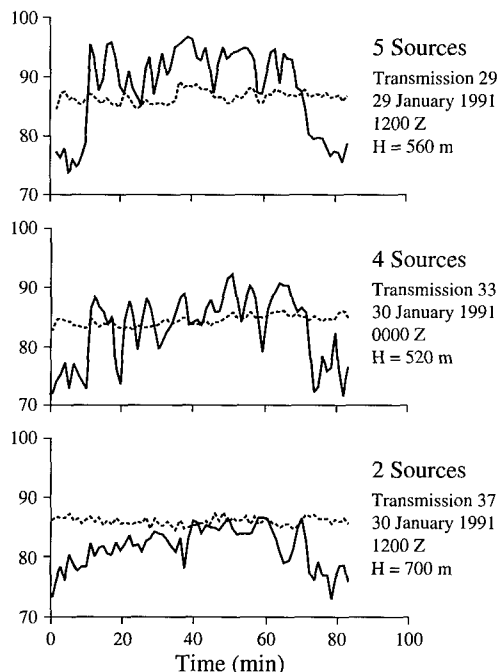


FIG. 7. Reception of the 57-Hz cw signal at Krylov Seamount in the Eastern North Atlantic.⁵ Solid line is signal power; dotted line is noise power density averaged over adjacent frequency bands in units of dB re: $1 \mu\text{Pa}/\sqrt{\text{Hz}}$. The signal-to-noise ratio degrades as the number of operative sources decreases.

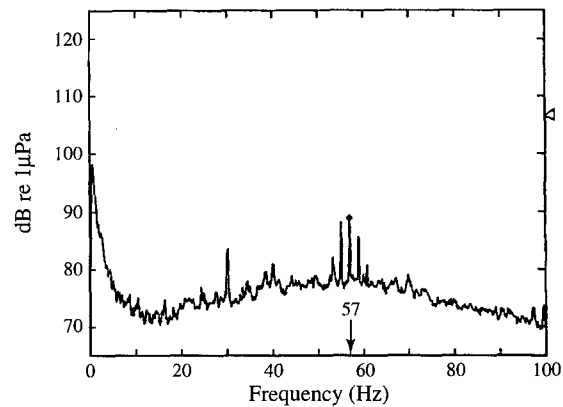


FIG. 8. Spectrum of pentaline signal at the Krylov Seamount.

(Fig. 9). The highly variable ocean hydrography associated with the Aguhlas Front and the extreme sea conditions (10-m swells) led to difficulties in deploying a hydrophone in an optimum location at sound channel axis depth.

A final example of data collected on a single, surface-suspended hydrophone is shown in Fig. 10. The top panel displays the incoherent 41-min average with excellent SNR. Comparison with the computed arrival pattern will be discussed later. The general conclusion is that single hydrophones can provide significant information.

V. RECORDS BY TOWED AND VERTICAL ARRAYS

Both towed arrays and vertical arrays were deployed during the HIFT to measure spatial properties of the HIFT signals as well as to provide array gain.

A. Canadian towed arrays

We were fortunate to have the participation of Canadian towed arrays from DREA (Defense Research Establishment Atlantic)⁶ and DREP (Defense Research Establishment Pacific).⁷ While designed for higher frequencies, both arrays

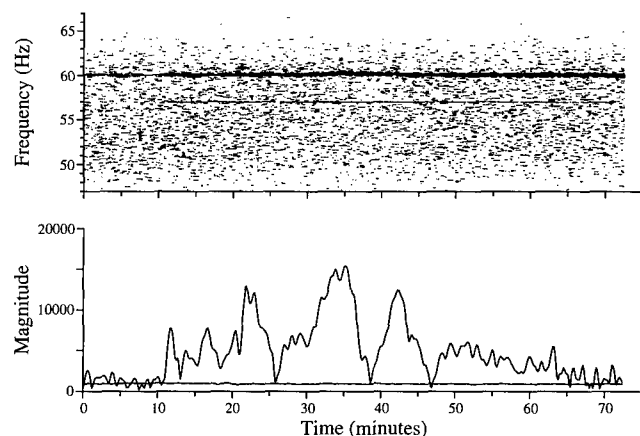


FIG. 9. The cw transmission received by the ship-suspended hydrophone off Capetown, S.A. (The line at ≈ 60 Hz is noise from the ship's electrical power.)

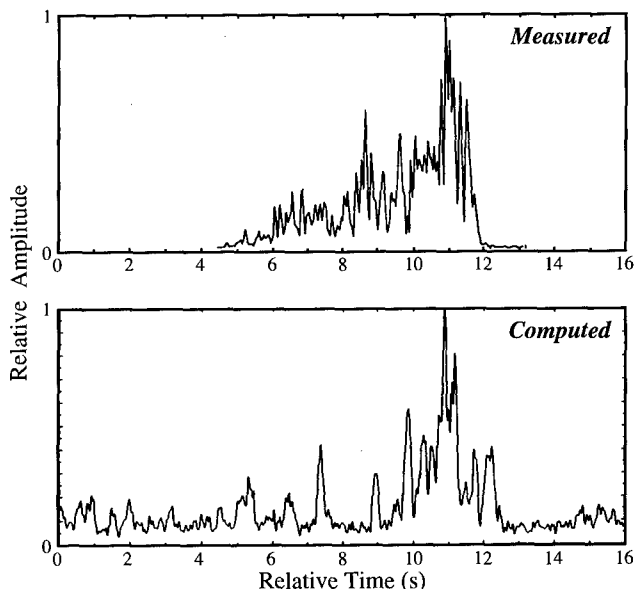


FIG. 10. Comparison of measured and computed arrival patterns at Christmas Island. The measured pattern is an incoherent average of 110 contiguous receptions (41 min) of a pulse compressed 255-digit M-sequence received on a surface-suspended hydrophone. The bottom panel computed by McDonald *et al.*¹⁷ uses 30 modes and 21 frequencies spanning from 52 to 62 Hz.

were very capable at HIFT frequencies; a large number of sensors and digital recording capability provided significant array gain.

The DREA towed array was deployed at depth between 100 and 200 m southeast of Cape Cod with unique opportunity to record signals on both sides of the Gulf Stream. The intensity of receptions varied with position consistent with hypotheses about bathymetric blockage by South America and mid-ocean islands. Figure 11 shows the estimated transmission loss as a function of position relative to the northern boundary of the Gulf Stream. Losses are approximately 135 dB south of the boundary and decrease (the intensity increases) by 10 dB toward the north as the SOFAR axis shoals to the array tow depth.

Along the West Coast, the DREP towed array was deployed off Monterey and San Diego, based upon the predictions of Chiu *et al.*¹⁵ In addition, we had available a U.S.

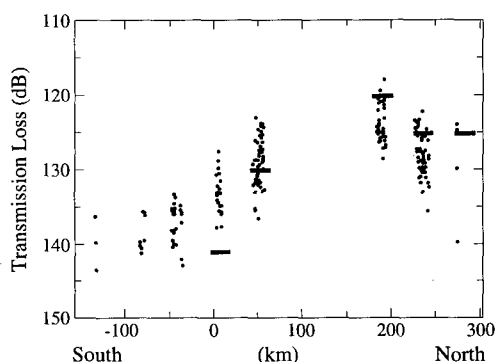


FIG. 11. Transmission loss (increasing downward) as function of position relative to the northern boundary of the Gulf Stream off Newfoundland⁷ at a range of 16.8 Mm.

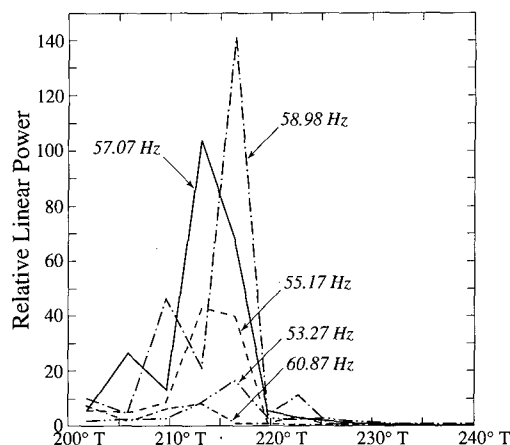


FIG. 12. Relative power as function of arrival bearing angle off California⁶ for the pentaline transmission 1500Z 29 January 1991.

Navy bottom-mounted horizontal line array and the vertical array off Monterey. Analyses were made difficult by large transmission losses, typically 140–150 dB, with signal levels of order 70 dB and SNR of -15 to -10 dB per Hz (single phone cw).

One of the speculations about global acoustics concerns horizontal refraction and multipaths,^{16,3} so measuring arrival power versus bearing was one of the principal goals for the towed array. Figure 12 plots power as a function of bearing for one of the pentaline transmissions to the DREP array⁶ towed at a depth of 300 m. There is a faint suggestion of horizontal multipath, but because of the low SNR the bearing and sidelobe variability can be equally well accounted for by noise effects.

B. Monterey vertical array

The vertical distribution of signal power is a major issue in the use of global acoustics to monitor ocean climate. In the HIFT two vertical arrays were deployed to measure the modal distribution of the received signals.⁸ One array was placed off Bermuda, but unfortunately it sank and no data were recovered. The second array, off Monterey, had 32 hydrophones with 45-m spacing covering the water column from 345 to 1740 m. It was tethered to the R/V POINT SUR.

The expectation prior to the HIFT was that all but the lowest-order modes would be strongly attenuated and the signals at long range would consist only of the gravest one or two SOFAR ducted modes. Several indications from the vertical array suggest that this is not the case. First, signal power is detected at depths up to 1700 m, which requires mode 6 or higher to be present. Second, an estimate of the vertical distribution of signal power can be found by measuring the frequency-vertical wave-number spectrum of the array data (Fig. 13). There are several peaks in the 57-Hz frequency band (slightly downshifted for Doppler). The separation in wave number of these peaks suggests up/down power up to at least mode 7. Unfortunately, the low SNR on the California coast limited the resolution of the wave-number spectra.

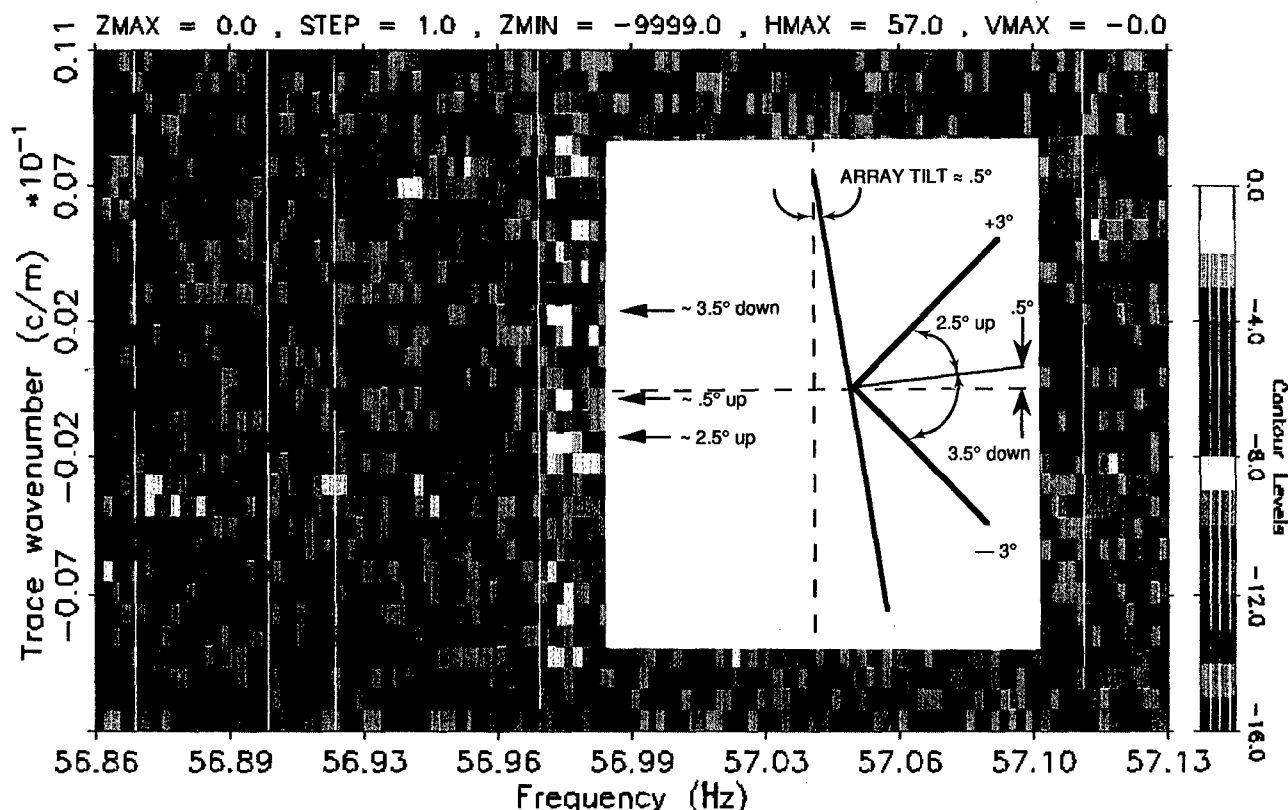
Narrowband 23 Channels
Wavenumber vs. Frequency

FIG. 13. Frequency wave-number spectrum for a cw signal recorded at the vertical array off Monterey.⁸ An intensive band centered at 56.97 Hz (down Doppler) has peaks at vertical wave numbers of approximately -0.002 , 0.000 , 0.002 , and 0.003 cycles/m. The spread in vertical wave numbers suggests the presence of modes up to mode number 7.

VI. PROBLEMS OF GLOBAL ACOUSTICS

HIFT has raised a series of issues largely ignored in the usual propagation experiments but critical to propagation on a global scale. Very few of the issues are "solved" in the HIFT papers, but the results obtained have suggested a strategy for future work.

A. Refracted geodesics

It has long been appreciated that the departure of the Earth from spherical shape is associated with a significant departure of geodesics (shortest distance between two points on a spheroid) from great circles. The departure increases sharply as one approaches antipodal ranges, and for points separated by exactly 180° there are, of course, an infinite number of great circles. In preparing for HIFT the computed ray paths were *refracted* geodesics, that is, they allowed for horizontal gradients in sound speed in addition to Earth flattening;² however, refraction was computed only for the horizontal gradients at the depth of the sound axis.

Heaney *et al.*³ generalized the foregoing treatment by computing the refracted geodesics separately for each mode. (In this sense, the pre-HIFT axial calculations constitute the limit of low mode numbers and high frequencies.) More im-

portantly, the Heaney constructions allowed for refraction by bottom topography, in addition to the effects of sound speed gradients and Earth flattening. The general statement governing refraction is that acoustic paths are repelled by shallow depths, high sound speed (warm water), and high latitudes. We refer to McDonald *et al.*¹⁷ for a discussion of these issues.

Over a flat bottom the separation in horizontal paths for low and high modes (or for axial and steep rays) is small as compared to the horizontal dimensions of the ocean temperature structure. Accordingly different modes measure nearly the same ocean structure. The situation may be quite different when one considers the combined effect of thermal and bathymetric refraction. Quite small differences in horizontal deflection may lead to grossly different bottom interactions and accordingly widely separated paths, so that different modes may sample quite different ocean regions. This appears to have been the case for at least one of the HIFT transmission paths.

B. Launch angles

One of the anticipated complications of HIFT was that the source ship moved at about 3 knots into the prevailing

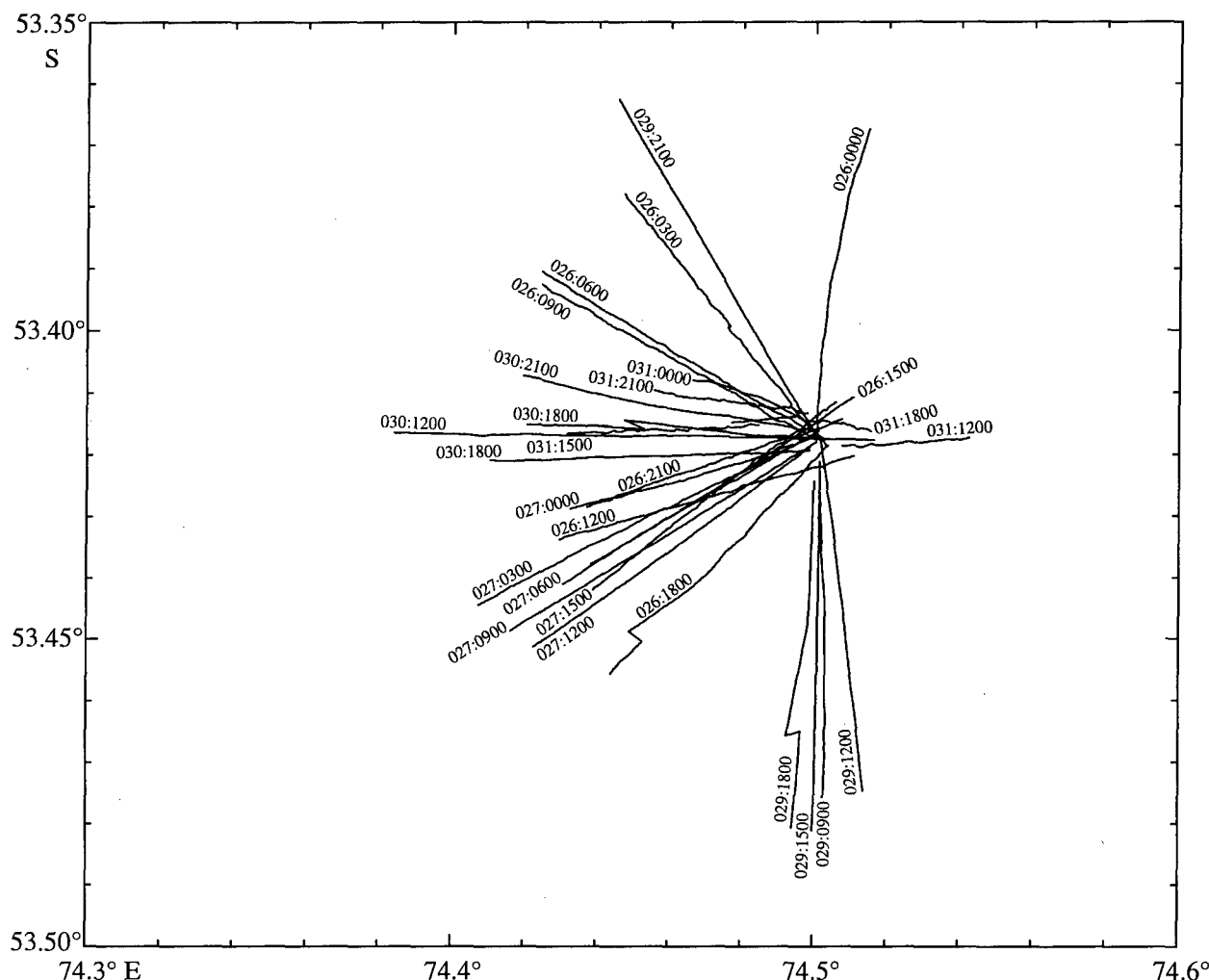


FIG. 14. GPS tracks of transmission runs at stated yeardays and start times. Starting point was kept as close as possible to 53.42° S, 74.5° E. All runs were on automatic pilot at 3 kn heading into the wind and waves.

wind and sea and induced a Doppler shift in the carrier frequency. This was removed early in the processing of received signals. To our surprise, even a *variability* in the ship's motion by a few percent as detected by Global Positioning Satellite (GPS) measurements was in excellent agreement with a slight Doppler variability.¹⁸ This is perhaps the most vivid demonstration of phase-coherent processing at megameter ranges.

An unexpected bonus occurred from knowing the precise Doppler shift for each reception. When combined with GPS navigation data from the R/V CORY CHOUEST, the observed Doppler shift allowed us to calculate horizontal launch angles from the source toward individual receivers.¹⁹ These angles were consistent even though the ship's course differed widely for different transmission runs (Fig. 14). Under the conditions of HIFT, Doppler-derived launch angle could be computed to an accuracy of $\pm 0.1^\circ$. (The accuracy could be further improved in future experiments.) From Heard Island to Ascension Island, the Doppler-derived azimuth was $268.06^\circ \pm 0.1^\circ$, compared to 266.05° for the refracted geodesic launch angle of mode 1 at 57 Hz. The conclusion is that the *a priori* estimate of the ray path was correct.

For comparison we note that the computed Ascension launch angle for the axially refracted geodesic is 260.18° and for the unrefracted geodesic it is 265.91° .

C. Tasman blockage

The situation is altogether different for the eastward path to the American West Coast.²⁰ One of the earliest confirmations that the signals from Heard Island had crossed the Pacific was from Whidbey Island. Calculation of the refracted geodesics from Heard Island through the Tasman Sea to this facility predicted receiver azimuths of 230° – 235° ; beam-forming at Whidbey Island indicated that the signals arrived from 20° further south, 215° . Using the Doppler-derived launch azimuth technique discussed earlier, we found that the signals arriving at Whidbey left Heard Island at an azimuth of 130° , not 115° as derived for the Tasman geodesic. Evidently the acoustic path went south and east of New Zealand through the "Polynesian window." A similar situation was found off the coast of southern California, where Heard and Chapman⁶ towed a horizontal line array and measured an arrival angle of 214° consistent with the Polynesian window.

These results raise two questions: (i) Do refracted paths

through the Polynesian window exist? (ii) Can one account for the absence of the “direct” path through the Tasman window? The answer to the first question is “yes.” McDonald *et al.*¹⁷ (their Table I and Fig. 5) list Polynesian paths to Monterey and southern California with moderate bottom losses; however, the computed signal intensity is larger for the Tasman path than for the Polynesian path. One can only surmise that the bottom losses were unexpectedly higher for the Tasman path and they rapidly increased for receiver locations to the north of Oregon. With regard to the second question, Forbes²⁰ suggests that the Tasman path was blocked by the ridges that lie in the northeastern sector of the Tasman Sea, between New Zealand and Fiji (and Samoa). The New Zealanders did receive strong signals in the center of the Tasman Sea, but the Japanese, listening near Samoa on the “downstream” side of the Lau Ridge, did not receive any of the HIFT signals. The rugged bathymetry that intrudes into the SOFAR channel near Fiji, Tonga, and Samoa appears to have severely attenuated the HIFT signals.

D. Differential Doppler

In megameter-range tomography, ray tilt is routinely measured by a short vertical array and has proven very useful in viewing the arrival pattern in tilt-travel time space. In the normal SOFAR sequence, the early arrival of steep rays is followed by the late arrivals of flat rays. Dzieciuch and Munk²¹ suggest that *differential* Doppler can be used to measure vertical tilt of rays even with a single hydrophone. For a horizontally moving source, steep rays should experience a smaller Doppler than flat rays. (The dependence of Doppler upon the projection of the ship’s course onto the horizontal launch azimuth has already been discussed in Sec. VI B.) It was found that differential Doppler for the 5-Mm transmission to Christmas Island does not follow the normal SOFAR sequence. However, the differential Doppler is not inconsistent with transmission through a sharp (nonadiabatic) front separating a polar surface duct from a temperate interior sound channel. Moreover, a moving source is associated with the creation and destruction of eigenrays at a rate comparable to what is observed. This raises the issue whether the transmission from a moving source through a sharp front might be responsible for some of the observed complexity of the arrival pattern. The following topics deal with theoretical efforts to explore this issue.

E. Ray propagation through a front

For orientation consider the situation in Fig. 15. The solid line corresponds to an axial (near-surface) polar ray that is converted at a discontinuous front into a fairly steep temperate ray. The dashed ray is axial in the temperate ocean, and a fairly steep RSR ray in the polar ocean. The path for each of these two rays consists then of two sectors: a slow axial sector and a rapid nonaxial sector. The sequence of arrival of these two rays (or of any other rays) is not obvious; it depends, among other considerations, on the relative length of the polar and temperate sectors, the ray tilt at the front (here set to zero), and the sound-speed profiles. The

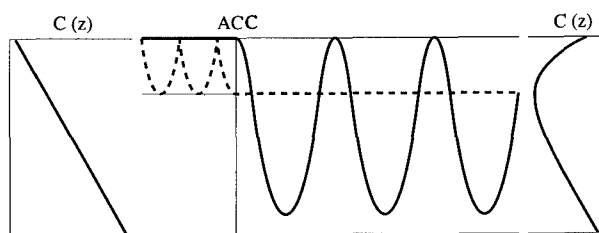


FIG. 15. Cartoon for a transition from RSR to RR propagation across the Antarctic Circumpolar Convergence (ACC). The temperate sound-speed profile (right) is associated with an interior sound channel; the high-latitude sound-speed profile (left) is associated with an axis along the surface. Dashed and solid lines represent limiting rays that are axial at temperate and polar latitudes, respectively.

figure is a convenient caricature to portray an essential element of the Heard Island transmissions through the Antarctic Circumpolar Convergence (ACC).

F. Mode propagation through a front

The most detailed discussion of modal propagation is given in the paper by McDonald *et al.*¹⁷ Their final result for Christmas Island is reproduced in Fig. 10 (bottom). Given the lack of synoptic information about sound speed along the path, this is as close as we can get to a comparison between measured and computed transmissions. The temporal spread and pulse shape are in reasonable accord. The calculations appear to capture the complexity in the arrival structure, but not the details.

Mode coupling is strong (we refer to the figures in Ref. 17). For the transmission to California, with an initial condition of mode 1 excitation only, the energy is redistributed over the New Zealand plateau among approximately the first eight modes. Past Chatham Rise, most of the energy is in modes 3 and 5. With a multimodal initial condition of modes 1–25 appropriate to a point source at 175 m depth, there is a modest exchange of energy until the New Zealand plateau, when modes above 9 disappear, with only a moderate redistribution thereafter. The result is consistent with the finding of Baggeroer *et al.*⁸ using the vertical array off Monterey, California.

Shang *et al.*²² have also used a modal decomposition to simulate some of the HIFT transmissions. They find strong coupling at the ACC. The computed spread for the lowest six modes is consistent with the measured spread. The authors emphasize that the relation between arrival time and frequency is not simple and monotonic, and it is possible to have multiple arrival peaks for any one mode, and a reversal in the expected order of mode arrivals.

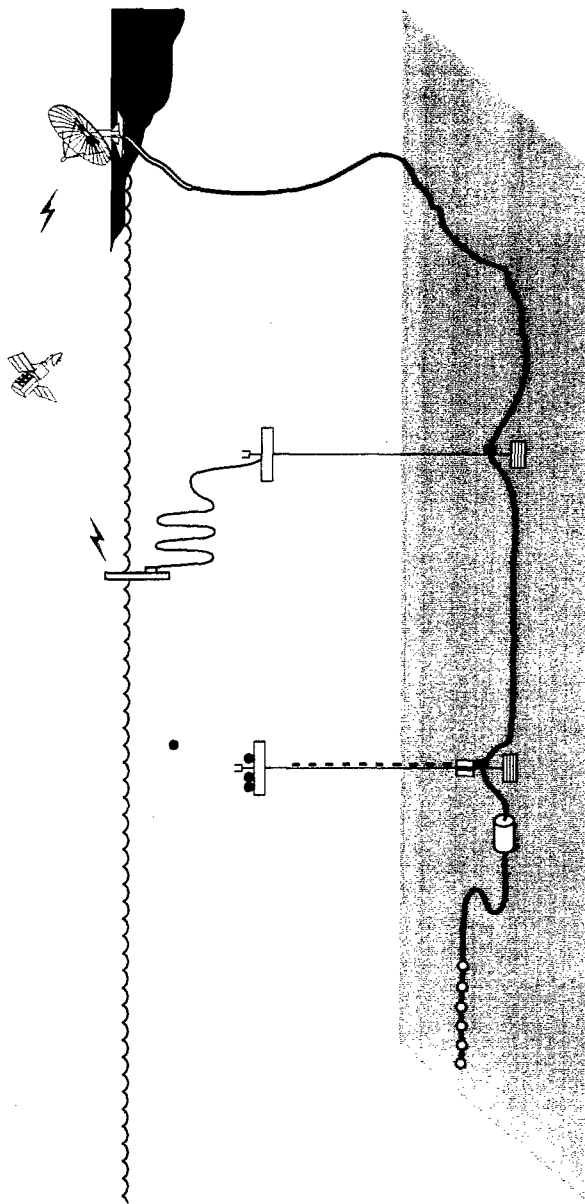
We make no attempt here to compare the different approaches. There is agreement that mode coupling across the ACC is an important consideration that needs to be taken into account for any interpretation of the observations. The ACC is associated with a change in the shape of the sound-speed profile, a transition from a surface duct to an internal duct. The corresponding ray transformation is from RSR to RR. Similarly, an intense warm eddy can split the SOFAR sound channel into a dual channel, and such a change in shape is accompanied by severe mode coupling, as expected.

ACOUSTIC THERMOMETRY OF OCEAN CLIMATE



ATOC - Node Engineering Advances for Global Network Expansion

- Sensors - 10-100 hydrophones (3-20dB gain)
- Processing - Low power signal analysis/clocks/control
- Battery options for 1-2 year life (refurbishable)
- Telemetry - Low cost fiber optics (\$2000/km)
 - Pop-up recorder modules
 - Spar buoy INMARSAT links
 - Low cost sea/shore interfaces & remote INMARSAT



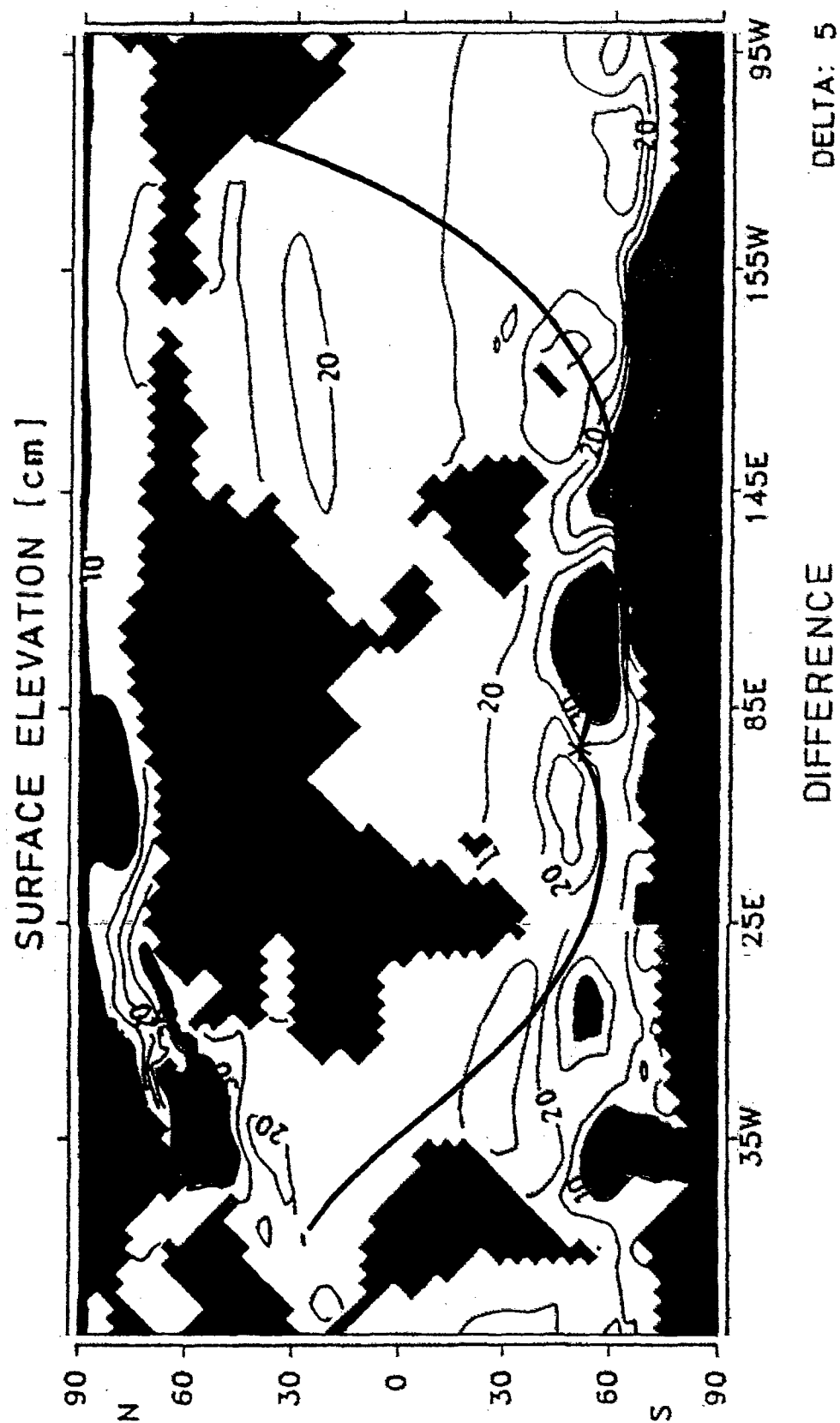


FIGURE 3. The change in sea level 50 years following CO₂ doubling (according to the Hamburg model). Here sea level serves as surrogate for upper ocean warming, and indicates the spatial structure of greenhouse warming.

G. Random field coupling

We need to be concerned also with mode coupling due to short scale inhomogeneities. A case in point is that of a horizontally homogeneous sound channel with a weak superposed field of mesoscale eddies. The analogous problem of mode coupling by an internal wave field has been studied by Dozier and Tappert.^{23,24} Their calculations indicate strong mode coupling between neighboring modes at distances of order 1 Mm. It is important that these problems be studied. Topological fronts, such as the ACC, can perhaps be avoided in future ATOC transmissions, but there is no way of escaping the ubiquitous presence of the mesoscale and internal wave fields.

VII. ACOUSTIC THERMOMETRY OF OCEAN CLIMATE (ATOC)

HIFT (planned for 10 days, carried out for 5 days) was, of course, never intended to address problems of climate variability. Upon returning from Heard Island, planning was initiated for obtaining the appropriate climate-oriented time series of acoustic travel times. The ATOC program did not get underway until early 1993.

Heard Island is not a candidate site for ATOC. It is too inaccessible, and its unique dual-ocean access is not appropriate for climate studies. We will concentrate on 5- to 10-Mm ranges; these appear to be acoustically feasible, and they are the appropriate scale for the study of climate variability. The reduced ranges permit sources of less intensity than those used for the HIFT.

Building on the experience gained from HIFT, we have designed and built sources of lower intensity (195 dB re: 1 μ Pa @ 1 m) and somewhat higher frequency (60–90 Hz) than those used for the global transmissions. At temperate latitudes where the sound channel axis is near 1 km, the intensity in the biologically important upper ocean will be reduced by more than 30 dB relative to HIFT.

The plan is to deploy two acoustic sources, one for transmission from Hawaii into the northern Pacific, the other for transmission from California northwestward into the North Pacific and southwestward toward a receiver at New Zealand. For receivers we shall again depend on the cooperative use of the bottom-mounted horizontal arrays at U.S. Navy NAVFAC stations. In addition we shall deploy several large-aperture vertical line arrays that were designed to resolve vertical modes up to mode 10. This is in response to the HIFT result that a major effort to understand the modal distribution is required for the interpretation of long-range transmissions. We regard this as an interim measure; in the long run we expect to depend upon simple, inexpensive autonomous receivers.

A crucial problem that has not been resolved by HIFT is the resolution, identification, and stability of individual features in the arrival pattern. It was necessary, if only for reasons of safety, for the R/V CORY CHOUEST to be underway during transmissions, headed into the winds and sea. Ship-towed arrays and surface suspended hydrophones were also in motion. We attribute some of the complexity in the HIFT arrivals to this motion and have designed ATOC for a fixed—

fixed geometry. Crossing the Antarctic Front must be a major contributor to the complexity of HIFT arrivals, and accordingly we have chosen more benign paths for ATOC. B.E. McDonald (personal communication) has suggested that mode coupling, once properly understood, may provide an opportunity (rather than a liability) for gaining range-dependent information.

Topographic blocking and scattering is a major problem. Sound is refractively repelled from shoaling water, and there are acoustic multipaths associated with islands, seamounts, and other topographic features. This has, of course, long been known, but was driven home by the unexpected West Coast arrival through the Polynesian window, which owes its existence to bathymetric scattering. We have placed a great effort in selecting ATOC paths that are as free as possible from bathymetric effects. It may be possible to identify stable scattered arrivals to provide temperature information along additional paths. HIFT records typically show a 15- to 20-min “afterglow” following the transmission, see Fig. 4.) For this and other reasons it would be worthwhile to include a moving cw source interlude in the proposed fixed geometry transmissions; this will provide very precise information on launch angle and help in the identification of scattered paths.

We do not view acoustic thermometry as a stand-alone methodology for monitoring ocean climate variability. For example, satellite altimetry with its fine horizontal resolution at the ocean surface nicely complements the acoustically derived information of the ocean interior.²⁵ The interaction with ocean modeling and prediction is of particular importance. The forthcoming ATOC measurements will provide the opportunity for interaction with an ongoing real-time modeling effort.

While the initial phase of ATOC concentrates its efforts in the Pacific, the long-term objective is to deploy sources and receivers in all the world's oceans. Plans are now being formulated in cooperation with several nations for monitoring the Atlantic, Indian, and Arctic Oceans.

¹S. Manabe and R. Stouffer, “Century scale effect of increased atmospheric CO₂ on the ocean-atmosphere system,” *Nature* **364**, 215–218 (1993).

²M. Munk and A. M. G. Forbes, “Global ocean warming: an acoustic measure?,” *J. Phys. Oceanogr.* **19**, 1765–1778 (1989).

³K. D. Heaney, W. A. Kuperman, and B. E. McDonald, “Perth–Bermuda sound propagation (1960): Adiabatic mode interpretation,” *J. Acoust. Soc. Am.* **90**, 2586–2594 (1991).

⁴A. Bowles, M. Smultea, B. D. P. De Master, and D. Palka, “Relative abundance and behavior of marine mammals exposed to transmissions from the Heard Island Feasibility Test,” *J. Acoust. Soc. Am.* **96**, 2469–2484 (1994).

⁵S. V. Burenkov, A. N. Gavrilov, A. Y. Uporin, and A. V. Furduev, and N. N. Andreyev, “Long-range sound transmission from Heard Island to Krylov Underwater Mountain,” *J. Acoust. Soc. Am.* **96**, 2458–2463 (1994).

⁶G. J. Heard and N. R. Chapman, “Heard Island Feasibility Test: Analysis of Pacific path data obtained with a horizontal line array,” *J. Acoust. Soc. Am.* **96**, 2389–2394 (1994).

⁷I. A. Fraser and P. D. Morash, “Observation of the Heard Island signals near the Gulf Stream,” *J. Acoust. Soc. Am.* **96**, 2448–2457 (1994).

⁸A. B. Baggeroer, B. Sperry, K. Lashkari, C. -S. Chiu, J. H. Miller, P. N. Mikhalevsky, and K. von der Heydt, “Vertical array receptions of the Heard Island transmissions,” *J. Acoust. Soc. Am.* **96**, 2395–2413 (1994).

⁹T. Birdsall, K. Metzger, and M. Dzieciuch, “Signals, signal processing, and general results,” *J. Acoust. Soc. Am.* **96**, 2343–2352 (1994).

¹⁰W. A. Kuperman and F. Ingenito, “Attenuation of the coherent component

- of sound propagating in shallow water with rough boundaries," J. Acoust. Soc. Am. **61**, 1178–1187 (1977).
- ¹¹R. C. Spindel, "Signal processing in ocean tomography," in *Adaptive Methods in Underwater Acoustics*, edited by H. G. Urban (Reidel, Dordrecht, The Netherlands, 1985), pp. 637–710.
 - ¹²D. R. Palmer, T. M. Georges, J. J. Wilson, L. D. Weiner, J. A. Paisley, R. Mathiesen, R. R. Pleshek, and R. R. Mabe, "Reception at Ascension Island, South Atlantic, of the transmissions from the Heard Island Feasibility Test," J. Acoust. Soc. Am. **96**, 2432–2440 (1994).
 - ¹³T. M. Georges, L. R. Boden, and D. R. Palmer, "Features of the Heard Island signals received at Ascension," J. Acoust. Soc. Am. **96**, 2441–2447 (1994).
 - ¹⁴G. B. Brundrit and L. Krige, "Heard Island signals through the Agulhas retroflection region," J. Acoust. Soc. Am. **96**, 2464–2468 (1994).
 - ¹⁵C. -S. Chiu, A. J. Semtner, C. M. Ort, J. Miller, and L. L. Ehret, "A ray variability analysis of sound transmission from Heard Island to California," J. Acoust. Soc. Am. **96**, 2380–2388 (1994).
 - ¹⁶W. Munk, W. C. O'Reilly, and J. L. Reid, "Australia to Bermuda, sound transmission experiment (1960) revisited," J. Phys. Oceanogr. **18**, 1878–1898 (1988).
 - ¹⁷B. E. McDonald, M. D. Collins, W. A. Kuperman, and K. D. Heaney, "Comparison of data and model predictions for Heard Island to California," J. Acoust. Soc. Am. **96**, 2357–2370 (1994).
 - ¹⁸M. Dzieciuch, W. Munk, and A. Forbes, "Interpretation of GPS offsets from a steady course," J. Atmos. Ocean Technol. **9**, 862–866 (1992).
 - ¹⁹A. Forbes and A. Munk, "Doppler-inferred launch angles of global acoustic ray paths," J. Acoust. Soc. Am. **96**, 2425–2427 (1994).
 - ²⁰A. M. G. Forbes, "The Tasman Blockage—an acoustic sink for the Heard Island Feasibility Test," J. Acoust. Soc. Am. **96**, 2428–2431 (1994).
 - ²¹M. Dzieciuch and W. Munk, "Differential Doppler as a diagnostic," J. Acoust. Soc. Am. **96**, 2414–2425 (1994).
 - ²²E. C. Shang, Y. Y. Wang, and T. M. Georges, "Dispersion and repopulation of Heard–Ascension modes," J. Acoust. Soc. Am. **96**, 2371–2379 (1994).
 - ²³L. B. Dozier and F. D. Tappert, "Statistics of normal mode amplitudes in a random ocean. I. Theory," J. Acoust. Soc. Am. **63**, 353–365 (1978).
 - ²⁴L. B. Dozier and F. D. Tappert, "Statistics of normal mode amplitudes in a random ocean. II. Computations," J. Acoust. Soc. Am. **64**, 533–547 (1978).
 - ²⁵W. Munk and C. Wunsch, "Observing the oceans in the 1990's," Philos. Trans. R. Soc. **307**, 439–464 (1982).

Signals, signal processing, and general results

Theodore G. Birdsall and Kurt Metzger

Department of Electrical Engineering and Computer Science, The University of Michigan, Ann Arbor, Michigan 48109-2122

Matthew A. Dzieciuch

Scripps Institution of Oceanography, University of California, San Diego, La Jolla, California 92093

(Received 23 August 1992; revised 17 May 1994; accepted 7 June 1994)

Acoustic path lengths in the Heard Island Feasibility Test ranged from under 1 Mm to 18 Mm (1 Mm is 1000 km). The signal set consisted of three basic waveforms: cw, pentaline, and M-sequence-modulated carrier. This set offered the opportunity for successful measurements given the large uncertainty in prior estimates of propagation loss, stability, and arrival spread. Receivers ranged from simple sonobuoy systems to elaborate horizontal and vertical arrays. International collaborators acquired data at a variety of sites worldwide. The resulting data has been collected and subjected to a summary form of frequency domain processing. Variations in the recorded spectral phases are largely the result of nonuniformity in the speed of the source ship as determined by GPS comparison. Time domain processing has shown that at all ranges the receptions exhibit exceptional stability.

PACS numbers: 43.30.Qd, 43.30.Pc, 43.60.Rw

INTRODUCTION

The fundamental question to be answered by the Heard Island Feasibility Test (HIFT) was whether the signaling techniques used in ocean acoustic tomography¹ could measure travel times to sufficient accuracy to detect global climate variability. The signal designer/processor's task was to choose a set of waveforms and processing techniques that would allow such measurements over distances ranging up to 18 Mm. Specific questions were (i) could signals propagate over paths of global length with sufficient energy to be useful, (ii) would the arrivals be stable, and (iii) would the arrivals be resolvable?

The transmitting site near Heard Island was chosen to acoustically illuminate the Atlantic and the Pacific ocean basins simultaneously. Propagation over ranges up to 18 Mm, using electrically controlled sources with precise wave shapes in contrast to explosive sources, had never before been attempted.

This paper describes the considerations that affected the signal design and source level requirements, the support provided to many of the participants, the resulting data set, and the frequency domain analysis of the initial data set. New techniques were used in discovering the cause of the common phase trajectory of the broadband receptions and in trying to understand the discrepancies between coherent and incoherently averaged arrival patterns.

I. SIGNAL DESIGN

Design considerations: The design goal was 20 dB processed output signal-to-noise ratio (SNR) on every significant arrival. Within the usual arrival time search this yields a negligibly small false alarm probability. The time-of-arrival precision is then $\frac{1}{10}$ of the nominal resolution of W^{-1} (the

reciprocal of the transmission 3-dB bandwidth). A precision of about 10 ms for the climate measurement goals of HIFT requires a bandwidth of at least 10 Hz.

The choice of the signal waveforms and the transmission schedule was influenced by the available acoustic sources and the long acoustic ranges. The propagation factors affecting the signal design are attenuation, spreading, scattering, and blockage.

Volume attenuation demands the use of very low frequencies (attenuation increases exponentially with the square of frequency). Using Thorpe's formula,² the 18-Mm attenuation loss at 57 Hz was estimated to be 5 dB for the Atlantic path and 3 dB for the Pacific path (because of differences in dissolved salts). A frequency of 57 Hz was chosen to avoid electrical machinery noise at both 50 and 60 Hz.

Geometric spreading is the major component of transmission loss for low-frequency propagation. Another component is the arrival time spreading between different ray paths (geometric dispersion), or equivalently the dependence on frequency of group speed (chromatic dispersion) of the underlying modal structure. At 18 Mm, minimum estimates were 3 s of time spread for a three mode model, but with some respected opinions that "60 to 100 seconds shouldn't be ruled out" (based on a "traveltime/150" deep ocean rule-of-thumb). The working conclusion was a (135 ± 10) -dB space-time spreading loss at 18 Mm.

Scattering by random boundaries can cause severe problems for RSR (refracted, surface reflected) paths passing through Antarctic polar water. At HIFT frequencies, the surface scattering is normally low, but could be fatally high with 20-m/s winds.

Refraction by seamounts was taken into account,³ but in the final analysis geometric blockage became a question for the actual measurements. An important finding was that the Tasman Sea window between Australia and New Zealand was closed.⁴

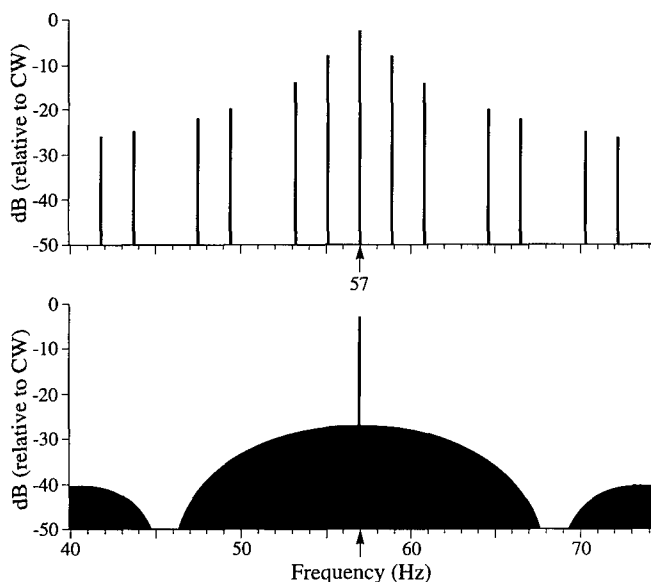


FIG. 1. Power spectra of pentaline (top) and M1 (bottom) signals.

Background noise at HIFT frequencies is set by shipping traffic. Expected levels of noise spectral density at 57 Hz range from 65 dB/ $\mu\text{Pa}/\sqrt{\text{Hz}}$ near quiet New Zealand to as high as 90 dB/ $\mu\text{Pa}/\sqrt{\text{Hz}}$ off the U.S. coast.²

The processing gain can be modeled as coherent averaging followed by incoherent averaging. Both styles of processing improve the SNR linearly with time, that is, by 3 dB per data doubling; however, there is a statistical efficiency factor,^{5,6} $\eta \leq 1$, in conversion from the coherent variable to the incoherent variable; $\eta \approx \frac{2}{3}$ when the conversion is done at high SNR, but much lower when the conversion is done at low SNR. (This is the basis for the fairly well-known *square law suppression* effect in radar and radio communications.) A conservative estimate for the length of time that coherent integration is effective in the ocean is 50 s, yielding a 17-dB gain. Adding a full hour of incoherent averaging raises the processing gain by another 14.3 dB (assuming SNR=5.7 dB after coherent averaging and a corresponding efficiency factor $\eta=0.37$).

The source level necessary to meet the experiment design goals was therefore based on 135-dB space-time spreading loss, 5-dB attenuation (Atlantic), spherical earth convergence beyond 10 Mm balancing a mild scattering loss, and a noise spectral density of 85 dB/ $\mu\text{Pa}/\sqrt{\text{Hz}}$. All of the long-range stations had horizontal arrays that would raise the input level at least 10 dB above the single hydrophone level. A full hour of coherent/incoherent processing was assumed to give a 31.3-dB gain. This implies that a source of at least 204 dB re: 1 μPa @ 1 m with a 10-Hz bandwidth was required.

Source considerations: The U.S. Navy provided the use of the R/V Cory Chouest with its vertical array of ten Hydroacoustics HLF4LL acoustic sources. The array was suspended through a well and centered on the sound channel axis at 175 m. The array spacing was 3.81 m. Each of the ten units could emit sound at a level of 206 dB re: 1 μPa @ 1 m (3.25 kW acoustic power). In the original specification, a source could not be energized for more than a few minutes

because of overheating of the hydraulic drive pumps. An elaborate scheme was therefore devised to energize sources in sets for short times and to allow sufficient time to cool before using the same ones again. It was not until 22 months later, in November of 1990, that it was determined that the HLF4LLs could sustain a full hour of transmission, and that enough units would be available so that five could be energized in parallel, raising the total transmitted power by 7 dB, and raising the axial beam power by yet another 7 dB.

The HLF4LL operating frequency of 57 Hz with a 14-Hz 3-dB bandwidth-matched HIFT's need for time resolution. An 88-ms pulse, consisting of 5 cycles at 57 Hz (11.4 Hz equivalent rectangular bandwidth), passed through the transducer, corresponds to a transmitted resolution of 112 ms and a matched filtered resolution of 142 ms. At high SNR (above 20 dB), the travel time precision is 11 ms.

Signal considerations: A computer (PC) synthesized the analog waveforms and controlled on/off scheduling. A crystal oscillator with a time stability of 1 part in 10^5 was included in the PC and used as the master oscillator. This was a very carefully considered decision. Absolute travel time was not an issue for the feasibility test but stability of the receptions was. For a transmission bandwidth of 11.4 Hz and transmission time of 3600 s, the time bandwidth product is 41 040, more than enough for stability analysis. The oscillator stability was also considered adequate since ship motion of up to 3 kn was expected (1 part in 10^3 variation of center frequency).

Three basic waveforms were chosen: a continuous-wave transmission of 57 Hz carrier alone (cw); a three-digit M sequence⁷ modulated carrier having five major spectral lines (pentaline, P); and four M-sequence modulated waveforms of different lengths for arrival time measurements (M1 through M4).

The cw is simple and the most noise penetrating. Pentaline is a three-digit M sequence with 10 carrier cycles per digit and a 45° modulation angle. It allows estimation of the received SNR from visual inspection of a power spectral analysis plot, as shown in Fig. 1 (top). The five dominant spectral lines contain 94% of the signal power.

The M-sequence technique uses well developed pulse compression processing to determine the multipath structure.⁷ The sequence modulates the carrier phase angle by $\pm 45^\circ$. This places half the waveform's power into the carrier line (matching the Pentaline's noise penetration, and also allowing detection on a spectrum analyzer) and the remaining half into the sideband lines. A digit of 5 carrier cycles was based on the HLF4LL bandwidth and the desired time resolution. The fundamental design numbers of "5 cycles" and "45°" were fixed in 1989.

The M-sequence periods should be chosen long enough to encompass all significant arrivals, yet short enough that coherent integration is not degraded. The periods are slightly less than 22.5, 45, 90, and 180 s for M1 to M4, respectively, compared to the conservatively estimated minimum coherent integration time of 50 s. The corresponding sequence laws in octal format⁸ are 537, 1473, 2033, 5747 (digit lengths 255, 511, 1023, 2047). All four M-sequence signals have power spectral densities proportional to $\text{sinc}^2[(f-57)/11.4]$. Figure

TABLE I. Transmission time (GMT), signals, source elements energized (element 1 on top), power level (*re*: 1 μ Pa @ 1 m, including directivity), ship speed (m/s) and heading (degrees East of North, **no GPS). Unless otherwise noted, transmissions terminated 1 h after starting until 31 January, when they terminated 0.5 h after starting.

| Time | Signal | Elements | | | | | SL+DI | Speed | Heading |
|-----------------|--------|----------------------------------|---|---|----|----|-------|-------|---------|
| 26 January 1991 | | | | | | | | | |
| 0000:51 | cw | 1 | 3 | 5 | | | 215.1 | 1.5 | 9.58 |
| 0002 | | 1 | 3 | 5 | 7 | | 217.6 | | |
| 0050:51 | | Off | | | | | | | |
| 0053 | | 1 | 3 | 5 | 7 | | 217.6 | | |
| 0300 | P | 1 | 3 | 5 | 7 | 10 | 219.5 | 1.61 | 320.70 |
| 0600 | M1 | 2 | 4 | 6 | 8 | 10 | 221.1 | 1.64 | 300.08 |
| 0900 | M3 | 2 | 4 | 6 | 8 | 10 | 221.1 | 1.58 | 298.93 |
| 1200 | cw | 2 | 4 | 6 | 8 | 10 | 221.1 | 1.54 | 254.53 |
| 1500 | P | 2 | 4 | 6 | 8 | 10 | 221.1 | 1.54 | 232.71 |
| 1525 | | 4 | 6 | 8 | 10 | | 219.3 | | |
| 1800 | M1 | 1 | 4 | 6 | 8 | 10 | 220.7 | 1.60 | 224.96 |
| 1819 | | 3 | 4 | 6 | 8 | 10 | 221.0 | | |
| 2100 | M4 | 3 | 4 | 6 | 8 | 10 | 221.0 | 1.34 | 251.67 |
| 27 January 1991 | | | | | | | | | |
| 0000 | cw | 3 | 4 | 6 | 8 | 10 | 221.0 | 1.29 | 254.09 |
| 0300 | P | 3 | 4 | 6 | 8 | 10 | 221.0 | 1.92 | 243.69 |
| 0600 | M1 | 3 | 4 | 6 | 8 | | 218.7 | 1.50 | 239.70 |
| 0601 | | 3 | 4 | 6 | 8 | 10 | 221.0 | | |
| 0900 | M2 | 3 | 4 | 6 | 10 | | 218.2 | 1.81 | 238.66 |
| 0902 | | 1 | 3 | 4 | 6 | 10 | 219.8 | | |
| 0918 | | 3 | 4 | 6 | 10 | | 218.2 | | |
| 0950 | | 3 | 4 | 6 | 7 | 10 | 220.2 | | |
| 1200 | cw | 1 | 3 | 4 | 6 | 10 | 219.8 | 1.71 | 234.36 |
| 1204 | | 1 | 3 | 4 | 6 | | 217.9 | | |
| 1205 | | 1 | 3 | 4 | 6 | 7 | 220.0 | | |
| 1215 | | 3 | 4 | 6 | 7 | | 218.5 | | |
| 1230 | | 3 | 4 | 5 | 6 | 7 | 220.6 | | |
| 1500 | P | 3 | 4 | 5 | 6 | 7 | 220.6 | 1.55 | 237.90 |
| 1513 | | 3 | 4 | 5 | 6 | | 218.7 | | |
| 1516 | | 1 | 3 | 4 | 5 | 6 | 220.2 | | |
| 1544 | | 3 | 4 | 5 | 6 | | 218.7 | | |
| 1600 | | Array recovered for refurbishing | | | | | | | |
| 28 January 1991 | | | | | | | | | |
| 0900 | M3 | 2 | 3 | 4 | 5 | 9 | 220.6 | 1.68 | 178.91 |
| 0910 | | 3 | 4 | 5 | 9 | | 219.1 | | |
| 0912 | | 3 | 4 | 5 | 6 | 9 | 220.8 | | |
| 0914 | | Each off. | | | | | 218.8 | | |
| 0916 | | 3 | 4 | 5 | 6 | 9 | 220.8 | | |
| 1200 | cw | 3 | 4 | 5 | 6 | 9 | 220.8 | 1.77 | 172.96 |
| 1500 | P | 3 | 4 | 5 | 6 | 9 | 220.8 | 1.81 | 180.95 |
| 1800 | M1 | 3 | 4 | 5 | 6 | 9 | 220.8 | 1.74 | 183.96 |
| 1837 | | 3 | 4 | 5 | 6 | | 218.7 | | |
| 2100 | M4 | 3 | 4 | 5 | 6 | | 218.7 | 1.98 | 328.91 |
| 30 January 1991 | | | | | | | | | |
| 0000 | cw | 3 | 4 | 5 | 6 | | 218.7 | 1.03 | 335.** |
| 0300 | P | 3 | 4 | 5 | 6 | | 218.7 | 1.49 | 313.** |
| 0600 | M1 | 3 | 4 | 5 | 6 | | 218.7 | 1.59 | 300.** |
| 0900 | M2 | 3 | 5 | | | | 212.4 | 1.70 | 270.** |
| 0940 | | 3 | 6 | | | | 211.4 | | |
| 1200 | cw | 3 | 6 | | | | 211.4 | 2.09 | 270.63 |
| 1500 | P | 4 | 6 | | | | 213.0 | 1.61 | 268.28 |
| 1800 | M1 | 4 | 6 | | | | 213.0 | 1.77 | 273.07 |
| 2100 | M3 | 3 | 4 | 6 | | | 216.2 | 1.44 | 280.29 |
| 2117 | | 3 | 6 | | | | 211.4 | | |
| 31 January 1991 | | | | | | | | | |
| 0000 | cw | 6 | | | | | 205.2 | 1.16 | 289.17 |
| 0300 | P | 6 | | | | | 205.2 | 1.44 | 10.** |
| 0600 | M1 | 6 | | | | | 205.2 | 2.06 | 327.** |
| 0900 | M4 | 6 | | | | | 205.2 | 1.59 | 328.** |
| 1200 | cw | | | | | | | 1.27 | 266.41 |
| 1213 | | 3 | | | | | 205.6 | | |
| 1500 | P | 3 | | | | | 205.6 | 1.91 | 267.84 |
| 1800 | M1 | 3 | | | | | 205.6 | 1.41 | 273.48 |
| 2100 | M2 | 3 | | | | | 205.6 | 1.62 | 277.28 |

TABLE II. Nominal site locations, distances, and expected travel times. International participants were from Australia, Canada, France, India, Japan, New Zealand, South Africa, Soviet Union, and the United States.

| Nominal site | Latitude | Longitude | Distance | | Travel time | |
|------------------------|----------|-----------|----------|---------|-------------|------|
| Ascension Island (USA) | 8.07 S | 14.42 W | 9.21 Mm | 4974 nm | 102 m | 27 s |
| Bermuda (USA) | 31.92 N | 64.17 W | 15.95 Mm | 8615 nm | 177 m | 26 s |
| Cape Town (SA) | 36.95 S | 16.90 E | 4.72 Mm | 2547 nm | 52 m | 27 s |
| Los Angeles (CA) | 34.00 N | 124.00 W | 17.40 Mm | 9396 nm | 193 m | 31 s |
| Nova Scotia (CA) | 38.00 N | 68.00 W | 17.40 Mm | 9396 nm | 193 m | 30 s |
| Christmas Island (AU) | 10.73 S | 105.97 E | 5.51 Mm | 2973 nm | 61 m | 14 s |
| Sri Lanka (IN) | 3.00 N | 82.00 E | 6.31 Mm | 3407 nm | 70 m | 10 s |
| Heard Island (USA) | 53.42 S | 74.50 E | 0.00 Mm | 4 nm | 0 m | 5 s |
| Kerguelen (FR) | 47.63 S | 80.98 E | 0.62 Mm | 335 nm | 6 m | 53 s |
| Krylov Seamount (SU) | 17.54 N | 30.14 W | 12.52 Mm | 6762 nm | 139 m | 16 s |
| Mawson Station (AU) | 67.60 S | 62.83 E | 1.69 Mm | 915 nm | 18 m | 50 s |
| Monterey (USA) | 35.50 N | 123.00 W | 17.59 Mm | 9499 nm | 195 m | 38 s |
| Tasman Sea (NZ) | 33.73 S | 162.13 E | 6.91 Mm | 3733 nm | 76 m | 52 s |
| Samoa (JA) | 9.00 S | 177.00 W | 10.39 Mm | 5611 nm | 115 m | 34 s |
| Tasmania (AU) | 43.93 S | 146.00 E | 5.12 Mm | 2767 nm | 56 m | 59 s |
| Whidbey Island (USA) | 33.00 N | 120.00 W | 17.46 Mm | 9428 nm | 194 m | 11 s |

1 (bottom) shows the line spectrum of the 255-digit M1 signal. The individual lines are so close that they plot as a solid area; the carrier power is 24 dB above the adjacent sideband lines. For the longer sequences, this ratio increases by 3 dB with each period doubling.

Dispersion was a concern in the design of the experiment. An advantage of the M-sequence processing⁷ is that chromatic dispersion has no effect on the pulse compression of the waveform. The processed waveform is the same as that of a single digit transmitted periodically, using the same period, digit duration, and total energy. The processed output is dispersed as it would be from the equivalent isolated pulse. Identification and correction for dispersion can be accomplished after the M-sequence processing.

The planned transmission schedule was 1 h on, and then 2 h off. The waveforms were sent in the sequence

cw, P, M1, M2; cw, P, M1, M3; cw, P, M1, M4

and then repeated after 36 h, starting on 0000Z 26 January 1991 (Z is Greenwich Mean Time). Table I lists the transmissions during the 6-d test.

II. RECEIVERS

Table II lists the nominal locations of the receiving sites along with the ranges and expected propagation times to the sites from the transmitter location.

The United States provided self-contained receiving systems to international investigators who would station a ship at a receiving site. In particular, receivers were provided at Cape Town, Christmas Island, Sri Lanka, Kerguelen, Mawson Station, Tasman Sea, and Tasmania.⁹ Each system consisted of sonobuoys, an associated FM radio transmitter and receiver, and a data acquisition computer. These systems received, amplified, bandpass-filtered, sampled, and digitized a single hydrophone channel. Sampling at four times the carrier greatly simplifies the complex demodulation process. The sample rate was $4 \times 57 = 228$ Hz. The sample rate clocks

were derived from low-cost, commercially available 0.01% accurate crystal oscillator modules (corresponding to a Doppler shift of about 0.3 kn).

The stations manned at Bermuda and Whidbey Island monitored U.S. Navy bottom-mounted hydrophone arrays in the Atlantic and Pacific, respectively. Data were taken with an eight-channel version of the computer used in the sonobuoy systems. At Ascension Island, eight spatially distributed bottom-mounted hydrophones (roughly at axial depth), which are part of the U.S. Air Force Missile Impact Landing System (MILS) were monitored. Data were taken on two four-channel versions of the sonobuoy systems.

A Soviet research ship near Krylov Seamount manned a vertical array. Electronics problems limited the number of hydrophones to 3 at near axial depth. Japanese scientists recorded data from a hydrophone located at axial depth onto digital audiotape. They were located near the island of Samoa in the tropical Pacific. Canadian Defence Research Establishment scientists from Pacific and Atlantic laboratories were involved. The Pacific group (DREP) towed a 128-element horizontal array about 750 km west of Los Angeles and the Atlantic group (DREA) towed an 8-element horizontal array a few hundred kilometers south of Nova Scotia. A multi-institutional U.S. effort placed a 21-element vertical array a few hundred kilometers southwest of Monterey.

III. PROCESSING

The computers used in the sonobuoy, NOAA, and University of Michigan systems were economical 16-MHz 386SX PCs, plus an analog-to-digital converter, and a clock/filter board designed specifically for HIFT.

On-line processing: The computer's time-of-day clock was set manually and used to start data acquisition based on the receiver position. To assay the local background noise and to allow for inaccuracies in clock time, the sampling started 12 min prior to the first expected arrival and lasted 12 min beyond the last expected arrival. A real-time spectral analysis program complex-demodulated the data, formed

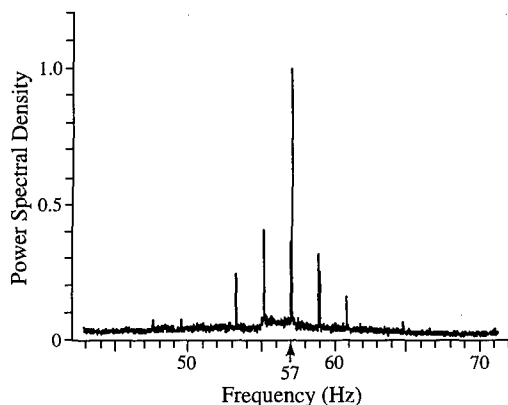


FIG. 2. On-line display of a pentaline reception at Bermuda. The power spectrum was generated by incoherently averaging 16 consecutive demodulating type FFTs with time window of 71.9 s each. The signal peak is at 57.06 Hz and the output SNR is 27.61.

FFTs, and displayed an incoherent average of the most recent transforms (Fig. 2).

The University of Michigan surveyed for reception quality and archived the data onto optical disk. This data was immediately available to the HIFT Principal Investigators, and to others since February 1993.

Data survey: The initial data survey consisted of a single page of frequency domain derived information for each reception. The *spectrogram* (Fig. 3, top) was formed by taking successive 71.9-s FFTs with a data overlap of 7/8 between transforms. The FFTs were "demodulator style" (i.e., they preserved phase across computational time boundaries) and the data were amplitude weighted with a Hamming window. The frequency range was then restricted to ± 10 Hz around the nominal carrier and the median magnitude level was determined in this range (median computation is fast and provides a background level that is relatively uncontaminated by the signal if the band analyzed is sufficiently wide). Each frequency bin output with magnitude 2.5 times the median was noted by plotting a dot at the appropriate frequency and time.

This result is very effective in displaying the frequency structure of the reception, both signal and noise. The transmission shown in Fig. 3 is a pentaline signal. The dominant noise near 50 and 58 Hz is due to the monitoring ship's propellers. The carrier and two adjacent lines continue for about 5 min past the direct reception (at 72–77 min), probably as a result of reflections from distant seamounts.

Going downward in Fig. 3, the *restricted bin* plot spans that portion of the frequency range corresponding to a ± 6 -knot Doppler around the carrier. The index of the bin containing the largest value exceeding 2.5 times the median was *marked*. A histogram was computed and the bin containing the greatest number of marks was declared *the carrier bin*. The center frequency of the carrier bin is the primary estimate of the received carrier frequency. This *qualified voter* technique is new; it is based on detection theory. This is our first experience with a carrier from a moving source that was stable for such a long duration.

A new technique developed for HIFT is the refined es-

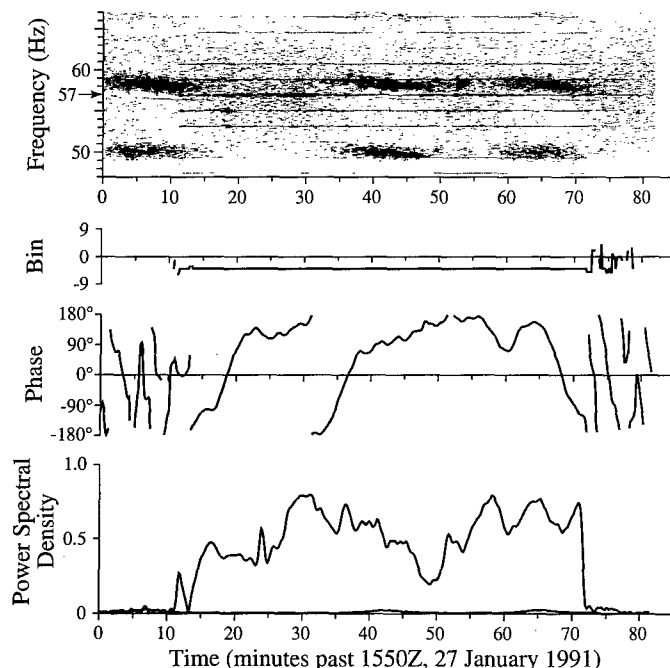


FIG. 3. An *f* summary at Christmas Island, 27 January 1500Z transmission. Top shows spectrogram of reception data, a restricted bin plot showing the most likely carrier bin, the carrier phase using the final estimated Doppler, and the magnitude of the carrier bin. Arrival time is reckoned from 1549:56Z. Frequency bin width is 13.9 mHz.

timate of the received carrier Doppler shift using the measured phase of the carrier. A two-pass method was used. On the first pass the phase change between successive transforms was calculated. If both magnitudes exceeded 2.5 times the median level and if the phase change was less than 90° , the change was included in the average. The phase record was then adjusted to remove this average phase rate. The same process was repeated, and the second average phase change added to the first. Two passes reduces the ambiguity caused by large phase jumps between records. The average phase rate therefore corresponds to a constant instantaneous frequency or an adjustment to the Doppler shift of the carrier line. The resulting value can be scaled using the appropriate sound speed; this was used to estimate the ship speed projected in the direction of the receiver and hence the launch angle of the sound at the source.¹⁰ The third plot is the residual phase after removing the final average phase rate.

The fourth plot is the magnitude of the carrier plus noise. The magnitude of the median is also plotted and is evident along the baseline. The low power carrier reception between 72 and 77 min can also be seen.

The marks from the restricted bin plot were used to determine when the carrier was in the carrier bin and to determine when no signal was present (no mark in any restricted bin). The signal level *S* on the designated carrier line was computed using the rms carrier level. The noise level *N* was estimated by the average median value of the spectral magnitude in a 20-Hz band centered around the carrier when the signal was off. The S/N ratio is tabulated as the processed SNR. The noise level *N* estimated by the median is 1.18 times the standard deviation of the noise assuming Gaussian

TABLE III. An index number (modulo 10) from 1 to 62 is placed on the top and bottom. Transmission signals consist of waveforms C for carrier, P for Pentaline, and 1, 2, 3, 4 for M sequences. *F* summary plots at each of the stations are coded as follows: C, carrier receptions of sufficient quality to determine magnitude and frequency; P, Pentaline reception with at least two lines adjacent to the carrier line that are discernable; 1, 2, 3, or 4, M sequence reception of sufficient quality for time domain processing; X, data set acquired but there are no significant indications of a received signal; O, source was not active but data was acquired; T, trouble in the recording; A, data are being analyzed by other investigators.

| | |
|---------------------|---|
| Transmission Index | 1234567890123456789012345678901234567890123456789012 |
| Transmission Signal | CP13CP14CP12CP_____3CP14CP12CP13CP14CP12_____ |
| Ascension Island | CPCCPCCCPCCCP_____3CP14CP12CP13CTCCCCC2O_____ |
| Bermuda | CPCCCP14CP12CPOO_____OO3CP14CPCCCP1CCPCCCPCCOOOO |
| Cape Town | _____XXX_____OO_____O_OOOXXXCXCPXXXXCXXX_XXXXXOOO_ |
| Los Angeles | _____AAAAAAAAAAAAAAAAAAAAA_____ |
| Nova Scotia | _____AAAAAA_ AAA_____ |
| Christmas Island | _____3CP14CP12CPOOOTOTOT_____TTTPCCCPCC_____ |
| Sri Lanka | CP_____PCCX_____CCPOOOOOOO_O_____OCCPC_____PCCCC_____O_____ |
| Heard Island | _____CP14CP12_____4_____ |
| Kerguelen | _____P_P_____C_____3C_____ |
| Krylov Seamount | CPCCCP4CP1CCP_____CCPCCCPCCCPCCCCCCCCC_____ |
| Mawson Station | _____X_XXOO_O_OOOOOOOO_____XX_XXXXTXXXXTXX_____ |
| Monterey | _____AAAA_AAAA_____AA_____AA_____ |
| Tasman Sea | _____C_____C_PCC_____OO_____ |
| Samoa | _____XXXX_____XXOO_____OOOO_____XXXX_____XXXX_____OOOO_____ |
| Tasmania | _____OOOXXXXXXXXXXXXXXXXXXXXTXXO_____ |
| Whidbey Island | CXXXXXXXXCPCCCP_OOOOOOOO_____OCCXXCPCCCCCXXXXXXXO_____ |
| Transmission Index | 1234567890123456789012345678901234567890123456789012 |

statistics. The equivalent bandwidth of a Hamming weighted FFT bin is 1.36 times the (1/71.9-Hz) bandwidth without weighting.¹¹ Using these bandwidth corrections, the signal-power-to-noise-power spectral density ratio is then

$$\frac{S}{N_0} = \frac{S}{N} \frac{S(1.18)(1.36)}{(71.9)}, \quad \left(\frac{S}{N_0} \right)_{\text{dB}} = \left(\frac{S}{N} \right)_{\text{dB}} - 16.5. \quad (1)$$

Table III summarizes the individual receiving sites and indicates the transmissions acquired at each site.

IV. PROPAGATION LOSS

The first question for HIFT was "how loud was it?" The answers sought were the propagation losses from Heard Island to the various receivers, to provide estimates for future long-range experiments.

Ten sites had sufficient data to estimate the transmission loss (Fig. 4). The Krylov Seamount, Nova Scotia, and Los Angeles receivers were calibrated. At other stations, we depend on the measured SNR and the very rough estimates of local noise level. The transmission loss (TL) is the difference of the transmitted power level and the received level. The transmitted power level is the total source level (SL), plus the array gain (DI, directivity index), compensated by the fraction of the signal power assigned to the sidebands (SB). The axial beam level (SL+DI) is tabulated in Table I. The received level is then estimated according to

$$TL = (SL + DI - SB) - [(N_0)_{\text{dB}} + (S/N_0)_{\text{dB}}]. \quad (2)$$

A least-squares fit of $(S/N_0)_{\text{dB}}$ and axial source level over all receptions at Ascension Island and Bermuda confirmed that

the stations were responding to axial source level (SL+DI), not average source level (SL).

Cylindrical and spherical spreading loss curves are given by

$$Dr_e \sin(R/r_e), \quad Rr_e \sin(R/r_e), \quad (3)$$

respectively, where R is the range, r_e is the radius of the Earth, and $D=5$ km is a conservative depth ensonification. For $R \ll r_e$, the equations reduce to the standard flat earth approximation. For long ranges, the losses are roughly 104 dB for cylindrical spreading and 137 dB for spherical spreading, and are surprisingly range-insensitive.

Since the measurements are single-frequency single-depth without resolution into individual ray paths or modes, one expects something like cylindrical spreading. The measured/estimated losses range from 115 to 150 dB, 10–45 dB above cylindrical spreading. A minor amount of the measured loss is attributable to attenuation and surface scattering. We attribute the loss above spherical spreading to blockage, in the Atlantic (Bermuda) perhaps by the mid-Atlantic ridge, and in the Pacific (Whidbey and Los Angeles) perhaps by the Antarctic continental shelf and by the Chatham Rise. The high Tasman Sea loss on 30 January 0600Z occurred when the receiver was in the acoustic shadow of Tasmania. Observations from Whidbey Island confirmed that the path through the Tasman Sea to Samoa was blocked and that the sound reached to a latitude of about 40°N on the U.S. west coast from a path to the east of New Zealand.⁴

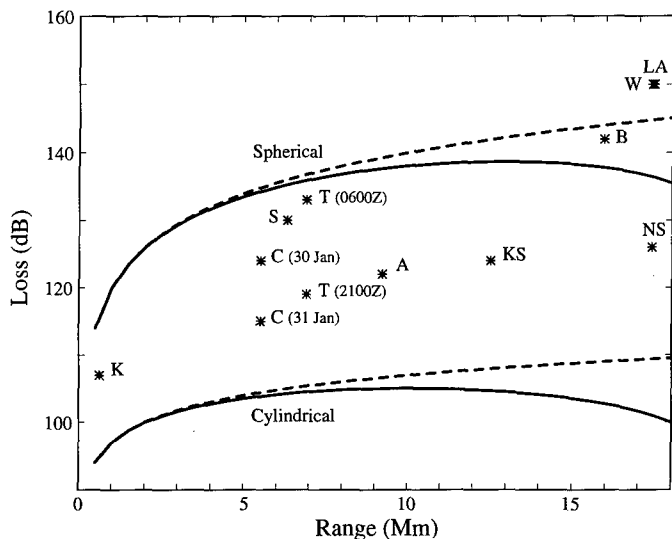


FIG. 4. Spreading loss as compared to cylindrical and spherical models; dashed line is the flat Earth approximation. The stations are coded as follows: K, Kerguelen; C, Christmas Island; S, Sri Lanka; T, Tasman Sea; A, Ascension; KS, Krylov Seamount; B, Bermuda; NS, Nova Scotia; W, Whidbey Island; and LA, Los Angeles.

V. PHASE STABILITY

The measured phases were stable beyond our wildest expectations. The data revealed that the carrier stayed in the same 13.9-mHz-wide spectral bin during each hour-long reception. When the carrier phase was tracked and detrended, the phase repeatedly followed a parabolic or half-sinusoidal track over the hour, with a maximum instantaneous frequency deviation of about 2 mHz (4 cycles/h), better than 1 part in 10^6 (Fig. 3). This pattern was observed for all sites with sufficient SNR.

This stability meant that the measured carrier frequency

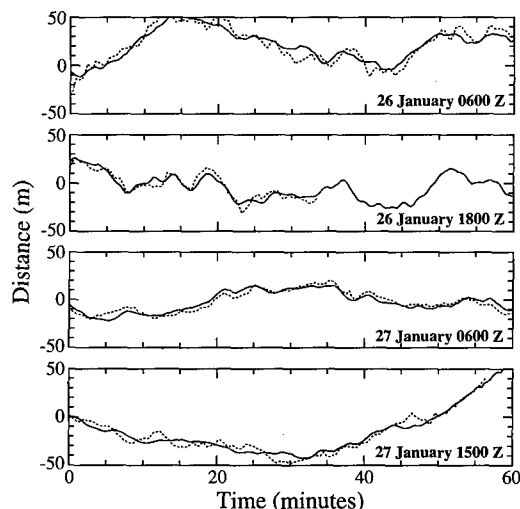


FIG. 5. Comparison of ship motion measured on the R/V Cory Chouest and at Ascension Island. Solid curve is the GPS component offset in the direction of 267°T (the launch angle of the refracted geodesic toward Ascension Island). Dashed curve is motion derived from the IAP1 measurement at Ascension Island with a time shift to allow for acoustic transmission time. The four comparisons from the top are 26 January 0600Z M1, 26 January 1800Z M1, 27 January 0600Z M1, and 27 January 1500 P.

Doppler shift could be used to infer a *projected source speed*, which together with the actual ship speed inferred a launch angle relative to the ship's heading. Assuming a negligibly small vertical launch angle, the inferred horizontal launch angle agreed very well with the calculated angle.¹⁰

VI. SHIP MOTION

A GPS receiver aboard the R/V CORY CHOUEST recorded the position of the ship every 10 s during the transmissions.¹² The helmsman attempted to be at the same location at the start of each transmission. Different headings were needed to keep the ship into the wind and waves. The ship's speed and course were held constant to within a few acoustic wavelengths during the active source times. Table I lists the ship speed and heading for the best linear fit to the GPS data (in the least-squares sense).

Small changes in travel time, fractions of a wavelength per signal period, can be estimated by the IAP1 method.^{13,14} IAP1 measures a period-to-period common spectral phase change, then integrates this to a phase trajectory $\Phi(t)$. This phase trajectory is proportional to a distance trajectory $d(t)$ using the center frequency wavelength λ_c ,

$$d(t) = (\lambda_c / 2\pi) \Phi(t). \quad (4)$$

The deviation of the ship's trajectory from uniform motion (surge), projected onto the direction of the receiver was then compared to $d(t)$ at the receiver (Fig. 5). Three degrees of freedom were allowed in aligning these two trajectories, a vertical shift to account for the arbitrary IAP1 origin, a slight time shift to account for discrepancy between the clock origins, and a slight rotation to account for the discrepancies in clock frequencies. The alignment criterion was minimum mean-squared discrepancy. The rms discrepancies were 6.97, 4.48, 3.76, and 4.91 m which are extraordinary results. We conclude that the major contributor to fluctuations in the

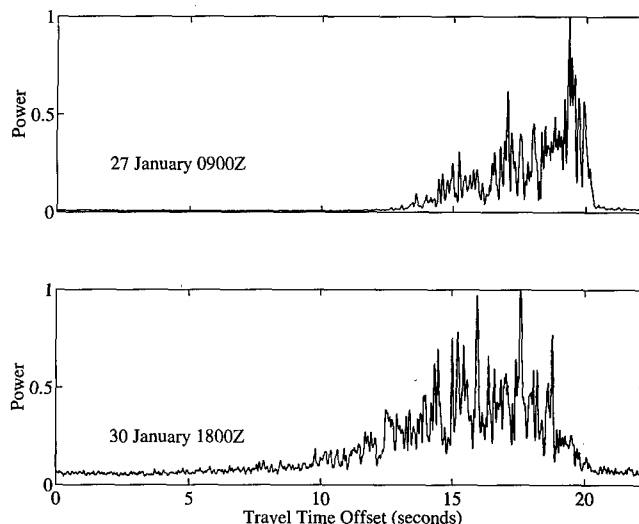


FIG. 6. Full-hour incoherent average of the 27 January 0900Z transmission to Christmas Island (top) and the 30 January 1800Z transmission to Ascension Island (bottom). Arrival power is shown as a function of travel time reckoned to an arbitrary offset.

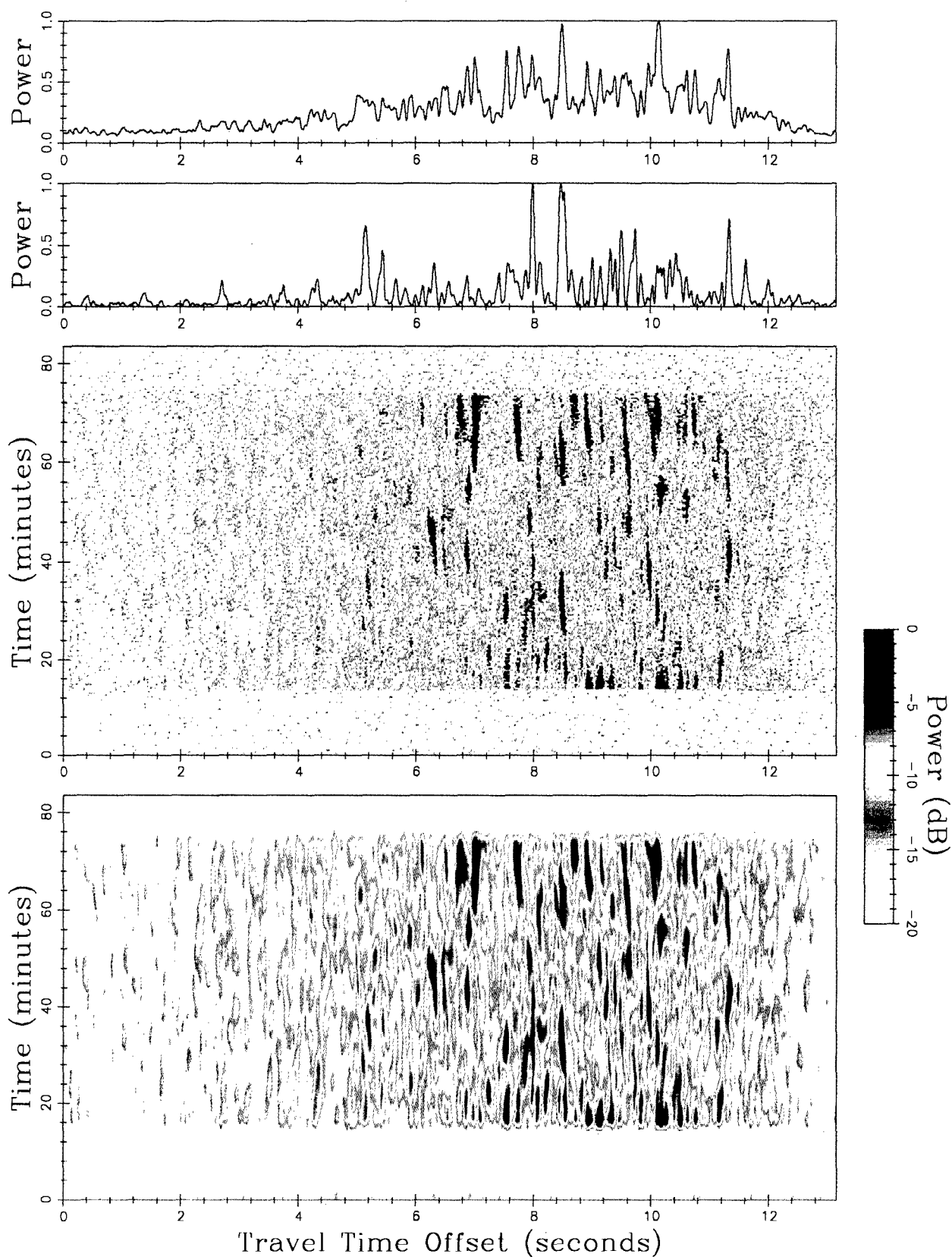


FIG. 7. Details of the 30 January 1800Z transmission to Ascension Island. Averages of power (top) are shown as a function of travel time. Also shown are arrival power as a function of travel time and clock time with single period processing (middle), and with eight-period moving average processing (bottom). Travel time is reckoned to an arbitrary offset.

IAP1 phase of the received signal is the ship's surge, and not fluctuations in the propagation path.

VII. M-SEQUENCE PROCESSING

The M-sequence data sets were processed to obtain the arrival structures, the waveforms that would have been received using single periodic pulses with the same energy, duration, and period. The M-sequence processing with Doppler compensation is discussed in the Appendix.

These single-period arrival structures were then incoherently averaged over the entire transmission hour for two sites (Fig. 6). The Christmas arrival pattern spans about 8 s with a typical *SOFAR crescendo*. The Ascension arrival pattern spans about 13 s and a *SOFAR crescendo* is not observed. The Ascension path is about twice as long (9.2 vs 5.5 Mm) as the Christmas path and spends a much longer time in Antarctic polar waters. It also passes through the eddy-generating Agulhas retroflexion region southwest of the Cape of Good Hope. The incoherent average at Ascension stays significantly above the axis at all times, confirming that the SNR was lower on the Ascension record than the Christmas record. The source was 5 dB weaker on the Ascension record than on the Christmas record. These general features persist but the details differ from transmission to transmission.

A full hour coherent average is the squared magnitude of the single-period arrival structures averaged in their complex form (Fig. 7, top). The coherent and incoherent averages are different because the arrival structure changes during the hour (Fig. 7, middle). This also explains why the time resolution seems poor in sections of the hour-long averages, as the averages merged different arrivals.

If phase fluctuations were limiting integration time, correcting them with the IAP1 processing would allow longer coherent integration and would improve the SNR. After IAP1 correcting the received phases for ship's surge, an eight-period (178.9-s) periodic moving average was applied (Fig. 7, bottom). This smoothing duration must be long enough to improve the SNR but short enough to avoid excessive smoothing of the faster changes. A value of eight periods was the best for this case. The false alarms are gone from the 12-min guard intervals before and after the real reception and the individual arrivals are clearer.

Although many individual arrivals can be tracked for up to 20 min, they appear and disappear, sometimes merging, and sometimes splitting apart, as one might expect for transmissions from a moving ship.

VIII. SUMMARY

HIFT had 35 transmissions. We have processed 1173 receptions—364 from the ten sonobuoy and seamount sites and 809 collected at the three U.S. sites. The Canadian and Monterey arrays had an additional 43 array receptions. The best data sets we have processed are from Christmas Island and Ascension Island.

The total CW propagation loss ranged from 115 to 150 dB, 10–50 dB above range times depth cylindrical spreading. Major bathymetry effects, the mid-Atlantic ridge and the

Chatham Rise east of New Zealand, are believed to be of major importance at ranges beyond 12 Mm. Transmission though the Tasman Sea was blocked by bathymetry.

The propagation was amazingly phase-stable. After correcting for constant ship motion the phase deviations of the carrier swing over a couple of cycles of carrier in an hour, a frequency stability of better than ± 2 mHz. Most of this appears to be deterministic, caused by ship surge. Comparing the GPS ship tracks to the IAP1 processed sequence data accounts for most of the change in the received phase and yields rms residuals of a few meters (compared to the acoustic wavelength of approximately 26 m).

The multipath response records, corrected for the source ship motion, show that stable arrivals exist for tens of minutes at ranges of up to 9 Mm. We conclude that a lower bound for coherent integration time for deep-water fixed-site measurements is 20 min. This is consistent with longer time scale changes being caused by slowly varying ship-receiver geometry¹⁵ and not by time-dependent ocean variability.

ACKNOWLEDGMENTS

Tony Haddad of the University of Michigan programmed the on-line spectral analysis program. James Daws also at the University of Michigan built the keyer electronics and eight-channel front ends used at the Navy facilities. Ron Stein of the Applied Physics Laboratory, University of Washington, was responsible for the production and distribution of the international sonobuoy and associated data acquisition systems. The valuable comments of the anonymous reviewers is much appreciated. Walter Munk also provided needed critical advice on the manuscript and the figures are much improved because of Breck Betts.

APPENDIX: PROCESSING PERIODIC M-SEQUENCE SIGNALS

The basic steps in processing an M-sequence reception are as follows.

(i) Sample the reception at a rate f_s equal to an integer number of samples per digit. Typically rates of four or eight times the carrier frequency f_c are used. Such rates lead to efficiencies in processing.

(ii) Form complex demodulates by downshifting the sampled reception from carrier to baseband by multiplying the k th sample value by $\exp(-j2\pi k f_c / f_s)$. Then low-pass with an equal weight FIR filter, where N is the number of nonzero coefficients. Choosing N to be an integer multiple of f_s / f_c eliminates the $-2 f_c$ spectral component. This has proven adequate for many applications and is computationally efficient compared to filters not using equal-valued coefficients. For wideband (low- Q) situations apply the filter twice.

(iii) Form a periodic sum of the complex demodulates creating a single period result for subsequent processing. The SNR increases by a factor equal to the number of periods summed when the received signal is truly periodic.

(iv) Divide the spectrum of the single-period complex demodulate sum by the M-sequence modulation spectrum to

compress the signal energy of an entire period into an equivalent pulse.^{7,16} This step increases the SNR by

$$\frac{(L+1)\sin^2 \theta(L^2 \cos^2 \theta + \sin^2 \theta)}{L(L-1)\cos^2 \theta + 2 \sin^2 \theta}, \quad (\text{A1})$$

where θ is the modulation angle. HIFT used $\pm 45^\circ$, so the gain is very close to $L/2$. This procedure is called factor inverse filtering (FIF) and is not the same as matched filtering. FIF has better time resolution than matched filtering at the expense of 1–2 dB less SNR.

Hadamard processing: The FIF sequence removal can be efficiently done in the time domain with the Hadamard transform method,^{17,18} if the sample rate evenly divides the digit rate. Let N_d be the integer number of samples per digit. Demultiplex the single-period demodulate sums into N_d sets. Each set of demodulate values are reordered, multiplied by a Hadamard matrix, and then reordered. The Hadamard matrix elements are ± 1 's and a fast multiplication procedure that requires only $N_d L \log_2 L$ additions exists. Finally the N_d sets are remultiplexed. The input and output reorderings depend upon the specific M sequence used.

Doppler Processing: The Doppler effect is often expressed in terms of a frequency shift. Because this has led to the mistaken impression that all frequencies shift by the same amount, the authors prefer to characterize Doppler in terms of a factor β . If $s(t)$ is the transmitted waveform then in the simplest situation the received waveform is proportional to $s(t - \tau(t))$, which characterizes the effect of Doppler for all frequencies. For linear Doppler, the travel time is $\tau(t) = \tau_0 + \tau'_0 t$ and $\beta = 1 - \tau'_0$.

Doppler is not a problem if the data can be sampled at a rate that gives an integer number of samples per sequence digit. Data are often acquired without prior knowledge of the Doppler. Typically the data are sampled at f_s , the rate in the absence of Doppler, and the desired sample rate is $f_s' = \beta f_s$. Thus the samples or demodulates need to be interpolated at the desired rate. Linear interpolation of demodulates is used in practice, and processing proceeds as usual.

Since the Doppler factor β is unknown it is necessary to search for the correct value. Consider a cw signal transmitted at f_c Hz that experiences a Doppler factor β . After downshifting by f_c Hz, the demodulated signal rotates at $(1 - \beta)f_c$ Hz. Its average over T seconds is $\text{sinc}[(1 - \beta)f_c T]$, so the Doppler bin width corresponds to $(1 - \beta)f_c T = 1$. In velocity

terms the bin width is $v = c/(f_c T)$, i.e., the speed of sound divided by the number of carrier cycles in the reception.

It is of historical interest that in 1979 we implemented a wideband Doppler processing by manually adjusting the sampling rate while observing the demodulated carrier on an oscilloscope. The demodulated carrier phase was held fixed or slowly drifting, ensuring that the sampling rate was accounting for the Doppler.

¹ P. F. Worcester, B. D. Cornuelle, and R. C. Spindel, "A review of ocean acoustic tomography: 1987–1990," Rev. Geophys. Suppl. 557–570, U.S. National Report to IUGG 1987–1990 (1991).

² R. J. Urick, *Principles of Underwater Sound* (McGraw-Hill, New York, 1975), 2nd ed.

³ W. H. Munk and F. Zachariasen, "Refraction of sound by islands and seamounts," J. Atmos. Oceanic Tech. 8, 554–574 (1991).

⁴ A. M. G. Forbes, "The Tasman Sea blockage—an acoustic sink for the HIFT?," J. Acoust. Soc. Am. 96, 2428–2431 (1994).

⁵ D. E. Lamphiear and T. G. Birdsall, "Approximations to the non-central chi-square distributions with applications to signal detection models," E.D.G. Tech. Report No. 101, Electrical Engineering Dept., The University of Michigan (1960).

⁶ W. P. Tanner and T. G. Birdsall, "Definitions of d' and η as psychophysical measures," J. Acoust. Soc. Am. 30, 922–928 (1958).

⁷ T. G. Birdsall and K. Metzger, Jr., "Factor inverse matched filtering," J. Acoust. Soc. Am. 79, 91–99 (1986).

⁸ K. Metzger, Jr. and R. J. Bouwens, "An ordered table of primitive polynomials over GF(2) of degrees 2 through 19 for use with linear maximal sequence generators," Cooley Electronics Laboratory Technical Memorandum No. 107, University of Michigan (1972).

⁹ W. Munk, R. Spindel, A. Baggeroer, and T. Birdsall, "The Heard Island Feasibility Test," J. Acoust. Soc. Am. 96, 2330–2342 (1994).

¹⁰ A. M. G. Forbes and W. Munk, "Doppler-inferred launch angles of global acoustic ray paths," J. Acoust. Soc. Am. 96, 2425–2427 (1994).

¹¹ S. L. Marple, Jr., *Digital Spectral Analysis with Applications* (Prentice-Hall, Englewood Cliffs, NJ, 1987).

¹² M. Dzieciuch, W. Munk, and A. Forbes, "Interpretations of GPS offsets from a steady course," J. Atmos. Oceanic Tech. 9, 862–866 (1992).

¹³ J. L. Spiesberger, P. J. Bushong, K. Metzger, Jr., and T. G. Birdsall, "Ocean acoustic tomography: estimating the acoustic travel time with phase," IEEE J. Oceanic Eng. 14, 108–119 (1989).

¹⁴ T. G. Birdsall, K. Metzger, M. Dzieciuch, and J. Spiesberger "Integrated Autocorrelation phase at one period lag," J. Acoust. Soc. Am. 96, 2353–2356 (1994).

¹⁵ M. Dzieciuch and W. Munk, "Differential Doppler as a diagnostic," J. Acoust. Soc. Am. 96, 2414–2424 (1994).

¹⁶ T. G. Birdsall and K. Metzger, "M-sequence signal tutorial," CSPL Memorandum, The University of Michigan (1988).

¹⁷ M. Cohn and A. Lempel, "On fast M-sequence transforms," IEEE Trans. Inf. Theory IT-23, 135–137 (1977).

¹⁸ T. G. Birdsall and K. Metzger, "Hadamard processing of M-sequences, tutorial examples," CSPL Memorandum, The University of Michigan (1988).

Integrated autocorrelation phase at one period lag

Theodore G. Birdsall and Kurt Metzger

Department of Electrical Engineering and Computer Science, The University of Michigan, Ann Arbor, Michigan 48109-2122

Matthew A. Dzieciuch

Scripps Institution of Oceanography, University of California, San Diego, La Jolla, California 92093

John Spiesberger

Pennsylvania State University, University Park, Pennsylvania 16802

(Received 23 August 1992; revised 20 April 1994; accepted 7 June 1994)

Various types of phase measurements have been introduced into ocean acoustic measurements since the early 1960s, many utilizing the increased precision possible with digital processing. These are usually considered natural and basic by their developers, but are frequently misunderstood and mistrusted by those they were designed to benefit. This paper explains a recent phase technique which was used in the Heard Island Feasibility Test data analysis of the Ascension Island receptions. It revealed that the common phase fluctuations of the wideband M-sequence receptions were not random, but were caused by minor deviations of the source ship track 9200 km away.

PACS numbers: 43.30.Qd, 43.30.Pc, 43.60.Rw

INTRODUCTION

In typical long-range ocean acoustics experiments the receptions are both geometrically and chromatically dispersed. Whatever the cause, it is not always possible to resolve individual features (rays or modes) in the data record. As in any multipath channel, small changes in geometry or in the medium can cause large changes in the data as the wavefronts constructively and destructively interfere. However, accurate measurements of travel time changes in ocean acoustic experiments can be tracked even if individual features in the receptions cannot be. It is possible to do this if the small changes in the propagation affect all the arrival energy in a common way. This paper describes how to extract such information from the receptions.

The goal is to measure overall travel time changes from period to period of a repeated measurement. The method is to convert the real-time series to a complex one for which a phase (corresponding to travel time) exists. The phases will then be averaged in a special way to estimate the overall drift in phase and hence the overall drift in arrival time.

Three ideas are brought together in this work. The first is the use of phase in measuring small travel-time changes; e.g., when a pure sine wave is delayed slightly, the effect is to decrease the phase proportionately. The second is the use of complex signals to describe real signals and the corresponding physical realization by complex demodulation. The third is the use of autocorrelation to compare the receptions of a periodic transmission when one reception begins an integer number of periods after the reference reception.

Our experience in long-range underwater acoustic propagation has been that amplitude fluctuations seem to be larger and faster than the associated phase fluctuations, that coherent integration is profitable far beyond what is considered the coherence time, and that apparently simple correlation measurements are anything but simple. For example, by following the conventional forms, we have measured a cor-

relation bandwidth of 0.25 Hz, using a coherently processed signal with a 25-Hz nominal bandwidth.¹ The Heard Island Feasibility Test² (HIFT) measurements, with hour-long transmissions of precision signals projected from a precision-position source ship, yielded complicated receptions with fascinating autocorrelations. At Ascension Island, at a range of 9200 km, these correlations displayed a conventional *correlation time* of about 5.5 min, yet the phase of the correlation was used to track the source ship nonuniformity to within a 4-m standard deviation (0.15λ) for a full hour.³

As far as we know, the authors were the first to discover the method of integrated autocorrelation phase at one period lag (IAP1) in 1986. A specific application was reported in 1989.⁴ The extraordinary results from the HIFT has prompted us to give a fuller disclosure of the method, so that it may be used by other researchers.

I. SIGNAL PROCESSING BACKGROUND

This section discusses phase in the time domain, and its measurement. We will discuss (i) the meaning of the *phase* of a real waveform, (ii) complex demodulation as a means of measuring the phase, and (iii) the effect of time delay on the complex demodulated signal and its spectrum.

A. Waveform phase

A complex-valued waveform $c(t) = a(t)e^{i\theta(t)}$, where $a(t)$ and $\theta(t)$ are real, has a well defined *phase* $\theta(t)$ up to an integer multiple of 2π . The phase of a waveform is itself a waveform, something that may change in time. The phase of a real waveform $s(t)$ is not so simple. An easily understandable case is a real *bandpass* waveform with a nominal *center frequency* or *carrier frequency* f_c . Such waveforms are frequently written as

$$s(t) = a(t)\cos[2\pi f_c t + \theta(t)], \quad (1)$$

where the bandwidth of $s(t)$ is less than f_c . [This also usually means the amplitude $a(t)$ and the phase $\theta(t)$ are band-limited to less than f_c .] Equation (1) can be rewritten as

$$s(t) = \text{Real}[a(t)e^{i[2\pi f_c t + \theta(t)]}]. \quad (2)$$

The *complex baseband equivalent* or *baseband analytic signal* for $s(t)$ centered at f_c is $\tilde{s}(t)$:

$$\tilde{s}(t) = a(t)e^{i\theta(t)}, \quad s(t) = \text{Real}[\tilde{s}(t)e^{i2\pi f_c t}]. \quad (3)$$

This definition of the phase $\theta(t)$ is not unique. If someone should choose to use a center frequency 7 Hz higher than what everyone else used, the resulting phase would compensate by decreasing 7 cycles per second from everyone else's result. The common phrase is "the phase is unique, up to a linear term." This nonuniqueness opens up a *freedom* to manipulate the linear component of phase and is used by signal processors to remove or insert trends into $\theta(t)$.

Equation (3) can be meaningful for a real baseband signal $s(t)$ as well, that is, when $f_c = 0$ and $s(t) = a(t)\cos[\theta(t)]$. The difficulty arises because it is not obvious how to factor $s(t)$ into its amplitude $a(t)$ and the phase-caused amplitude factor $\cos[\theta(t)]$. The solution, by convention, is that the proper $\tilde{s}(t)$ must have a purely positive-frequency spectrum; that is, $\tilde{s}(t) = a(t)e^{i\theta(t)}$ will have no negative frequency components.

One way to convert a real $s(t)$ to a complex-valued $\tilde{s}(t)$ is by *complex demodulation*; another way is by the Hilbert transform method. Complex demodulation is practical and is used in real-time processing. The Hilbert transform method is not realizable by a causal filter.

B. Complex demodulation

First select the desired *center frequency* f_c . If the waveform is a baseband waveform, choose f_c to be about half the waveform's bandwidth.

Step 1: Multiply the $s(t)$ waveform shown in Eq. (1) by the *complex rotator* $2e^{-i2\pi f_c t}$ [the 2 comes into play in $2\cos(\xi) = e^{i\xi} + e^{-i\xi}$]:

$$\begin{aligned} s_1(t) &= 2e^{-i2\pi f_c t}s(t) \\ &= 2a(t)\cos[2\pi f_c t + \theta(t)]e^{-i2\pi f_c t} \\ &= a(t)(e^{i[2\pi f_c t + \theta(t)]} + e^{-i[2\pi f_c t + \theta(t)]})e^{-i2\pi f_c t} \\ &= a(t)e^{i\theta(t)} + a(t)e^{-i\theta(t)}e^{-i4\pi f_c t}, \\ s_1(t) &= \tilde{s}(t) + \tilde{s}^*(t)e^{-i4\pi f_c t}. \end{aligned} \quad (4)$$

The waveform $\tilde{s}^*(t)$ is the complex conjugate of $\tilde{s}(t)$.

Step 2: Low-pass filter $s_1(t)$ in order to pass the $\tilde{s}(t)$ term and reject the undesired *double frequency* term, which is centered about $-2f_c$ Hz. This filtering is relatively simple if the waveform were originally bandpass with a center frequency to bandwidth ratio Q much greater than 1; it becomes more difficult as $Q \rightarrow \frac{1}{2}$ and the waveform becomes a baseband waveform. (In underwater acoustics these two steps usually follow sampling and A/D conversion, so the multiplication and filtering are done digitally; $Q \geq 2$ is handled routinely.)

C. Time delay

If the real waveform were delayed by τ seconds it would be written

$$\begin{aligned} s(t - \tau) &= \text{Real}[\tilde{s}(t - \tau)e^{i2\pi f_c(t - \tau)}] \\ &= \text{Real}[\tilde{s}(t - \tau)e^{-i2\pi f_c \tau}e^{i2\pi f_c t}]. \end{aligned} \quad (5)$$

Therefore the proper real bandpass waveform to complex demodulated waveform relationship is

$$s(t) \leftrightarrow \tilde{s}(t), \quad s(t - \tau) \leftrightarrow \tilde{s}(t - \tau)e^{-i2\pi f_c \tau}. \quad (6)$$

This is consistent with the positive frequency axis spectral action, that is, with the spectrum of the real signal being the baseband spectrum of the complex demodulated signal shifted up by f_c cycles.

II. SPECTRAL PHASE AS A DIFFERENTIAL TIME MEASUREMENT

A. General paradigm

The following paradigm is considered in increasing layers of sophistication. A bandpass transmission is repeated every T seconds through a medium that is linear and time invariant, or changing quite slowly in time. The distant reception is segmented into periods for analysis. Each period is compared to the previous one to measure what changes occurred, with particular interest in *travel-time* changes from period to period.

If the transmission is a pure sine wave or a narrowband pulse of many cycles, and if the travel-time change is so small that the result is observed as just a phase change, then comparison of successive receptions can determine very small travel-time changes, corresponding to range changes of a fraction of a wavelength.

When the effect of noise is introduced, one moves to building up the received signal energy by increasing the observation time or the period. An obvious remark is that *period* need not mean T seconds; any integer multiple of T is also a period. The choice of "the period" for the analysis is a balance between being long enough to increase the measurement energy, yet short enough to ensure that the phase does not become aliased by changing more than half a cycle between periods. This choice becomes more complicated when the analyst incorporates an integration after each comparison; for example, if one wants to know the change over $100T$ seconds but is restricted to periods of $5T$ by the maximum anticipated phase rate, one may measure in $5T$ periods, but then *integrate* or *cumulatively sum* over 20 successive measurements. The acronyms that will be used in the paper would label the measurements comparing each $5T$ period with the previous $5T$ period P1 (phase, one period lag), and the cumulative sum IP1 (integrated P1).

The next layer of sophistication comes when the transmission changes from a sine wave or a pulse modulating a sinusoidal carrier to a complicated waveform with period T . The linear, slowly time-varying propagation that retains the sinusoidal nature of a sinusoidal transmission may really scramble the appearance of a broadband signal. Multipath and multimode propagation have these effects. When this

occurs, signal phase is no longer obvious. For example, consider measuring the discrete spectrum of the reception for each analysis period, $S_k(f_m)$. Here, k denotes the k th period and $f_m = m/T$ denotes the m th frequency. In a very low noise environment one could measure the spectral phase change between periods for each frequency. Since there are several thousand individual frequencies in a typical HIFT spectrum, some sort of averaging would have to be devised to estimate the average or mean phase change.

In Sec. II B it will be shown that the phase of the autocorrelation is a reasonable choice for the desired common phase change.

B. Mean spectral phase change is AP1

Let S_k be the Fourier spectrum of the k th period, and $S_k(f_m)$ be the spectral value at the m th frequency. To investigate phases, we use the polar form

$$S_k(f_m) = |S_k(f_m)| e^{i\theta_k(f_m)}. \quad (7)$$

The desired phase difference between the k th period and its predecessor is $\theta_k(f_m) - \theta_{k-1}(f_m)$. This phase difference appears in the expression for the product of the k th spectrum and the complex conjugate of its predecessor:

$$S_k(f_m) S_{k-1}^*(f_m) = |S_k(f_m)| |S_{k-1}(f_m)| e^{i[\theta_k(f_m) - \theta_{k-1}(f_m)]}. \quad (8)$$

Two considerations are now presented about averaging phases.

(i) Since phases are defined circularly, modulo 2π , care must be taken to avoid artificial introduction of $\pm 2\pi$ steps. One might use an algorithm to scan the data and limit differences to $\pm \pi$. An alternative procedure that is simple and effective when the differences are small is to average the phasors, $e^{i\theta}$, i.e., the phase difference in Eq. (8) rather than the phase θ .

(ii) The weighting of the contributions from the various frequencies should reflect how much each frequency contributes to the signal energy. The product of the spectral magnitudes in Eq. (8) accomplishes this.

These considerations argue that a reasonable measurement of ϕ_k , the average spectral phase change between two successive periods, is the phase of $\sum_m S_k(f_m) S_{k-1}^*(f_m)$. The mathematical key is that this sum is proportional to the autocorrelation of the reception at one period separation. This is known as the inner product identity of Fourier analysis. Equation (9) is the correct form for DFT calculation.⁵

Lemma: Suppose that $a(t_n)$ and $b(t_r)$ are M -point sequences whose discrete time Fourier spectra are $A(f_m)$ and $B(f_m)$. Then

$$\sum_{m=0}^{M-1} A(f_m) B^*(f_m) = \frac{1}{M} \sum_{n=0}^{M-1} a(t_n) b^*(t_n). \quad (9)$$

This Lemma is applied to each of the successive data periods with spectra $S_k(f_m)$ and $S_{k-1}(f_m)$, and sample waveforms $\tilde{s}(t_n + kT)$ and $\tilde{s}(t_n + kT - T)$. Substituting into Eq. (9),

$$\sum_{m=0}^{M-1} S_k(f_m) S_{k-1}^*(f_m) = \frac{1}{M} \sum_{n=0}^{M-1} \tilde{s}(t_n + kT) \tilde{s}^*(t_n + kT - T). \quad (10)$$

The right-hand side is the autocorrelation of the reception $\tilde{s}(t)$ at one period lag. In more formal notation we might write

$$R_{\tilde{s}}[k] = \frac{1}{M} \sum_{n=0}^{M-1} \tilde{s}(t_n + kT) \tilde{s}^*(t_n + kT - T), \quad (11)$$

with magnitude and phase

$$R_{\tilde{s}}[k] = |R_{\tilde{s}}[k]| e^{i\phi[k]}. \quad (12)$$

Our acronym AP1 stands for the *autocorrelation phase at one period lag*, meaning $\phi[k]$. IAP1 stands for the *integrated AP1*, the cumulative sum of the phase changes. This is written as a staircase waveform, a function of continuous or finely sampled time:

$$\Phi(t) = \sum_{k \leq t/T} \phi[k]. \quad (13)$$

The IAP1 measures the total mean spectral phase change from the beginning of the measurement record through time t .

C. AP1 is the differential travel time change

Long-range ocean acoustic receptions are the sum of many arrivals, which may be viewed as either rays or modes. The word arrival is used in this paper to denote either type of reception without distinction. A notation to describe this situation indexes the various ray or mode arrivals by the letter a , and the waveforms arriving during the k th time interval or period by $\tilde{m}_{a,k}(t)$. The received signal during the k th interval is thus

$$\tilde{s}_k(t) = \sum_a \tilde{m}_{a,k}(t - \tau_{a,k}) e^{-i2\pi f_c \tau_{a,k}}. \quad (14)$$

The corresponding Fourier spectrum is

$$S_k(f) = \sum_a \tilde{M}_{a,k}(f) e^{-i2\pi(f+f_c)\tau_{a,k}}, \quad (15)$$

and the cross spectrum is therefore

$$S_k(f) S_{k-1}^*(f) = \sum_a \sum_{a'} \tilde{M}_{a,k}(f) \tilde{M}_{a',k-1}^*(f) e^{-i2\pi(f+f_c)(\tau_{a,k} - \tau_{a',k-1})}. \quad (16)$$

This double sum is more complicated than necessary, as we are going to do a Fourier inversion to the time-shift domain of the autocorrelation function and then concentrate our attention at zero time shift. If the arrival times for the *matching* arrivals, $a = a'$, are much closer than the arrival times for *different* arrivals, $a \neq a'$, we need only retain the matching arrivals. The relevant cross spectrum is then

$RCS_k(f)$

$$= \sum_a \tilde{M}_{a,k}(f) \tilde{M}_{a,k-1}^*(f) e^{-i2\pi(f+f_c)(\tau_{a,k}-\tau_{a,k-1})}. \quad (17)$$

The cross-correlation function, the inverse Fourier transform of Eq. (17), is

$$\int_{-\infty}^{\infty} RCS_k(f) e^{i2\pi ft} df, \quad (18)$$

and this integral, evaluated at $t=0$, is the autocorrelation at one period lag or AP1,

$$R_s[k] = \int_{-\infty}^{\infty} \sum_a \tilde{M}_{a,k}(f) \tilde{M}_{a,k-1}^*(f) \times e^{-i2\pi(f+f_c)(\tau_{a,k}-\tau_{a,k-1})} df. \quad (19)$$

If there is a common time delay change on all arrivals from one period to the next, it is meaningful to write

$$\tau_{a,k} - \tau_{a,k-1} = \delta T_k + \nu_{a,k}, \quad (20)$$

where the ν 's are arrival dependent and the δT_k is arrival independent. Proceed by substituting Eq. (20) into Eq. (19):

$$R_s[k] = e^{-i2\pi f_c \delta T_k} \sum_a \int_{-\infty}^{\infty} \tilde{M}_{a,k}(f) \tilde{M}_{a,k-1}^*(f) \times e^{-i2\pi(f+f_c)\nu_{a,k}} e^{-i2\pi f \delta T_k} df. \quad (21)$$

If all of the arrival time fluctuations are very small compared to the common part, which itself is small, then

$$|\nu_{a,k}| \ll |\delta T_k| < 1/f, \quad (22)$$

and we could reasonably approximate the integral with

$$R_s[k] \approx e^{-i2\pi f_c \delta T_k} \sum_a \int_{-\infty}^{\infty} \tilde{M}_{a,k}(f) \tilde{M}_{a,k-1}^*(f) \times e^{-i2\pi f \delta T_k} df. \quad (23)$$

Denote the individual arrival correlation functions by $R_a[k]$, so we have

$$R_s[k] \approx e^{-i2\pi f_c \delta T_k} \sum_a R_a[k]. \quad (24)$$

If the phase change, $f_c \delta T_k$, is less than 1 cycle, and the resolution of the individual arrival waveforms is of the order of several cycles, then the phase of each arrival correlation will be very small since these are the correlations of base-band complex waveforms. The result is that the phase of the sum in Eqs. (21)–(24) should be very close to zero. Under these conditions, one should expect

$$AP1(k) = \arg(R_s[k]) = -2\pi f_c \delta T_k, \quad (25)$$

to a very high degree of accuracy.

III. SUMMARY OF IAP1 PROCEDURE

- (i) Complex demodulate the data.
- (ii) Segment the data into nonoverlapping intervals of one period duration.

(iii) Calculate the correlation between successive intervals.

(iv) Denote the sequence of correlation phases as AP1.

(v) Accumulate these phases to form the staircase waveform of integrated autocorrelation phases, IAP1.

(vi) Adjust the data by multiplying the data by $e^{-i\Phi(t)}$.

IV. CONCLUDING REMARKS

Although it is our custom when using M-sequence spread-spectrum transmissions to calculate the autocorrelation after using factor inverse matched filtering (FIF) processing to *pulse-compress* the reception to a pulse-like *arrival structure*, the autocorrelation could just as well have been calculated on the spread-spectrum reception. The key is that the M-sequence FIF processing has a flat spectrum, i.e., it is a spectral phase-only processing. When the spreading/compression uses a flat spectrum modulation, the spectral product corresponding to the autocorrelation at one period lag differs only by a constant magnitude factor from the autocorrelation after pulse compression. This change in magnitude does not affect the autocorrelation phase.

One must segment the received data into periods quite precisely. The degree of precision is approximately the duration of a quarter of a carrier cycle or less over the observation period T , the same as if one were measuring Doppler using the carrier. Any error in specifying the period will add linearly to the AP1 result; that is, if the period is short by ϵ of a carrier cycle, then AP1 will be high by $2\pi\epsilon$ radians, and the IAP1 will show an excessive linear ramp of $2\pi\epsilon$ radians every T seconds.

The IAP1 technique is relatively new and has proved most powerful in three applications to date. It was used originally because it seemed like a natural technique to use when receptions were so complex we could not decompose them into discrete ray paths or mode components; it showed integrated phase changes similar to tidal travel-time changes and supported experiment design decisions. It was used in the 1989 paper⁴ to average the effects of internal waves; the applicability was questionable as it is not clear from physical models that internal waves are barotropic and thus affect all components of the signal equally. Its use in the HIFT analysis is the most successful to date.

We have not subjected IAP1 to mathematical investigation. The development in Sec. II is new and it replaces lengthy time-domain arguments used in earlier developments. With more vigor than rigor, we are still searching for deeper truth.

¹ T. G. Birdsall and F. Khan, "Implications of multipath propagation for two-frequency coherence measurements," J. Acoust. Soc. Am. **78**, 105–111 (1985).

² A. Baggeroer and W. Munk, "The Heard Island Feasibility Test," Phys. Today **45**, 22–30 (September 1992).

³ T. G. Birdsall, K. Metzger, and M. A. Dzieciuch, "Signals, signal processing, and general results," J. Acoust. Soc. Am. **96**, 2343–2352 (1994).

⁴ J. L. Spiesberger, P. J. Bushong, K. Metzger, and T. G. Birdsall, "Ocean acoustic tomography: estimating the acoustic travel time with phase," IEEE J. Oceanic Eng. **14**, 108–119 (1989).

⁵ A. V. Oppenheim, A. S. Willsky, and I. T. Young, *Signals and Systems* (Prentice-Hall, New York, 1983).

Comparison of data and model predictions for Heard Island acoustic transmissions

B. Edward McDonald, Michael D. Collins, W. A. Kuperman,^{a)} and Kevin D. Heaney^{a)}
Naval Research Laboratory, Washington, DC 20375

(Received 23 August 1992; accepted for publication 7 June 1994)

Propagation paths and signal characteristics from the Heard Island Feasibility Test are modeled using a combination of adiabatic mode theory, coupled mode theory, and parabolic equation (PE) methods. Adiabatic mode theory predicts the horizontal propagation paths (including small grazing angle reflections from bathymetry), group travel times, and estimates of signal loss due to bottom interaction. The PE calculations are performed primarily to illustrate modal coupling near sharp oceanic fronts and bathymetry intruding into the sound channel. They are carried out in depth and range along selected horizontal ray paths. For the Heard Island to Christmas Island path, we carry out a time domain pulse transmission using coupled mode equations. The result gives a pulse envelope in approximate agreement with observations.

PACS numbers: 43.30.Qd, 43.30.Dr, 43.30.Pc

INTRODUCTION

Our purpose is to examine theoretically and numerically the propagation paths and travel times from the acoustic source array used in the Heard Island Feasibility Test (HIFT) to various receiver locations in the Atlantic, Indian, and Pacific Oceans. A vertical towed array of ten low-frequency sources covering the frequency range 57 ± 5 Hz spanned depths between 120 and 230 m near a location (53° S, 74° E) just south of Heard Island. At this high southern latitude, the sound channel axis is shallow (approximately 150 m deep), allowing injection of trapped acoustic energy into the ocean waveguide while keeping the sources within their operating depth (less than 300 m).

In analyzing results from HIFT, it is important to establish with some confidence what ocean volumes and bathymetric features have been sampled by the various received signals. For example, if it were suspected that a reception contained horizontal multipaths, signal processing techniques would have to be appropriately designed. Because global scale acoustic transmission experiments have been so few and because the paths cover great expanses of open ocean, we do not have detailed experimental verification of signals in flight (time signature, vertical and horizontal structure) in order to establish horizontal deviations in propagation path. Propagation modeling must then be used to provide estimates of path deviations due to small but cumulative effects such as horizontal variation in the ocean waveguide and the rotationally-induced ellipticity of the earth.

Prior to HIFT, we carried out an analysis¹ of the 1960 acoustic transmission² from a set of depth charges detonated off Perth, Australia, to hydrophones near Bermuda. Approximately 13 000 s after each detonation, a pair of arrivals was recorded near Bermuda separated by roughly 30 s. Our analysis, which is summarized in Fig. 1, pointed to horizontal multipath as the explanation of the double arrival. Our interpretation is that sound in the southern lane took a longer

path through colder (and slower) waters than did the sound in the northern lane. The existence of widely separated eigenpaths in our numerical description of the 1960 experiment resulted from three conditions, the first two of which likely affected HIFT: (a) The eigenpaths each experienced grazing reflection from different bathymetric features. This accounts for the micro-multipath within each propagation lane. (b) The index of refraction for a given ocean acoustic eigenmode has a systematic horizontal gradient connected with "shoaling" of the sound channel axis (combined with a geometric effect which tends to repel rays from the poles of an oblate ellipsoid) in high latitudes. Under appropriate conditions, the shoaling/polar repulsion locally counteracts the tendency of rays to bend toward colder water, allowing a ray to turn north at its southernmost point of the southern lane. (c) The receiver in the 1960 experiment was within 200 km of the source's antipode. In the absence of horizontal refraction on a spherical or ellipsoidal Earth, all rays (geodesics) from a point converge on the point's antipode. This would tend to happen in Fig. 1, but rays between the two lanes are blocked by Kerguelen Island and its banks.

In Sec. I we outline the normal mode theory used to calculate horizontal propagation paths for each of the normal mode signals. We include mode coupling terms, which turn out to be important in shallow waters with sloping bottoms and in deep waters near the Antarctic Circumpolar Convergence (ACC). In Sec. II we discuss mechanisms that can lead to multiple receptions from the transmission of a single pulse. In Sec. III we give numerical results for (a) horizontal ray paths from the HIFT source to several receivers, (b) PE (parabolic equation) calculations in range and depth along selected rays showing the distribution of energy in the water column and the evolution of modal excitations, and (c) pulse propagation results from coupled mode theory. Our pulse calculation from Heard to Christmas Island gives an arrival structure in reasonable agreement with observation.

^{a)}Present address: Scripps Institution of Oceanography, La Jolla, CA 92093.

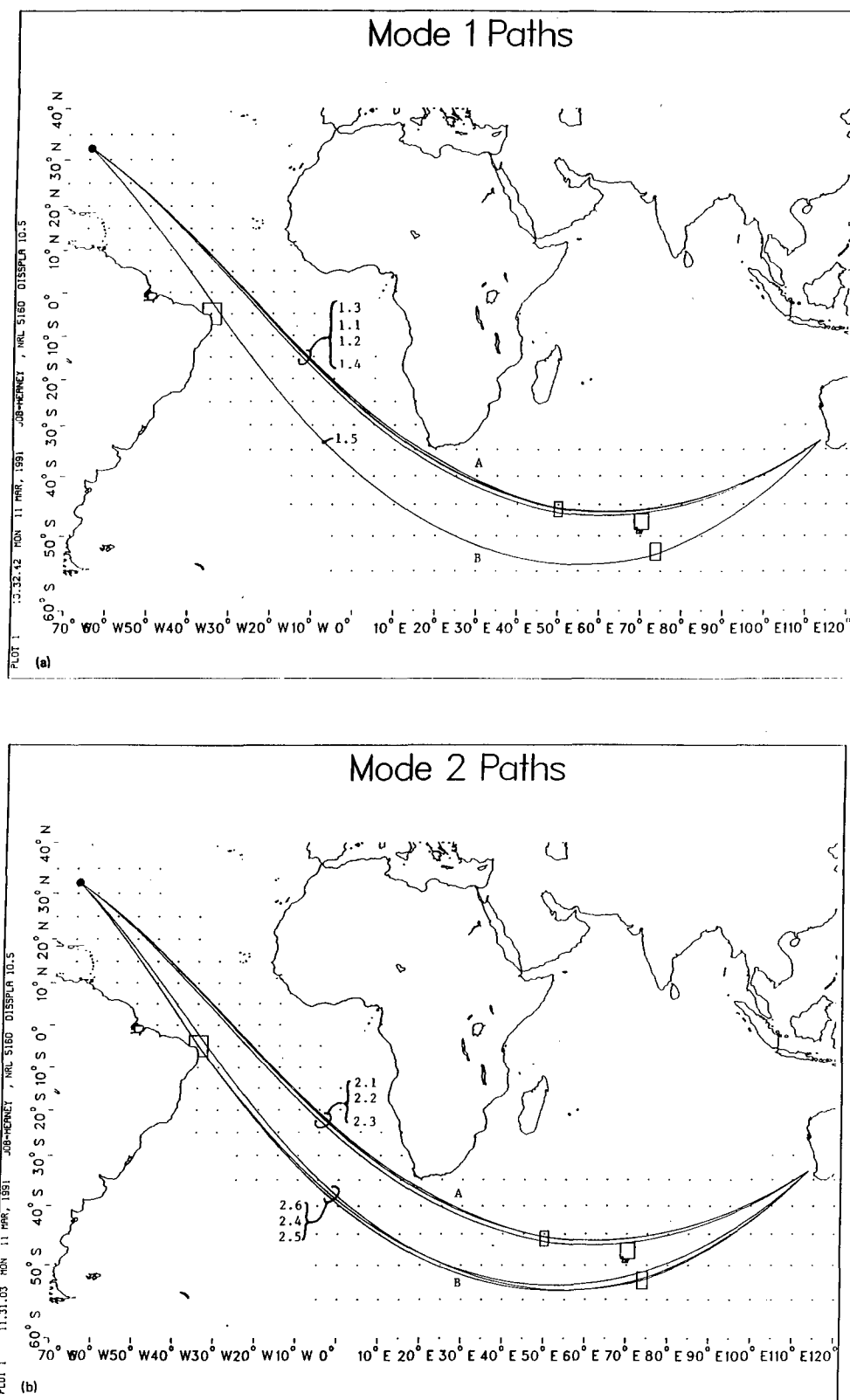


FIG. 1. Propagation paths from a point off Perth to Bermuda as calculated from adiabatic mode theory. (a) mode 1; (b) mode 2. Individual ray labels refer to Table I of Ref. 1. The multiplicity of rays within the northern and southern lanes is due to bathymetric reflection in regions denoted by small rectangles.

I. THEORY

We have chosen a combination of normal mode and PE solutions to model three-dimensional wave propagation within the ocean waveguide. Adiabatic normal mode theory (coupling terms neglected) predicts the dominant horizontal

propagation paths for each of several modes. Energy conserving PE^{3,4} solutions then illustrate two-dimensional (range–depth) dependence of the signal along the ray paths. In normal mode theory, the three-dimensional wave equation is represented as a series of two-dimensional wave equations

for each of the locally defined vertical eigenmodes of the waveguide.^{1,5,6} Range dependence in the waveguide structure (horizontal variations within the water column and bathymetry) will lead to mode coupling.^{7,8} In upslope propagation⁹ mode coupling will contribute to bottom losses. Since dissipation and boundary losses generally increase with vertical mode number, one hopes to capture primary features of global transmission by retaining several of the lowest modes. We had anticipated that four would be adequate, but receptions on the vertical array of Baggeroer *et al.*⁸ suggest that about twice this many were received off the coast of California. The PE results in Sec. III include cases in which modes up to almost number 30 are involved.

A. Normal mode representation

Adopting local Cartesian coordinates (x, y, z) with z normal to the ocean surface, the three-dimensional Helmholtz equation for the acoustic pressure p assuming time dependence $e^{-i\omega t}$ is

$$\rho \nabla \cdot \rho^{-1} \nabla p + k^2(x, y, z)p = 0, \quad (1)$$

where

$$k^2(x, y, z) \equiv \omega^2 / c^2(x, y, z), \quad (2)$$

ω is radian frequency, $c(x, y, z)$ is sound speed, and ρ is density. Effects of Earth curvature are included in Sec. I C. The possibility of vertical variation in ρ is retained to account for stratification in the ocean bottom. Local vertical eigenmodes $\psi_n(z; x, y)$ of the ocean waveguide are defined for mode numbers $n=1, 2, \dots$ by the eigenvalue problem

$$\rho \partial_z \rho^{-1} \partial_z \psi_n + k^2 \psi_n = \kappa_n^2(x, y) \psi_n. \quad (3)$$

Boundary conditions for Eq. (3) are $\psi_n(0; x, y) = 0$ (pressure release surface) and $\psi_n \rightarrow 0$ as $z \rightarrow -\infty$, corresponding to trapping by the ocean waveguide. The ocean/bottom interface boundary condition is that both ψ_n and $\rho^{-1} \partial_z \psi_n$ are continuous.

Figure 2 shows the sound-speed profile measured at the HIFT source location and the vertical structure of the first 16 modes. Also shown is the profile from the Levitus database¹⁰ to give an indication of the possible variation of the real ocean from monthly climatological averages. The bottom (depth 680 m) is taken to be a homogeneous fluid of density 1.5 times that of water, and sound speed 1568 m/s (a 100 m/s increase over the water sound speed near the bottom). The source array is indicated by dots near the sound-speed minimum. The first four modes are fairly well trapped, while bottom interaction begins to set in for modes five and higher.

For each (x, y) the ψ_n form an orthonormal set [with associated inner product $(*, *)$] satisfying

$$(\psi_n, \psi_m) \equiv \int \psi_n \rho^{-1} \psi_m dz = \delta_{m,n}. \quad (4)$$

The trapped portion p_{tr} of the total acoustic pressure field (i.e., the portion capable of surviving long-distance propagation) is expressed as a sum over trapped modes with amplitude coefficients $p_n(x, y)$:

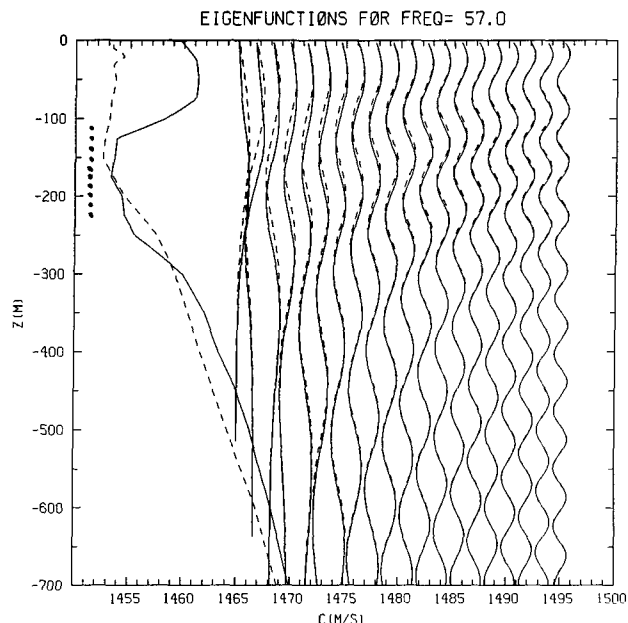


FIG. 2. Solid line: Sound speed as measured during HIFT and resulting eigenfunctions. Dash line: The sound-speed profile taken from Levitus (Ref. 10). The vertical array location is indicated by dots.

$$p_{tr}(x, y, z) = \sum_n p_n(x, y) \psi_n(z; x, y). \quad (5)$$

The analysis to follow in this section and the next extends the theory of Weinberg and Burridge⁶ to include mode coupling terms as explicit integrals involving environmental parameters and modal eigenfunctions. To our knowledge these explicit forms have not been calculated before.

The mode amplitudes satisfy horizontal wave equations which are obtained by substituting (5) into (1), using (3) to eliminate z derivatives, then from the result projecting out the coefficient of ψ_n . The result is

$$\nabla_{\perp}^2 p_n(x, y) + \kappa_n^2(x, y) p_n(x, y) = -C_n(x, y) = O[(kL)^{-1}], \quad (6)$$

where the horizontal Laplacian $\nabla_{\perp}^2 = \partial_x^2 + \partial_y^2$. The mode coupling term C_n is discussed in Sec. I B and L is a measure of the scale length for significant horizontal variation in the eigenfunctions.

Our numerical results for horizontal propagation paths and total travel times in Sec. III A are not significantly affected by the term C_n , and we neglect it in that section. We will, however, include C_n in pulse propagation calculations presented in Sec. III C. We have observed that as a signal propagates over changing bathymetry, the mode coupling term effectively launches new high-order modes. These high-order modes are dispersive and lead to pulse spreading. We will demonstrate in Sec. III B with a PE calculation that redistribution of energy within the vertical modes results from bathymetric interaction and from propagation through the ACC.

B. Mode coupling

We will give expressions for mode coupling terms C_n in (6) due to horizontal variation in the ocean waveguide. Two investigations^{7,8} of the Heard Island signals have suggested that modal conversion is significant in some of the received signals. Our numerical work has also indicated that mode coupling over variable bathymetry may contribute to pulse dispersion.

The mode coupling term in (6) is obtained by substituting (5) into (1) and taking the inner product of the result with ψ_m (neglecting horizontal density variation):

$$C_n = \sum_m 2(\psi_n, \nabla_{\perp} \psi_m) \cdot \nabla_{\perp} p_m + (\psi_n, \nabla_{\perp}^2 \psi_m) p_m. \quad (7)$$

As long as the waveguide's horizontal length scales are much greater than the acoustic wavelength (approximately 25 m), the first term on the right of (7) dominates. Defining a mode coupling matrix

$$A_{mj} \equiv (\psi_j, \nabla_{\perp} \psi_m), \quad (8)$$

the dominant term of (7) becomes

$$C_n(x, y) \approx 2 \sum_m A_{mn} \cdot \nabla_{\perp} p_m. \quad (9)$$

In principle, one could calculate ψ_n at all points (x, y) in the horizontal plane and straightforwardly apply (8) to get the mode coupling coefficients. It is possible, however, to derive A_{mn} at a point (x, y) with knowledge of eigenfunctions only at that point, plus derivatives of environmental parameters. The derivation of the coupling coefficients requires careful treatment of the parameter discontinuities at the ocean/bottom interface and will be given in detail elsewhere.¹¹ By taking horizontal derivatives of (3) and interface conditions, and neglecting horizontal variation of ρ within the ocean and bottom separately, one can express the mode coupling coefficients as

$$A_{mm} = -\frac{1}{2} \nabla_{\perp} h(x, y) \frac{\psi_m^2}{\rho} \Big|_b^w, \text{ and for } n \neq m, \quad (10a)$$

$$A_{mn}(\kappa_m^2 - \kappa_n^2) = (\psi_n, \psi_m \nabla_{\perp} k^2) + \nabla_{\perp} h(x, y) \times \left(\psi_n \psi_m \frac{k^2 - \kappa_m^2}{\rho} + \frac{\psi'_m \psi'_n}{\rho} \right) \Big|_b^w. \quad (10b)$$

Here, $h(x, y) > 0$ is the ocean depth, with the bottom at $z = -h(x, y)$, and subscripts w and b denote evaluation on the water and bottom sides of the ocean/bottom interface, respectively. The first term on the right-hand side of (10b) reflects volume mode coupling (from inhomogeneities within the water column), while all other terms in (10) are bathymetric in nature (they are proportional to the bottom slope and depend on parameters evaluated at the bottom). The strongest mode coupling in our results (Sec. III) occurs for signals incident upon varying bathymetry in the sound channel.

Equation (6) is integrated along ray paths by substituting

$$p_n = B_n(x, y) e^{i \int \kappa_n \cdot dx} \quad (11)$$

into (6) and (7), retaining only first-horizontal derivatives of presumed slowly varying quantities B_n, κ_n, ψ_n in comparison with the rapidly oscillating exponential in (11). The coupled equations for the mode amplitudes are

$$\frac{d}{ds} p_n + \frac{1}{2} p_n \frac{d}{ds} \log \kappa_n = i \kappa_n p_n - \sum_m \frac{\kappa_m}{\kappa_n} p_m A_{mn}, \quad (12)$$

where ds is arc length along a horizontal ray path and A_{nm} is the component of A_{nm} in (8) along the ray direction.

C. Refraction on an ellipsoidal earth

As a first step in a trans-oceanic propagation calculation, we determine horizontal eigenrays between source and receiver. We obtain ray solutions to (6) by mapping out horizontal wave numbers κ_n on an ellipsoid representing the Earth as distorted by rotation and using Fermat's principle¹ to minimize phase speed-based travel times integrated along the surface between fixed source and receiver points. This procedure introduces earth curvature effects into the ray equations.

We use geographic coordinates (ϕ, λ, α) for ray integration, where ϕ is geographic latitude (the angle between the surface normal and the equatorial plane), λ is longitude, and α is the ray heading measured clockwise from north. The resulting equations for "refracted geodesics" are equivalent to those of Munk *et al.*:¹²

$$\dot{\phi} = \frac{\cos \alpha}{\mu(\phi)}, \quad (13a)$$

$$\dot{\lambda} = \frac{\sin \alpha}{\nu(\phi) \cos \phi}, \quad (13b)$$

$$\dot{\alpha} = \frac{\sin \alpha}{\nu(\phi)} \tan \phi - \left(\frac{\sin \alpha}{\mu(\phi)} \frac{\partial}{\partial \phi} - \frac{\cos \alpha}{\nu(\phi) \cos \phi} \frac{\partial}{\partial \lambda} \right) \log \kappa_n, \quad (13c)$$

where

$$\mu(\phi) = \frac{r_{eq}(1 - \epsilon^2)}{(1 - \epsilon^2 \sin^2 \phi)^{3/2}}, \quad (14)$$

$$\nu(\phi) = \frac{r_{eq}}{(1 - \epsilon^2 \sin^2 \phi)^{1/2}}.$$

Overdot represents differentiation with respect to arc length along the ray, r_{eq} and r_p are equatorial and polar Earth radii, and $\epsilon^2 \equiv 1 - r_p^2/r_{eq}^2$ defines the eccentricity of the ellipsoid. For the Earth, $\epsilon = 0.0818$.

II. SOURCES OF MULTIPLE ARRIVALS

A dominant feature of HIFT receptions reported to date is the multiplicity of arrivals following the transmission of a single (synthesized) short pulse. Two basic phenomena will result in multiple receptions from a single event: (a) horizontal multipath resulting from bathymetric reflections, and (b) differences in group speeds among the vertical eigenmodes (i.e., dispersion). These are discussed in the next paragraphs.

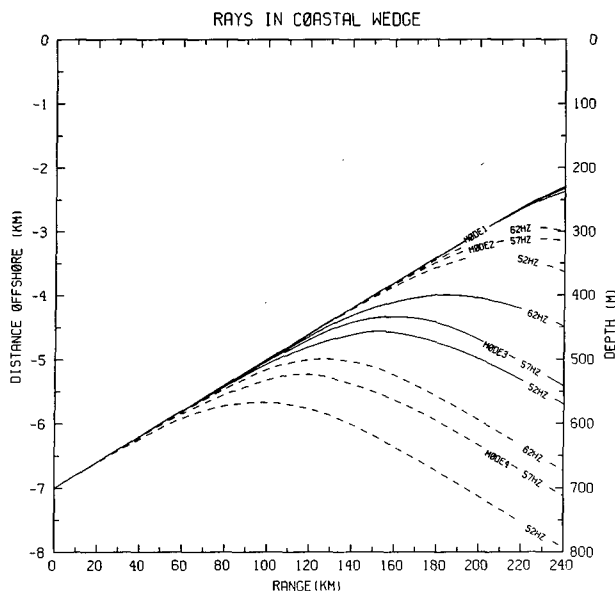


FIG. 3. Initially parallel rays for 52, 57, and 62 Hz fired shoreward at a small angle $\tan^{-1} 0.1$ to the coastline are split by bottom interaction into separate modes and frequencies. Even modes are dashed lines, and odd modes are solid.

A. Bathymetric refraction

A sloping ocean bottom generally causes κ_n and thus the index of refraction for mode n to decrease toward shallow water, resulting in deflection of rays toward deep water. The physics of horizontal refraction due to bathymetry within the adiabatic mode theory may be illustrated¹¹ using a simple model consisting of a coastal wedge with a sloping homogeneous bottom and a water sound-speed profile depending on depth only.

To illustrate the relative importance of frequency and mode number in bathymetric refraction, Fig. 3 gives horizon-

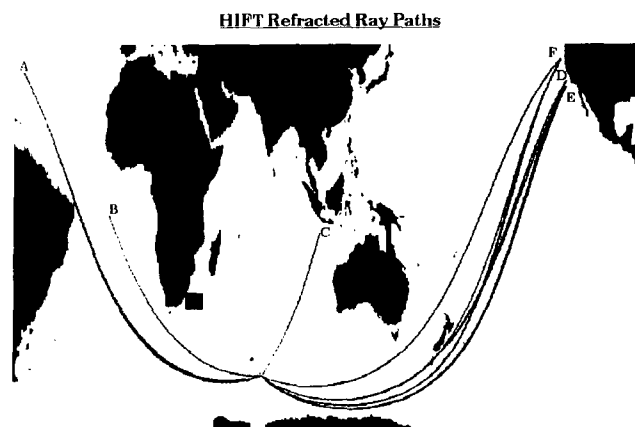


FIG. 5. Ray paths corresponding to entries in Table I.

tal ray paths in a Cartesian coordinate system for a steep bottom (slope 0.1 chosen for illustrative purposes). Rays are launched shoreward at a small angle $\tan^{-1} 0.1$ to the coastline. Results are shown for modes 1–4 and frequencies 52, 57, and 62 Hz, assuming a sound-speed profile approximating that of the Heard Island source location. One sees that refraction toward deep water increases strongly with mode number (the higher modes occupy more vertical space in the sound channel and thus feel the bottom more strongly). The bending of rays toward deep water decreases with frequency, since again low-frequency modes occupy more of the vertical sound profile. The net result is that bathymetric interaction can have a prismlike effect, splitting an incoming beam into separate frequency and modal components. As a result, a bathymetrically reflected ray between a fixed source and receiver will have an effective reflection point which depends upon mode number and frequency. This accounts for the path differences between mode 1 and 2 rays in Fig. 1. We believe

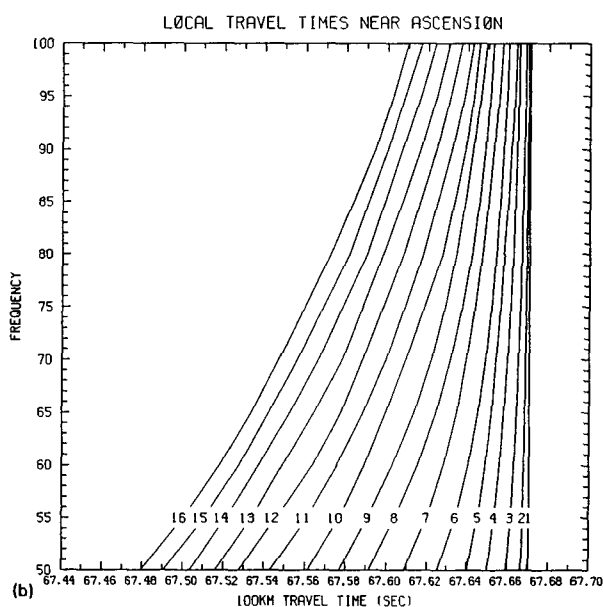
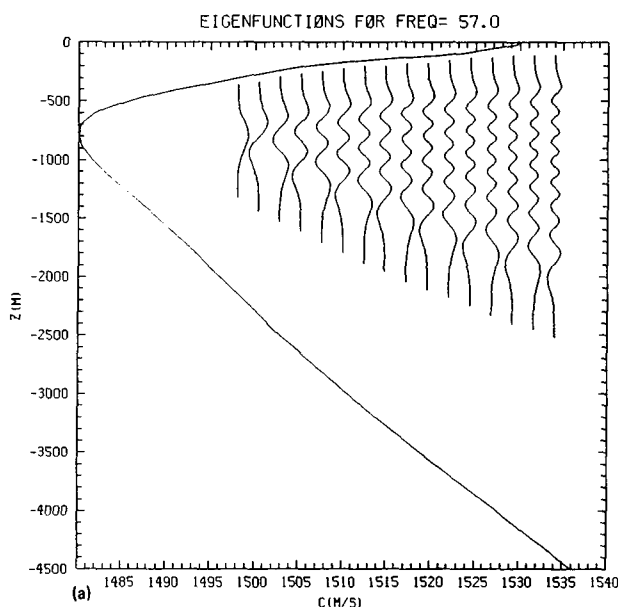


FIG. 4. (a) Deep water SSP and eigenmodes just south of Ascension Island. (b) Group travel times for modes 1–16 as a function of frequency for a 100-km path.

the frequency and mode splitting effects illustrated in Fig. 3 come into play in many of the paths to the HIFT receivers.

B. Modal dispersion

A result from adiabatic mode theory¹ gives the range dependent modal group velocities as

$$v_{g_n}^{-1}(x, y) = \frac{\partial \kappa_n}{\partial \omega}$$

$$= v_{p_n}(x, y) \int_{-\infty}^0 \rho^{-1} \psi_n^2(x, y, z) c(x, y, z)^{-2} dz. \quad (15)$$

In a deep sound channel v_{g_n} generally increases with mode number n and decreases with frequency because higher modes/lower frequencies sample the faster waters away from the channel axis. This is illustrated in an idealized arrival time diagram (Fig. 4), which shows mode structure and group travel times for a hypothetical 100 km transmission through a range independent ocean. Figure 4(b) illustrates the "SOFAR crescendo" from a modal point of view; namely a sequence of mode arrivals whose separation in time decreases rapidly until the final arrival (mode 1). ("SOFAR" in the present context may be loosely translated "sound channel," whereas its original derivation is from Sound Fix-

TABLE I. Eigenray parameters to six receiver locations. Ray launch/arrival angles are in degrees counterclockwise from north. Stations D, E, and F are affected by horizontal multipath. Separate eigenray bundles (e.g., D1, D2) to the same receiver are primarily due to grazing reflections from bathymetry. Bottom loss greater than 15 dB indicated by () may mean the path is not viable.

| Frequency = 57.0 Hz | | | | | | |
|--------------------------|------|--------------|--------------|-----------------|------------------|-------------------|
| Receiver vicinity | Mode | Launch angle | Arrive angle | Travel time (s) | Bottom loss (dB) | Minimum depth (m) |
| A. Bermuda | 1 | 255.772 | 135.028 | 10857.4 | 0.000 | 639.374 |
| | 2 | 254.520 | 135.568 | 10857.4 | 0.004 | 639.374 |
| | 3 | 253.644 | 136.080 | 10853.2 | 0.044 | 639.374 |
| | 4 | 253.620 | 136.213 | 10848.1 | 0.210 | 639.374 |
| B. Ascension I. | 1 | 268.350 | 142.051 | 6266.0 | 0.045 | 561.680 |
| | 2 | 268.664 | 142.195 | 6264.4 | 0.217 | 557.450 |
| | 3 | 270.235 | 142.273 | 6263.1 | 0.919 | 529.890 |
| | 4 | 286.028 | 142.159 | 6265.0 | (48.808) | 126.924 |
| C. Christmas I. | 1 | 41.910 | 204.428 | 3715.7 | 1.112 | 514.612 |
| | 2 | 41.945 | 204.441 | 3714.9 | 2.034 | 514.308 |
| | 3 | 41.865 | 204.450 | 3714.4 | 2.613 | 516.917 |
| | 4 | 41.535 | 204.467 | 3713.8 | 3.619 | 515.025 |
| D1. San Diego California | 1 | 124.790 | 219.628 | 11976.1 | (35.135) | 263.522 |
| | 2 | 125.255 | 219.598 | 11970.8 | (43.570) | 258.206 |
| D2. San Diego California | 1 | 131.333 | 214.393 | 11963.3 | 7.949 | 414.683 |
| | 2 | 131.528 | 214.250 | 11954.2 | 9.465 | 438.344 |
| | 3 | 131.551 | 214.096 | 11942.4 | 10.750 | 468.530 |
| | 4 | 131.817 | 213.881 | 11938.2 | 8.315 | 639.374 |
| E1. Monterey California | 1 | 124.699 | 219.312 | 11860.9 | (54.156) | 247.708 |
| | 2 | 125.182 | 219.287 | 11854.8 | (56.390) | 244.079 |
| E2. Monterey California | 1 | 131.118 | 214.445 | 11841.2 | 10.682 | 229.323 |
| | 2 | 131.339 | 214.305 | 11832.0 | 13.190 | 335.557 |
| | 3 | 131.355 | 214.140 | 11819.8 | (16.232) | 419.724 |
| | 4 | 131.537 | 213.963 | 11816.8 | (15.837) | 448.149 |
| F1. Oregon | 1 | 112.742 | 229.716 | 12224.9 | 7.464 | 639.374 |
| | 2 | 113.416 | 229.740 | 12222.9 | 9.175 | 639.374 |
| | 3 | 113.863 | 229.758 | 12214.8 | 10.073 | 639.374 |
| | 4 | 113.870 | 229.792 | 12212.4 | 11.452 | 639.374 |
| F2. Oregon | 1 | 125.220 | 218.370 | 12238.8 | (63.903) | 104.075 |
| F3. Oregon | 1 | 129.075 | 215.899 | 12257.2 | (24.122) | 64.020 |
| | 2 | 129.207 | 215.997 | 12249.2 | (26.614) | 107.095 |
| | 3 | 129.097 | 216.523 | 12237.9 | (36.320) | 133.168 |
| | 4 | 129.012 | 216.335 | 12232.7 | (39.654) | 165.365 |

ing and Ranging.) An illustrative experimental example of the SOFAR crescendo resulting from deep water transmission of an acoustic pulse may be found in Fig. 3 of Duda *et al.*¹³

More relevant to HIFT is transmission involving partial shallow water paths and range dependent SSP, in which case the monotonicity of arrivals evident in Fig. 4(b) may not be preserved. This is partly because in shallow waters $v_{g,n}$ generally decreases with n as the mode's effective angle with the horizontal increases.

III. NUMERICAL RESULTS

In this section we use three separate numerical models to calculate expected properties of acoustic signals transmitted during HIFT. Details and results of the respective models are discussed in Secs. III A, B, and C below. In Sec. III A we use an adiabatic mode model to calculate horizontal paths taken by different modal components from source to receiver locations. Along selected paths calculated in Sec. III A, in Sec. III B we use an established and benchmarked two-dimensional (range-depth) PE model³ to illustrate the range dependence in the signal induced by range-dependent acoustic parameters and bathymetry. In Sec. III C we simulate pulse transmission from Heard Island to Christmas Island and show general agreement with the experimental results. We chose for this calculation the coupled adiabatic mode theory developed in Sec. I B over the PE model for reasons of numerical tractability.

A. Ray paths from adiabatic mode theory

We solve the modal eigenvalue problem (3) on a $\frac{1}{2}$ -deg latitude-longitude grid using sound-speed profiles from Levitus¹⁰ (keeping in mind that the environment may fluctuate significantly about tabulated values, as illustrated in Fig. 2). For each receiver site to be considered, we grid up a swath of ~ 1000 km width between Heard Island and the chosen site. The width of this swath is more than adequate, being more than 10% of the longest propagation path. Where the ocean is less than 1 km deep, the grid is refined to 0.1° .

After determining up to 30 modal eigenvalues κ_n at each of the grid points, the ray equations (13) are integrated numerically. Ray fans for each of the first 30 modes were initiated from the source location to estimate eigenray launch angles. Each fan consisted of rays launched at 1° bearing increments within $\pm 20^\circ$ of the great circle bearing to the receiver site. The possibility of multipath to the receiver from rays outside this fan was investigated and ruled out because of the large bottom losses (of order 40 dB) during large grazing angle interaction with bathymetry.

We have calculated modal ray paths from the HIFT source location to the following receiver locations (Fig. 5): (a) Bermuda; (b) Ascension Island; (c) Christmas Island; (d) a vertical array off Monterey, California; (e) a horizontal array off San Diego; and (f) a hydrophone array off the Oregon coast. Parameters for the ray solutions are listed in Table I. Our calculated ray launch angles (Table I) are in close agreement (W. Munk, personal communication) with Doppler inferred launch angles observed during HIFT.

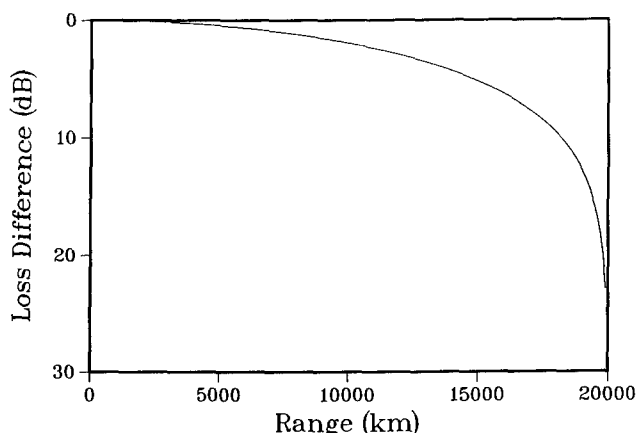


FIG. 6. Cylindrical spreading loss minus that for rays on a spherical earth.

B. Importance of mode coupling: PE results

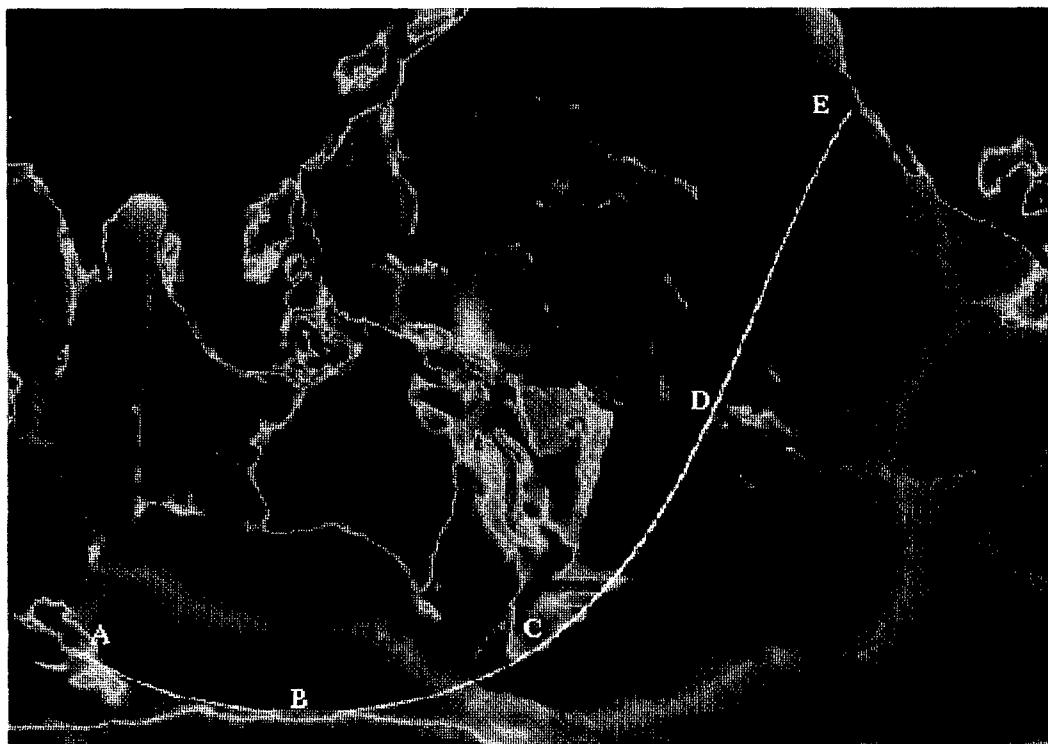
Shang *et al.*⁷ have shown that the range-dependent sound speed in the ACC, a water-column feature, can give rise to strong mode coupling. One must also consider the likelihood of bathymetric mode coupling near the source and other places where bathymetry is in, or close to, the sound channel. To illustrate the importance of mode coupling in some of the HIFT paths, we solve the two-dimensional wave equation (range and depth) along ray paths described in Sec. III A. We can obtain an estimate of vertical mode coupling and of the bathymetric contribution to transmission loss by propagating all of the modes along a selected mode path if the mode paths do not diverge too much.

To handle range-dependent, global-scale problems accurately and efficiently, we use the energy-conserving PE.³ The cylindrical spreading factor $1/\sqrt{r}$ usually assumed in ocean PE calculations overestimates spreading loss for global-scale problems. Rays confined to the surface of a sphere or ellipsoid eventually cease diverging and reconverge on the antipode of their source. We replace the cylindrical spreading factor with one appropriate to rays on the surface of a sphere, $1/\sqrt{r_e \sin(r/r_e)}$, where r_e is the mean radius of the Earth. (Perturbations in spreading loss due to the Earth's ellipticity are negligible.) The spherical surface spreading factor reduces to the cylindrical spreading factor in the limit $r/r_e \ll 1$. In Fig. 6, we illustrate the difference between cylindrical and spherical surface spreading loss. For the 18 000-km Heard Island to California path, the difference is about 13 dB. The spherical surface spreading factor may not be appropriate for problems involving significant horizontal refraction.

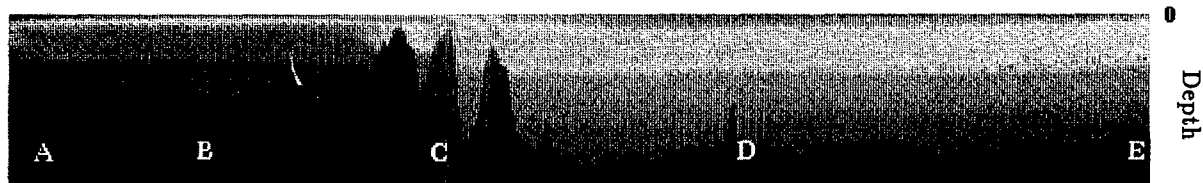
Figure 7 shows the evolution of the 57-Hz PE solution along the mode 1 path from Heard to the array off San Diego for an initial condition consisting of mode 1 only. Figure 7(b) illustrates modal excitation along the ray path. Mode 1 propagates fairly unimpeded until it reaches the New Zealand plateau (C). At this point, energy begins to redistribute into approximately the first eight modes. Past the Chatham rise, energy has redistributed into modes 3 and 5. The signal continues to propagate fairly unaffected en route to California.

Figure 8 repeats the calculation of Fig. 7 along the mode 3 path with initial excitation of mode 3 only. Mode 3 also

(a) Mode 1 Path



(b) Mode 1 Path PE TL



(c) Modal Excitation vs Range

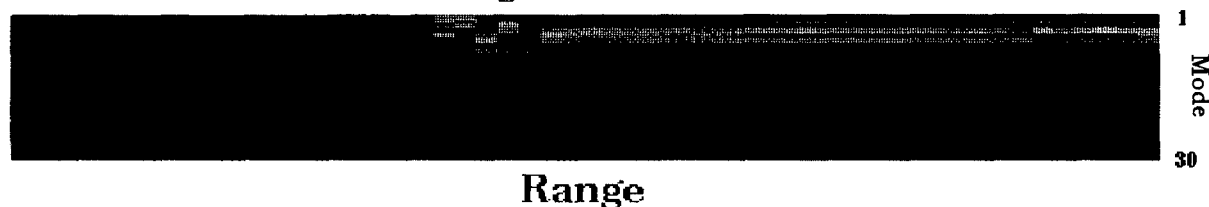


FIG. 7. Depth-range PE calculation from Heard Island to the array off San Diego for initial excitation of mode 1 only. (a) The ray path used is that for mode 1 at 57 Hz. (b) Transmission loss and bathymetry along the ray. The scale on the right gives depth in km. (c) Modal excitation along the ray path for modes 1–30. the vertical extent of part (c) is divided into 30 strips for modes 1–30 (the mode number scale is on the right). The maximum mode amplitude at any given range is represented by red, and the minimum by black.

proceeds to the New Zealand plateau before bathymetric mode coupling is evident. Over the next approximately 1000 km, energy bounces among the first seven modes. After departing the Chatham rise and entering deep water, the signal is once again dominated by mode 3 all the way to California.

Figure 9 repeats the calculation of Fig. 7 along the mode 1 path, but with a multimodal initial condition appropriate to a point source at 175-m depth. In Fig. 9(b) one sees evidence of bottom loss from Heard to the southernmost point (B) of the ray path, and then on the shoulders (C) of the New Zealand plateau. Many modes are present at zero range as a result of point source excitation. As in Fig. 7, one sees rather

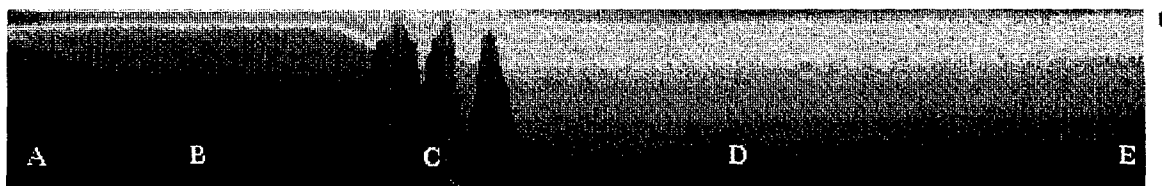
modest exchange of energy between modes until just before the ray encounters the New Zealand plateau (C). Just before the ray encounters the shallowest water along the path, modes higher than about 9 suddenly disappear. The transmission loss at this point in Fig. 8(b) indicates the sudden presence of deeply penetrating sound in the bottom; i.e., mode dumping. Past the Chatham rise, there is only modest modal redistribution. When the ray reaches California, the first eight modes are well populated. This result and those of Figs. 6 and 7 are consistent with the vertical array finding roughly eight modes off California.

Propagation along the Heard–Christmas Island path is

(a) Mode 3 Path



(b) Mode 3 Path PE TL



(c) Modal Excitation vs Range

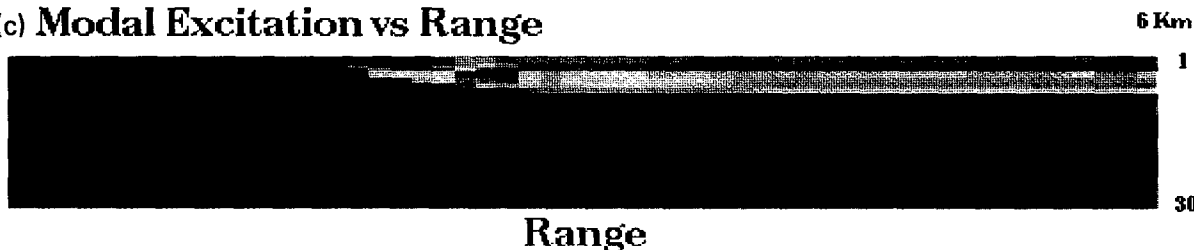


FIG. 8. The calculation of Fig. 7 repeated for mode 3, 57 Hz.

shown in Fig. 10. The initial field is that for a point source at 175 m as in Fig. 9. The apparent difference in modal excitation [Fig. 9(c) versus Fig. 10(c)] near the source is due to mode coupling on a scale smaller than the horizontal plotting raster. In Fig. 10(b) one sees gradual coupling into modes up to about 28 from Heard Island to the north side of the Amsterdam Fault Zone (B). Until the Broken Ridge (C) just north of the Diamantina Trench, mode coupling is slow due to the absence of bathymetry in the sound channel. Strong coupling occurs at the ridge (C), with little further modal evolution all the way to Christmas Island. At the receiver (D), roughly ten of the first 26 modes are significantly excited.

Figure 11 shows propagation from the point source ini-

tial condition of Fig. 5 to Ascension Island. Very little mode coupling occurs until the Prince Edward Fracture Zone. From there to the Agulhas Plateau, mode 1 dominates, but some energy is transferred to modes as high as 23. After the Wolvis Ridge the dominant mode is 4, and little redistribution occurs for the rest of the path. The final configuration at Ascension is dominated by modes 2 and 3, with only a smattering of energy in about ten other modes ranging up to about number 24.

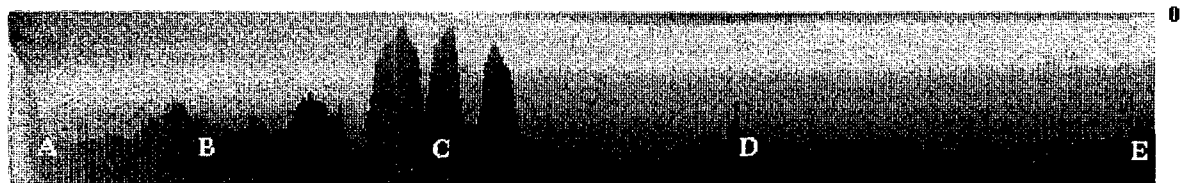
C. Pulse propagation

One of the HIFT exercises explored "pulse compression" by transmitting different frequency components of a

(a) Mode 1 Path



(b) Mode 1 Path PE TL



(c) Modal Excitation vs Range

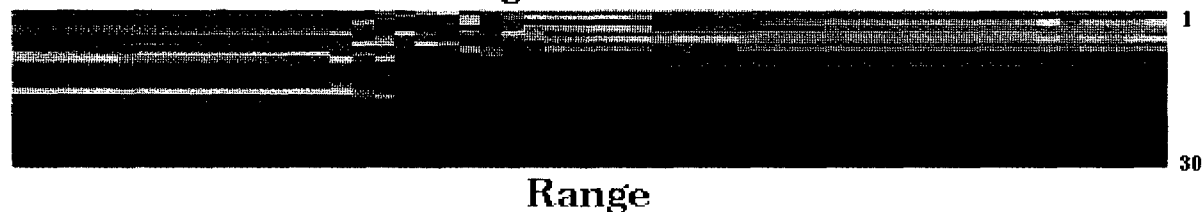


FIG. 9. Repeating the calculation of Fig. 7 with the multi-modal initial field excited by a point source at 175-m depth.

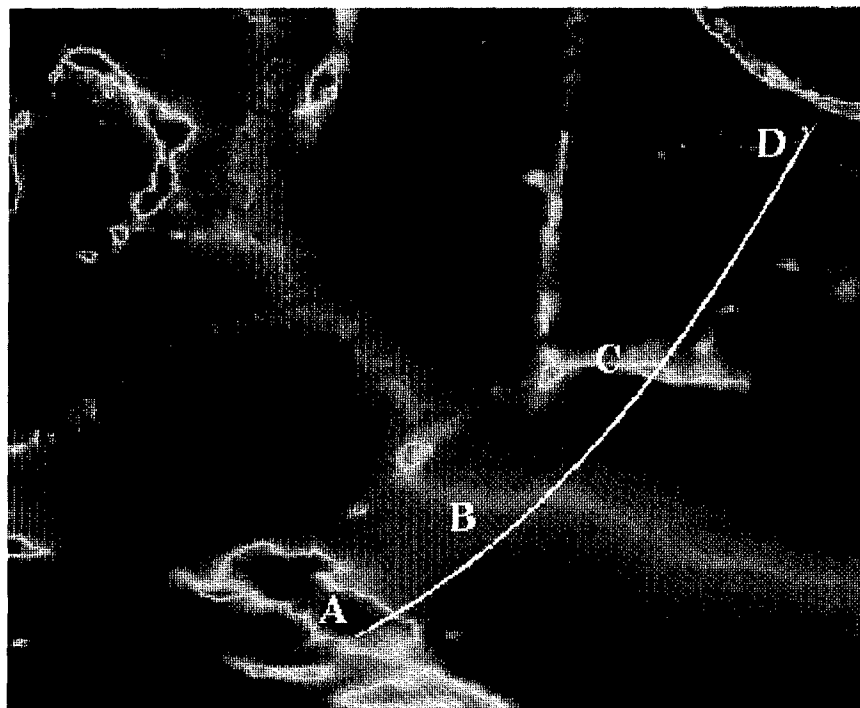
short pulse in different time windows. The frequency components were later combined in a common time window during signal processing. The synthesized wavetrain consisted of five cycles of a 57-Hz sine wave, for a total pulse length of ~ 0.09 s.

After propagating a distance of 5000 km (Heard to Christmas Island), the signal components were recorded and later superimposed numerically. The compressed pulse consisted of multiple arrivals with an envelope of width ~ 5 s. On the Heard–Ascension Island leg (9000 km), the compressed pulse had spread to roughly 7 s. Different transmissions of the same pulse along the same path resulted in different microstructure in the reconstructed pulse, but the

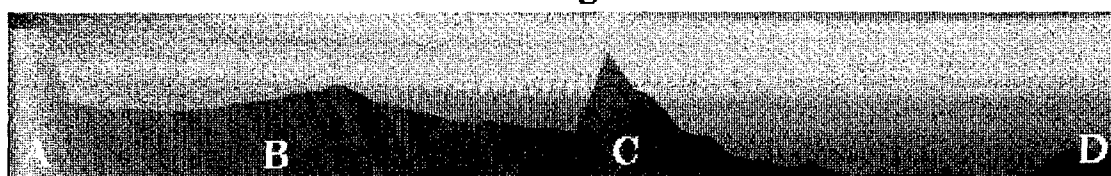
length of the synthesized pulse train was fairly consistent from transmission to transmission.

We hypothesize that since horizontal multipath is not evident in the Heard–Christmas Island path, the observed pulse spreading at Christmas Island results from modal dispersion (determined by essentially unchanging ocean parameters) and that microstructure variation in the received signals is a scintillation effect resulting from combination of source motion and small-scale environmental fluctuation throughout the propagation path. Mode coupling along the first half of this path [Fig. 10(c)] is seen to be significant. The route to Christmas from the HIFT source begins with approximately 200 km of water whose depth ranges between

(a) Heard - Christmas Refracted Path



(b) Mode 1 Path PE TL vs Range



(c) Modal Excitation vs Range

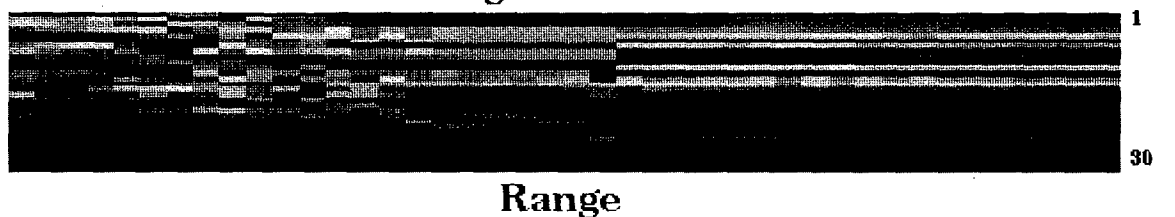


FIG. 10. Heard-Christmas Island PE result along the ray path for mode 1, 57 Hz. The initial field is that for a point source at 175-m depth.

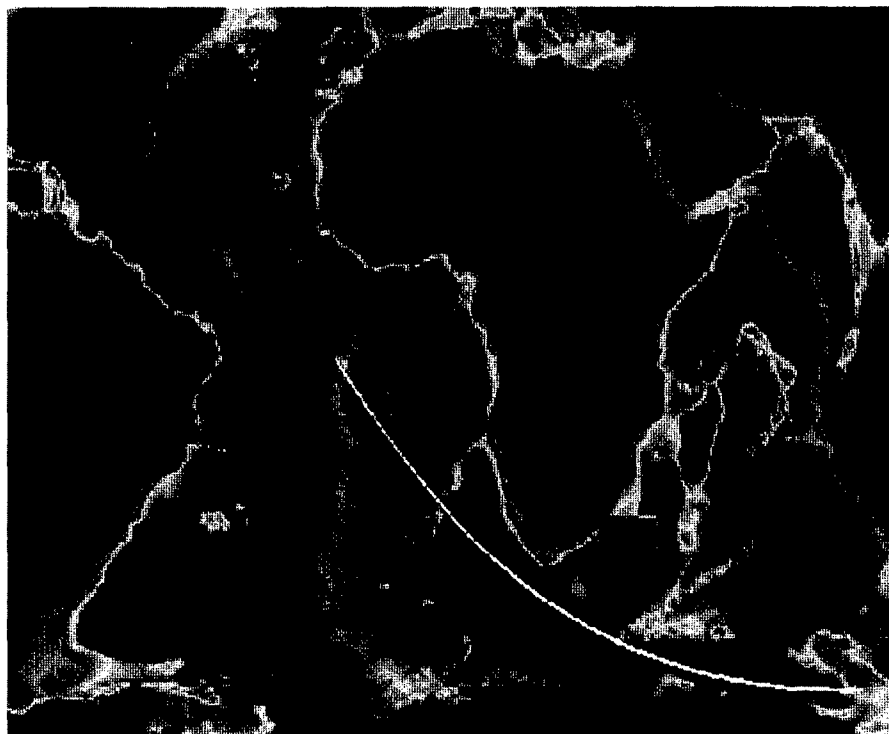
500 and 800 m. Modes higher than approximately one or two are dispersive in these depths. High-order modes experience a balance between energy loss to the bottom, and repopulation due to bathymetric mode coupling [Eqs. (9) and (10)]. At the end of the shallow part of the path, a steep sill leads to coupling into some of the higher modes of the deep water path.

We will now present model calculations of time domain pulse structure in order to compare pulse spreading to data. We will not assign precise meaning to calculated pulse microstructure because of uncertainties in the model and the database it uses. (Indeed, the observed microstructure changed with each pulse transmission series.)

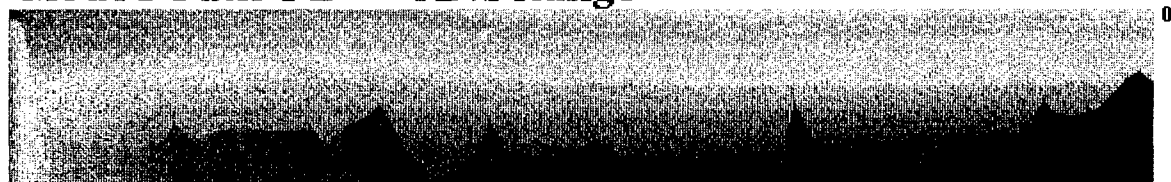
Our numerical Heard-to-Christmas Island pulse trans-

mission was carried out using the coupled mode Eqs. (6), (9), and (10). We chose the modal theory rather than the PE approach for multifrequency synthesis of a time domain pulse after comparing efficiency and accuracy of methods. If it were sufficient to transmit a small number of frequency components along known paths, the PE would be the method of choice. We decided, however, to transmit a highly resolved frequency spectrum (512 frequencies between 52 and 62 Hz). The eikonal solution of (6) involves parameters which interpolate well between adjacent frequencies, while PE results at large ranges probably do not. A benchmark comparison between the coupled mode and PE models at fixed frequencies is in progress, with results to date from both models appearing qualitatively correct. We take the

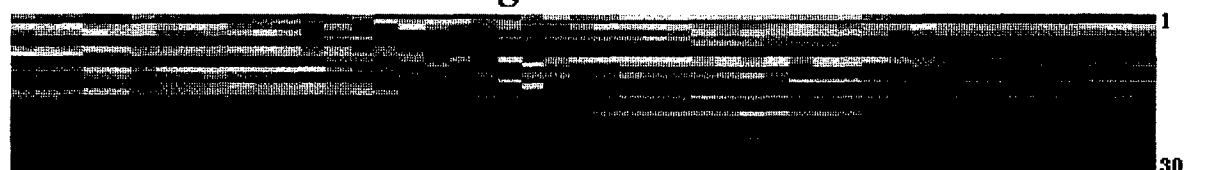
(a) Heard – Ascension Refracted Path



(b) Mode 1 Path PE TL vs Range



(c) Modal Excitation vs Range



Range

FIG. 11. Heard–Ascension Island PE result along the ray path for mode 1, 57 Hz. The initial field is that for a point source at 175-m depth. Other details are as described in Fig. 7.

agreement between coupled mode results and HIFT observations (Fig. 12) to be an empirical benchmark of the coupled mode model.

The calculation excited 30 vertical modes appropriate to point source excitation at 175-m depth. Twenty-one equally-spaced frequencies were used from 52 to 62 Hz. Modal eigenvalues κ_n were then interpolated to a finely spaced set of 512 frequencies covering the same frequency range, and coupled mode solutions to (12) were integrated along a common ray path for each of the 512 frequencies. Although this compromises the separate identity of modal paths, Fermat's principle states that the path integrated phases are stationary to first order in ray displacement.

Numerical errors in integrating phase factors over great distances can be minimized by transforming the problem to a frame moving horizontally with the propagating signal. This is comparable to the removal of a carrier frequency in the derivation of the parabolic equation. The phase advancements resulting from the imaginary term in (12) are accumulated in a coordinate system translating with a group speed \bar{v}_g . We use the maximum group speed over all modes as \bar{v}_g . The phases are accumulated in multiplicative increments

$$\exp[i(\kappa_n - \omega/\bar{v}_g)\delta s].$$

This phase factor is appropriate to a time origin shifted to match a group arrival at a given location, $t_a = \int ds/\bar{v}_g$. Fol-

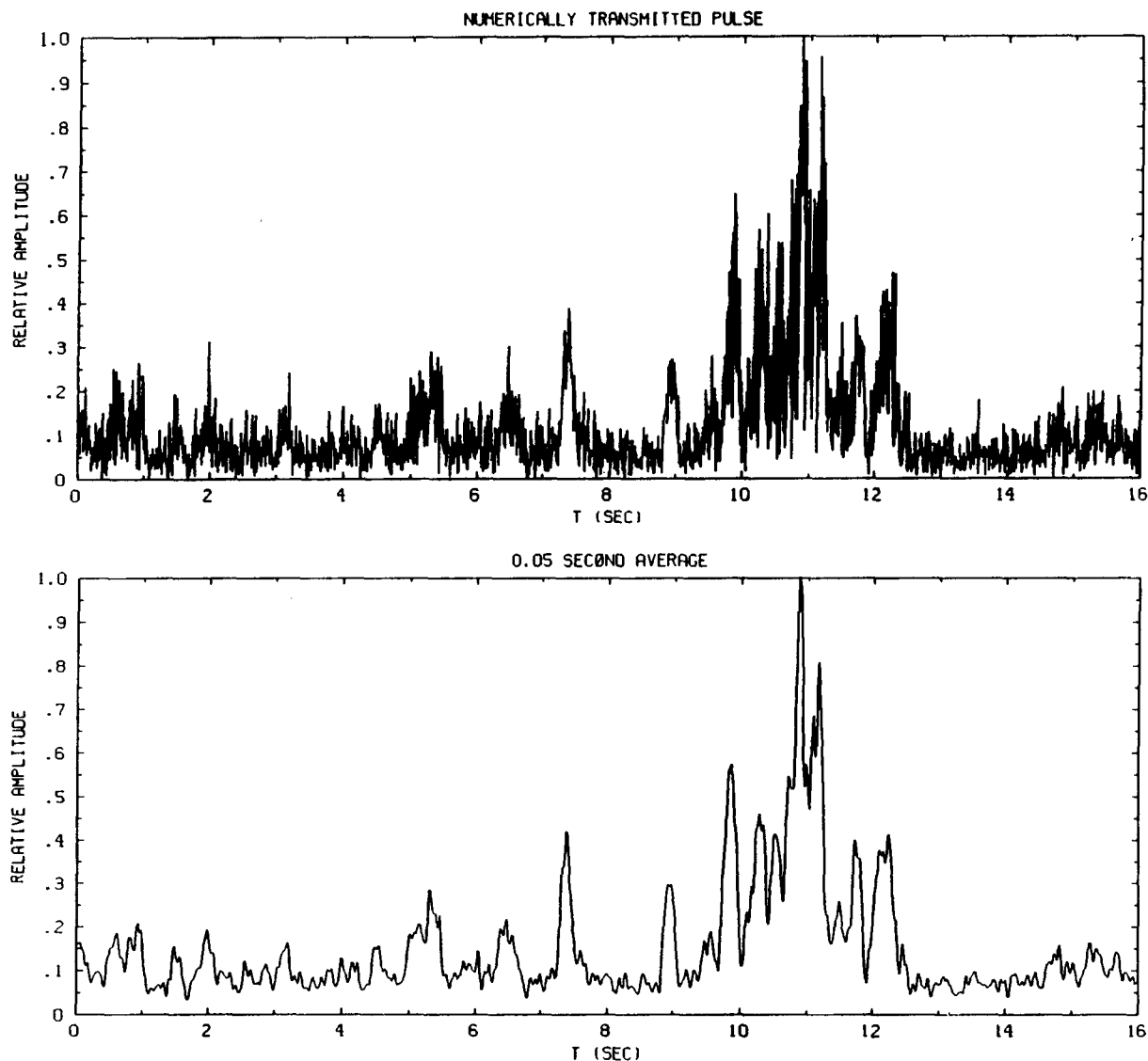


FIG. 12. (a) Heard-Christmas Island pulse calculation using 30 modes and 21 frequencies spanning 52 to 62 Hz. (b) Result in (a) smoothed with a cosine window with full-width at half-maximum of 0.05 s.

lowing the phase advancement, the mode coupling terms in (12) are integrated by finite differences. The step size δs ranges between 20 km in dispersive environments to 60 km in the deep ocean.

The mode amplitudes at the source were taken from the spectrum of the ten cycle sine wave pulse to be transmitted. Phases, coupling terms, and bottom attenuations¹ for the different modes and frequencies are integrated along the ray path for mode 1 at the center frequency of 57 Hz. After the path integrations for each of 21 frequencies (interpolated to 512) and 30 modes, the resulting spectral amplitudes at the receiver were Fourier transformed to the time domain with appropriate phases $-i\omega t$ relative to the initial arrival time t_a .

A finely-spaced time series was generated by summing over modes and frequencies on a set of 512 points covering 10 s [Fig. 12(a)]. The results were then smoothed incoherently [Fig. 12(b)] to recover the approximate time resolution displayed in pulse compression calculations (Metzger¹⁴). The

smoothing consisted of a cosine window with full-width at half-maximum of 0.05 s.

In Fig. 13 we overlay our numerically transmitted pulse (time origin arbitrarily adjusted for comparison) onto a composite over 110 pulse compression results for Christmas Island.¹³ While microstructure in our result differs considerably from that of the composite pulse compression, the temporal spread of energy and shape of the pulse envelope is fairly reasonable. One should not even hope for detailed agreement with observed microstructure, since the observed microstructure changed between each pulse transmission cycle. The approximate agreement in wavetrain envelope indicates that our calculated modes are subject to approximately the right levels of dispersion (i.e., differences in group velocity). In any event, our calculation appears to capture "the complex arrival structures not anticipated for this path..."¹⁵ i.e., a multiplicity of arrivals from a single pulse in the absence of bathymetric reflections.

We argue that meaningful pulse shape estimates may be

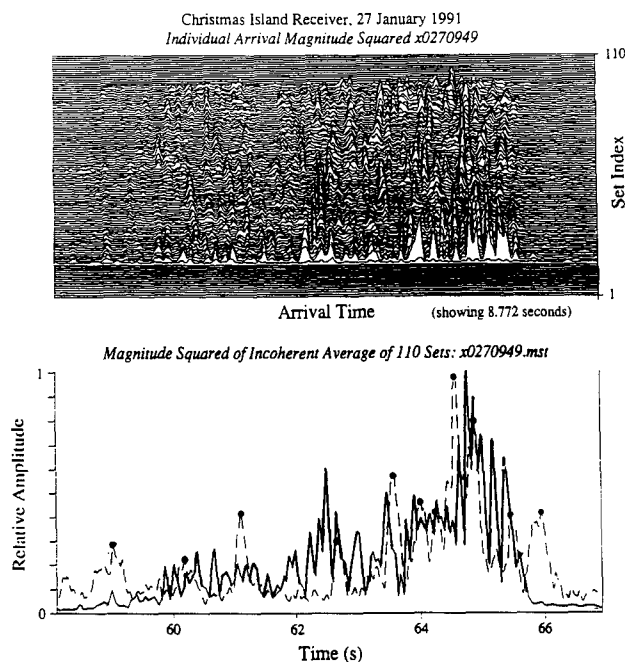


FIG. 13. (a) An example of 110 M-sequence pulse receptions at Christmas Island after pulse compression.¹³ (b) Solid line: incoherent average of the 110 compressed pulses. Dashed line: model pulse transmission of Fig. 12(b) with time origin shifted for comparison. Dots: significant peaks in the model result.

obtained with improved calculations and data bases, in spite of large uncertainties in the environment and in the numerical approximations used to obtain results. The envelope of a pulse is determined by the spread in path integrated group travel times for the different components. Its shape is much more robust than locations of the individual extrema, which are sensitive to large differences in integrated phase.

The pulse compression experimental results at Ascension Island showed more dispersion than did the Christmas results, presumably primarily because the path is longer (9000 km as compared to 5000 km). Numerical calculations are currently in progress for pulse transmission from Heard to Ascension, and will be reported at a future data.

IV. SUMMARY

We have demonstrated that certain features of the Heard Island Feasibility Test can be understood using a combination of adiabatic normal mode theory to define baseline propagation paths, plus two-dimensional range-depth PE calculations along those paths for representing propagation in range dependent ocean environments. Our results predict the

reception of several vertical modes off Monterey. Our calculated ray launch angles (Table I) are in close agreement (W. Munk, personal communication) with Doppler inferred launch angles observed during HIFT. Our numerical pulse propagation calculation from Heard to Christmas produced reasonable agreement with observed levels of dispersion and signal complexity. We believe that calculated pulse microstructure details are subject to large uncertainties due to path integrated phase errors. The shape of the pulse envelope, however, is not subject to phase errors, since it depends on the spread in integrated group travel times. Thus we have some confidence that overall pulse shape may be meaningfully investigated with the numerical methods we have described.

- ¹K. D. Heaney, W. A. Kuperman, and B. E. McDonald, "Perth-Bermuda sound propagation (1960): Adiabatic Mode Interpretation," *J. Acoust. Soc. Am.* **90**, 2586 (1991).
- ²R. C. Shockley, J. Northrop, P. G. Hansen, and C. Hartdegen, "SOFAR Propagation Paths from Australia to Bermuda: Comparison of Signal Speed Algorithms and Experiments," *J. Acoust. Soc. Am.* **71**, 51 (1982).
- ³M. D. Collins and E. K. Westwood, "A higher-order energy-conserving parabolic equation for range-dependent ocean depth, sound speed, and density," *J. Acoust. Soc. Am.* **89**, 1068-1075 (1991).
- ⁴M. D. Collins, "Benchmark calculations for higher-order parabolic equations," *J. Acoust. Soc. Am.* **87**, 1535-1538 (1990).
- ⁵A. D. Pierce, "Extension of the Method of Normal Modes to Sound Propagation in an Almost-Stratified Medium," *J. Acoust. Soc. Am.* **37**, 19 (1965).
- ⁶H. Weinberg and R. Burridge, "Horizontal Ray Theory for Ocean Acoustics," *J. Acoust. Soc. Am.* **55**, 63 (1974).
- ⁷E. C. Shang, Y. Y. Wang, and T. M. Georges, "Dispersion and Repopulation of the Heard-Ascension Modes," *J. Acoust. Soc. Am.* **96**, 2371-2379 (1994).
- ⁸A. B. Baggeroer, K. Lashkari, J. Miller, C.-S. Chiu, P. N. Mikhalevsky, and K. von der Heydt, "Vertical Array Receptions off Monterey for the Heard Island Feasibility Test Signals," *J. Acoust. Soc. Am.* **96**, 2395-2413 (1994).
- ⁹G. B. Deane and M. J. Buckingham, "An Analysis of the Three-Dimensional Sound Field in a Penetrable Wedge with a Stratified Fluid or Elastic Basement," *J. Acoust. Soc. Am.* **93**, 1319 (1993).
- ¹⁰S. Levitus, "Climatological Atlas of the World Ocean" NOAA prof. paper 13, U. S. Government Printing Office, Washington, DC (1982).
- ¹¹B. E. McDonald, "Bathymetric and Volumetric Contributions to Horizontal Refraction in Adiabatic Mode Theory," (unpublished).
- ¹²W. H. Munk, W. C. O'Reilly, and J. L. Reid, "Australia-Bermuda Sound Transmission Experiment (1960) Revisited," *J. Phys. Oceano.* **18**, 1876 (1988).
- ¹³T. F. Duda, S. M. Platté, J. A. Colosi, B. D. Cornuelle, J. A. Hildebrand, W. S. Hodgkiss, Jr., P. F. Worcester, B. M. Howe, J. A. Mercer, and R. C. Spindel, "Measured wave-front fluctuations in 1000-km pulse propagation in the Pacific Ocean," *J. Acoust. Soc. Am.* **92**, 939-955 (1992).
- ¹⁴K. Metzger, "A Brief Christmas Island multipath study," memo to Heard Island Feasibility Test investigators, 16 Jan 1992.
- ¹⁵G. Duingha and D. Farmer, "SCOR Working Group 96 Meeting: Summary, Plans, and Recommendations" Scripps Institute of Oceanography, p. 22 (10 June 1992).

Dispersion and repopulation of Heard-Ascension modes

E. C. Shang and Y. Y. Wang

CIRES, University of Colorado, Boulder, Colorado 80309 and NOAA Environmental Technology Laboratory, Boulder, Colorado 80303

T. M. Georges

NOAA Environmental Technology Laboratory, Boulder, Colorado 80303

(Received 22 August 1992; accepted for publication 7 June 1994)

The propagation of acoustic modes over the 9140-km underwater path to Ascension during the Heard Island Feasibility Experiment is simulated. Using a modal decomposition of the parabolic-equation field, we find that mode coupling at the circumpolar front has significant impact on modal dispersion and modal repopulation, which complicates the pulse-arrival sequence. Modal dispersion and modal repopulation are calculated at eleven frequencies from 52 to 62 Hz, and the effects on pulse spreading are shown.

PACS numbers: 43.30.Qd, 43.30.Bp

INTRODUCTION

The Heard Island Feasibility Test (HIFT) was conducted in January 1991 to test the global propagation of low-frequency (57 Hz) sound through the ocean.¹ Of the 19 worldwide receiving stations, the strongest receptions were recorded at Ascension Island in the South Atlantic Ocean, approximately 9140 km from Heard Island. The station was operated by NOAA scientists in cooperation with the U.S. Air Force.² Companion papers by Boden *et al.*³ and Palmer *et al.*² describe some observed properties of the Ascension receptions.

In this paper, we numerically simulate the acoustic propagation along the Heard-to-Ascension path. The first ten acoustic modes are calculated as a function of range by decomposing the parabolic-equation field. This method accounts for modal coupling where the sound-speed profile varies quickly with range, in particular, where the path crosses the circumpolar front and a double sound channel occurs. For comparison, adiabatic mode calculations have also been done. How accurately the global-scale or basin-scale temperature changes could be monitored with an "acoustic thermometer"⁴ depends on the spreading feature of the acoustic arrival pattern, which is basically determined by the dispersion character for a deterministic channel. Modal dispersion in a range-independent SOFAR channel has been well known, but the modal dispersion in a range-dependent channel with strong mode coupling has not been well understood. Our main purpose in this paper is to investigate the impact of mode coupling on the arrival pattern (modal dispersion). Modal dispersion is investigated using the stationary-phase method for estimating travel times for 11 acoustic frequencies from 52 to 62 Hz. Modal repopulation is also simulated, i.e., the redistribution of modal amplitudes after the energy exchange between modes due to mode coupling.

I. THE OCEAN MODEL

Twenty sound-speed profiles at 500-km intervals along the Heard-Ascension path are given by the ocean model

developed by Semtner and Chervin's global ocean circulation model,⁵ initialized with the Levitus 0.5° climatological data set.⁶ The model was run to 28 model years to eliminate transients, and sound-speed data were derived from a 30-day average. The final SSP data are provided by Chiu.⁷

The horizontal Heard-Ascension paths for the first four adiabatic normal modes are provided by Heaney and McDonald (Fig. 1).⁸ We neglected the small differences in sound-speed profiles between the four paths because the path separations are mostly smaller than the Levitus data grid and take the averaged one as the "reference" path. The twenty sound-speed profiles, corresponding to points "b" through "u" in Fig. 1, are shown in Fig. 2 along with the bathymetry along the path. Our propagation model linearly interpolates sound-speed values between profiles. An idealized liquid bottom is modeled by $C_b=1697$ m/s, $\rho_b=1.87$ g/cm³, and the attenuation $B=1.14$ dB/λ.

II. PROPAGATION MODEL

A full-wave acoustic field can be represented by an expansion in terms of local modes. Any three-dimensional field, $P_{3D}(x,y,z)$, can be decomposed into modes according to

$$P_{3D}(x,y,z) = \sum_m P_m(x,y) Z_m(z;x,y), \quad (1)$$

where $Z_m(z;x,y)$ is the local mode defined by

$$\left(\frac{\partial^2}{\partial z^2} + [k^2(z;x,y) - k_m^2(x,y)] \right) Z_m(z;x,y) = 0, \quad (2)$$

using the pertinent boundary conditions. In practice, we can extract the modal amplitude $P_m(x,y)$ from the computed parabolic equation (PE) field $P_{PE}(x,y,z)$ by using the orthogonality of Z_m :

$$P_m(x,y) = \int P_{PE}(x,y,z) Z_m(z;x,y) dz. \quad (3)$$

Spectral decomposition of the PE field has been used by Jensen and Schmidt⁹ for investigating the relative energy dis-

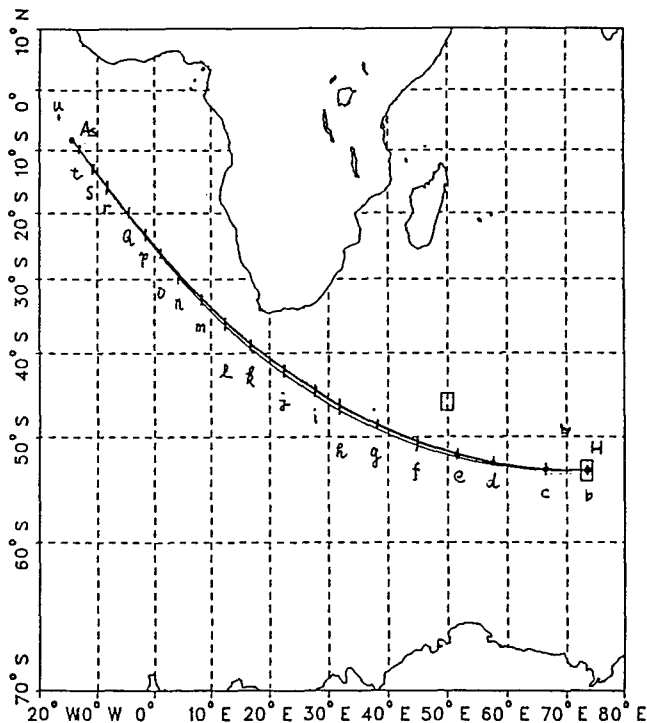


FIG. 1. The horizontal refracted ray paths for modes 1-4 from Heard to Ascension by Heany and McDonald.⁸

tribution between modes in a wedge-shaped ocean. Here, we use the modal spectrum of the PE field (MOSPEF) incorporated with the stationary-phase method to calculate the modal travel time involving strong mode coupling.¹⁰

To simplify computations, we replace a full three-dimensional PE calculation with a two-dimensional (r, z) PE calculation that marches along the average horizontally refracted ray path as the "reference" path described in the

Introduction. This approximation neglects the travel-time differences due to different horizontal modal paths that Heaney and McDonald calculated.

Fortunately, the four modal ray paths to Ascension differ only slightly from each other (Fig. 1), allowing us to treat modal dispersion and repopulation only in the (r, z) plane. If the modal rays were more widely separated (such as in the Perth-Bermuda experiment¹¹), it would be difficult to identify a single "reference" ray path.

Our PE solution is obtained using an implicit finite difference (IFD) (wide-angle) PE code (or WAPE),¹² and the local mode solution is obtained using the KRAKEN code.¹³ For a two-dimensional PE field, we have

$$P_{PE}(r, z; \omega) = (1/\sqrt{r}) \Psi_{PE}(r, z; \omega) e^{ik_0 r}, \quad (4)$$

where k_0 is a reference wave number, and ω is the angular frequency. Substituting the PE solution Eq. (4) into Eq. (3), we get the modal field

$$\begin{aligned} \sqrt{r} \cdot P_m(r; \omega) &= \left(\int \Psi_{PE}(r, z; \omega) Z_m(z; r; \omega) dz \right) e^{ik_0 r} \\ &= A_m(r; \omega) e^{ik_0 r} = |A_m(r; \omega)| e^{i\Phi_m(r; \omega)}, \end{aligned} \quad (5)$$

where the complex modal amplitude is

$$A_m(r; \omega) = \int \Psi_{PE}(r, z; \omega) Z_m(z; r; \omega) dz, \quad (6)$$

and the modal phase is

$$\Phi_m(r; \omega) = k_0 r + \arg[A_m(r; \omega)]. \quad (7)$$

Effects of modal repopulation are given by range variations in $|A_m(r; \omega)|$, and the dependence of modal dispersion on range and frequency is given by $\Phi_m(r; \omega)$.

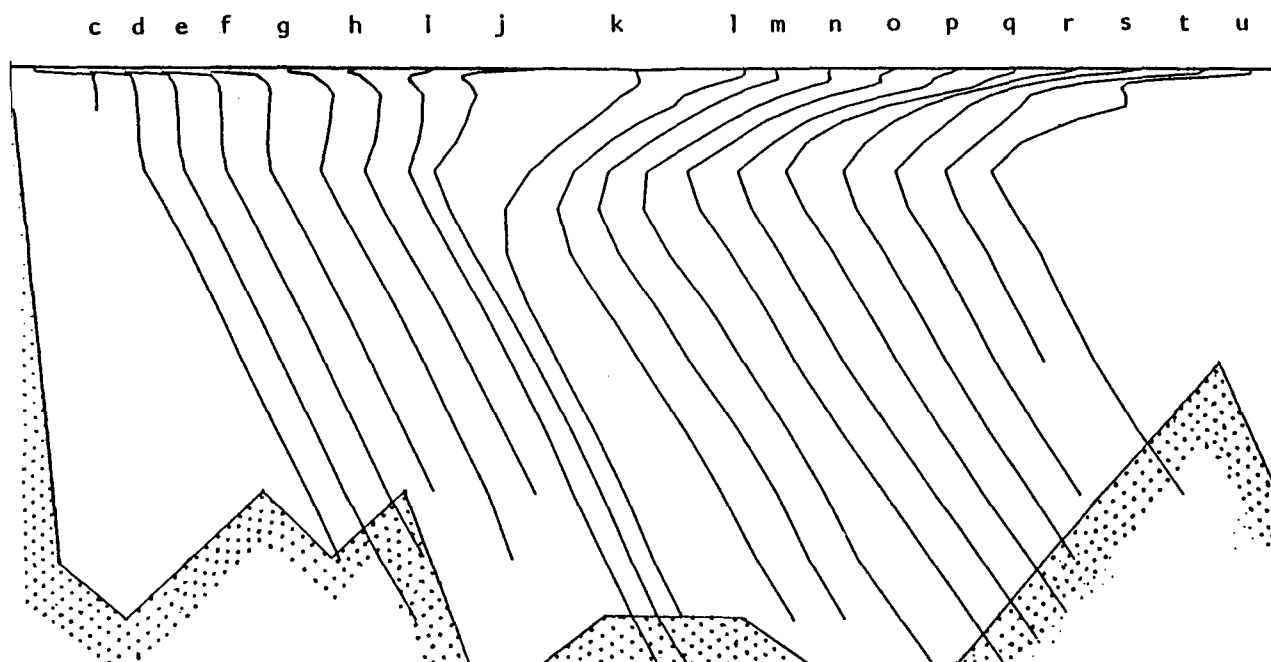


FIG. 2. The sound-speed profiles (SSP) of each point along the Heard-Ascension path.

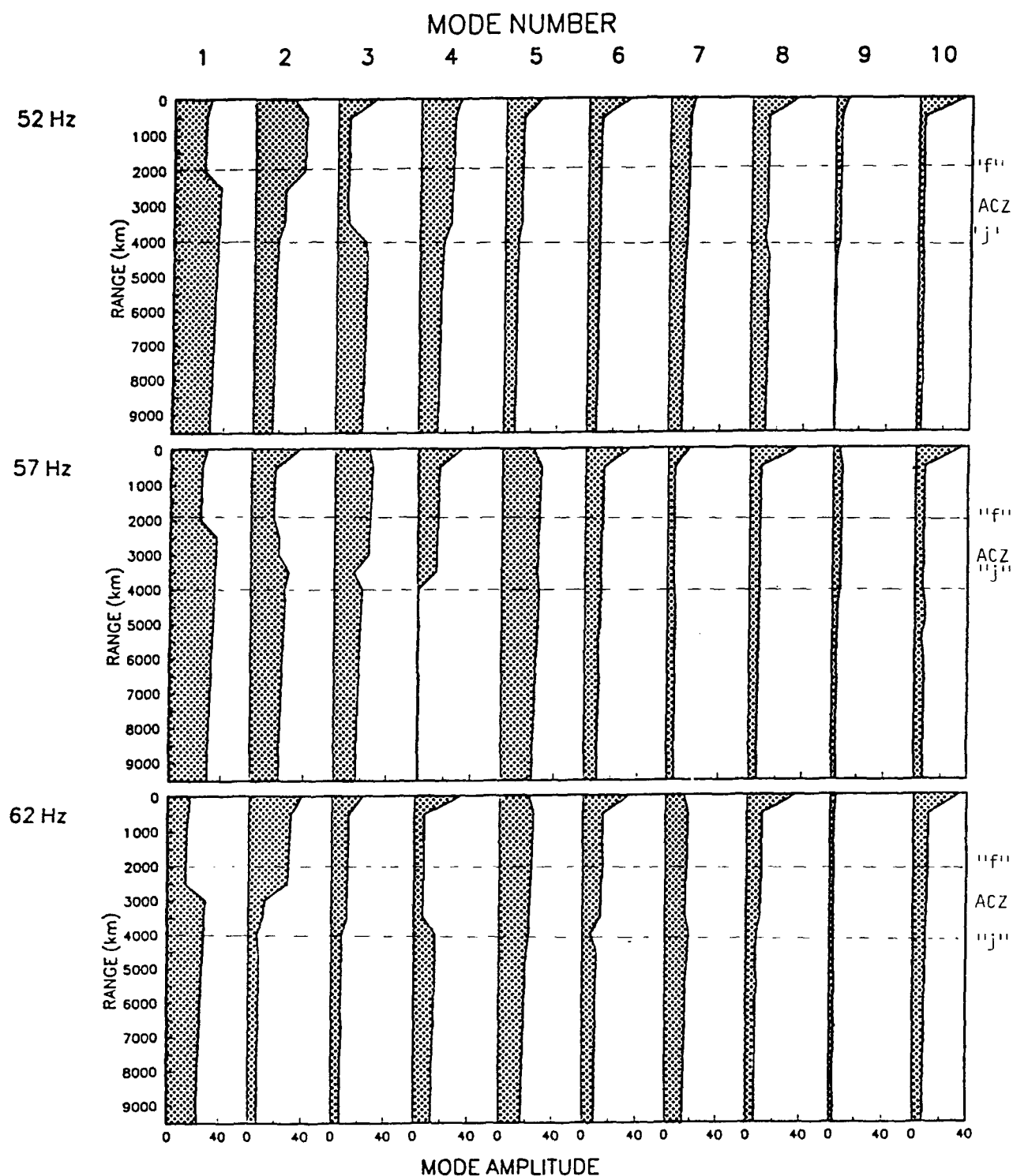


FIG. 3. Modal repopulation of 52-, 57-, and 62-Hz frequency components.

When the adiabatic mode approximation is valid (that is, no mode coupling), our results for Eqs. (6) and (7), respectively, should reduce to

$$|A_m(r; \omega)| \sim Z_m(z_s; r_s), \quad (8)$$

$$\Phi_m(r; \omega) \sim \int_{r_s}^r k_m(r) dr. \quad (9)$$

To show where mode coupling is significant, we will compare MOSPEF results with adiabatic-mode calculations. Mode coupling is also evident when the MOSPEF amplitudes of different modes are plotted versus range.

It is well known that there are phase (and thus travel-time) errors in the PE solution, which are a function of vertical aperture angle θ (with respect to the horizontal) and range.^{14,15}

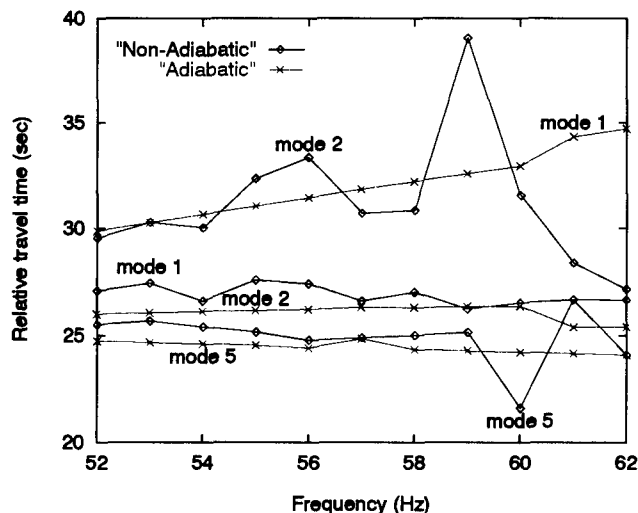


FIG. 4. Modal dispersion from point "b" to point "u" (across ACZ).

$$(\Delta\phi)_{PE} = F(\theta)k_0r, \quad (\Delta t)_{PE} = F(\theta)r/C_0, \quad (10)$$

where $F(\theta)$ is a function of the aperture angle given by

$$F(\theta) = \begin{cases} \frac{1}{2}(1 - \cos \theta)^2, & \text{for standard PE,} \\ \frac{1}{4}(1 - \cos \theta)^3, & \text{for WAPE.} \end{cases} \quad (11)$$

Taking 9140 km for range and 9° for aperture angle, the travel-time errors for the Heard-Ascension path are:

$$(\Delta t)_{PE}^{ST} \leq 450 \text{ ms}, \quad (\Delta t)_{PE}^{WA} \leq 3 \text{ ms}.$$

It should be noted that the above error analysis is based on a range-independent medium, and thus serves only as a rough estimation.

III. MODAL DISPERSION AND REPOPULATION

A. Modal repopulation

For a range-independent waveguide, the energy distribution among modes is fixed by the initial modal excitation—there is no repopulation. Here, the term *modal repopulation* means that the energy distribution between modes is changed from range to range due to mode coupling. Because we ex-

pect mode coupling to depend on frequency, we calculated modal amplitudes versus range for 11 frequencies between 52 and 62 Hz, the nominal bandwidth of the Heard Island M-sequence transmissions. For example, results showing modal repopulation for three of the 11 frequencies (52, 57, and 62 Hz) and the first ten modes are displayed in Fig. 3. As we can see from Fig. 3, significant modal repopulation occurs between $R=2000$ km (point "f") to $R=4000$ km (point "j"), corresponding to the Antarctic Convergence Zone (ACZ). There is almost no modal repopulation after $R=4000$ km, and this is consistent with the strong adiabaticity indicated by modal travel time from point "l" to point "u" shown in Table II.

B. Modal pulse in the time domain

If the source's frequency spectrum is $S(\omega)$, then the time-domain pressure field is given by the Fourier integral,

$$p(r, z; t) = \frac{1}{2\pi} \int S(\omega) p(r, z; \omega) e^{-i\omega t} d\omega. \quad (12)$$

Substituting Eq. (5) into Eq. (12), we obtain

$$p(r, z; t) = (2\pi\sqrt{r})^{-1} \int S(\omega) \times \sum_m |A_m(r; \omega)| Z_m(z; r; \omega) e^{i[\Phi_m(r, \omega) - \omega t]} d\omega. \quad (13)$$

Exchanging the order of integration and summation, the total time-domain signal is

$$p(r, z; t) = (2\pi\sqrt{r})^{-1} \sum_m p_m(r, z; t), \quad (14)$$

where $p_m(r, z; t)$ is the time-domain signal for mode m :

$$p_m(r, z; t) = \int S(\omega) |A_m(r; \omega)| Z_m(z; r; \omega) e^{i[\Phi_m - \omega t]} d\omega. \quad (15)$$

The time-domain signal, or pulse shape, for mode m can be computed by evaluating Eq. (15) numerically using an FFT. In this paper, we do not process FFT to numerically

TABLE I. Modal arrival time for 11 frequencies (at point "u," -6400 s).

| f (Hz) | Mode 1 | | Mode 2 | | Mode 3 | | Mode 4 | | Mode 5 | | Mode 6 | |
|----------|--------|-------|--------|-------|--------|-------|--------|-------|--------|-------|--------|-------|
| | PE | AD | PE | AD | PE | AD | PE | AD | PE | AD | PE | AD |
| 52 | 27.06 | 29.86 | 29.54 | 25.98 | 27.51 | 24.69 | 25.08 | 24.16 | 25.50 | 24.72 | 25.08 | 25.15 |
| 53 | 27.43 | 30.26 | 30.28 | 26.04 | 24.39 | 24.65 | 24.34 | 24.09 | 25.67 | 24.66 | 25.05 | 25.12 |
| 54 | 26.59 | 30.65 | 30.03 | 26.10 | 25.64 | 24.62 | 24.83 | 24.04 | 25.39 | 24.59 | 25.26 | 25.10 |
| 55 | 27.58 | 31.04 | 32.34 | 26.15 | 25.43 | 24.59 | 24.75 | 23.99 | 25.16 | 24.53 | 25.48 | 25.07 |
| 56 | 27.40 | 31.43 | 33.36 | 26.20 | 25.72 | 24.56 | 25.05 | 23.94 | 24.77 | 24.40 | 25.04 | 25.04 |
| 57 | 26.60 | 31.83 | 30.71 | 26.30 | 24.40 | 24.69 | ... | 24.18 | 24.89 | 24.84 | 24.78 | 25.60 |
| 58 | 27.01 | 32.20 | 30.85 | 26.29 | 23.54 | 24.51 | 26.77 | 23.86 | 25.00 | 24.33 | 25.74 | 24.98 |
| 59 | 26.23 | 32.57 | 39.05 | 26.33 | 27.00 | 24.49 | 27.17 | 23.83 | 25.14 | 24.27 | 24.86 | 24.94 |
| 60 | 26.52 | 32.94 | 31.55 | 26.36 | 23.02 | 24.47 | 27.18 | 23.80 | 21.61 | 24.21 | 25.03 | 24.91 |
| 61 | 26.66 | 34.33 | 28.38 | 25.38 | ... | 24.45 | 26.22 | 23.78 | 26.66 | 24.15 | 25.48 | 24.87 |
| 62 | 26.56 | 34.71 | 27.15 | 25.39 | 30.06 | 24.43 | 28.54 | 23.76 | 24.09 | 24.08 | 26.82 | 24.83 |

TABLE II. Modal amplitude for 11 frequencies (at point "u").

| | Mode 1 | Mode 2 | Mode 3 | Mode 4 | Mode 5 | Mode 6 |
|----------|--------------------|--------------------|--------------------|--------------------|--------------------|--------------------|
| f (Hz) | amplitude P_1 | amplitude P_2 | amplitude P_3 | amplitude P_4 | amplitude P_5 | amplitude P_6 |
| 52 | 18.3 | 6.3 | 2.2 | 1.4 | 4.7 | 9.4 |
| 53 | 14.1 | 8.1 | 1.4 | 1.5 | 3.5 | 4.0 |
| 54 | 7.5 | 6.2 | 8.8 | 3.4 | 7.0 | 8.4 |
| 55 | 19.9 | 7.0 | 6.3 | 3.4 | 9.4 | 2.0 |
| 56 | 8.6 | 3.3 | 3.8 | 0.3 | 14.4 | 9.0 |
| 57 | 11.7 | 29.5 | 4.7 | ... | 23.6 | 3.0 |
| 58 | 10.1 | 3.0 | 1.8 | 1.7 | 14.2 | 3.0 |
| 59 | 16.5 | 1.1 | 1.6 | 18.6 | 2.2 | 7.6 |
| 60 | 24.4 | 2.6 | 0.2 | 2.0 | 0.8 | 7.6 |
| 61 | 31.7 | 1.3 | ... | 0.8 | 1.8 | 4.0 |
| 62 | 31.1 | 2.1 | ... | 0.7 | 2.3 | 1.6 |

obtain the modal pulse in the time domain. Alternatively, we use the stationary-phase method to estimate Eq. (15) for analysis purposes.

The value of the integral in Eq. (15) can be estimated using the stationary-phase method, provided the amplitude is slowly varying and the phase of the integrand is rapidly varying except in the vicinity of an isolated stationary-phase point, where

$$\left(t - \frac{\partial \Phi_m(r; \omega)}{\partial \omega}\right)_{\omega_s} = 0. \quad (16)$$

Using this method,¹⁶ Eq. (15) can be estimated as

$$p_m(r, z; t) \approx \sqrt{\frac{2\pi}{\Phi_m''(\omega_s)}} e^{\pm i(\pi/4)} S[\omega_s(t)] |A_m[r; \omega_s(t)]| \times Z_m(z; r; \omega_s) e^{i[\Phi_m \omega_s(t) - \omega_s t]}. \{1 + \dots\}, \quad (17)$$

where the $\{ \}$ term is

$$\{1 + \dots\} = \left\{ 1 + \frac{1}{r} \left[\frac{-5(\Phi_m''')^2}{24(\Phi_m'')^3} + \frac{(\Phi_m''''')}{8(\Phi_m'')^2} \right] + O\left(\frac{1}{r^2}\right) \right\}. \quad (18)$$

The stationary-phase point condition (16) determines the modal group velocity and a mapping relationship between frequency and arrival time, and hence describes the frequency dispersion of each mode. For a given frequency and range, then, the energy arrival time of a decomposed mode is given by

$$t_m(r; \omega) = \left(\frac{\partial \Phi_m(r, \omega)}{\partial \omega} \right)_{\omega}. \quad (19)$$

Substituting (7) into (19), we get the MOSPEF arrival time

$$t_m^{PE}(r; \omega) = \frac{r}{C_0} + \frac{\partial}{\partial \omega} [\arg A_m(r, \omega)]. \quad (20)$$

In obtaining Eqs. (19) and (20), mode splitting by horizontal refraction is not considered, but the arrival splitting for a decomposed mode due to mode coupling is included. The multiple arrival for a single decomposed mode represents the fact of "multi-path" in mode space due to mode-mode scattering (see Fig. 4), and this information is contained in the decomposed modal phase $\Phi_m(r; \omega)$.

For comparison, the adiabatic modal arrival time is

$$t_m^{AD}(r; \omega) = \int_0^r \frac{dr}{U_m(\omega; r)}, \quad (21)$$

where the modal group velocity $U_m(\omega; r)$ is calculated by^{17,18}

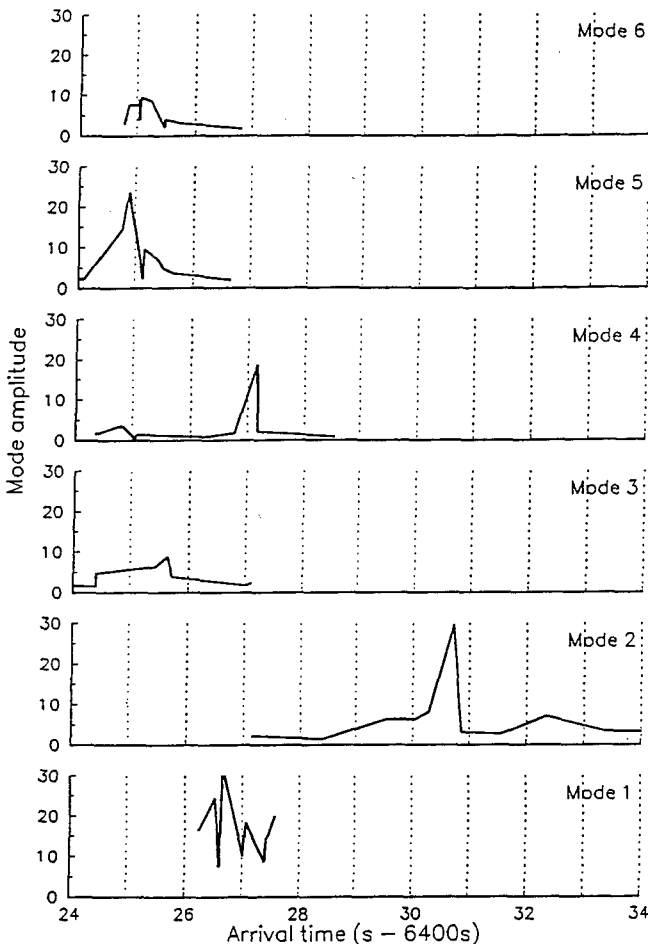


FIG. 5. The estimated arrival patterns of modes 1–6 at point "u."

TABLE III. Modal travel time for 11 frequencies (from point "L" to point "u").

| <i>F</i> (Hz) | Mode 1 | | Mode 2 | | Mode 3 | | Mode 4 | | Mode 5 | | Mode 6 | |
|---------------|---------|---------|--------------|---------|--------------|---------|--------------|---------|---------|---------|--------------|---------|
| | MOSPEF | ADIAB | MOSPEF | ADIAB | MOSPEF | ADIAB | MOSPEF | ADIAB | MOSPEF | ADIAB | MOSPEF | ADIAB |
| 52 | 3036.26 | 3036.25 | 3035.60 | 3035.60 | 3035.19 | 3035.19 | 3034.73 | 3034.72 | 3034.17 | 3034.21 | 3033.58 | 3033.58 |
| 53 | 3036.28 | 3036.32 | 3035.73 | 3035.62 | 3035.31 | 3035.27 | 3034.75 | 3034.77 | 3034.28 | 3034.25 | 3033.67 | 3033.68 |
| 54 | 3036.27 | 3036.32 | 3035.65 | 3035.63 | 3035.33 | 3035.36 | 3034.78 | 3034.80 | 3034.29 | 3034.30 | 3033.73 | 3033.75 |
| 55 | 3036.31 | 3036.33 | 3035.56 | 3035.65 | 3035.23 | 3035.35 | 3034.81 | 3034.84 | 3034.33 | 3034.34 | 3033.75 | 3033.82 |
| 56 | 3036.31 | 3036.34 | 3035.75 | 3035.65 | 3035.30 | 3035.32 | 3034.85 | 3034.87 | 3034.37 | 3034.38 | 3033.87 | 3033.89 |
| 57 | 3036.32 | 3036.35 | 3035.64 | 3035.66 | 3035.26 | 3035.34 | ^a | 3034.90 | 3034.41 | 3034.42 | 3033.91 | 3033.95 |
| 58 | 3036.31 | 3036.36 | 3035.59 | 3035.67 | 3035.27 | 3035.36 | 3034.91 | 3034.93 | 3034.43 | 3034.45 | 3033.95 | 3034.01 |
| 59 | 3036.34 | 3036.37 | ^a | 3035.68 | 3035.38 | 3035.38 | 3034.97 | 3034.96 | 3034.53 | 3034.49 | 3034.03 | 4034.06 |
| 60 | 3036.34 | 3036.37 | 3035.62 | 3035.69 | ^a | 3035.39 | 3034.94 | 3034.99 | 3034.35 | 3034.52 | 3034.10 | 3034.11 |
| 61 | 3036.34 | 3036.38 | 3035.79 | 3035.70 | ^a | 3035.40 | 3034.97 | 3035.01 | 3034.56 | 3034.56 | 3034.15 | 3034.16 |
| 62 | 3036.36 | 3036.39 | 3035.60 | 3035.71 | ^a | 3035.42 | 3035.13 | 3035.04 | 3034.64 | 3034.59 | ^a | 3034.21 |

^aNote: *MOSPEF travel time is not available due to very weak amplitude.

$$U_m(\omega; r) = \left(C_m(\omega; r) \int Z_m^2(z; r; \omega) \frac{1}{C^2(z; r)} dz \right)^{-1}. \quad (22)$$

C. Modal dispersion and arrival pattern

Modal dispersion character is determined by the modal phase behavior expressed in Eq. (16) or (19). By implementing the finite difference operation, modal travel times of each decomposed mode can be obtained. Modal travel time results at point "u" ($R=9500$ km) for modes 1–6 at eleven frequencies (52–62 Hz) are listed in Table I. The corresponding adiabatic modal travel times given by Eqs. (21) and (22) are also listed in Table I for comparison. Examples of the modal dispersion curves, the mapping relationship between frequency and arrival time $t_m(\omega_s) \sim \omega_s$, are plotted in Fig. 4, where the heavy lines represent the MOSPEF results and the light lines represent the adiabatic mode results.

The modal arrival pattern can be constructed based upon Eq. (17). The decomposed modal energy as a function of the arrival time (pulse shape) can be calculated by using Eq. (17) with the mapping relationship given by Eq. (16). The process is as follows. For a given frequency ω_s , Eq. (16) determines an arrival time, $t_m(\omega_s)$, and the amplitude p_m corresponding to this arrival time is given by Eq. (17). Of course, p_m will depend on several factors, including $Z_m(z; r; \omega)$ (here, z is the receiving depth), $A_m(r; \omega_s)$, the original signal spectrum $S(\omega_s)$, and the factor of $\sqrt{1/\Phi_m''(\omega_s; r)}$, which represents the amplitude reduction due to the time spreading. The calculated amplitude of p_m for a receiving depth at $Z=800$ m and a Gaussian-like spectrum function $S(\omega)$ are listed in Table II, and the combined arrival pattern of $p_m[t(\omega_s)]$ are plotted in Fig. 5.

D. Results of a shorter path without ACZ

In order to illustrate the significant mode coupling impact caused by ACZ, we consider only the part of the path between point "l" (near South Africa) and point "u" (range = 5000 to 9500 km), where the sound channel varies slowly and it appears that negligible mode coupling occurs. For that partial path, we compare the arrival sequence computed by the MOSPEF method with that computed using adiabatic

normal models. Results of modal arrival times are listed in Table III. Modal dispersion curves are plotted in Fig. 6, and the modal arrival sequences are plotted in Fig. 7. As we can see from Table III, the nonadiabatic travel times and the adiabatic travel times are very close, indicating a strong adiabaticity for this partial path.

IV. CONCLUSIONS

(1) Acoustic propagation simulation based on Semtner–Chervin's ocean model reveals the significance of mode coupling across the ACZ.

(2) In consequence of mode coupling, two interesting features of the mode dispersion can be found (see Fig. 4).

- The mapping relationship between arrival time and frequency is no longer simple and monotonic, and it is possible to have multiple "arrival peaks" for one mode (see Table I for mode 1).
- Mode coupling can change the ordinary adiabatic arrival order. In our example, mode 1 is no longer the latest arrival but mode 2 is the latest arrival.

An explanation of these features is discussed in the Appendix.

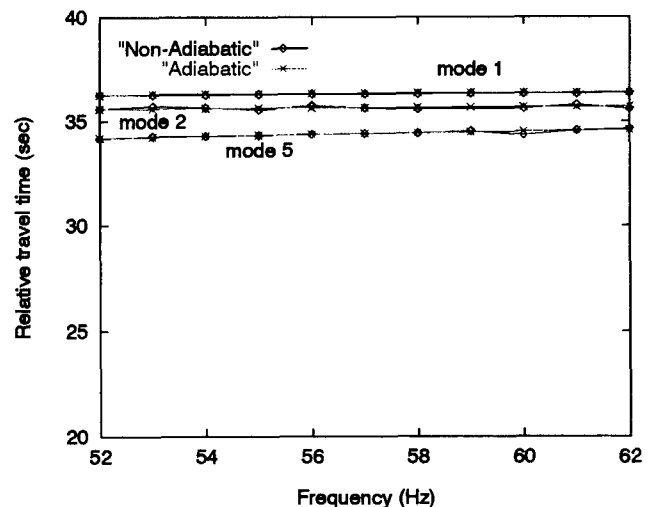


FIG. 6. Modal dispersion from point "l" to point "u" (without ACZ).

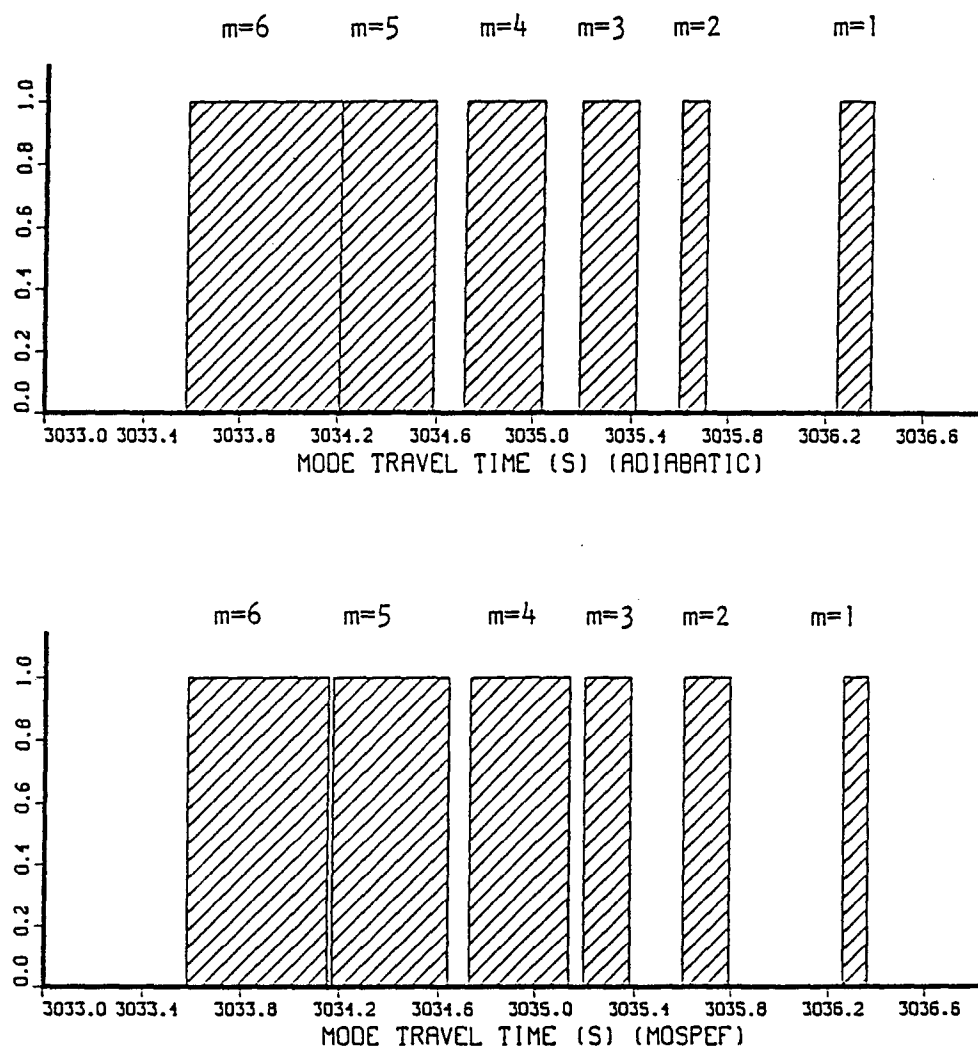


FIG. 7. The arrival sequence from point "l" to point "u."

(3) It is too coarse to consider the detailed structure of the arrival pattern based on our 11 frequency components calculation. However, the estimation of the arrival spread, about 7 s, given by the lowest six modes does make sense and is consistent with the measured spread.³

(4) In contrast to the adiabatic mode, in the coupled mode regime, details of the arrival pattern are sensitive to initial conditions, such as source depth, the bathymetry near the source, and source motion. These effects should be taken into account in any detailed study.

(5) An adiabatic mode model might be used to adequately estimate the propagation and arrival structure for a path without ACZ (see Table III and Fig. 6).

(6) Finally, results of simulation in this paper are expected to stimulate comparisons with the HIFT data set in the near future.

ACKNOWLEDGMENTS

This work was supported by the Office of Naval Research (ONR) and the National Oceanic and Atmospheric Administration (NOAA). We thank Dr. C. S. Chiu for providing his sound-speed data, and Dr. K. Heaney for providing his horizontal ray-path data and for helpful discussions.

APPENDIX: INTERPRETATION OF THE MODAL ARRIVAL FEATURES

For interpretation purposes, we consider a simplified environmental model by assuming that mode coupling only takes place at range $r=r_c=2000$ km and the SSP has been changed suddenly from profile "f" to profile "g" at that range. On the two sides of that range (regions of $r<r_c$ and $r>r_c$), the field can be represented by adiabatic modes. Then, we have

$$p(r, z; \omega) = \sum_m a_m e^{\exp\left(i \int_0^{r_c} k_m dr\right)} \cdot Z_m(z, r) \quad (r < r_c), \quad (A1)$$

$$p(r, z; \omega) = \sum_n b_n e^{\exp\left(i \int_{r_c}^r k_n dr\right)} \cdot \bar{Z}_n(z, r) \quad (r > r_c). \quad (A2)$$

The one-way field matching condition at $r=r_c$ gives

$$b_n = \sum_m a_m e^{\exp\left(i \int_0^{r_c} k_m dr\right)} \cdot C_{mn}, \quad (A3)$$

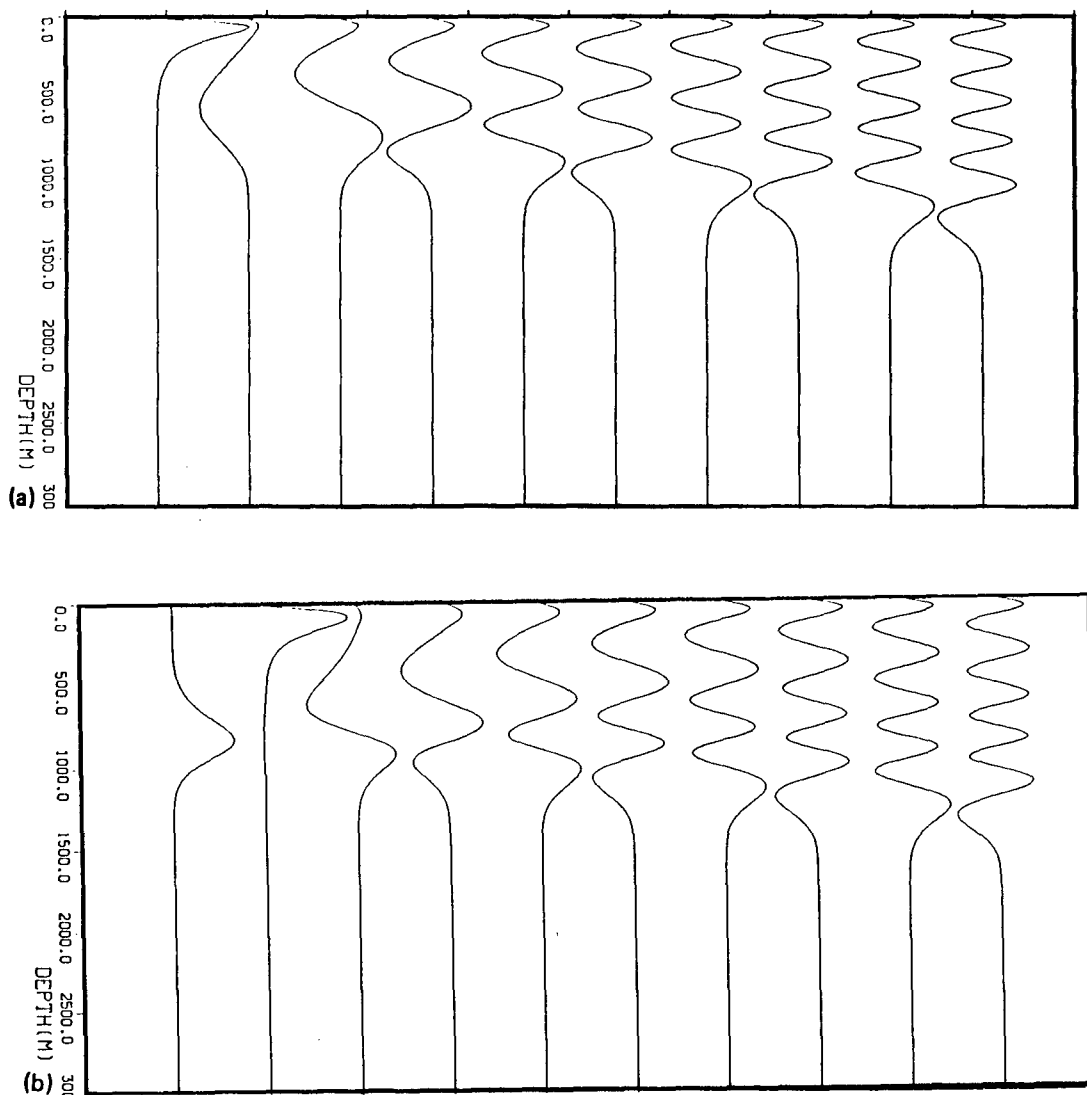


FIG. A1. (a) The local mode eigenfunctions at point "f." (b) The local mode eigenfunctions at point "g."

where the coupling coefficient C_{mn} is

$$C_{mn} = \int Z_m(z, r_c) \cdot \tilde{Z}_n(z, r_c) dz. \quad (A4)$$

By using the local modes at "f" as $Z_m(z, r_c)$ [see Fig. A1(a)] and the local modes at "g" as $\tilde{Z}_n(z, r_c)$ [see Fig. A1(b)], C_{mn} are calculated and the results are listed in Table A1. Substituting Eq. (A3) into (A2), we get

$$p(r, z; \omega) = \sum_n p_n(r, z; \omega), \quad (A5)$$

$$p_n(r, z; \omega) = \sum_m a_m \cdot C_{mn} \cdot \tilde{Z}_n(z, r) \cdot e^{\exp\left(i \int_0^{r_c} k_m dr + i \int_{r_c}^r k_n dr\right)}. \quad (A6)$$

TABLE A1. Mode coupling matrix at $r_c = 2000$ km.

| mode (n) | (f=57 Hz profile f-m profile g-n) | | | | | |
|-------------|-----------------------------------|---------|---------|---------|---------|---------|
| | (m=1) | 2 | 3 | 4 | 5 | 6 |
| 1 | 0.0198 | -0.5866 | 0.6217 | -0.4663 | 0.2166 | -0.0531 |
| 2 | 0.9855 | -0.0122 | -0.0529 | -0.0352 | -0.0625 | -0.0540 |
| 3 | 0.0149 | 0.7237 | 0.1575 | -0.4908 | 0.3982 | -0.2202 |
| 4 | 0.0261 | 0.3600 | 0.6654 | 0.1784 | -0.4784 | 0.3683 |
| 5 | 0.0370 | 0.0281 | 0.3703 | 0.6000 | 0.2118 | -0.5409 |
| 6 | 0.0462 | -0.0033 | 0.0643 | 0.3733 | 0.5859 | 0.2081 |

TABLE AII. Adiabatic modal travel times before r_c and after r_c .

| m | $t_m^{\text{Ad}}(r_c)$ (s) |
|-----|----------------------------|
| 1 | 1365.42 |
| 2 | 1360.50 |
| 3 | 1360.73 |
| 4 | 1360.99 |
| 5 | 1361.84 |
| 6 | 1362.80 |

| |
|--|
| $t_1^{\text{Ad}}(r_u - r_c) = 5066.40$ (s) |
| $t_2^{\text{Ad}}(r_u - r_c) = 5065.80$ (s) |

For example, the arrival patterns of the resolved mode 1 and mode 2 at $r = r_c$ are given by

$$p_1(r, z; t) = \sum_m a_m C_{m1} \tilde{Z}_1(z, r) \cdot p_{m1}(t), \quad (\text{A7})$$

$$p_2(r, z; t) = \sum_m a_m C_{m2} \tilde{Z}_2(z, r) \cdot p_{m2}(t), \quad (\text{A8})$$

where

$$p_{m1}(t) = \int S(\omega) e \exp \left(i \int_0^{r_c} k_m dr + i \int_{r_c}^r k_1 dr \right) \cdot d\omega \quad (\text{A9})$$

$$p_{m2}(t) = \int S(\omega) e \exp \left(i \int_0^{r_c} k_m dr + i \int_{r_c}^r k_2 dr \right) \cdot d\omega. \quad (\text{A10})$$

By using the stationary-phase method, $p_{m1}(t)$ and $p_{m2}(t)$ will have arrival times given by

$$t_{m1} = t_m^{\text{Ad}}(r_c) + t_1^{\text{Ad}}(r_u - r_c), \quad (\text{A11})$$

$$t_{m2} = t_m^{\text{Ad}}(r_c) + t_2^{\text{Ad}}(r_u - r_c). \quad (\text{A12})$$

Values of $t_m^{\text{Ad}}(r_c)$ and $t_n^{\text{Ad}}(r_u - r_c)$ are listed in Table AII.

For simplicity, we take a_m as a constant and combine the C_{mn} values in Table AI with the t_m^{Ad} values in Table AII. The arrival patterns of mode 1 and mode 2 are plotted in Fig. A2.

This coupling model is too simple to give a fine arrival pattern, but it can provide an easy way to understand the multiple arrival structure of a single mode due to mode-mode scattering, and it is also good enough to explain the changing of ordinary adiabatic arrival order. Feature "a" in the conclusion can be explained as follows: According to the mode coupling matrix, the "new" mode 1 (after coupling) is mainly contributed by the "old" modes 2, 3, 4, and 5 (before coupling). Each contribution brings its own "old" travel times [$t_m^{\text{Ad}}(r_c)$ in Eq. (A11)] and thus makes the multiple arrival peaks in mode 1. Feature (b) in the conclusion can be explained as follows: As we can see from Table AII, the 5 s delay of mode 1 traveling in the surface duct

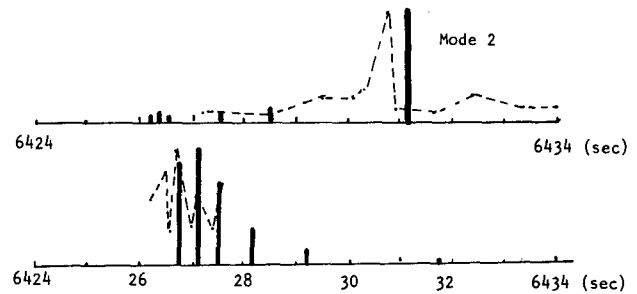


FIG. A2. The arrival patterns of mode 1 and mode 2 given by a simple mode coupling model (solid lines) and the results given by MOSPEF (dashed lines).

[$t_1^{\text{Ad}}(r_c) = 1365.42$ s vs $t_2^{\text{Ad}}(r_c) = 1360.50$ s] has been adopted by mode 2 due to a *strong* coupling ($C_{12} = 0.98$). This adoption plus the weak C_{11} and C_{22} produce the result of reversal arrival order.

- ¹W. H. Munk, R. C. Spindel, A. B. Baggeroer, and T. G. Birdsall, "The Heard Island Feasibility Test," J. Acoust. Soc. Am. **96**, 2330–2342 (1994).
- ²D. Palmer, T. Georges, J. Wilson, L. Weiner, A. Paisley, R. Mathiesen, R. Pleshek, and R. Mabe, "Reception at Ascension Island, South Atlantic, of the transmissions from the Heard Island Feasibility Test," J. Acoust. Soc. Am. **96**, 2432–2440 (1994).
- ³T. M. Georges, L. R. Boden, and D. R. Palmer, "Features of the Heard Island signals received at Ascension," J. Acoust. Soc. Am. **96**, 2441–2447 (1994).
- ⁴W. Munk, "Global ocean warming: An acoustic measure?," J. Phys. Ocean. **19**, 1765–1778 (1989).
- ⁵A. Semtner and R. Chervin, "A simulation of the global ocean circulation with resolved eddies," J. Geophys. Res. **93**(C12), 15502–15522 (1988).
- ⁶S. Levitus, "Climatological atlas of the world's oceans," NOAA Prof. Paper 13, U.S. Gov't. Printing Office, Washington, DC (1982).
- ⁷C. S. Chiu (private communication, December 1990).
- ⁸K. Heaney and E. McDonald (private communication, November 1991).
- ⁹F. B. Jensen and H. Schmidt, "Spectral decomposition of PE field in a wedge-shaped ocean," in *Progress in Underwater Acoustics*, edited by H. Merklinger (Plenum, New York, 1987), pp. 557–564.
- ¹⁰E. C. Shang and Y. Y. Wang, "Acoustic travel time computation based on PE solution," J. Comput. Acoust. **1**(1), 91–100 (1993).
- ¹¹K. Heaney, W. Kuperman, and B. McDonald, "Perth-Bermuda Sound Propagation (1960): Adiabatic mode interpretation," J. Acoust. Soc. Am. **90**, 2586–2594 (1991).
- ¹²D. Lee and G. Botseas, "An implicit finite-difference (IFD) computer model for solving the parabolic equation," NUSC TR-6659, Naval Underwater Systems Center, New London, CT (1982).
- ¹³M. Porter, "The KRAKEN normal mode program," SACLANT Undersea Research Center (1988).
- ¹⁴S. T. McDaniel, "Parabolic approximation for underwater sound propagation," J. Acoust. Soc. Am. **58**, 1178–1185 (1975).
- ¹⁵H. Y. Chen and E. C. Shang, "The applications of PE method in shallow water sound field," Master's thesis, Institute of Acoustics, Academia Sinica, Beijing, China (1986).
- ¹⁶L. Brekhovskikh, *Waves in Layered Media* (Academic, New York, 1980), 2nd ed.
- ¹⁷R. Koch, C. Penland, P. Vidmar, and K. Hawker, "On the calculation of normal mode group velocity and attenuation," J. Acoust. Soc. Am. **73**, 820–825 (1983).
- ¹⁸D. Chapman and D. Ellis, "The group velocity of normal modes," J. Acoust. Soc. Am. **74**, 973–979 (1983).

A ray variability analysis of sound transmission from Heard Island to California

Ching-Sang Chiu, Albert J. Semtner, Coenraad M. Ort, James H. Miller,
and Laura L. Ehret

Naval Postgraduate School, Monterey, California 93943

(Received 26 July 1992; accepted for publication 7 June 1994)

The influence of mesoscale and seasonal ocean variability on three-dimensional acoustic ray paths from Heard Island through the Southern and Pacific Oceans to the California coast is investigated. For the simulation of these global acoustic ray paths, a three-dimensional Hamiltonian ray-tracing code was used. The input sound-speed fields to the acoustic ray model were interpolated from gridded temperature and salinity output data from the Semtner–Chervin eddy-resolving, global, general circulation model. The ray-tracing results have provided input to experimental planners for receiver placement off the California coast in the Heard Island Feasibility Test and shed light on the variability of the acoustic paths, insonified locations, arrival azimuthal angles, and travel times.

PACS numbers: 43.30.Qd, 43.30.Cq

INTRODUCTION

In 1989, Munk and Forbes¹ presented a new idea of early detection of global warming. The proposed technique uses sound waves generated by a “permanent” projector in the ocean. Cross-basin acoustic signal travel time variability over an estimated period on the order of ten years will be measured by hydrophones distributed worldwide.

In addition to the possibility of detecting global warming at an early stage, a permanent cross-basin acoustic transmission system could enhance ocean prediction capability. Travel time fluctuations along paths going through different basins would contain information on the gyre scale and mesoscale processes in those basins. Although the corresponding acoustic fluctuations are considered “noise” in the greenhouse detection problem, they are useful “signals” for the calibration of eddy-resolving global ocean circulation models. The statistics of the measured travel time variability can be used to check the statistics of the ocean circulation model output for consistency.

Uncertainties, however, exist regarding the variability of the cross-basin acoustic paths in the presence of the inherent ocean variability. Three fundamental acoustic issues must be carefully addressed prior to installation of permanent sound sources and receivers. The first issue is acoustic reliability. Locations of insonified and shadowed zones are determined by the location of the sound source. The zones are a function of time due to ocean variability. We must know which sites can be insonified on a year-round basis. The issue of acoustic stability comes second. At those reliable sites, we must know whether the acoustic arrival patterns, or at least parts of them, do not change significantly over a long period of time. Useful travel-time time series can only be estimated from stable arrivals. Geophysical noise is the third issue. The size of travel time change caused by frontal oscillations, mesoscale eddies, and seasonal cycles affect how long we need to observe before a statistically significant trend can be discerned. Acoustic paths through different regions experience ocean fluctuations of different strengths. The size of arrival

time fluctuations therefore varies from site to site. Given selected source locations, optimal receiving sites are those which are reliable, where stable arrivals can be obtained, and where geophysical noise integrated along stable paths are minimal.

The issue of acoustic reliability was assessed in the Heard Island Feasibility Test (HIFT) in January 1991.² The HIFT has proven that low-frequency sound can be transmitted halfway around the world using electronically controlled sources. Because of the short duration of the experiment, the effects of the background ocean variability on the variability of acoustic paths, travel times, sound intensities, and insonified or shadowed areas over geophysical time scales were not studied.

Geophysical time-scale acoustic variability can be investigated using global ocean circulation models. A demonstration of this is the thrust of this paper. Specifically, we present the results of a ray variability simulation of sound transmission from Heard Island to the west coast of the United States. This simulation of acoustic variability was accomplished by interfacing the Hamiltonian Acoustic Raytracing Program for the Ocean (HARPO)³ with the gridded temperature and salinity fields simulated by the Semtner–Chervin Global Ocean Circulation Model (SCGCM).⁵ HARPO is a fully three-dimensional (3-D) raytracing computer program originated from National Oceanic and Atmospheric Administration (NOAA). The basic formulation and capabilities of HARPO are summarized in Sec. I. SCGCM is an eddy-resolving ocean circulation model that has a global domain. The output of this ocean model constitutes the only global data set available today, that has mesoscale resolution, both spatially and temporally. SCGCM and its output are briefly described in Sec. II. Since HARPO requires a continuous sound-speed field as input, the interface to this enormous set of gridded global data requires an interpolation procedure. A rather efficient one developed for this simulation work is presented in Sec. III.

Most of the simulation work presented here was completed prior to the 1991 HIFT with a primary objective to

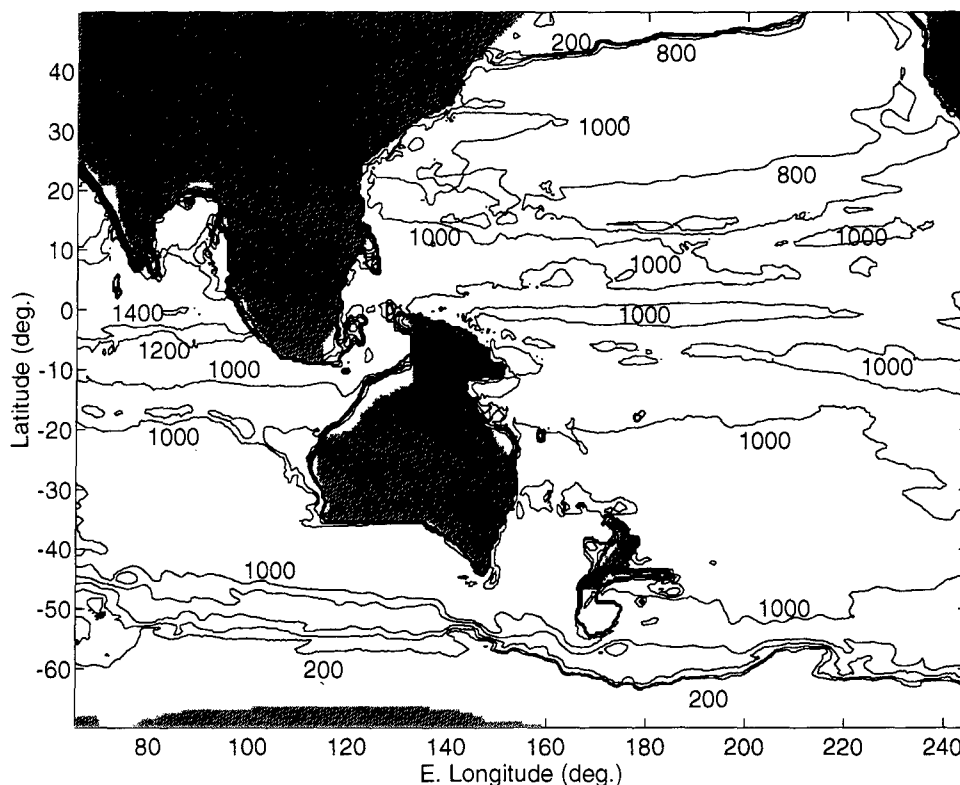


FIG. 1. Contour map of sound channel depth in the Southern and Pacific Oceans. The values were extracted from an annual mean ocean field simulated by SCGCM. Contour interval is 200 m.

provide immediate acoustic modeling support for the field test. With respect to the acoustic issues mentioned above, another objective was to assess the viability of using Heard Island as a permanent source site for the anticipated 10-yr experiment. Thus our foci were

(1) to estimate the locations along the west coast of the United States, which are insonified by the Heard Island sound source (Are Monterey and Coos Bay good listening sites?), and

(2) to estimate the variations in arrival position, azimuthal arrival angle, path trajectory and travel time along the 3-D paths, caused by ocean meso- and gyre-scale variability.

Our simulation results provided useful information to the planners of the HIFT on the placements of both the vertical and towed horizontal receiver arrays off the coast of California. Additionally, they suggest that Heard Island may not be an optimal permanent source site. The simulation results are presented in Sec. IV with conclusions given in Sec. V. In particular, the shortfalls of this initial 3-D, global ray acoustic simulation are discussed and future work is proposed.

I. HARPO

The acoustic model that we use is the Hamiltonian Acoustic Raytracing Program for the Ocean (HARPO). Jones *et al.*³ created HARPO in 1986. The original code, which required sound-speed and current-field representations with smooth first derivatives, and bottom topography with smooth first and second derivatives, could only handle canonical, analytic ocean and bathymetry variations. Since

then, HARPO has gone through various upgrades and modifications including a significant one by researchers at the Woods Hole Oceanographic Institution (WHOI) and Naval Postgraduate School (NPS).⁴ Specifically, they have generated a modified version together with supplementary, peripheral routines for efficient eigenray finding and interpolation of gridded sound-speed, current, and bathymetry input data. Modifications of the WHOI-NPS version have allowed us to perform all our global raytracing on a workstation.

HARPO traces 3-D rays by numerically integrating Hamilton's equations of motion in spherical polar coordinates using an Adams-Moulton predictor-corrector method with a Runge-Kutta starter. Initial conditions for the integration are specified in terms of ray launch angles (wave numbers). Since HARPO works in polar spherical coordinates, Earth curvature effects are automatically accounted for (although geodesic veering as influenced by Earth's ellipticity is not). For a detailed discussion on the formulation of HARPO, the reader is referred to Jones *et al.*³

II. THE GLOBAL OCEAN DATA SET

Semtner and Chervin^{5,6} have developed an eddy-resolving model for the global ocean circulation (SCGCM). The model has smooth but realistic bottom topography, a domain extending from 75°S to 65°N, and a horizontal spatial resolution of 1/2°. Vertically, the model contains 20 levels, with a resolution of approximately 25 m in the first 100 m, and then resolution gradually decreases with increasing depth.

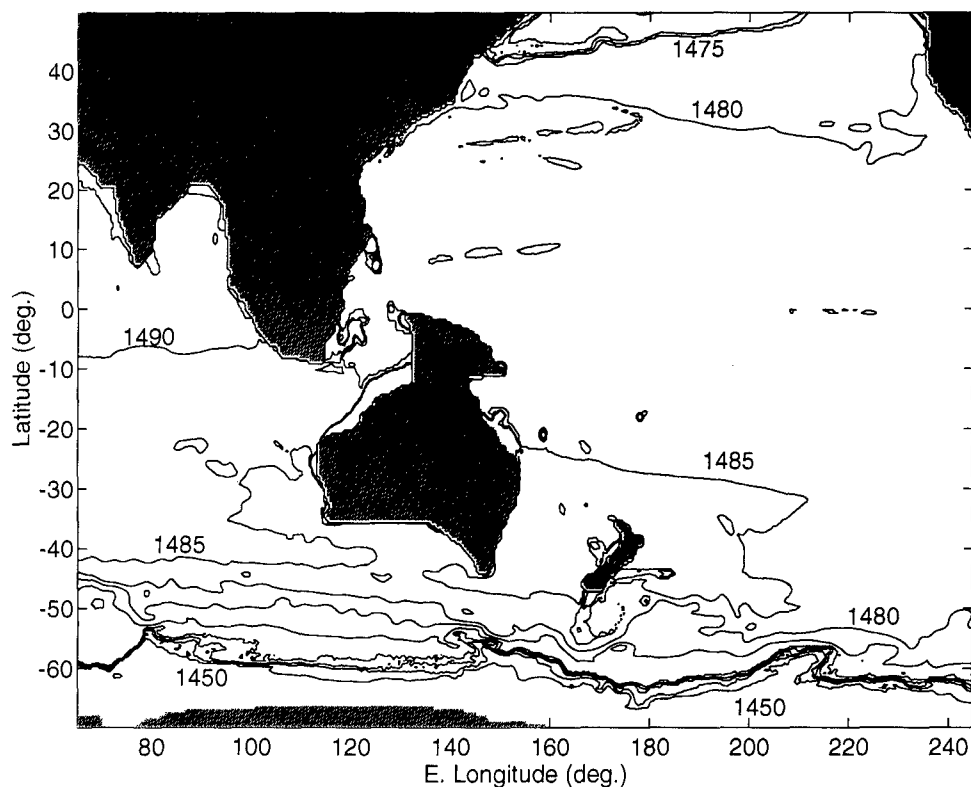


FIG. 2. Contour map of speed of sound at the channel axis in the Southern and Pacific Oceans. The values were extracted from an annual mean ocean field simulated by SCGCM. Contour interval is 5 m/s.

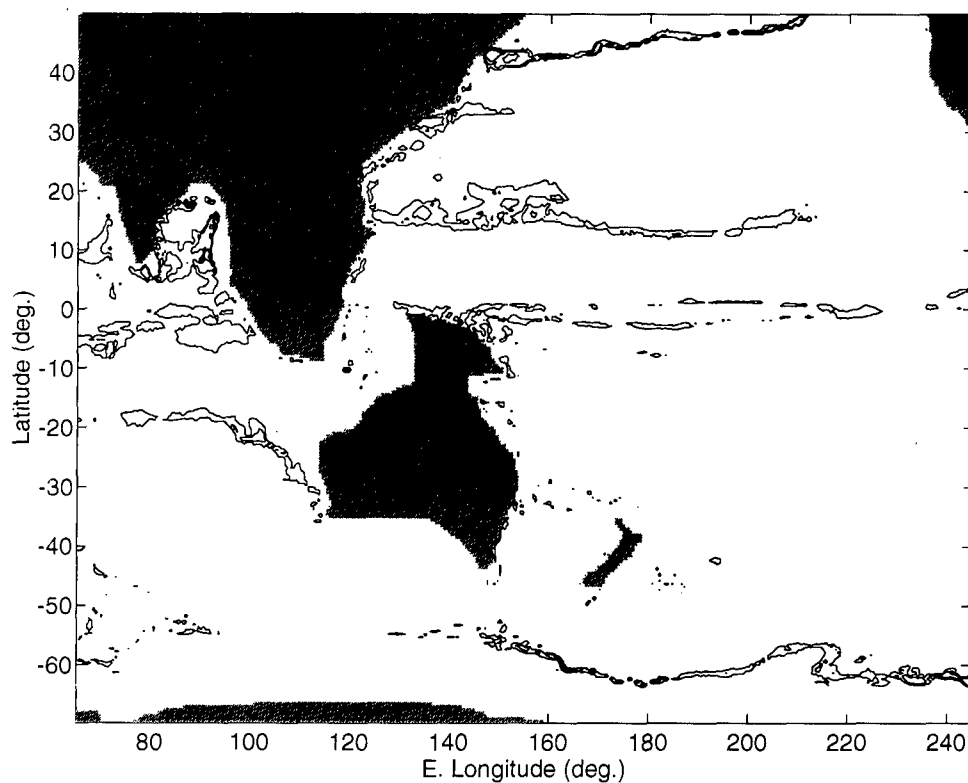


FIG. 3. Contour map of the standard deviations of sound channel depth in the Southern and Pacific Oceans. The deviations were derived from the ocean fields simulated by SCGCM over an annual cycle. Contour interval is 100 m.

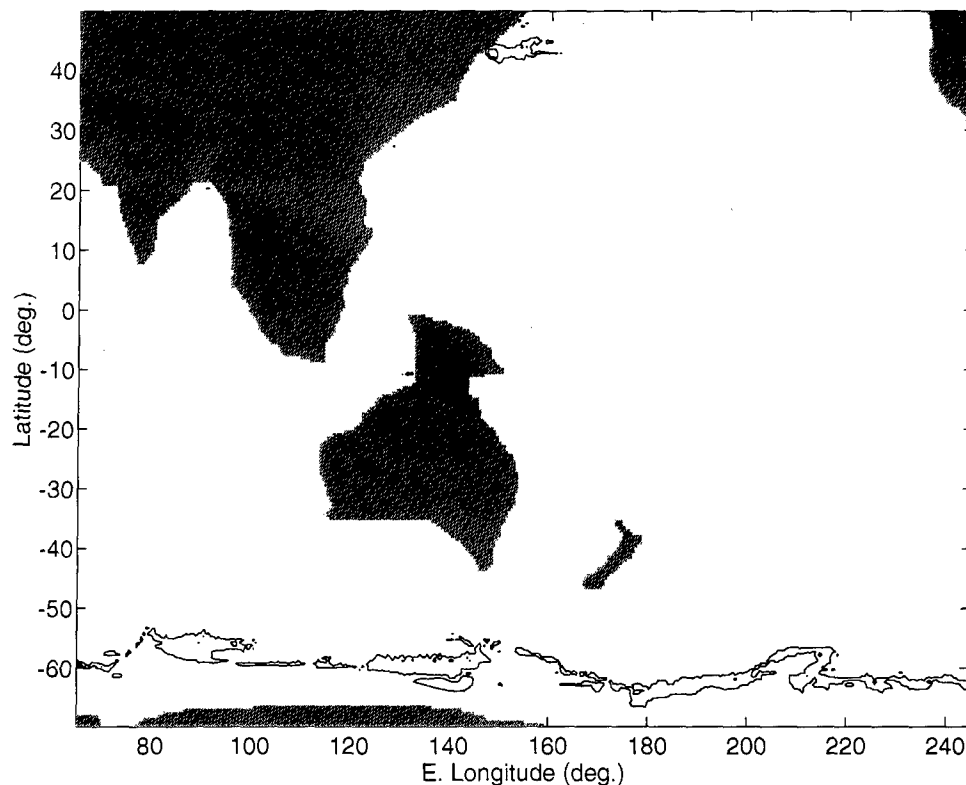


FIG. 4. Contour map of the standard deviations of sound speed at the channel axis in the Southern and Pacific Oceans. The deviations were derived from the ocean fields simulated by SCGCM over an annual cycle. Contour interval is 5 m/s.

SCGCM was integrated for a simulated time of 32.5 yr. Following an 18-yr spin-up, annual mean wind stress and then monthly forcing from Hellerman and Rosenstein⁷ were applied. Realistic mesoscale variability resembling many of the observed features in the global ocean were simulated in the last 12.5 model years. Realistic seasonal variability was also simulated in the last 10.5 yr. The output data were archived at a simulation time interval of 3 days at the National Center for Atmospheric Research (NCAR). Approximately 200 Mbytes of data were generated per simulation day.

In Figs. 1–4, we display some of the ocean variability simulated by SCGCM. Figures 1 and 2 show the geographical variations of sound channel depth and sound speed at that depth extracted from the mean sound-speed field of model year 25. Rapid changes of the sound channel depth as well as sound speed are observed between latitudes 60°S and 40°S where the Antarctic circumpolar current is located. In this zone, the sound channel deepens 800 m in less than 10° equatorward while the axial sound speed increases by more than 30 m/s over the same distance. These strong gradients are expected to have significant environmental effects on the acoustic paths. Away from the transition zone, the spatial variations are more gradual. On the other hand, Figs. 3 and 4 show the temporal variability of the sound channel axis and axial sound speed over an annual cycle, respectively. The standard deviation values contoured in the two figures were derived from the ocean fields simulated in model year 25. Significant temporal variability is found in the Kuroshio, Subarctic and Subtropical gyres, and again in the Antarctic circumpolar current.

III. OCEAN-ACOUSTICS INTERFACE

A procedure to interface HARPO to gridded data generated by the regional-domain Harvard Open Ocean Model⁸ was developed earlier by Newhall *et al.*⁴ This interface procedure has been successfully adopted with modifications for use with the global data set in our cross-basin ray variability study. The global data set generated by SCGCM is enormous and was archived at NCAR. Since we were restricted by our computational resources to perform the acoustic calculations locally on a workstation that has limited memory and hard disk space, the task to interface HARPO to the global data set was not trivial.

We first subsampled the temperature, salinity, and bathymetry data in the domain of our interest from the global data set. This domain only includes the Pacific and part of the Southern Ocean. The subsampled temperature and salinity data were then converted to sound speed using the Mackenzie empirical formula⁹ which has a standard error of 0.070 m/s. Only the subsampled sound-speed and bathymetry data were ported to the local workstation. The subsampled sound-speed data set was still huge for a workstation environment. The acoustic computation would come to a halt if we tried to process all the data at the same time. To make the computation tractable, we took the following approach:

- (1) A rectangular window of 5°×5° (lat.–lon.) was used to move in a discrete fashion with the ray being traced.

- (2) Data inside a sub-region with boundaries defined by the window were extracted. Inside this sub-region, sound speed was expressed as a sum of the mean speed $\bar{c}(z)$, a

function of depth only, and the perturbed speed δc , i.e.,

$$c(\theta, \phi, z) = \bar{c}(z) + \delta c(\theta, \phi, z). \quad (1)$$

The perturbation was further expressed as a linear combination of empirical orthogonal functions (EOFs), i.e.,

$$\delta c(\theta, \phi, z) = \sum_{i=1}^N a_i(\theta, \phi) f_i(z), \quad (2)$$

where N is the number of vertical levels in the ocean model, and a_i are the (horizontal) coefficients.

(3) A layered mean sound-speed profile $\bar{c}(z_k)$ and layered perturbation profiles $\delta c(\theta_j, \phi_j, z_k)$ at each horizontal grid point within the window were computed. The mean at the k th vertical layer is simply

$$\bar{c}(z_k) = \frac{1}{M} \sum_{j=1}^M c_j(\theta_j, \phi_j, z_k), \quad (3)$$

where M is the number of horizontal grid points.

(4) Empirical orthogonal functions (EOFs) of the perturbation profiles were constructed by solving the eigenvalue/eigenvector problem

$$\mathbf{A}^T \mathbf{A} \mathbf{f}_i = \lambda_i \mathbf{f}_i \quad (4)$$

where the matrix \mathbf{A} contains all the layered perturbation profiles, and \mathbf{f}_i is the vector (or layered) representation of the EOFs f_i .

(5) Horizontal coefficients of the EOFs were computed by projecting the layered perturbation profiles on the layered EOFs.

(6) Cubic splines were fitted to the mean profile as well as to the EOFs, and bi-cubic splines were fitted to the EOF coefficients, to produce a smooth and continuous sound speed field for HARPO.

(7) Bi-cubic splines were also fitted to the bathymetry data to produce a smooth and continuous ocean bottom depth for HARPO.

(8) After the ray was traced to a point near the edge of the window, the window was moved to center at that point. New sub-region data were then extracted and processed with the same procedure.

IV. CROSS-BASIN RAYTRACING RESULTS

This acoustic ray variability study was based on the ocean data simulated by SCGCM in model years 21 and 25, respectively. The former subset of data contains mesoscale ocean variability only whereas the latter contains both mesoscale and seasonal variability. Raytracing through consecutive instantaneous fields separated at 30-day simulation time intervals in model year 21 was performed prior to the Heard Island Experiment in an effort to determine the insonified regions and their variability along the west coast of the United States.¹⁰ It should be pointed out that we did not use the ocean data that contain seasonal cycles in the pre-experimental acoustic modeling work simply because these data were not archived then. However, the monthly mean fields in model year 25 were used in a post-experimental

effort to estimate the travel time variability along a Heard Island-to-California eigenpath as well as to check the pre-experimental simulation results.

Prior to the experiment, we did not know the actual source location. Thus, an arbitrary position at a depth of 110 m and in 300 m of water near Heard Island was picked as the source point in the raytracing. To determine whether there are reliable rays to the west coast of the United States, we used a straightforward procedure. Using each of the instantaneous fields of model year 21, large fans of rays were traced with varying azimuthal and elevation angles. The angular increments were 0.5° in both directions. We define reliable rays as those that are not impeded by land masses and have no bottom interaction away from Heard Island. Bottom bounces of less than five in number close to the source were allowed because of the uncertainty of the actual source location.

Reliable rays insonifying the California coast were found. However, they are all confined within a rather thin envelope bounded by initial azimuthal angles of 133° and 136° (measured clockwise from the north) and elevation angles of $\pm 2^\circ$. The horizontal trajectory of this ray envelope is shown in Fig. 5 along with the bottom topography. One can easily see that there are two factors limiting the width of the beam, namely, the rather shallow Campbell Plateau to the south of New Zealand and Antarctica. Rays with initial azimuthal angles smaller than 133° run into Campbell Plateau while rays with initial azimuthal angles larger than 136° run into Antarctica. A positive result is that this envelope escapes blockage by the Polynesian Islands to the south of the Equator and reaches the California coast.

Based on 12 independent reliable ray envelope calculations using different instantaneous ocean fields, the dimensions of the envelope were found to be basically invariant in time near the source, but can be quite variable at the California coastline due mainly to the large variability of the Antarctic circumpolar current in the Southern Ocean. It is rather obvious that a slight change of the envelope dimensions in the Southern Ocean can be translated into a larger change along the coastline. The envelope, generally confined between San Francisco Bay and Point Arguello on the west coast, has a mean width of 150 km. This width, however, is quite variable and can deviate by as much as a half of the mean width. The maximum and minimum widths were found to be 287 and 73 km, respectively. The center of the envelope was also found to fluctuate quite a bit. The center position varied around a mean latitude of 36°N on the California coastline. A latitudinal standard deviation of 0.24° along the coastline was obtained. In Fig. 6, we display the maximum width of this predicted envelope in a close-up look near California. In addition, we show in this figure the locations at which the California vertical array was deployed during the Heard Island Experiment.¹¹ Estimated arrival azimuthal angles of the rays in the envelope are between 34° and 45° . The Canadian group led by Heard and Chapman¹² used this information of arrival angle and towed their horizontal array inside the predicted envelope during the experiment. Our postexperimental raytracing using the monthly mean fields have produced consistent results, with all the computed reli-

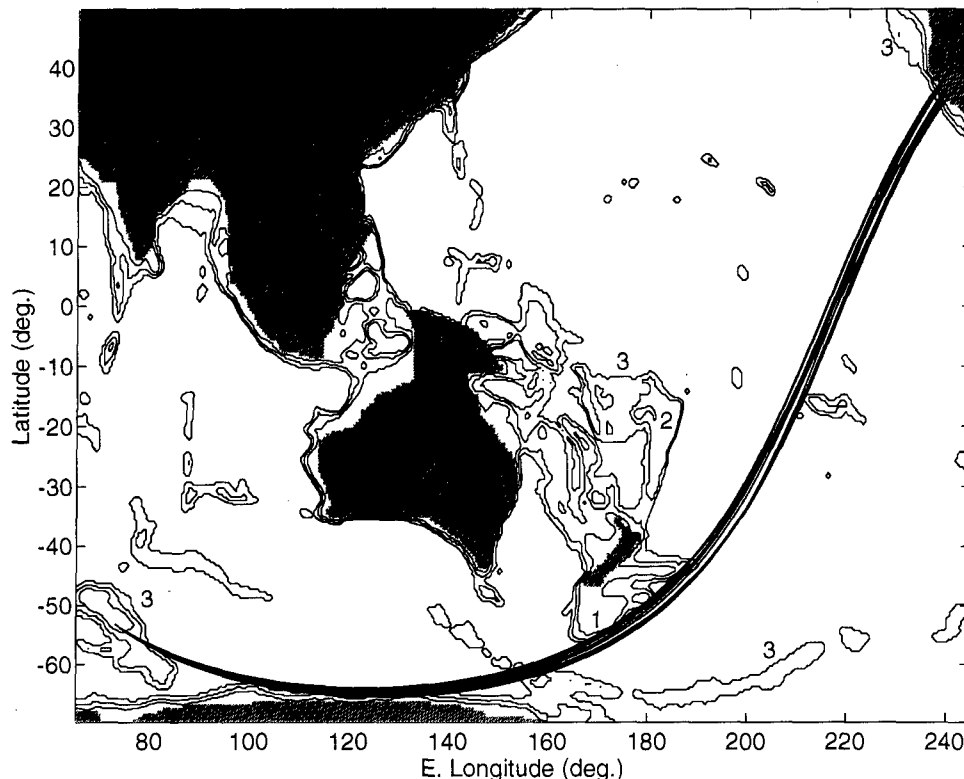


FIG. 5. Horizontal trajectory of the reliable ray envelope from Heard Island to California along with the modeled bottom bathymetry. Contour interval for bottom bathymetry is 1 km and depths greater than 3 km are not contoured.

able rays lying well within the envelope shown in Fig. 6.

A plausible acoustic path from Heard Island to Oregon was also suggested by Munk and Forbes.¹ A disappointing result is that no other reliable ray envelope to the west coast from Heard Island was found in our calculation other than the one to Monterey. Frequent bottom interaction resulting from the bottom-limited downward refracting profiles in the

shallow Tasman Sea renders those paths unreliable.

The computed reliable rays go through three very distinct types of acoustic environments: (1) a half-channel regime in the Southern Ocean; (2) a transition regime beginning at the Antarctic polar front, where the sound channel axis deepens equatorward; and (3) a deep channel regime where the axis remains at mid depth.

These three regimes are shown in Fig. 7 where the sound-speed profiles in the first 9000 km along a reliable acoustic path are displayed. Among all the reliable rays traced, a general distinction between two types of rays, type I and II, was found. In Figs. 8 and 9, the vertical trajectories of a type I and a type II ray are displayed, respectively. Both types are trapped very close to the surface in the first regime. In the transition regime, while type II rays start cycling into the deep channel, type I rays remain trapped close to the surface in the surface duct. Type II rays experience stronger along-the-path sound-speed gradients and therefore enter the deep channel sooner. Type I rays only make their way to the deep channel at a much greater distance where the surface duct is eroded. Because of the large separation between the entrance to the deep channel and the deep channel axis at this greater distance, type I rays cycle with a much larger cycling amplitude than those of the type II rays in the last regime. From the raytraces, it was also found that wavefronts propagating along type I rays arrive sooner, have more variable travel times, and are refracted more to the south. These phenomena can be displayed using an acoustic arrival scatterplot (Fig. 10). By terminating all the Heard Island-to-California rays, traced with the same initial elevation angle of -1° , on

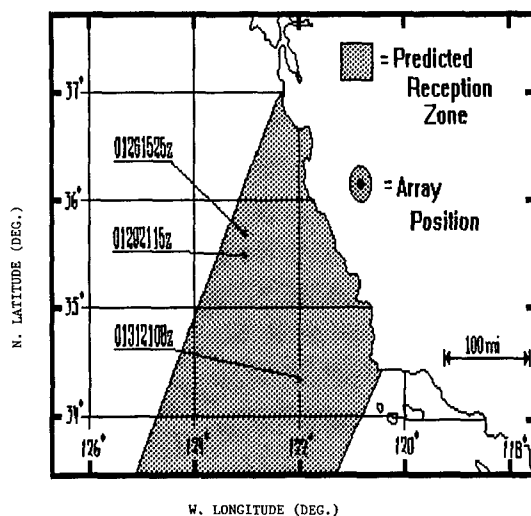


FIG. 6. A close-up look of the horizontal geometry of the reliable ray envelope near California. Envelope shown is the one with the maximum width. Locations where the California vertical array were deployed during the Heard Island Experiment are marked. (Note that the latitude axis and longitude axis plotted have different scales.)

SOUND SPEED PROFILES ALONG INTEGRATION PATH R = 1.9 - 9001.9 km

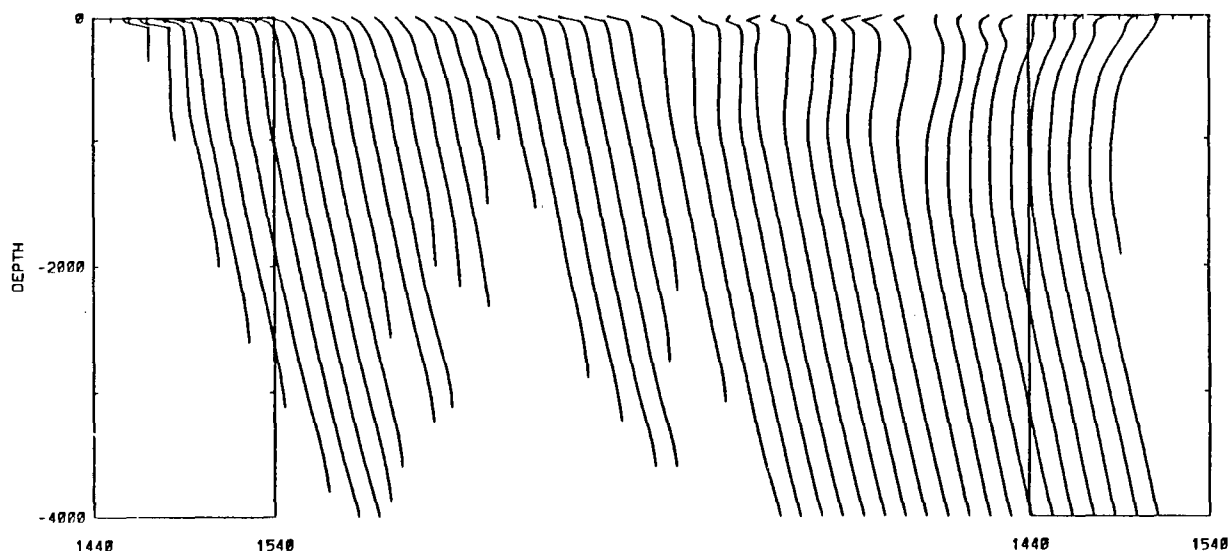


FIG. 7. Evenly spaced sound-speed profiles sampled along the first 9,000 km of a Heard Island-to-California acoustic path. Sound speed shown is in m/s and depth in m.

a straight line approximately normal to the incoming rays and parallel to the California coastline, we computed the corresponding travel times along both types of rays. The travel times are plotted against the arrival positions (in latitude) in Fig. 10. These all make sense because type I rays cycle through higher speed layers, spend more time in the main thermocline where most mesoscale ocean variability is confined, and have longer path lengths. The longer path lengths make them accumulate more horizontal refraction to the south while propagating equatorward.

These ray results also have implications on the acoustic normal modes. In the Pacific Ocean, type II rays are associated with low modes whereas type I rays are associated with

higher modes. Thus, it is implied that there is a modal spatial dispersion in the global transmission. Different modes arrive at different positions, and higher modes more to the south. Furthermore, the general geometry of the type I rays suggests that the low modes in the half-channel Southern Ocean are strongly coupled to the high modes in the Pacific Ocean. The propagation is thus highly nonadiabatic.

In addition to checking the pre-experimental calculations, we used the monthly mean ocean fields to provide an estimate of the travel time variations along a Heard Island-to-California eigenray over an annual cycle. For each of the 12 monthly fields, a type-II eigenray connecting the source and an arbitrary point off California was traced. This eigen-

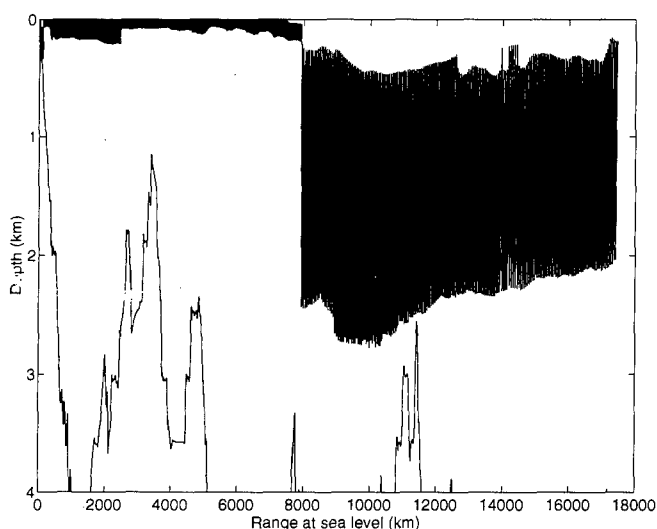


FIG. 8. Typical vertical trajectory of one type of cross-basin rays (type I) connecting Heard Island and California. Bottom bathymetry is also displayed.

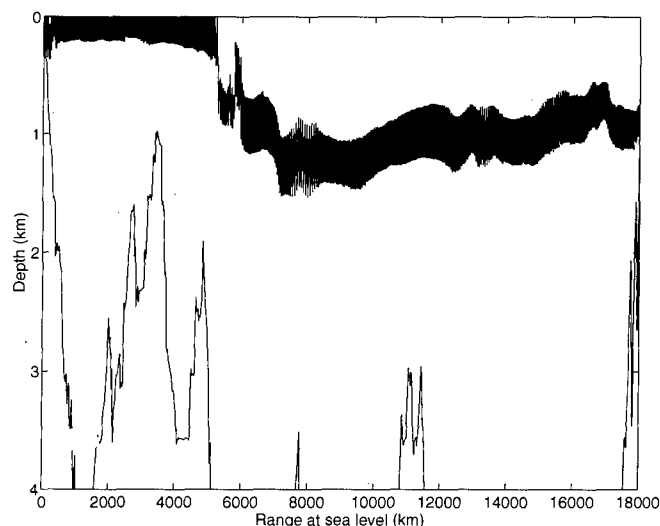


FIG. 9. Typical vertical trajectory of another type of cross-basin rays (type II) connecting Heard Island and California. Bottom bathymetry is also displayed.

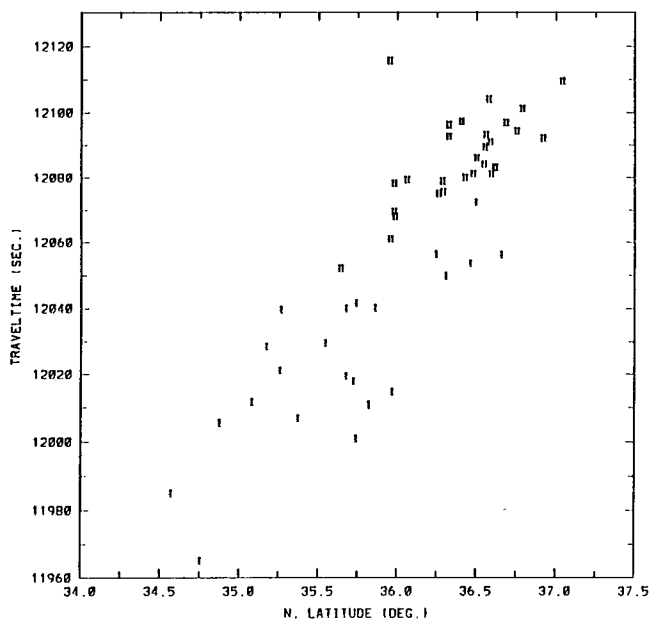


FIG. 10. Acoustic arrival scatterplot showing the general differences in arrival position and time between two different types of rays, I and II, from Heard Island to the coast of California.

ray has initial azimuthal and elevation angles of approximately 134° and -1° , respectively, and was computed by varying the two initial angles at very fine increments. A tolerance of one acoustic wavelength (i.e., 26 m) was used as the acceptance criterion. Figure 11 shows the corresponding travel time variations which have an rms value of 2.5 s. Figure 11 also shows the existence of a travel time trend. According to Semtner and Chervin,¹³ a probable cause of this trend is the continuing adjustment of the deep thermocline in the Pacific to imposed surface heat and moisture fluxes in the ocean simulation. The numerical ocean model has not reached final equilibrium in model year 25. Neglecting path changes and the cycling nature of the rays, Semtner

Travel Time over an Annual Cycle

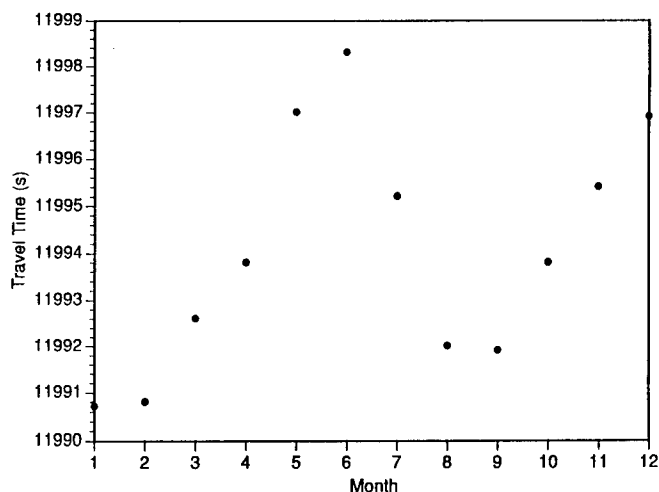


FIG. 11. Simulated eigenray travel-time variations over an annual cycle.

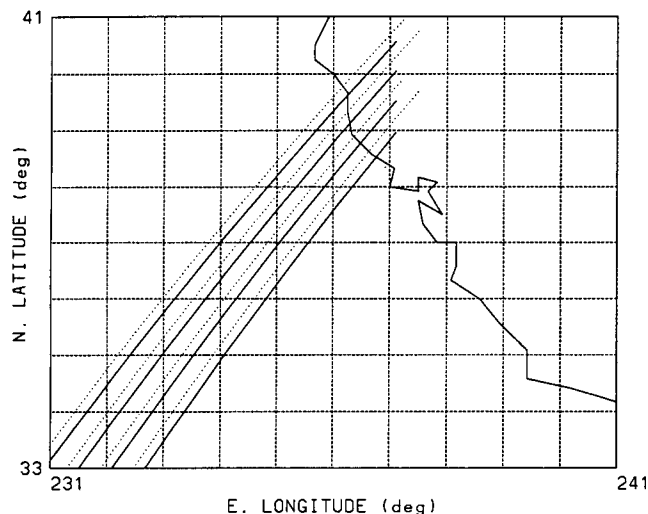


FIG. 12. "Nonacoustic," geodesic (dotted lines) and great circle (solid lines) paths originated from Heard Island with initial azimuthal angles between 133° (upper) and 136° (lower), respectively.

and Chervin¹³ have estimated the travel time variability to be 1.2 s for a Heard Island-to-California axial path in an earlier study. Here, we give an improved estimate by incorporating the physics of 3-D sound propagation. Our estimate is twice as large and thus has implications on the effectiveness of using the Heard Island-to-California path for the detection of the greenhouse signal. *The main implication is that the greenhouse signal along this path could not be reliably detected in 10 years.*

V. CONCLUSIONS

In this paper, we have shown that global acoustic simulations using global ocean circulation models are tractable and can produce realistic results that are very useful to the in-planning "Acoustic Thermometry of Ocean Climate Project" (ATOC). Although there are weaknesses associated with this initial 3-D simulation of global acoustic transmission variability, it has provided vital information for the placement of a vertical and a horizontal hydrophone array off California in the HIFT. An interesting result is the finding of only a single, reliable but variable, thin ray beam insonifying the west coast of the United States. Both the horizontal and vertical receiving arrays deployed inside the predicted envelope have successfully detected the 57-Hz sound signal transmitted from Heard Island.^{11,12} The unreliability of the Heard Island-to-Oregon path was also validated by the experimental data.¹⁴

The shortfalls of this simulation study include the use of an overly smoothed bottom, the neglect of ocean current effects, and the neglect of geodesic veering of the rays under the influence of Earth's ellipticity. However, the correction of these weaknesses is straightforward and should be included in future investigations. In particular, the geodesic-veering correction algorithm developed recently by Dworski and Mercer¹⁵ for HARPO should be incorporated. Since the Earth's ellipticity was not included in this initial global acoustic modeling, it is important for us to comment on the error that might have resulted. Figure 12 shows the "nona-

coustic," geodesic, and great circle paths with initial azimuthal angles of 133°, 134°, 135°, and 136°, respectively. These initial angles are the same as those of the reliable acoustic paths. It is seen from Fig. 12 that the differences between the geodesic and great circle paths are small: about 2/10 of a degree or approximately 20 km. This 20 km is expected to be the error associated with the horizontal ray-path trajectories calculated in this study. A comparison of the nonacoustic and acoustic paths (i.e., Figs. 12 and 6) reveals that the generally poleward decreasing sound-speed structure causes a horizontal refraction to the south by about 2° to 3°.

Ray theory is a high-frequency approximation. Therefore, the use of complementary full-wave models accounting for finite frequency dispersion effects is highly desirable, and should aid in the interpretation of the ray results and *vice versa*. McDonald *et al.*¹⁶ have initiated full-wave modeling for ATOC using adiabatic mode theory. Several fully 3-D acoustic wave models are available at present, including the parabolic equation model of Lee and Siegmund¹⁷ and the coupled normal-mode model of Chiu and Ehret.¹⁸ The latter is particularly suitable for very long-range transmission simulations.

Here, we have demonstrated that, the combined use of a global ocean circulation model and a global 3-D acoustic model can provide for a powerful means to effectively assess the fundamental acoustic issues that are of concern to ATOC. The availability of only a single reliable ray envelope through the Pacific Ocean, the complexity of the acoustic propagation and the added travel time variability due to appreciable path changes introduced by the highly energetic Antarctic circumpolar current have raised a serious concern on the utility of Heard Island as a permanent source site for the upcoming ten year experiment. Other more optimal source locations are being sought at this time for ATOC, with simplicity in logistics, maximal reliability and stability, and minimal geophysical noise in mind. The use of SCGCM and HARPO can assist in the search for optimal source and receiver sites by simulating acoustic variability as a function of geophysical time.

ACKNOWLEDGMENTS

The authors wish to thank the Naval Postgraduate School for sponsoring the research reported here. We are also grateful to Don Altman for supplying a code for the extraction of the Semtner–Chervin data.

- ¹W. H. Munk and A. M. G. Forbes, "Global Ocean Warming: An Acoustic Measure?," *J. Phys. Oceanogr.* **19**, 1765–1778 (1989).
- ²W. H. Munk, R. C. Spindel, A. Baggeroer, and T. G. Birdsall "The Heard Island Feasibility Test," *J. Acoust. Soc. Am.* **96**, 2330–2342 (1994).
- ³R. M. Jones, J. P. Riley, and T. M. Georges, "HARPO—a versatile three-dimensional Hamiltonian ray tracing program for acoustic waves in an ocean with irregular bottom," NOAA Wave Propagation Laboratory Report (October 1986).
- ⁴A. E. Newhall, J. F. Lynch, C.-S. Chiu, and J. R. Daugherty, "Improvements in three dimensional ray tracing codes for underwater acoustics," in *Computational Acoustics: Ocean Acoustic Models and Supercomputing*, edited by D. Lee, A. Cakmak, and R. Vichnevetsky (North-Holland, Amsterdam, 1990).
- ⁵A. J. Semtner and R. M. Chervin, "A simulation of the global ocean circulation with resolved eddies," *J. Geophys. Res.* **93** (C12), 15,502–15,522 and 15,767–15,775 (1988).
- ⁶A. J. Semtner and R. M. Chervin, "Ocean General Circulation From a Global Eddy-Resolving Model," *J. Geophys. Res.* **97** (C4), 5493–5550 (1992).
- ⁷S. Hellerman and M. Rosenstein, "Normal monthly wind stress over the world ocean with error estimates," *J. Phys. Oceanogr.* **13**, 1093–1104 (1983).
- ⁸A. R. Robinson, M. A. Spall, and N. Pinardi, "Gulf Stream Simulations and Dynamics of Rings and Meander Processes," *J. Phys. Oceanogr.* **18**, 1811–1853 (1988).
- ⁹K. V. Mackenzie, "Nine-term Equation for Sound Speed in the Ocean," *J. Acoust. Soc. Am.* **70**(3), 807–812 (1981).
- ¹⁰C. M. Ort, "Spatial and temporal variability of cross-basin acoustic ray paths," Naval Postgraduate School, Master thesis (December 1990).
- ¹¹A. B. Baggeroer, K. Lashkari, J. Miller, C.-S. Chiu, G. Frogner, P. N. Mikhalevsky, and K. von der Heydt, "Vertical array resolution of the normal modes from the Heard Island signals," *J. Acoust. Soc. Am.* **90**(4.2), 2330 (1991).
- ¹²G. J. Heard and N. R. Chapman, "Heard Island feasibility experiment: Analysis of the Pacific path data obtained with a horizontal line array," *J. Acoust. Soc. Am.* **90**, 2347(A) (1991).
- ¹³A. J. Semtner and R. M. Chervin, "Environmental Effects on Acoustic Measures of Global Ocean Warming," *J. Geophys. Res.* **95**(C8), 12,973–12,982 (1990).
- ¹⁴A. M. G. Forbes, "The Tasman blockage: An acoustic sink for the Heard Island feasibility test," *J. Acoust. Soc. Am.* **90**, 2346 (A) (1991).
- ¹⁵J. G. Dworski and J. A. Mercer, "Hamiltonian 3-D Ray Tracing in the Oceanic Waveguide on the Ellipsoidal Earth," Applied Physics Laboratory-University of Washington Technical Report 8929 (December 1990).
- ¹⁶B. E. McDonald, W. A. Kuperman, and K. Heaney, "Horizontal multipaths in transoceanic acoustic propagation: Model results and data," *J. Acoust. Soc. Am.* **90**, 2347(A) (1991).
- ¹⁷D. Lee and W. L. Siegmund, "A mathematical model for the 3-dimensional ocean sound propagation," *J. Math. Model* **7**, 143–162 (1986).
- ¹⁸C.-S. Chiu and L. L. Ehret, "Computation of Sound Propagation in a Three-Dimensionally Varying Ocean: A Coupled Normal Mode Approach," in *Computational Acoustics: Ocean Acoustic Models and Supercomputing*, edited by D. Lee, A. Cakmak, and R. Vichnevetsky (North-Holland, Amsterdam, 1990).

Heard Island Feasibility Test: Analysis of Pacific path data obtained with a horizontal line array

Garry J. Heard and N. R. Chapman

Defence Research Establishment Pacific, FMO Esquimalt, British Columbia V0S 1B0, Canada

(Received 23 August 1992; accepted for publication 7 June 1994)

Preliminary results from the Heard Island Feasibility Test are presented for data obtained with a towed horizontal line array off the coast of southern California. Signal characteristics examined include signal-to-noise ratios, sound-pressure levels, transmission loss, and arrival bearing angles. For the transmissions analyzed to date the mean sound-pressure level was found to be (63.8 ± 2) dB/1 μ Pa. The mean transmission loss was found to be (150 ± 3) dB which is significantly greater than that found for receivers in the Atlantic at similar ranges. The mean arrival angle was found to be $(214 \pm 3)^\circ$ T and a travel time of approximately 3 h 17 m was measured. Measurements compare favorably with model predictions which indicate that the relatively large transmission loss is due to bottom interactions in the south western Pacific.

PACS numbers: 43.30.Qd, 43.30.Pc, 43.60.Rw

INTRODUCTION

In this paper we report on the preliminary analysis of data collected in the Heard Island Feasibility Test (HIFT). This test was an international experiment to examine the use of ocean acoustic tomography to measure the possible warming rates of the world's deep oceans. The basic idea was that the ocean sound speed depends on the temperature of the water; therefore, changes in the ocean temperature will be observable in the acoustic travel times between widely separated source-receiver pairs. Munk and Forbes¹ and Mikolajewicz *et al.*² have elaborated on the motivation for using acoustics to measure the global warming (or cooling) rate.

Aside from providing an additional listening post for the main experiment, we were particularly interested in determining the arrival bearing angle and the transmission loss along the path from Heard Island to the west coast of North America near Los Angeles.

It should be emphasized that the HIFT was intended to test the practicality of measuring global temperature changes using acoustics. The analysis of this test does not, and was not intended to, answer the question of what the climatic trend is currently. The answer to that question will require an on-going program of acoustic measurements spanning at least a decade.³ The current effort provides answers to some unknowns related to the acoustics, in particular, to the question of propagation through the rough terrain of the Tasman Sea and the western Pacific. The information obtained from the HIFT will allow the refinement of equipment, techniques, and planning for future global acoustic temperature measurements.

The experiment was carried out in late January 1991. Acoustic signals were transmitted from the R/V CORY CHOUEST stationed near Heard Island (Australia), located in the south Indian Ocean at 53° S 73.5° E. Acoustic signals emitted by the projectors beneath CORY CHOUEST were received by teams of researchers in the Indian, Pacific, and Atlantic Oceans.

Our receiver, the Canadian Ocean Acoustic Measure-

ment System (COAMS) towed-line array, was towed from the research vessel CFAV ENDEAVOUR in an area approximately 420 km west of Los Angeles. The great circle source-receiver separation was approximately 17 400 km and the acoustic travel time was approximately 3 h 17 m. In our case, the source-receiver separation was one of the largest among the test participants. Our receiver was one of three, and the only towed array, operating near the west coast of North America. During the course of the test, we recorded 21 Heard Island transmissions.

The following section describes the experimental setup in more detail. In Sec. II we describe the spectral analysis of the recordings. In Sec. III we present the results of beamforming. In Sec. IV we attempt to put the results in perspective through comparisons with expectations, model results and results from other groups. Finally, in Sec. V we summarize our findings.

I. THE EXPERIMENT

CFAV ENDEAVOUR arrived on station at 2100 UTC on 27 January. The COAMS array was deployed to a depth of approximately 500 m corresponding to the sound channel axis depth at our location. Figure 1 shows ENDEAVOUR'S track during the test. Times are shown in day/hour-minute UTC, and the dots on the ship track indicate periods of 12 h. Three types of signals were transmitted; these signals have been described fully elsewhere.⁴ The symbol cw is used here to refer to the 57 Hz continuous tone transmissions, P to the pentaline transmissions, and M to the M-sequence transmissions. In addition, the numbers 255, 511, 1023, and 2047 in conjunction with an M refer to the particular number of states in an M-sequence. Table I summarizes the data recorded on board CFAV ENDEAVOUR.

Prior to the test there had been considerable speculation on whether or not the west coast participants would be able to detect the Heard Island transmissions. Model results made available to us by Chiu⁵ had indicated that a window of favorable propagation might exist if the transmissions fol-

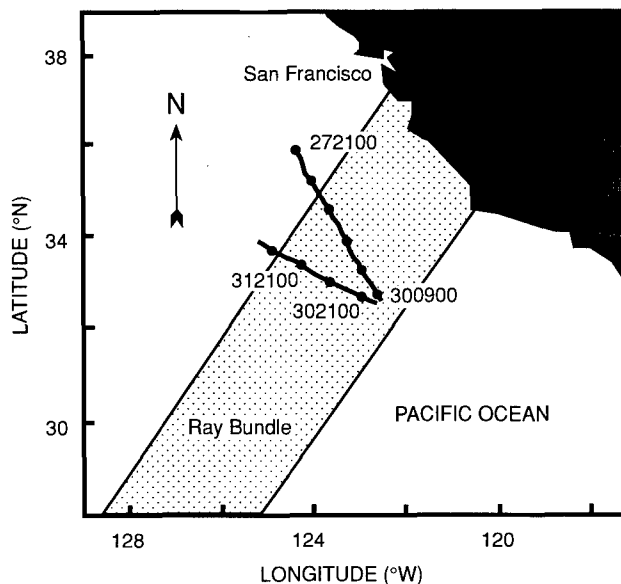


FIG. 1. CFAV ENDEAVOUR's track during the test. Dots show position at 12 h intervals. Times are in day/h-min UTC. Ray bundle indicated was the expected region of favorable propagation for the Heard Island transmissions.

lowed a path eastward between New Zealand and Antarctica. The bounds of this acoustic window are marked by the *ray bundle* shown in Fig. 1. Our original intentions were to deploy the COAMS array somewhat to the north of the ray bundle and tow south-east completely through the region.

During the test we received information regarding the status of the sound projector system and on the weather conditions at Heard Island. The 30/0900 transmission was received at a considerably reduced signal-to-noise, due to the fact that only two projector units were functioning. This in-

formation caused us to alter course after 1330 UTC on 30 January to stay within the ray bundle and thereby increase our chances of receiving as many of the remaining transmissions as possible. Also, the change in bearing could provide information on the vertical structure of the transmissions. In total, 21 Heard Island transmissions were recorded on board CFAV ENDEAVOUR. The transmissions have been identified in 20 of these recordings. The only uncertain case is that of cw 31/1213 whose analysis is not yet complete.

The COAMS towed-line array and data acquisition system have been described by Craig and McKee.⁶ To summarize, the array contains 128 hydrophone groups in four nested sub-arrays. The hydrophone groups are spaced over an interval of 1524 m and are sampled at approximately 700 Hz. The sensitivity of each hydrophone group and the gains of each preamplifier and post-amplifier are known to better than ± 1 dB. This known system response allows the computation of sound pressure levels (SPL) and transmission loss (TL) given the projector source level.

II. CW PROCESSING

In this section the results are presented of a power spectral analysis of the transmissions analyzed to date. Since the M and P type transmissions were designed to have approximately half the power in the carrier, each transmission was treated as a continuous tonal signal and subjected to a standard spectral analysis. Consecutive blocks of data representing 93.75 s duration from each hydrophone group were Fourier analyzed. The spectra from each of the 128 hydrophone groups were then averaged to obtain a stable estimate of the spectral density. These short-term average spectra were stored for later use. Long-term averages were formed by av-

TABLE I. Heard Island transmissions recorded on board CFAV ENDEAVOUR.

| Transmit time (dd/hhmm Z) | Type | Sources ^a (units) | Axis SL ^a (dB/1 μ Pa @ 1 m) | Comments |
|------------------------------|-------|---------------------------------|---|-----------------------------|
| 29/0900 | M1023 | 23469 | 220.8 | Problems in first 16 min |
| 29/1200 | cw | 34569 | 220.8 | |
| 29/1500 | P | 34569 | 220.8 | |
| 29/1800 | M255 | 34569 | 220.8 | 9 failed 1837. SL=218.7 |
| 29/2100 | M2047 | 3456 | 218.7 | |
| 30/0000 | cw | 3456 | 218.7 | |
| 30/0300 | P | 3456 | 218.7 | |
| 30/0600 | M255 | 3456 | 218.7 | |
| 30/0900 | M511 | 35 | 212.4 | 6 replaces 5,0940. SL=211.4 |
| 30/1200 | cw | 36 | 211.4 | |
| 30/1500 | P | 46 | 213.0 | |
| 30/1800 | M255 | 46 | 213.0 | |
| 30/2100 | M1023 | 346 | 216.2 | 4 failed at 2117. SL=211.4 |
| 31/0000 | cw | 6 | 205.2 | |
| 31/0300 | P | 6 | 205.2 | |
| 31/0600 | M255 | 6 | 205.2 | |
| 31/0900 | M2047 | 6 | 205.2 | |
| 31/1213 | cw | 3 | 205.6 | 3 replaces 6 |
| 31/1500 | P | 3 | 205.6 | |
| 31/1800 | M255 | 3 | 205.6 | |
| 31/2100 | M511 | 3 | 205.6 | Last transmission |

^aBased on information supplied by A. M. G. Forbes, Univ. of California, San Diego (personal communication, March 1991).

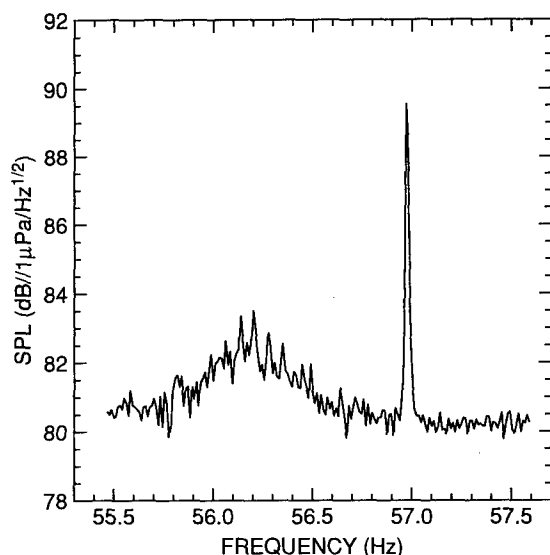


FIG. 2. Long-term average spectrum from raw data for the cw 30/0000 transmission.

eraging the results for adjacent blocks spanning the duration of the transmission. The spectral bin widths resulting from this analysis are 10.7-mHz wide.

As an example, Fig. 2 shows the average power spectral density for the cw 30/0000 transmission. This spectrum was obtained by averaging all 128 hydrophone group spectra over 45 consecutive data blocks of 93.75-s duration. After applying a bandwidth correction for the tonal, we find the SPL for this event to be 69.8 dB/1 μ Pa. The S/N_0 (signal-to-noise ratio for noise in a 1 Hz band) for this event is approximately -10.4 dB.

Transmission loss (TL) is computed by finding the difference between the source level, stated in Table I, and the measured SPL for the event. This calculation assumes that the sound energy being received is emitted along the projec-

tor array beam axis. Using the above example, we find the $TL=218.7-69.8=148.9$ dB. Table II summarizes the results of the SPL and TL measurements for the transmissions analyzed to date.

During the production of the short-term-average spectra, the spectrum of each hydrophone group was available for consecutive 93.75-s intervals. Inspection of the hydrophone group spectra revealed that the 57-Hz received SPL varied markedly along the length of the hydrophone array during each interval. The inter-element coherence was also observed to be less than unity and to vary along the length of the array. This might be explained by the action of multipath interference. One could view the situation as being similar to observing a distant light source through a turbulent atmosphere. Under these conditions, even closely spaced receivers can exhibit quite different received amplitude levels. The low S/N_0 and highly variable levels of the received transmissions have prevented the recognition of regions of constructive and destructive interference on a scale comparable to the array length. On a slightly longer length scale it has been possible to observe variations in SPL on the order of 8 dB by plotting the short-term-average carrier level as a function of time. Figure 3 shows the short-term-average SPL of the 57 Hz carrier during the cw 30/0000 transmission. The *turn-on* and *turn-off* of the signal are easily recognized. Also, it is clearly seen that the SPL experienced several fluctuations with a period on the order of 20 min. Unfortunately, it is very difficult to decipher the effects of temporal and spatial fluctuations with the current data set. The sound field is extremely complex and possesses considerable fine structure.

III. BEAMFORMING

Sections of the recorded data from the COAMS midfrequency sub-array were submitted to a conventional time-domain beamformer. The resulting beam time-series were then Fourier analyzed to determine the arrival bearing angle

TABLE II. Sound-pressure level and transmission loss for the Heard Island transmissions recorded on board CFAV ENDEAVOUR.

| Transmit time (dd/hhmm Z) | Type | Frequency (Hz) | SPL (dB/1 μ Pa) | TL dB | S/N_0 dB |
|------------------------------|-------|-------------------|------------------------|----------|---------------|
| 29/1500 | P | 53.27 | 61.8 | 147.1 | -18.6 |
| | | 55.17 | 63.9 | 151.1 | -16.2 |
| | | 57.08 | 65.2 | 155.6 | -14.6 |
| | | 58.98 | 64.0 | 150.0 | -16.7 |
| | | 60.87 | 61.2 | 147.7 | -18.6 |
| 29/2100 | M2047 | 56.94 | 68.1 | 150.6 | -16.7 |
| 30/0000 | cw | 56.97 | 69.8 | 148.9 | -10.4 |
| 30/0300 | P | 55.07 | 63.4 | 149.5 | -17.1 |
| | | 56.97 | 66.9 | 151.8 | -14.1 |
| | | 58.87 | 63.7 | 149.3 | -16.1 |
| | | 60.87 | 61.2 | 147.7 | -18.6 |
| 30/0600 | M255 | 56.95 | 63.9 | 154.8 | -15.4 |
| 30/0900 | M511 | 56.96 | 60.3 | 151.6 | -17.2 |
| 30/1200 | cw | 56.94 | 64.1 | 147.3 | -15.3 |
| 30/1500 | P | 55.07 | 60.9 | 146.3 | -18.6 |
| | | 56.97 | 63.6 | 149.4 | -16.3 |
| | | 58.87 | 62.5 | 144.7 | -18.5 |
| | | 60.87 | 61.2 | 147.7 | -18.6 |
| 30/1800 | M255 | 56.93 | 61.5 | 151.5 | -17.8 |
| 30/2100 | M1023 | 56.94 | 63.1 | 153.1 | -17.1 |

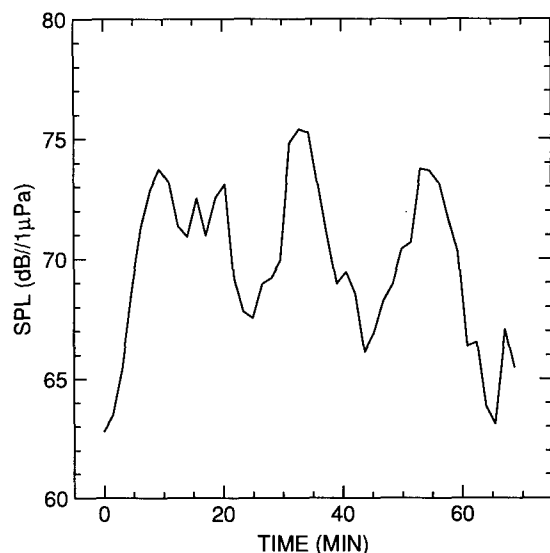


FIG. 3. Hydrophone short-term average spectrum versus time for the cw 30/0000 transmission.

at the array. The measurement of the arrival angle is important, because it aids in determining the acoustic path followed by the sound energy over its almost 18 000-km propagation distance.

The array gain resulting from the beamforming operation was considerably reduced from the maximum attainable, because of the loss of coherence in the 57 Hz carrier along the length of the array. Fortunately, significant gains were achieved due to the rejection of noise from shipping located, mostly, north of us on bearings approaching 180° from the Heard Island arrival.

The most immediate result of the beamforming operation is that all known arrival bearings lie near the mean arrival angle of $(214 \pm 3)^\circ$ True North (or T). This result implies the presence of a single dominant acoustic path (or bundle of closely spaced paths). Table III summarizes the arrival angle measurements. Arrival angles quoted in the column marked "Log" were derived from approximate measurements made during the HIFT using the COAMS on-line processing system which does not take ship motion into account and relies on the user to find the beam with the maximum signal level on a grey-scale display with limited dynamic range. More accurate results are quoted for some of the transmissions in the column marked "Post Analysis." These results allow for ship motion compensation, and determine the arrival directions from fitting a smooth curve to the levels from several beams.

Figure 4 shows the relative power of the 29/1500 pentaline transmission versus true bearing during a selected time segment. Each of the five dominant pentaline components is represented by a separate curve in the figure. Some scatter in the estimated bearings for each of the tonal components is apparent. The amount of scatter is comparable to the expected uncertainty due to equipment accuracy and computational limitations for the measurement. Note that during the processed time segment, the 58.98-Hz side-band possessed higher power than the 57-Hz carrier. This change in domi-

TABLE III. Arrival bearing angles for the Heard Island transmissions recorded on board CFAV ENDEAVOUR.

| Transmit time (dd/hhmm Z) | Type | Bearings ($^\circ$ T) | |
|------------------------------|-------|------------------------|---------------|
| | | Log ^a | Post-analysis |
| 29/0900 | M1023 | 212 | |
| 29/1800 | M255 | 219 | |
| 29/1500 | P | 218 | 215 |
| 29/2100 | M2047 | 213 | 216 |
| 30/0000 | cw | 212 | 214 |
| 30/0300 | P | 214 | 216 |
| 30/0600 | M255 | 214 | 217 |
| 30/0900 | M511 | 212 | |
| 30/1200 | cw | 215 | 215 |
| 30/1500 | P | 217 | |
| 30/1800 | M255 | 214 | |
| 30/2100 | M1023 | 213 | |
| 31/0600 | M255 | 214 | |
| 31/0900 | M2047 | 210 | |
| 31/1500 | P | 207 | |
| 31/1800 | M255 | 211 | |
| 31/2100 | M511 | 213 | |

^aApproximate measurements made while at sea using the array monitor system.

nance was a common occurrence and illustrates the degree of fluctuation that was observed. The long-term averages show the proper order of dominance, but show differences on the order of 2 dB between each of the side-bands—significantly less than the expected 6 dB.

The midfrequency sub-array of COAMS was chosen for the angle measurements, because its design (80-Hz) frequency is suited to the 57-Hz carrier of the Heard Island transmissions. This sub-array has an aperture of just over 600 m and the resulting beams are approximately 2.5° at broadside. By using the very-low-frequency (VLF) sub-array, with an aperture of over 1500 m, it is possible to obtain beams that are approximately 1° wide at broadside. A first look at beamforming the VLF sub-array is shown in Fig. 5. It was hoped that the narrower VLF beamwidths might be able to

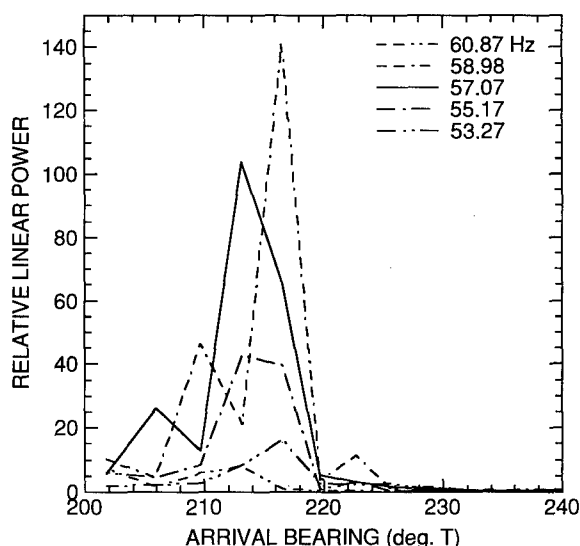


FIG. 4. Relative power versus arrival bearing angle for transmission P 29/1500 obtained from the mid-frequency sub-array beams.

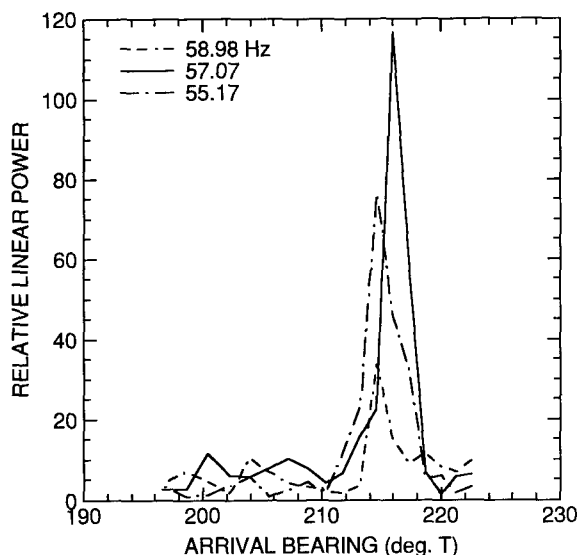


FIG. 5. Relative power versus arrival bearing angle for transmission P 29/1500 obtained from the aliased VLF sub-array beams.

resolve horizontal multipath arrival angles. Unfortunately, from this example at least, it does not appear that conventional beamforming techniques are sufficient to resolve the horizontal arrivals. Also, the second-order side-bands are below the noise background level in the VLF beams. Future work will deal further with these aspects.

IV. DISCUSSION

The HIFT data recorded on board CFAV ENDEAVOUR is a very rich data set. The results of the preliminary analysis reported in this paper merely scratch the surface. Our main goals in this work are to report the received signal characteristics— S/N_0 , SPL, TL and arrival bearing angle.

The measured S/N_0 (tonal level/noise level in a 1-Hz band) during the test was quite poor. The mean S/N_0 for all events and tonals analyzed to date is -16.4 dB. These levels are somewhat optimistic because the background noise levels were estimated in the immediate vicinity of the tonals. In most cases, high noise levels were present within a fraction of a Hz from the tonal.

The mean SPL for all the tonals analyzed to date is (63.8 ± 2) dB/1 μ Pa (this average includes the pentaline sidebands). Acoustic signals of this level are easily detectable when shipping densities are low. In our case, shipping densities were high; therefore, detection of the transmissions generally required averaging and/or beamforming operations.

The transmission loss predictions for our location were a subject of considerable controversy. Pre-test loss estimates varied from 120 dB to more than 170 dB. The lower loss value corresponds to spherical spreading out to approximately 2.5 times the water depth at the source followed by cylindrical spreading plus absorption. The higher loss value corresponds to spherical spreading plus absorption and losses due to sound channel blockages. Before the test was performed, a reliable model that could handle propagation over

such a long distance in a complex waveguide was not directly available to the authors.

For the transmissions analyzed to date the mean TL was determined to be 150 dB. Lacking accurate loss information from models, it is instructive to compare this empirical loss measurement to the losses that would be incurred from attenuation and geometrical spreading loss. Estimates of the attenuation along the 17 400-km long path vary from about 6–10 dB. The cause of the uncertainty appears to be largely due to the effects of scattering and the concentration of boric acid along the path. Cylindrical spreading and attenuation yields 78–82-dB losses; combining spherical spreading near the source followed by cylindrical spreading with attenuation yields 114–118 dB; for spherical spreading and attenuation the losses are 151–155 dB. The last estimate is very close to our measured loss; however, caution should be applied when comparing these numbers. Recall that scattering and bottom losses have not been accounted for in the above spreading plus attenuation loss figure. It is likely that our signals have experienced spreading losses somewhat less than that due to spherical spreading. Most of the predicted acoustic paths from Heard Island to receivers near the west coast of North America cross regions of relatively shallow water,^{5,7} where considerable energy could be lost into the bottom. Some of the acoustic paths are expected to be completely blocked by the island chain ridges of the south western Pacific that rise into the sound channel.⁸

Comparing the 150 dB mean TL with the results from other participants located in the Atlantic^{9,10} it is found that the Atlantic receivers generally experienced better propagation conditions. This finding is consistent with the fact that less bottom interaction was predicted for these receivers. Fraser¹⁰ has reported a 130-dB loss over a range of approximately 16 500 km, a source–receiver separation similar to our case.

The mean arrival bearing angle for our data is $214^\circ \pm 3^\circ$ T. This value compares very well with model results.⁷ The model predictions vary from 213.9° – 215.1° for the arrival angle depending on mode (only the first three modes were computed) and receiver location. Predicted travel times range from 11765.9–11827.2 s, again depending on mode and receiver location. These times agree well with our nominal travel time of 11820 s (3h 17m).

V. CONCLUSIONS

In summary, 20 transmissions were received and recorded on board CFAV ENDEAVOUR during the HIFT. A mean SPL of (63.8 ± 2) dB/1 μ Pa was measured for the transmissions that have been analyzed to date. This SPL corresponds to a mean TL of (150 ± 3) dB and a mean $S/N_0 = (-16.4 \pm 2)$ dB.

Measured bearing angles and travel times agree well with model predictions⁷ and indicate that a single group of acoustic paths dominate the propagation to our receiver location. Following this dominant path, the sound energy grazes Antarctica, turns northward and follows a course south of New Zealand, grazing the south slopes of Chatham Island (NZ). Further north, some bottom interaction is prob-

able in the volcanic ridges near Tahiti. Once north of Tahiti, the sound energy should then have a clear path to the location of our receiver.

- ¹W. H. Munk and A. M. G. Forbes, "Global Ocean Warming: An Acoustic Measure?" *J. Phys. Oceanogr.* **19**, 1765–1778 (1989).
- ²U. Mikolajewicz, B. Santer, and E. Maier-Reimer, "Ocean Response to Greenhouse Warming," *Nature* **345**, 589–593 (1990).
- ³M. G. Briscoe, "The Heard Island Global Program," *J. Acoust. Soc. Am.* **90**, 2329 (1991).
- ⁴K. Metzger, Jr., T. G. Birdsall, and M. A. Dzieciuch, "HIFE Signals and General Results," *J. Acoust. Soc. Am.* **90**, 2239 (1991).
- ⁵C. Chiu and A. J. Semtner, "A Simulation Study of Cross-Basin Sound Transmission from Heard Island to California," *J. Acoust. Soc. Am.* **88**, 592 (1990).
- ⁶D. W. Craig and L. McKee, "High Performance Shipboard Acoustics Data Acquisition, Imaging," *Sea Technol.* **31**(1), 51–53 (1990).
- ⁷B. E. McDonald, W. A. Kuperman, and K. Heaney, "Horizontal Multipath in Transoceanic Acoustic Propagation," *J. Acoust. Soc. Am.* **90**, 2347 (1991).
- ⁸A. G. Forbes, "The Tasman Blockage: An Acoustical Sink for the Heard Island Feasibility Test," *J. Acoust. Soc. Am.* **90**, 2346 (1991).
- ⁹D. R. Palmer, "The Ascension Island Listening Station," *J. Acoust. Soc. Am.* **90**, 2330 (1991).
- ¹⁰I. A. Fraser, "The Heard Island Experiment—DREA Data," Informal Letter Report to HIFT participants, Defence Research Establishment Atlantic, Dartmouth, NS, Canada (1991).

Vertical array receptions of the Heard Island transmissions

Arthur B. Baggeroer and Brian Sperry

Massachusetts Institute of Technology, Cambridge, Massachusetts 02139

Khosrow Lashkari

Monterey Bay Aquarium Research Institute, Monterey, California 93943

Ching-Sang Chiu and James H. Miller

Naval Postgraduate School, Monterey, California 93943

Peter N. Mikhalevsky

Science Applications International Corporation, McLean, Virginia 22102

Keith von der Heydt

Woods Hole Oceanographic Institution, Woods Hole, Massachusetts 02543

(Received 23 August 1992; accepted for publication 7 June 1994)

A long, vertical line array was deployed off Monterey, California during the Heard Island Feasibility Test to measure the modal content of the received signals. The array contained 32, equally spaced hydrophones spanning from 345 to 1740-m depth. The multichannel data were recorded through a tether to the R/V POINT SUR. The measurements had very low signal to noise ratios and indicated the cw transmission losses were approximately 140 dB for a source/receiver range of 17 000 km. Modal content was analyzed using (i) the modal extent versus depth, (ii) frequency-vertical wave-number spectra, (iii) modal beamforming and (iv) least squares fitting. All led to the conclusion that the modal population is surprisingly rich. There was strong evidence of population up to at least mode seven in the data.

PACS numbers: 43.30.Qd, 43.30.Bp, 43.60.Rw

INTRODUCTION

The Heard Island Feasibility Test (HIFT) demonstrated that coded acoustic signals could be detected at ranges up to 18 000 km with currently available source technology. This paper describes one component of the HIFT where a large aperture vertical line array was deployed off Monterey, California to monitor the signals transmitted from Heard Island.

One may pose the question: why use a vertical line array (VLA)? There are several responses to this. The first simply involved the signal-to-noise ratios (SNRs). The VLA provided array gain to improve upon the low SNR on a single hydrophone. The transmissions to both coasts of the United States were nearly antipodal. While explosive signals have been detected at these ranges, transmission loss measurements did not exist when the HIFT was being planned.¹ In fact, one of the major challenges prior to the HIFT was the prediction of the received signal amplitudes; estimates differed by more than ± 30 dB depending upon the assumptions made about the propagation! This spread was indicative of our uncertainty about transglobal acoustic propagation.

A second response concerns long range acoustic propagation. Signals must propagate axially in the SOFAR duct to be detected at these long ranges. At the 57-Hz center frequency of the HIFT these axial, or ducted, paths are efficiently described using a modal representation and the modal distribution is critical to understanding the acoustic propagation. The spatial distribution of the signals across the VLA provides information which is not available from a time series on a single hydrophone. The temporal separations of the low order modes, or the axial rays, were too small to be

resolved with the bandwidths and SNRs available in the HIFT; equally important was the fair amount of uncertainty about their arrival times.

Finally, the motivation for the HIFT was to test the feasibility of using global acoustics for monitoring basin-scale ocean climate. The modes, or raypaths, sample the vertical structure of the ocean. Since they span different vertical sections, they provide additional information about the ocean. At relatively short ranges, but still many hundreds of kilometers distant from the source, raypaths are well separated and they have been exploited in ocean acoustic tomography; the axial modes, which are the most energetic at the long ranges for monitoring ocean climate, have been difficult to identify since the separation of their arrival times have not been resolved with the available bandwidths. VLAs can separate these low-order modes spatially using modal beamforming, thus providing a means of modal tomography for basin-scale ocean climate.

It was late in the planning of the HIFT when the importance of vertical line arrays was recognized, so an intense effort was made to include two in the HIFT, one off Monterey, CA and the other off Bermuda. The VLAs provided valuable information about the HIFT signals. Probably the most important observation was that the modal structure is more populated than expected. Our expectation prior to the HIFT was that only the very first few modes would be detected at global ranges due to loss mechanisms such as internal waves and boundary interactions, especially in the first 5000 km in the Southern Ocean where the sound channel is at the surface. The VLA data unambiguously demonstrated

the presence of modes up to at least mode 7 and this has stimulated considerable research to explain the observed modal population. Hypotheses include nonadiabatic propagation through the Antarctic Circumpolar Current, bottom interactions at the Campbell Plateau and modal coupling accumulated over very long ranges.²

The high-transmission losses, some as high as 145 dB, observed on all the west coast receivers were the major disappointment.³ This required long integration times and consequently smeared the information about arrival times. Both the modal content and the low SNRs have been very important in our planning for future experiments using acoustics to monitor ocean climate.

I. BACKGROUND: NORMAL MODE REPRESENTATION OF ACOUSTIC PROPAGATION

Normal mode representations for acoustic signals are well established in the literature.⁴ Since they are important in interpreting the data, we include a very brief description of them. Normal modes are especially useful at low frequencies, e.g., 57 Hz, where a few modes often provide an efficient representation of ducted signals. A mode spans the water column between the depths where the sound speed equals the phase speed of the mode, or "turning depths," and they propagate with different group speeds. As a result the modes "sample" different sections of the water column and they can be separated both spatially by their shape and temporally by their group delays.

Normal modes are derived using a horizontally stratified environmental model. Since the ocean along the geodesic path from Heard Island to the site of the vertical array was range dependent, one must introduce approximations to use a normal mode representation. The *adiabatic approximation* is the simplest approximation used and it was used for many of the predictions of the HIFT propagation. It assumes that the range dependence is gradual enough that there is no transfer of energy among the modes and the modes change "adiabatically" with the ocean environment; nevertheless, there is considerable debate about how gradual the changes must be and over what distance for the propagation to be adiabatic. The HIFT data suggest that the propagation was not adiabatic and one should use coupled mode representations.^{5,6} Nevertheless, we introduce the adiabatic approximation here because it is useful in describing some of the modal concepts used in the data analyses.

With this approximation the propagation from a point source at a depth z_s to a VLA is given by

$$\mathbf{p}(\mathbf{r}_R) = W(\mathbf{r}_R)T(\mathbf{r}_R, \mathbf{r}_S)\mathbf{x}(\mathbf{r}_S), \quad (1)$$

where \mathbf{r}_S is the source location, \mathbf{r}_R is the array location, $\mathbf{x}(\mathbf{r}_S)$ represents the mode excitation at the source, $T(\mathbf{r}_R, \mathbf{r}_S)$ is a diagonal matrix which describes the adiabatic propagation from source to receiver, and $W(f, \mathbf{r}_R)$ is an observation matrix which projects the modes on the elements of the receiver array. (We have suppressed the notation indicating the frequency dependence hereafter. All quantities were computed for 57 Hz.) We denote the modes and horizontal wave numbers in the Helmholtz equation at location \mathbf{r} to be $\phi_i(z, \mathbf{r})$ and $\mathbf{k}_i(\mathbf{r})$, respectively. The mode excitation is given by

$$\mathbf{x}(\mathbf{r}_S) = \begin{bmatrix} \phi_1(z_S, \mathbf{r}_S) \\ \phi_2(z_S, \mathbf{r}_S) \\ \vdots \\ \phi_M(z_S, \mathbf{r}_S) \end{bmatrix}. \quad (2)$$

With the adiabatic assumption the off diagonal terms of the propagation matrix, T , are zero and the diagonal terms are given by

$$T_{i,i}(\mathbf{r}_R, \mathbf{r}_S) = \sqrt{\frac{2}{\pi}} \frac{e^{-j\pi/4}}{\sqrt{\mathbf{k}_i(\mathbf{r}_R)|\mathbf{r}_R - \mathbf{r}_S|}} \exp\left(j \int_{\mathbf{r}_S}^{\mathbf{r}_R} \mathbf{k}_i(\mathbf{r}) d\mathbf{r}\right). \quad (3)$$

With nonadiabatic propagation the off diagonal terms are nonzero. Note that the wave numbers $\mathbf{k}_i(\mathbf{r})$ may include a complex term which incorporates the modal attenuation from volume absorption and boundary losses. The observation matrix is given by

$$W(\mathbf{r}_R) = \begin{bmatrix} \phi_1(z_1, \mathbf{r}_R) & \phi_2(z_1, \mathbf{r}_R) & \cdots & \phi_M(z_1, \mathbf{r}_R) \\ \phi_1(z_2, \mathbf{r}_R) & \phi_2(z_2, \mathbf{r}_R) & \cdots & \phi_M(z_2, \mathbf{r}_R) \\ \vdots & \vdots & \ddots & \vdots \\ \vdots & \vdots & \phi_m(z_n, \mathbf{r}_R) & \vdots \\ \phi_1(z_N, \mathbf{r}_R) & \vdots & \vdots & \phi_M(z_N, \mathbf{r}_R) \end{bmatrix}. \quad (4)$$

Equations (1)–(4) are used in interpreting the VLA data in terms of their modal content. To be observed, a mode must have a significant expression at the depths of the VLA elements. In particular, a low-order mode trapped near the SOFAR axis cannot be observed at a sensor which is below the lower "turning depth." One can consider the columns of Eq. (4) to be effectively continuous and use a Fourier analysis versus vertical wave number of each mode. By using WKB methods this leads to an interpretation of each mode being the constructive interference of up and down going rays.⁴ The received signal is a linear superposition of modes in Eq. (1), so one can use modal beamforming in much the same way as plane wave beamforming for a field which is a superposition of plane waves. Alternatively, one can "fit" the field using a linear combination of modes. Each of these four interpretations are used in the sequel to analyze the HIFT VLA data.

II. EXPERIMENT

A. Vertical array receiver

The vertical array had 32 hydrophones equispaced at 45 m. The shallowest hydrophone was nominally at 345 m in the water column and the deepest at 1740 m. The array was connected to a data acquisition system aboard the R/V POINT SUR by a floating tether ~1 km away. The deployment configuration is illustrated in Fig. 1. The array had four subsystems: (i) the vertical line array; (ii) the surface wave isolation subsystem; (iii) the tracking and monitoring equipment and (iv) the data acquisition system.

HEARD ISLAND FEASIBILITY TEST MONTEREY VERTICAL ARRAY

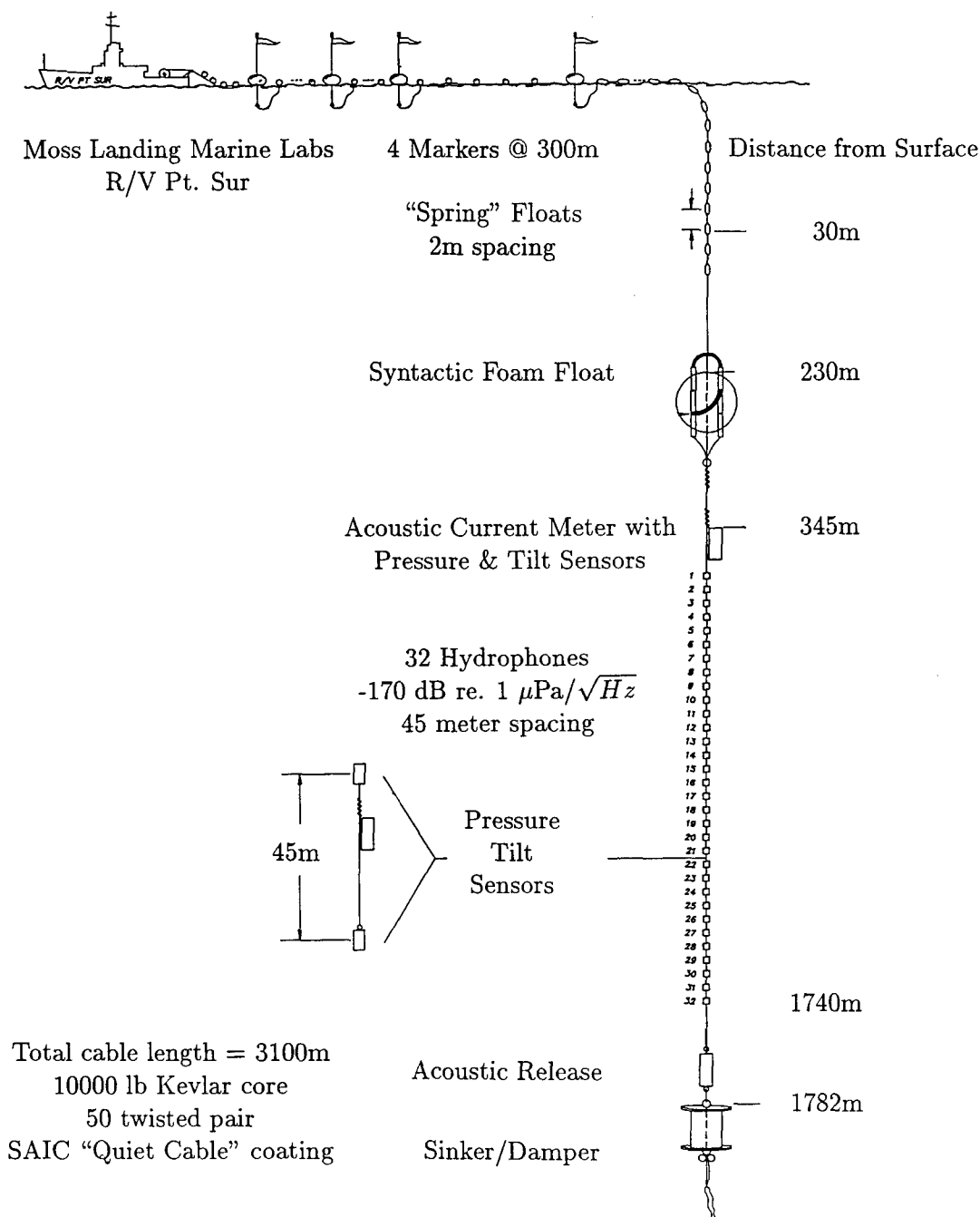


FIG. 1. Deployment configuration of the HIFT vertical array. The VLA had 32 hydrophones and spanned the water column from 345–1740 m; it was connected to the R/V POINT SUR on a 1-km tether and isolated from surface wave action by a "spring" of floats.

1. Vertical line array

The array was fabricated using 2900 m of a cable specially designed to reduce strum.⁷ The cable consisted of electrical conductors, an antistrumming external jacket on the vertical section, and the hydrophones. The electrical cable contained 50 twisted pairs of #28 AWG (American Wire Gauge) solid conductors. (We were well aware of the risk of fatigue with this wire gauge; its selection was based upon cable availability in the short time prior to the experiment.)

The data from the hydrophones used 32 of these pairs and each power bus was a group of three pairs. These conductors were covered by a Kevlar strength member and a waterproof jacket. This jacket had a triangular cross section wound in a reversing helix to reduce strumming induced by vortex-shedding water flow around the cable.⁷ After a 20-dB preamp gain the hydrophones had a net sensitivity of $-170 \text{ dB re: } 1 \text{ V}/\mu\text{Pa}$ over the range of 10–2000 Hz. The hydrophones were connected to the cable by waterproof, reinforced

"breakouts" through the Kevlar jacket. Roughly 1800 m of the cable was on the vertical section; the remaining 1100 m was a tether to the recording ship. This was done to provide a separation from the ship to reduce ambient noise and to isolate wind-induced ship motion.

2. Surface isolation subsystem

The sensitivity of the hydrophones to swell induced motion required a suspension system with a spring/mass/damper design which had a natural frequency far lower than the expected swell period. (A 3-cm displacement leads to a 1-V output for a hydrophone with a -170 dB re: $1 \text{ V}/\mu\text{Pa}$ sensitivity far exceeding output levels for signal and noise which are in the mV range.) The suspension system performed several functions: (i) positioning of the hydrophones in the SOFAR channel, (ii) isolating the vertical motion of the array in response to wave forces, and (iii) floating the tether section on the surface such that it could be tracked and not damaged by the ship. The vertical suspension consisted of a damper/ballast assembly at the bottom of the array, a floatation sphere at the top of the array and a vibration isolation section connecting to the surface. A perforated steel drum supplemented by 40 lb (18.1 kg) of lead weights for an overall weight in air of approximately 260 lb (117.9 kg) were used for the damper/ballast assembly. A 1-m spherical syntactic foam float provided 400 lb (1779 N) of buoyancy. The surface isolation had 25 syntactic foam "football" floats each providing 6.25 lb (27.8 N) of buoyancy.

3. Tracking and monitoring section

The trickiest part of deploying such a long array connected to a ship was to isolate the ship from the array with a very "loose" tether. The ship was driven downwind which pulled on the array and resulted in very high noise levels on the hydrophones. If we put slack in the tether by backing down on it, there was the very real danger of wrapping the cable around the propellers and this happened once. Operation at night and during high sea states was especially risky. The tracking and monitoring section consisted of "lobster pot" floats distributed along the tether to keep it on the surface and a set of strobe lights for night operation. The *modus operandi* involved positioning the ship before the data reception such that there was considerable slack in the tether; during reception the ship was allowed to drift downwind with minimum ship power applied until the vertical section of the array started to ascend; then the ship would attempt to back-down carefully on the cable tether to relieve the tension.

The deployment and/or current shear at the site led to the array acquiring a vertical tilt. The magnitude of this was monitored and it typically was 1° – 2.5° . For an aperture of 1380 m a 1° tilt leads to a horizontal displacement between the top and bottom hydrophones of 24 m compared to the 26-m wavelength at 57 Hz. Unfortunately, the azimuth sensor failed, so direction had to be inferred from the local currents. The surface current heading was generally to the southeast (approximately 150° T) and this was consistent with the results deduced from the data.

4. Data acquisition

The data were recorded using a multichannel automatic dynamic range (autoranging) acquisition system developed at WHOI for its Arctic field programs.⁸ Each channel was bandpass filtered between 10 and 80 Hz and sampled at 228 Hz, or four times the carrier of the HIFT signals. The acquisition had a dynamic range in excess of 130 dB, or $1.5 \mu\text{V}$ –5 V and a precision of 72 dB. (We specify dynamic range to be the ratio of the largest to the smallest signal which can be recorded and precision to be the number of significant bits in a recorded signal.) MBARI and the NPS also had data acquisition systems, but the results reported here are from the WHOI system.

B. Bermuda array

The depth and spacings of the hydrophones in the Bermuda array were identical to those on the Monterey array; however, the Bermuda array was moored from the bottom and included internal A/D and recording units which were in a cannister contained in a subsurface float. This design was used to decouple the array from surface waves and to isolate it from nearby ship noise. The array was deployed approximately due east of Bermuda in 4500 m of water. Apparently the mooring failed sometime during the HIFT; while the array was eventually recovered, there were no data on the tapes.⁹ Given the signal strength observed on the Bermuda bottom horizontal array, the data loss was a bitter disappointment.¹⁰

III. SITE SELECTION AND SHIP TRACKS

The siting of the vertical array was based upon the acoustic modeling of the propagation from Heard Island to the coast of California by Chiu *et al.*¹¹ An upgraded version of the Hamiltonian Acoustic Ray tracing Program for the Ocean (HARPO)¹² and gridded temperature and salinity data simulated by the Semtner–Chervin Eddy Resolving Global Ocean General Circulation Model¹³ were used for the propagation and environmental models.

In the analysis raypaths were computed using 11 consecutive, instantaneous fields extracted from the ocean model data set at 30-day intervals in the simulation. These 11 fields contained both meso- and gyre-scale variability. A reliable ray envelope criterion was established to be those paths not impeded by land masses and with less than five bottom interactions. The rays within this envelope and insonifying the west coast of California were determined. This is illustrated in Fig. 2. This envelope is a rather thin beam. It is bounded between azimuthal launch angles of 133° and 136° (measured clockwise from North) and in the vertical by launch angles between 0° and 2° . The horizontal envelope dimension of the ray bundle was nearly constant in time near the source but became quite variable at the receiver site off the California coast. The variability was introduced mainly in the Southern Ocean as the ray bundle traversed the Antarctic Circumpolar Current. The reception envelope has a mean direction of 32° (from 212° , or looking downwave) and mean width of 150 km. It encountered the coast in a region generally confined between Point Arguello and San Fran-

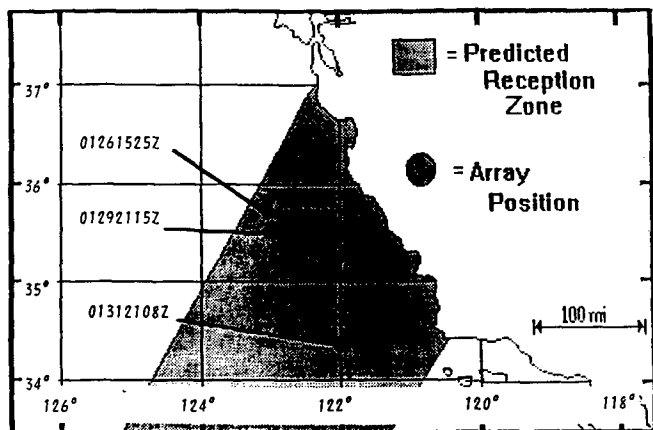


FIG. 2. Horizontal ray tubes for predicting receptions of HIFT transmissions based upon Semtner mesoscale model. The shaded area indicates the spread of arriving rays using a 3-D HARPO ray tracing code; the sites for the three cw receptions are designated by the approximate date/time code for the signal arrival from Heard Island [from Chiu *et al.* (Ref. 4)].

cisco Bay. Areas common to all fields were mapped to estimate the best receiving locations. No other reliable ray envelopes from Heard Island to California were found using this modeling approach. This analysis led to selecting a location roughly 200 km offshore at a site west of any major local bathymetry which would shadow the signals. This is labeled "01261525Z" in Fig. 2. This is closest to the site where the data subsequently discussed were acquired.

Since the R/V POINT SUR was not moored, it drifted on-average towards SE to SSE. The winds were relatively calm and the sea state was low so the R/V POINT SUR was able to maintain excellent station keeping during the array deployment and during the reception of January 26th and 27th. On January 28th the winds and sea state increased to the point where it was considered very risky to maintain the tether to the array because of the danger of backing down on it. As it turned out the R/V CORY CHOUEST transmitting the signals had to suspend operations at roughly the same time so few recording opportunities were lost. When the seas abated the array was reattached; however, there was a maneuvering error and the R/V POINT SUR backed down on the array and wrapped the cable around the port screw. This occurred at the location labelled "01292115Z". The array was recovered and repaired in port. It was redeployed at the site labeled "01312108Z" which was somewhat south of the original location. (We chose the more southerly location because we heard that there were strong receptions at the location of the Canadian ship CFAV ENDEAVOR. It turned out the SNRs on individual phones at both sites were roughly the same.)

IV. ENVIRONMENTAL DATA

CTD profiles were taken before and after both deployments from which local sound speed profiles were calculated. (CTDs were considered too risky during the VLA deployment.) These were consistent with climatological data for the winter near the coast of California. It had a shallow (100-m) mixed layer, an axis depth roughly at 600 m and a

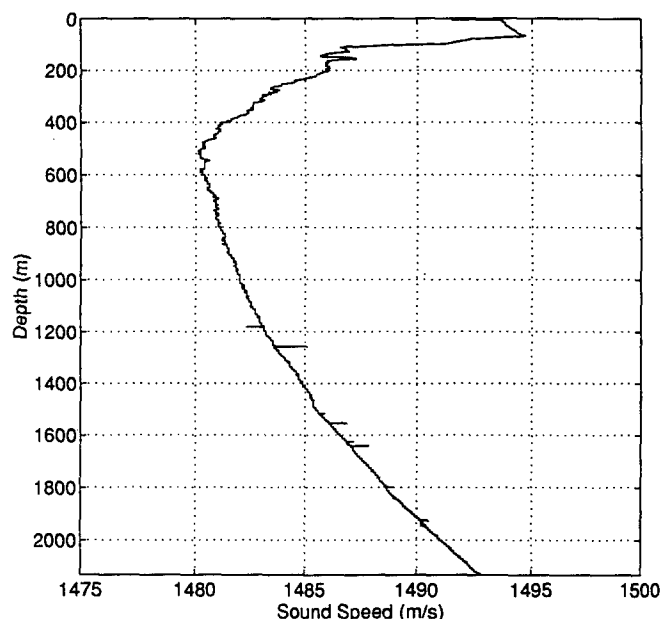


FIG. 3. Sound-speed profile derived from a CTD taken prior to HIFT receptions. The SOFAR axis is relatively broad and spans 400–600 m acquisition.

fairly broad minimum.¹⁴ Figure 3 illustrates the sound-speed profile taken closest to the time of data receptions subsequently discussed.

The first 10 normal modes were calculated from the sound-speed profile in Fig. 3. These are illustrated in Fig. 4. We have superimposed a set of horizontal lines indicating the nominal depths of hydrophones on which we have good quality data. Note that modes 1 and 2 are close to zero for hydrophones 18 and below and modes 3–6 are close to zero for the hydrophones 29–31 at the deepest part of the array. These observations become important in interpreting sonograms on the individual phones.

A normal mode can be interpreted as a coherent super-

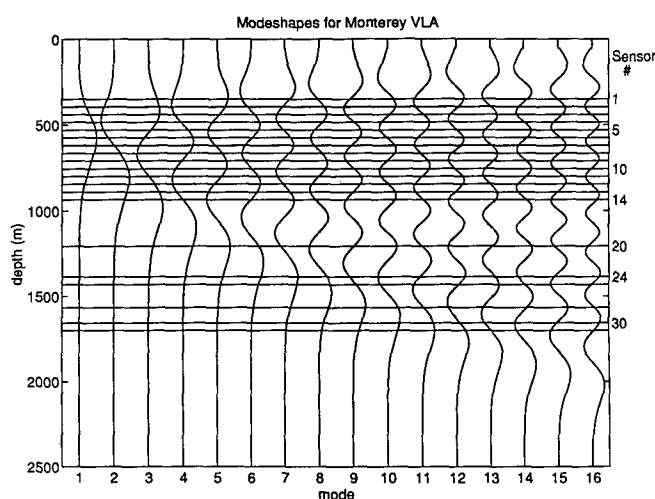


FIG. 4. The first sixteen modes at the receiver site using the sound-speed profile of Fig. 3. The modeshapes have been scaled for constant peak amplitude; the horizontal lines are depths where the VLA hydrophones operated.

TABLE I. Phase speeds, c_{pn} ; axis crossing angles; $\Delta\Theta_n$; upper and lower modal extents; Z_u , Z_l ; and channel coverage for modes 1–10.

| Mode | c_{pn} (m/s) | $\Delta\Theta_n$ (deg) | Z_u (m) | Z_l (m) | Channels |
|------|----------------|------------------------|-----------|-----------|----------|
| 1 | 1480.885 | 1.466 | 425 | 700 | 3–8 |
| 2 | 1481.787 | 2.479 | 375 | 925 | 2–13 |
| 3 | 1482.635 | 3.146 | 350 | 1100 | 2–18 |
| 4 | 1483.431 | 3.663 | 300 | 1225 | 1–20 |
| 5 | 1484.240 | 4.122 | 250 | 1325 | 1–23 |
| 6 | 1485.003 | 4.512 | 225 | 1425 | 1–25 |
| 7 | 1485.759 | 4.867 | 200 | 1500 | 1–26 |
| 8 | 1486.492 | 5.189 | 150 | 1575 | 1–28 |
| 9 | 1487.259 | 5.504 | 125 | 1650 | 1–30 |
| 10 | 1488.021 | 5.801 | 100 | 1725 | 1–31 |

position of up and down going rays with ray parameter given by the phase speed of the modes.⁴ For each mode these rays cross the sound channel axis at angles given by

$$\Delta\Theta_n = \pm \arccos(c_{\text{axis}}/c_{pn}), \quad (5)$$

where c_{axis} is the sound speed at the axis and c_{pn} is the phase speed of mode n . The phase speeds and axis crossing angles are tabulated in Table I; we refer to this when interpreting the $\omega-k$ frequency wave-number spectral analysis of the data.

The vertical extent of the modes can be determined by using the phase speed of the modes as well. The upper and lower extents Z_u , Z_l are given by the depths where the sound speed equals the phase speed. These are also tabulated in Table I. In addition, the channels which are included within this span are noted; we refer to this when interpreting the sonogram analysis of the data.

V. EXPERIMENTAL RESULTS

The analysis of the data concentrates on three reception periods in the first part of the experiment when continuous wave (cw) signals were transmitted. These are described in Table II and are denoted 01261525, 01270322, and 01271505 roughly corresponding to the date-time code for the start of data acquisition of the event at the VLA. There are several reasons which led to this concentration. The primary reason was the low SNR of the signals detected at the site off Monterey. The cw signals concentrated all the power in the carrier so very narrow-band filtering and long integration times could be done to improve SNR. The processing for M-sequences led to marginal detections which was probably the result of the drifting of the VLA.¹⁵ We use just the first three reception periods because both the transmitted signal levels from the R/V CORY CHOUEST near Heard Island

TABLE II. Comparison of predicted and measured Doppler shift for the cw signals received on the VLA.

| Data set | Source heading (deg, T) | Source speed (kts) | Launch angle (deg, T) | Predicted Doppler (mHz) | Measured Doppler (mHz) |
|----------|-------------------------|--------------------|-----------------------|-------------------------|------------------------|
| 01261525 | 254.5 | 2.99 | 133 | −31.5 | −30.5 |
| 01270322 | 252.0 | 2.51 | 133 | −24.5 | −24.0 |
| 01271505 | 234.5 | 3.21 | 133 | −12.6 | −12.5 |

were highest and the largest number of hydrophones of the VLA tethered to the R/V POINT SUR were functioning.

There were three analyses of the cw data: Sonograms of each sensor versus depth; Frequency-vertical wave number

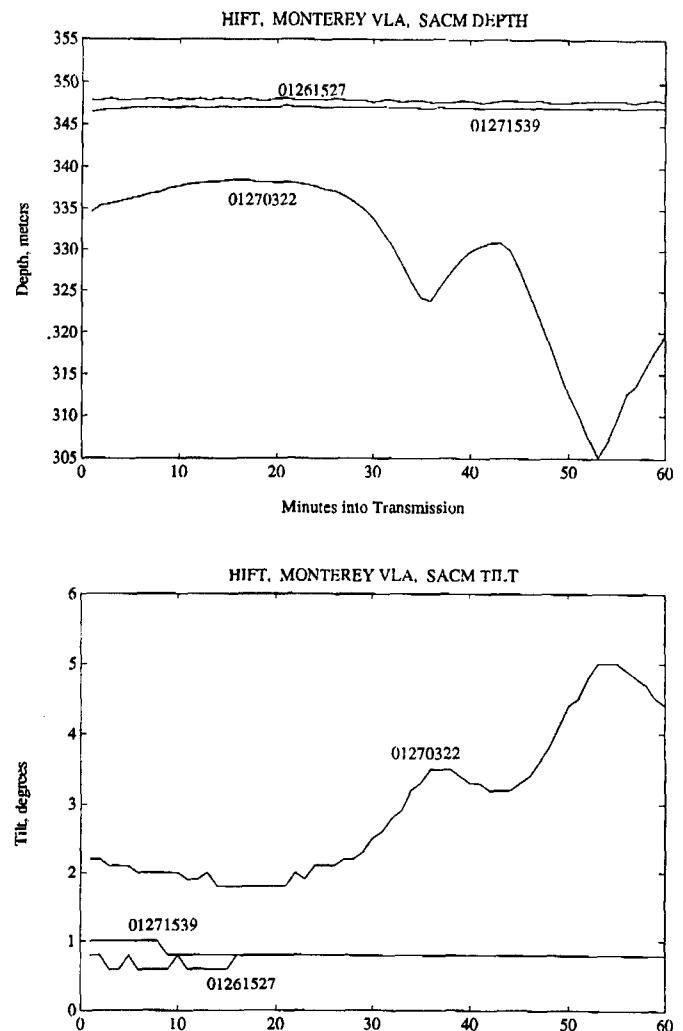


FIG. 5. Depth and tilt at the top of the VLA during the cw receptions. There are three date/time codes corresponding to each reception period; the 01261527 and 01271539 indicate that the VLA had a nearly constant geometry while both the depth and tilt on the 01270322 suggest a “quiet” period for roughly the first 30 min followed by a “noisy” one when the ship was attempting to back down on it to maintain constant depth.

Signal processing flow for HIFT data analysis

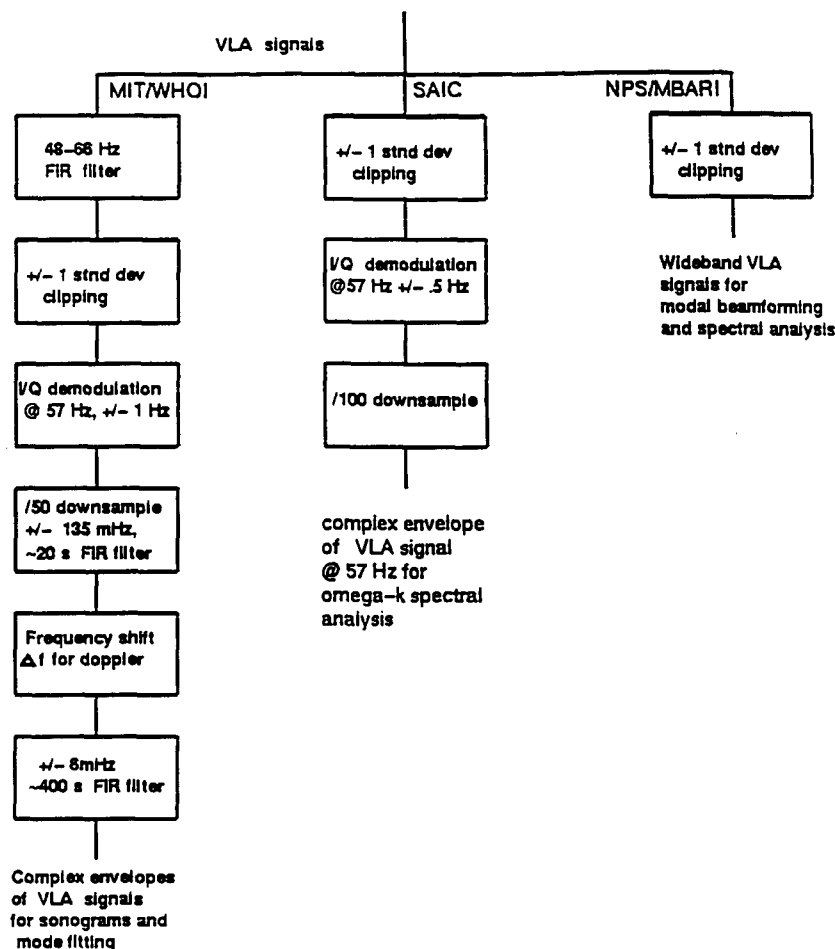


FIG. 6. Signal conditioning flow diagram for the MIT/WHOI, SAIC and NPS/MBARI VLA data analysis. There were three analysis efforts; however, all contained some form of clipping and narrow-band filtering.

$(\omega - k)$ spectra; Modal decompositions by beamforming and least-mean-square fitting.

A. VLA data quality

Low SNRs at the receiver were the major problem for the VLA data analysis. The average signal level at a near axis hydrophone was estimated to be approximately -75 dB *re*: $1 \mu\text{Pa}$ by factoring in the gain due to narrow-band filtering of the data. This level implies a transmission loss of 142 dB. (Note that this is the narrowband transmission loss and not the loss per identifiable path.) The ambient noise spectral level was measured several times in the course of the experiment and it was typically 89 dB *re*: $1 \mu\text{Pa}/\sqrt{\text{Hz}}$. This was done using a real time spectrum analyzer and averaging the levels in bands where there was little evidence of ship tonals from the R/V POINT SUR. The ship, or self-noise, was monitored continuously during the experiment using a sonogram display; it was most noticeable as tonals in spectra. The measured ambient noise level was 3–6 dB higher than the predictions from the U.S. Navy DANES model¹⁶ and the ANDES (Ver 2.2) model¹⁷ prior to the experiment and this may be attributed to the self-noise of the R/V POINT SUR. The 89-dB level is also consistent with a set of measurements made by Miller during tests for self noise made prior

to the experiment.¹⁸ The single channel SNR was typically -15 dB. The signal and noise levels are consistent with the measurements made by Heard,¹⁹ using a towed array from CFAV ENDEAVOR operating west of San Diego but in the same ray bundle from Heard Island.

There were three other problems with the VLA which influenced the data quality. Several hydrophones in the lower section of the array did not operate reliably. One known cause of this was the failure of a conductor powering some of the phones. We believe other phones failed because the continuous surface wave action caused the thin (#28) wires for the twisted pairs to fatigue and break.

Tilt, depth, and heading sensors were used to monitor motion at the top of the array (345 m) and below sensor 21 (1245 m). (See Fig. 1.) The deep sensor produced unreliable results and the compass in the shallow sensor did not operate reliably. As a result we have only the depth and tilt magnitude of the shallow sensor for inferring array geometry. The depth and tilt magnitudes for the three cw intervals are indicated in Fig. 5. We also had an acoustic current meter on the cable (see Fig. 1). One can attempt to make inferences about array tilt from the direction of the current; however, this is complicated by the station keeping of the R/V POINT SUR as

it attempted to keep slack on the tether and was not considered to be very accurate. We eventually used the stability of the shallow depth sensor to be an indication of the tension on the array and the absolute tilt. The data analyses which follow consider either an effective tilt towards the source or search over tilt azimuths.

The array tilt and depth are important in any signal processing because of the differential phase shift, $\Delta\phi_i$, it induced down the VLA. This is given by

$$\Delta\phi_i = (2\pi/\lambda)(z_i - z_0)\sin(\theta_{\text{tilt}})\cos(\phi_{\text{HI}} - \phi_{\text{tilt}}), \quad (6)$$

where z_0 is a reference depth (the top hydrophone of the VLA), ϕ_{HI} is the bearing on the geodesic away from Heard Island and θ_{tilt} , ϕ_{tilt} are, respectively, the array tilt and azimuth. We know ϕ_{HI} to be 214 °T and we estimate ϕ_{tilt} to be 150 °T which leads to a difference of approximately 64°. For example, tilt magnitudes of 2.5° were typical and would have led to a phase difference of 178°. If uncompensated, this leads to a significant degradation in array performance.

The array depth becomes an important issue when the spatial structure of the modes is included in the signal processing. Fortunately, the low-order modes are smooth functions, so minor changes are not consequential. The difficulties with inferring the VLA geometry on the HIFT suggest that reliable monitoring of array shape and heading is imperative for any signal processing of VLA data.

The final VLA data quality issue concerns the very high amplitude, random spikes which are present in the data. A broadband playback of the data indicated that there were infrequent, but strong, broadband transients propagating across the array. We believe that one of the hydrophone "breakouts" became loose and induced these transient vibrations on the cable. We have suppressed this by a combination of broadband filtering and clipping in the signal processing. This has been very effective in mitigating these transients.

B. Signal conditioning

Three groups—MIT/Woods Hole, SAIC, and NPS/MBARI—did the VLA data analysis; as a result, there are some minor differences in the signal conditioning done before each of the analyses. All involved some form of clipping to suppress the transients and some bandpass filtering to reject out-of-band noise. The signal flow for the three analyses is illustrated in Fig. 6. The results concerning the modal content, nevertheless, are very consistent.

The MIT/WHOI signal conditioning procedure is indicated on the left side of Fig. 6. The transients were suppressed by a short duration, broadband FIR (finite impulse response) filter with a passband from 48–66 Hz and then clipped at a level of 1 standard deviation. The complex envelope of the data about 57 Hz was formed by quadrature demodulation using a 1-Hz passband. This was followed by downsampling by a factor of 50 which leads to a sampling rate of 4.56 Hz and FIR filtering with a passband of ± 135 mHz. The data were then demodulated for the Doppler shift resulting from the ship motion and then passed through a final narrowband FIR filter with a bandwidth of ± 6 mHz. While the total duration of the final FIR filter is 400 s, its effective duration is approximately 150 s. The Doppler shifts

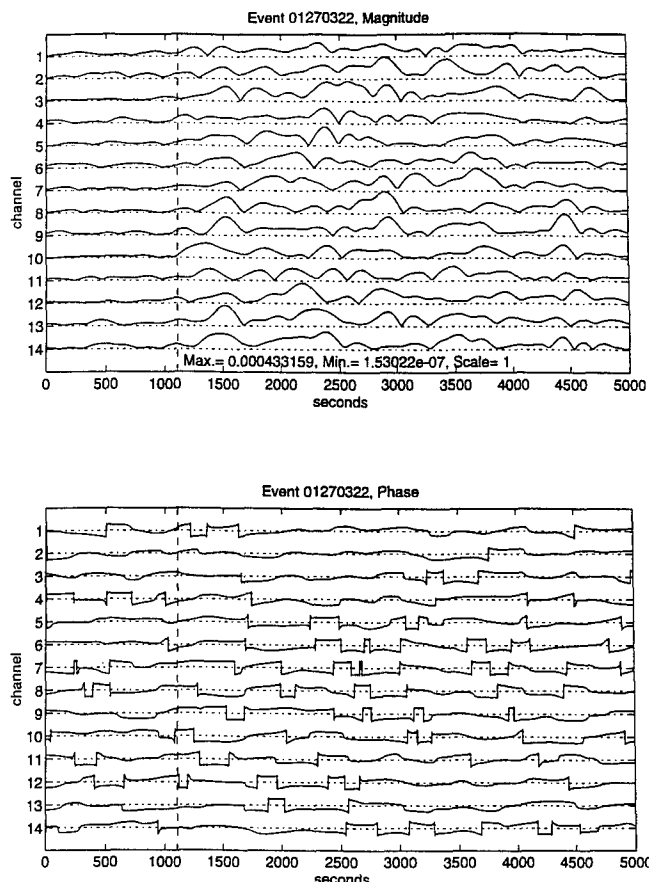


FIG. 7. Magnitude (linear) and phase for the 01270322 data set using the MIT/WHOI signal conditioning. The dotted vertical line indicates the predicted arrival of the signal; the discontinuities in the phase are due to cycle wrap around.

were checked to insure that the measured and estimated shifts were consistent. Table II compares the predicted and measured Doppler shifts. This resulted in a complex, low-pass signal which was the input to the several analyses. Figure 7 illustrates the magnitude and phase time series of the top 14 channels for transmission on 27 January 1991 trans-

TABLE III. Average signal levels in the interval 1500–3000 s for the data in Fig. 7 in dB re: 1 μPa . The transmission loss was computed by using a level of 221 dB based on the table from Birdsall *et al.* (Ref. 2). The levels have a 6-dB correction added to convert from one sided (complex envelope) to two-sided representation (baseband).

| Sensor | Depth (m) | Level dB | TL dB |
|--------|-----------|----------|-------|
| 1 | 345 | 78.9 | 142.1 |
| 2 | 390 | 77.9 | 143.1 |
| 3 | 435 | 81.6 | 139.4 |
| 4 | 480 | 78.0 | 143.0 |
| 5 | 525 | 79.8 | 141.2 |
| 6 | 570 | 78.9 | 142.1 |
| 7 | 615 | 80.0 | 141.0 |
| 8 | 660 | 81.0 | 140.0 |
| 9 | 705 | 79.6 | 141.4 |
| 10 | 750 | 78.5 | 142.5 |
| 11 | 795 | 77.8 | 143.2 |
| 12 | 840 | 78.1 | 142.9 |
| 13 | 885 | 80.1 | 140.9 |
| 14 | 920 | 79.8 | 141.2 |

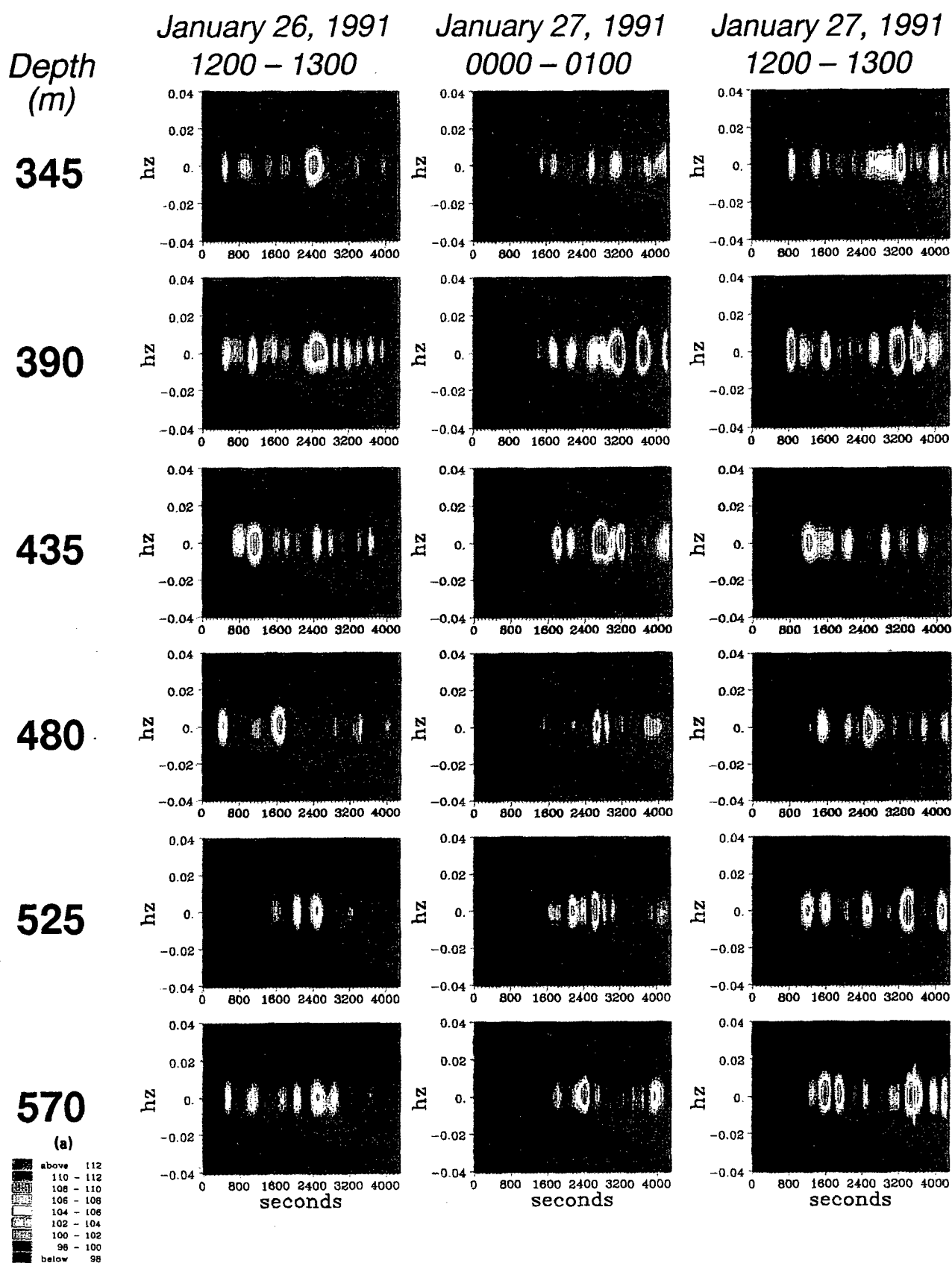


FIG. 8. Sonograms of 21 hydrophones for each of the cw signals on the VLA. Each column is an event, or cw transmission, and each row is a hydrophone. Note the onset of power and the presence of energy on the deeper hydrophones.

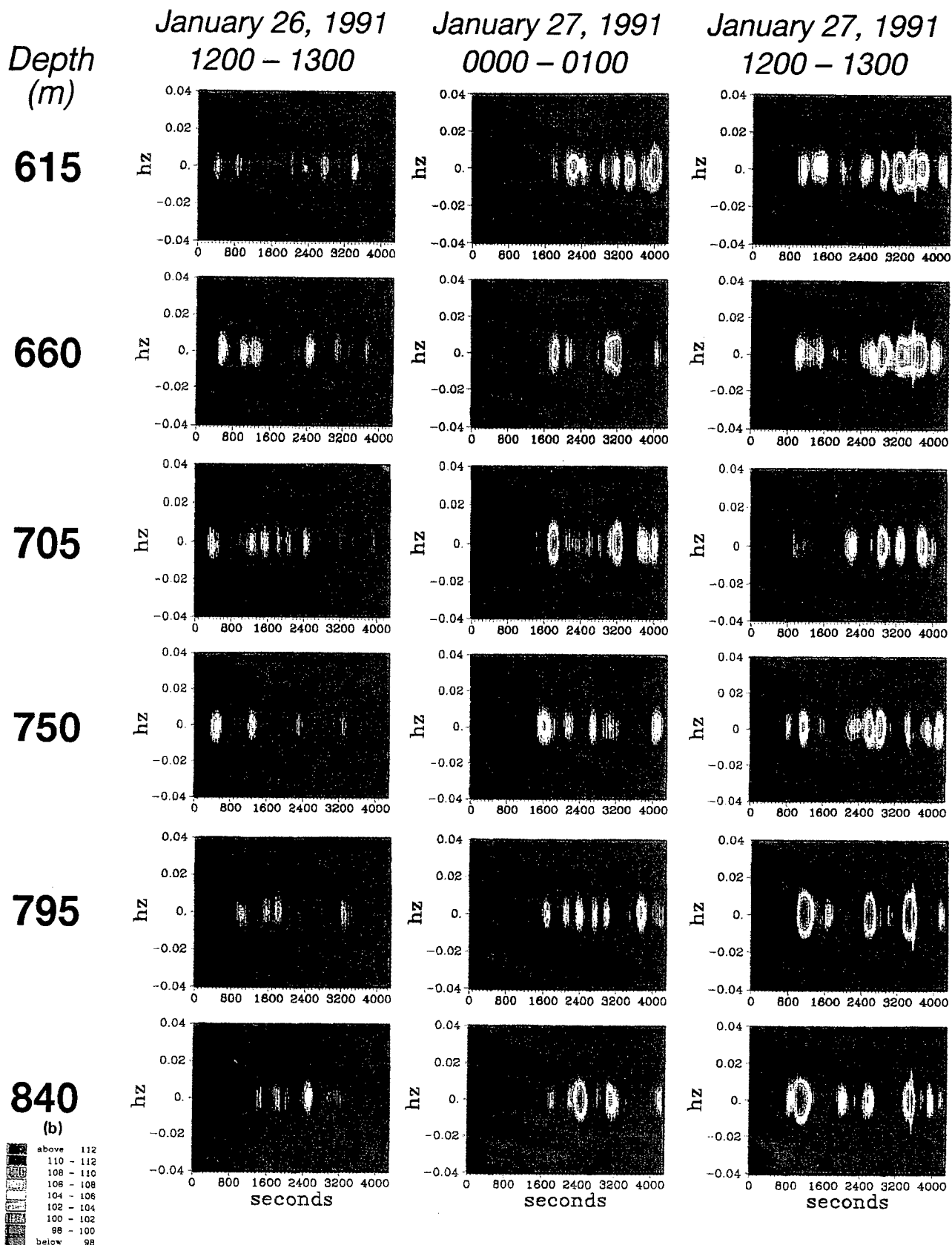


FIG. 8. (Continued.)

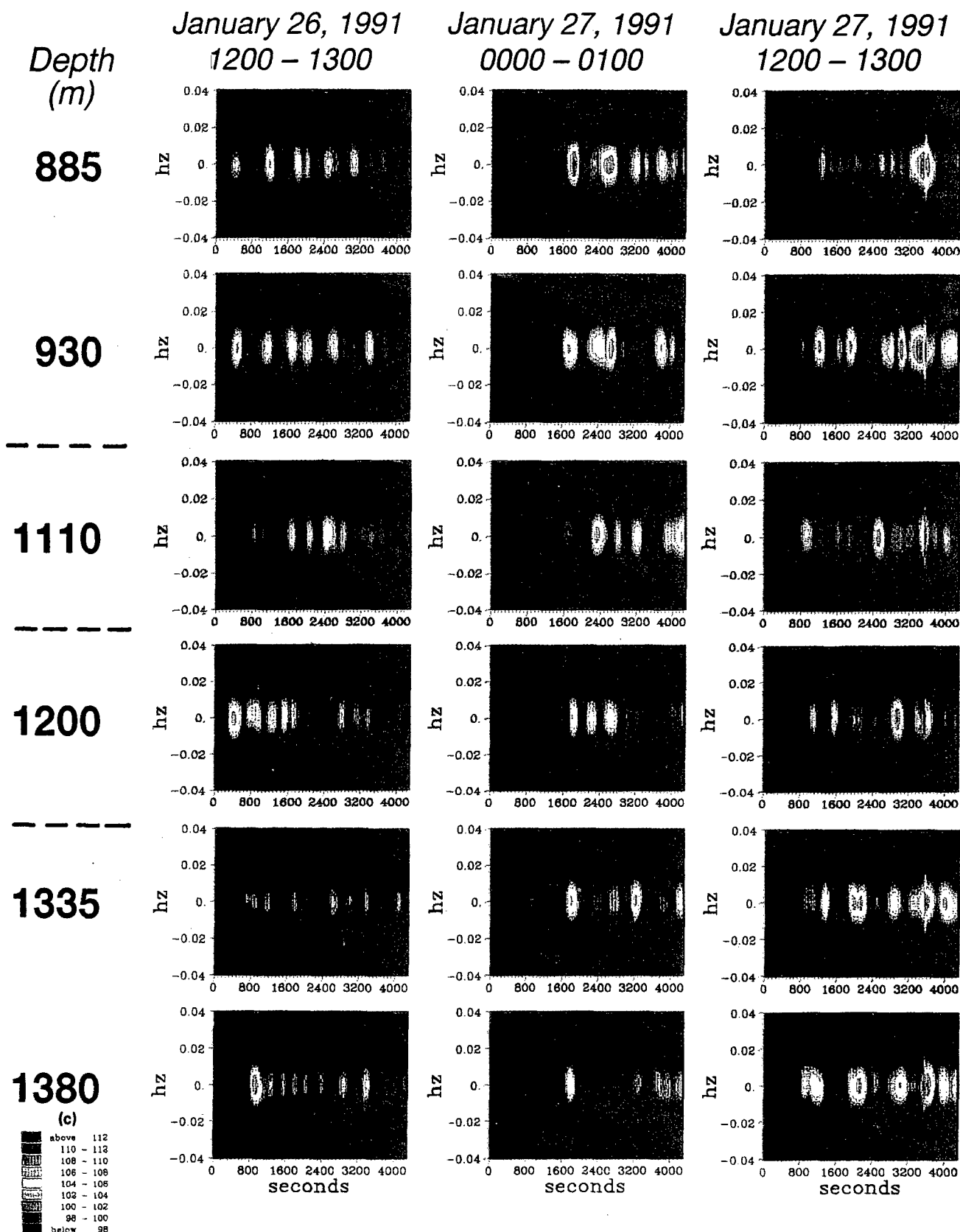


FIG. 8. (Continued.)

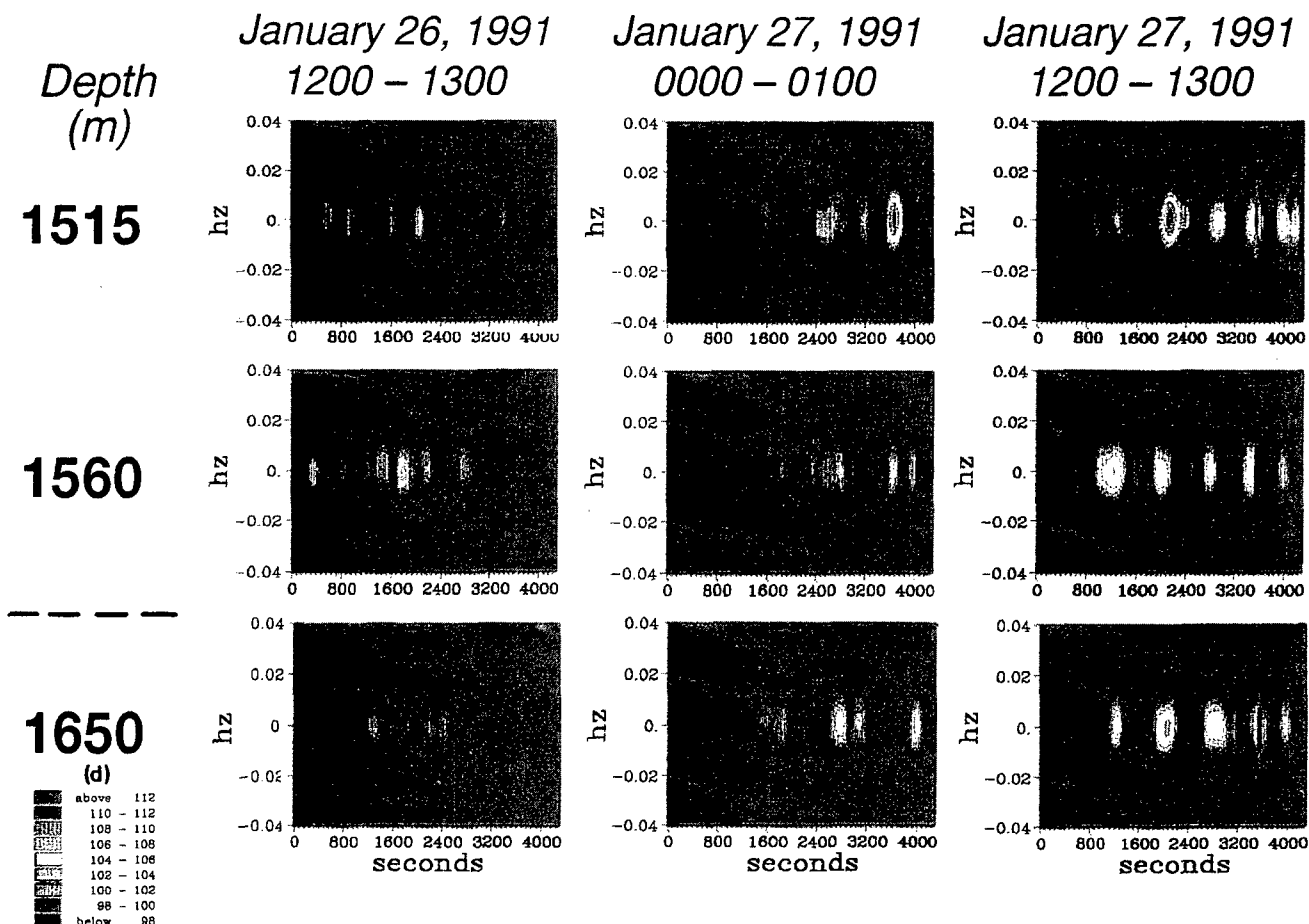


FIG. 8. (Continued.)

mitted at 0000Z and received at 0322Z. Note that the magnitude shows a fair amount of variability among the channels while the phase is much more consistent if one compensates for the wrapping. The fluctuating magnitude makes assigning an output SNR difficult, but a reasonable estimate is around 5–10 dB. The 6-mHz filter provides approximately 22 dB of processing gain, so the input SNR fluctuated between –15 to –10 dB on a single channel on a per-Hertz basis. Table III summarizes the root-mean-square signal level in the interval from 1500–3000 s and provides an estimate of the transmission loss (TL) based upon a 221-dB source level.¹⁰ (In this paper we are using the commonly used definition of transmission loss for a cw signal; in other contexts of the HIFT, e.g., Munk *et al.*,³ Birdsall *et al.*,¹⁰ the authors use the transmission loss per resolvable path or mode because of the need to measure travel times.) While the SOFAR axis is relatively broad, the TLs at the axis near 600 m are not significantly lower. The conditioning for the SAIC frequency-wave-number analysis was similar to that used by MIT/WHOI and is indicated in the center of Fig. 6. There is ± 1 standard deviation clipping, quadrature demodulation with a ± 0.5 -Hz band and downsampling by 100. The NPS/MBARI conditioning is on the right side of Fig. 6 and consisted solely of clipping before the modal beamformer and spectral analysis.

C. Sonograms versus depth

The simplest type of processing is to form sonograms of the data for each hydrophone on all three data sets. This was done using the MIT/WHOI signal conditioning illustrated on the left of Fig. 6. This gives an indication of the power distribution and its variability versus time and depth [Fig. 8(a)–(d)]. The sonograms for each event form a column. The time axis is positioned to the start of the data acquisition and not referenced to specific time. There is also a constant time delay for each event because of signal processing. We were confident of good quality data on 21 of the 32 channels; their depths are noted on left of the figures.

Several observations can be made directly from these sonograms. First, there is significant variability in both time and depth. The signals seem to fade in and out on a time scale consistent with the observations at some of the other sites. More surprisingly, the magnitude does not track consistently versus depth which seems to suggest some type of time-varying interference among several modes. Next, one can observe that power can be detected at even the deepest hydrophones. If one relates this to the depth dependence of the modal amplitudes in Fig. 4, this implies modes 6 or higher were present since lower-order modes do not have significant expression at these deepest hydrophones.

D. Frequency-wavenumber distribution

A frequency versus vertical wavenumber spectrum provides a measure of the vertical distribution of power. It also incorporates the relative phase information among the hydrophones which is not a factor in the sonogram analysis. While the array spanned an extent such that the inhomogeneity of the sound channel was significant and a plane wave analysis implicit in using wavenumbers does not strictly apply, the spectra do suggest the vertical angular distribution of the power. These plots evoke modal description as the interference of a pair of upward and downward going planewaves. For comparison Table I indicates the vertical crossing angle of each mode at the sound channel axis.

The data processing flow for the frequency-wavenumber spectra is shown in the center of Fig. 6. Each spectra used 19 min for each of three different cw time periods and the results are shown in Fig. 9(a)–(c). The intensity is displayed in 1-dB increments. The tilt of the array shifts the center of wavenumber distribution, but it is the *difference* in angles that determines modal correspondence.

The difference in arrival angles between upward- and downward-going angles is 6° for the data from 1527Z Jan 26 (event 01261527) and 0322Z Jan 27 (event 01270322). For the data from 1539Z Jan 27 (event 01271539) there are two

pairs with differences of 7° and 10° . Note that the energy is not uniformly distributed over these spreads but is clumped towards the extremes. This would indicate that energy is more concentrated in discrete rays and at the higher angles, or higher modes. We can attempt to develop a more consistent interpretation of these data by including an assumption about the tilt of the array. As explained in Sec. II the array was instrumented for tilt measurement, however, the compass failed for the direction of tilt so only the maximum apparent tilt is known. In the insets shown in Fig. 9(a)–(c) an array tilt is assumed that is consistent with measured tilts. Nominal tilt magnitudes were 1.0° – 2.5° , so a relative angle of 60° between the average drift direction and the signal direction from Heard Island yields an effective tilt of $\sim 0.5^\circ$ – 1.2° . These assumed tilts are away from the direction of propagation, that is, the bottom of the array is away from Heard Island which is also consistent with the drift track of the R/V POINT SUR with respect to the line of sound from Heard Island.

These tilt assumptions yield consistent pairs of upward- and downward-going arrivals at $\pm 3^\circ$ which correspond to modes 3 and 4 for the data from 1527Z Jan 26 and 0322Z Jan 27. For the data from 1539Z Jan 27 there are an upward- and downward-going pair at $\pm 3.5^\circ$ and another pair at

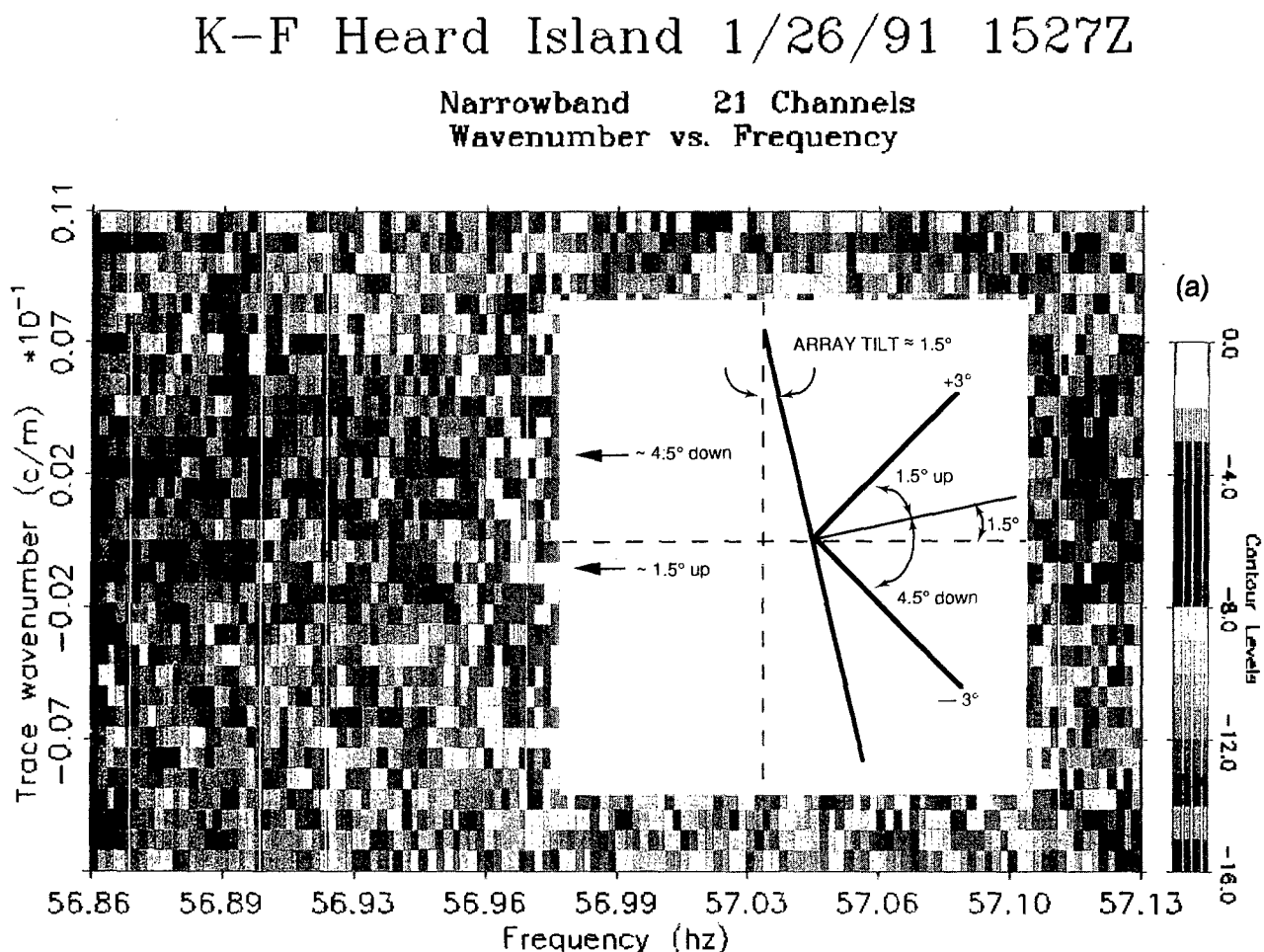


FIG. 9. Frequency-vertical wave-number spectra for each of the cw signals on the VLA. The insets hypothesize a consistent array tilt and the differences in angles suggest the concentration of the higher-order (3–4) modes.

K-F Heard Island 1/27/91 0322Z

Narrowband 23 Channels
Wavenumber vs. Frequency

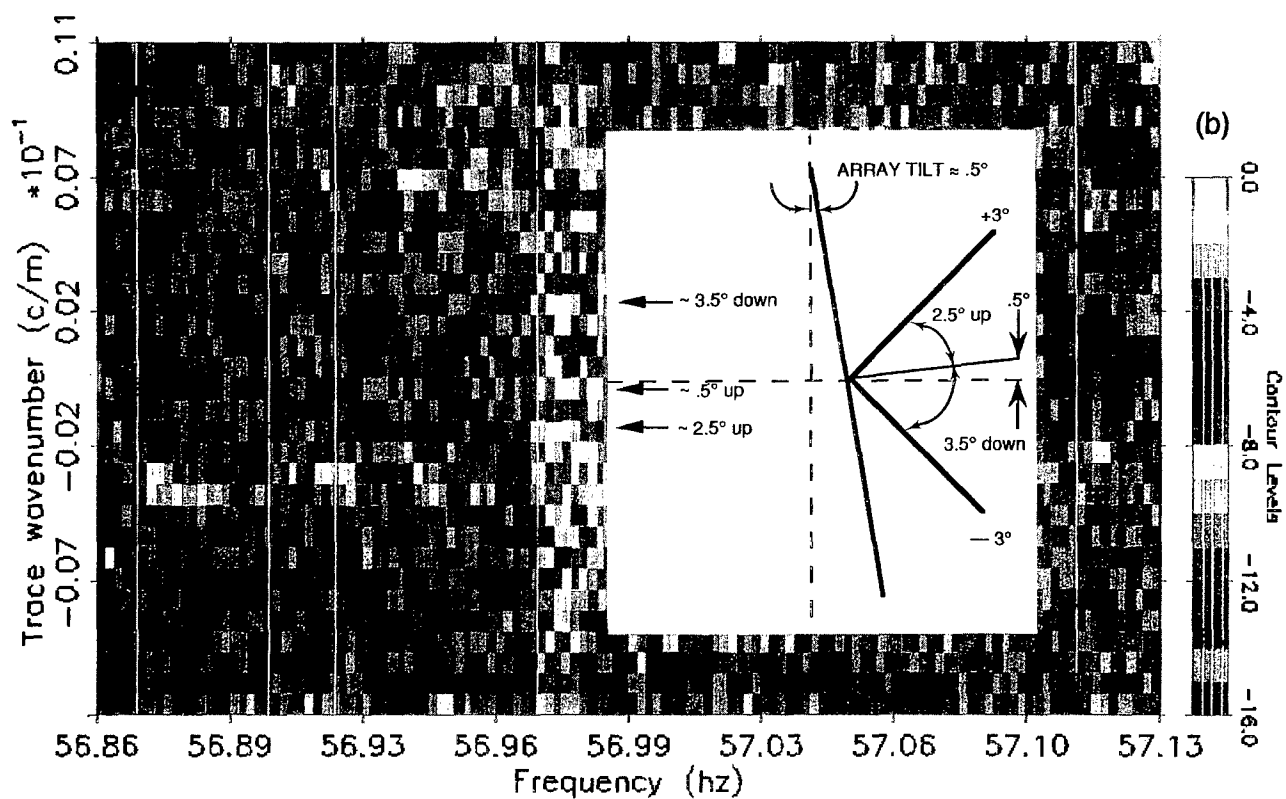


FIG. 9. (Continued.)

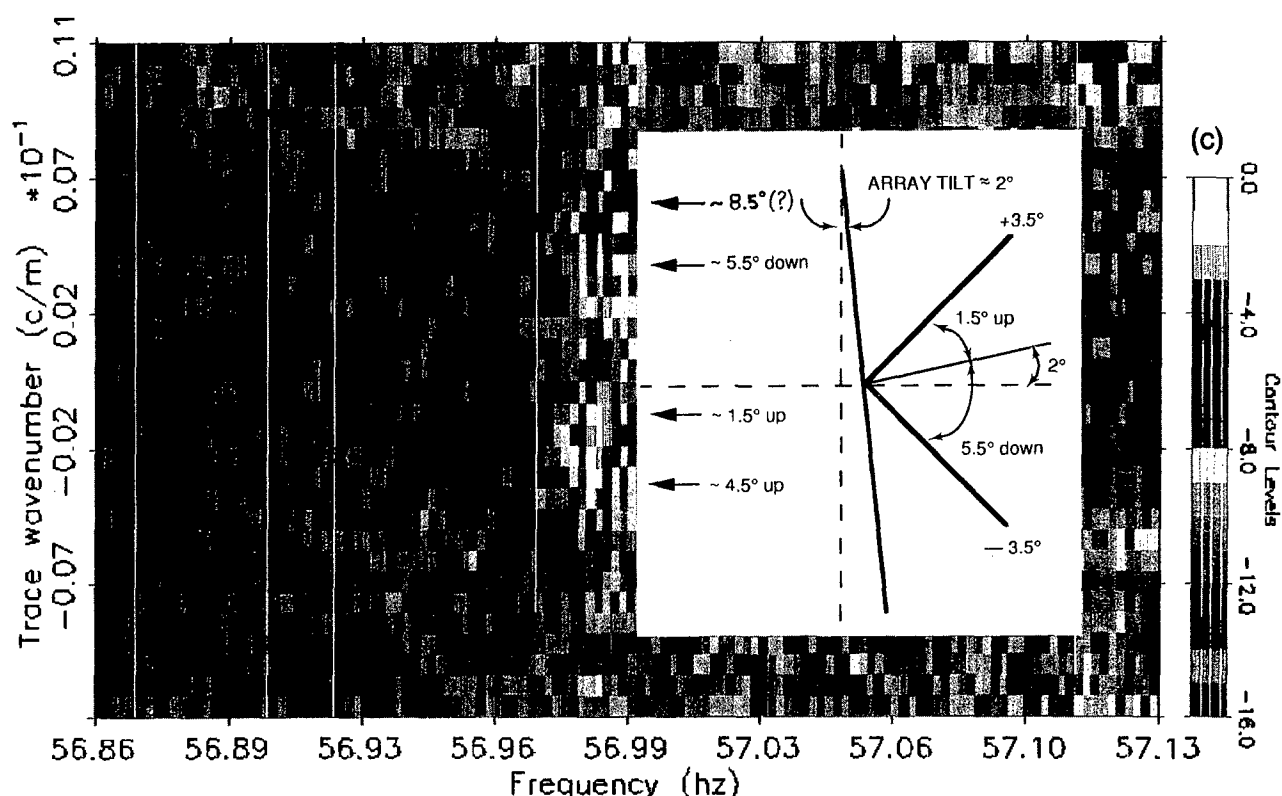
Narrowband 24 Channels
Wavenumber vs. Frequency

FIG. 9. (Continued.)

$\pm 6.5^\circ$. These correspond to modes 4 and 12; however, the arrival at down 8.5° is 3-dB lower than the other peak arrivals. If we ignore this arrival, a tilt of 0.5° towards Heard Island would give an upward and downward pair at $\pm 5^\circ$ which corresponds to mode 7. The sonograms in Fig. 8 for this last event suggest higher signal levels on the deeper hydrophones implying the presence of higher-order modes.

The lack of definitive tilt information is unfortunate, so one must avoid extracting too much detail from these figures. Nevertheless, independent of the tilt assumptions, the fact remains that the data do show discrete ray arrivals at high angles with separations that correspond to maximum modal levels at modes 3 and 4 and the suggestion of up to mode 7 in the energy arriving at the VLA off Monterey from Heard Island.

E. Modal beamforming

Modal beamforming is another array processing method for estimating the modal distribution at a VLA. In this technique one simply forms a linear combination of the data from each channel where the weighting is proportional to the modeshapes. Since the modeshapes are frequency dependent, it is easiest to use a discrete Fourier transform implementation for the array processing. The output for mode m is given by

$$Y_m(f) = \sum_{n=1}^N W_{m,n}(f) X_n(f); \quad (7)$$

the weighting, $W_{m,n}$, is given by

$$W_{m,n} = \frac{\phi_m(Z_n, f)}{\sum_{n=1}^N |\phi_m(Z_n, f)|^2}, \quad (8)$$

where $\phi_m(Z_n, f)$ is the amplitude of the m th mode at depth Z_n [see Eq. (4)]. After modal beamforming a spectral analysis of the beamformed signal, $y_m(t)$, can be done to compare the relative amplitude of the modes.

Modal beamforming was applied to the VLA data of event 01271525 (see Table II).¹⁵ The signal conditioning, which is indicated on the right column of Fig. 6, consisted of clipping to eliminate the effects of the wideband noise transients previously described. A very careful compensation for array depth was done and only the top 15 hydrophones were used to reduce the effects of array tilt. Figure 10 illustrates a spectral analysis of the data which indicates the Heard Island cw signal near 57 Hz using both a single channel and modal beamforming. The upper left panel Fig. 10 indicates the power spectral density of a single phone positioned near the SOFAR axis while the remaining panels are spectral density estimates of beamformer outputs for modes 1–5. The array

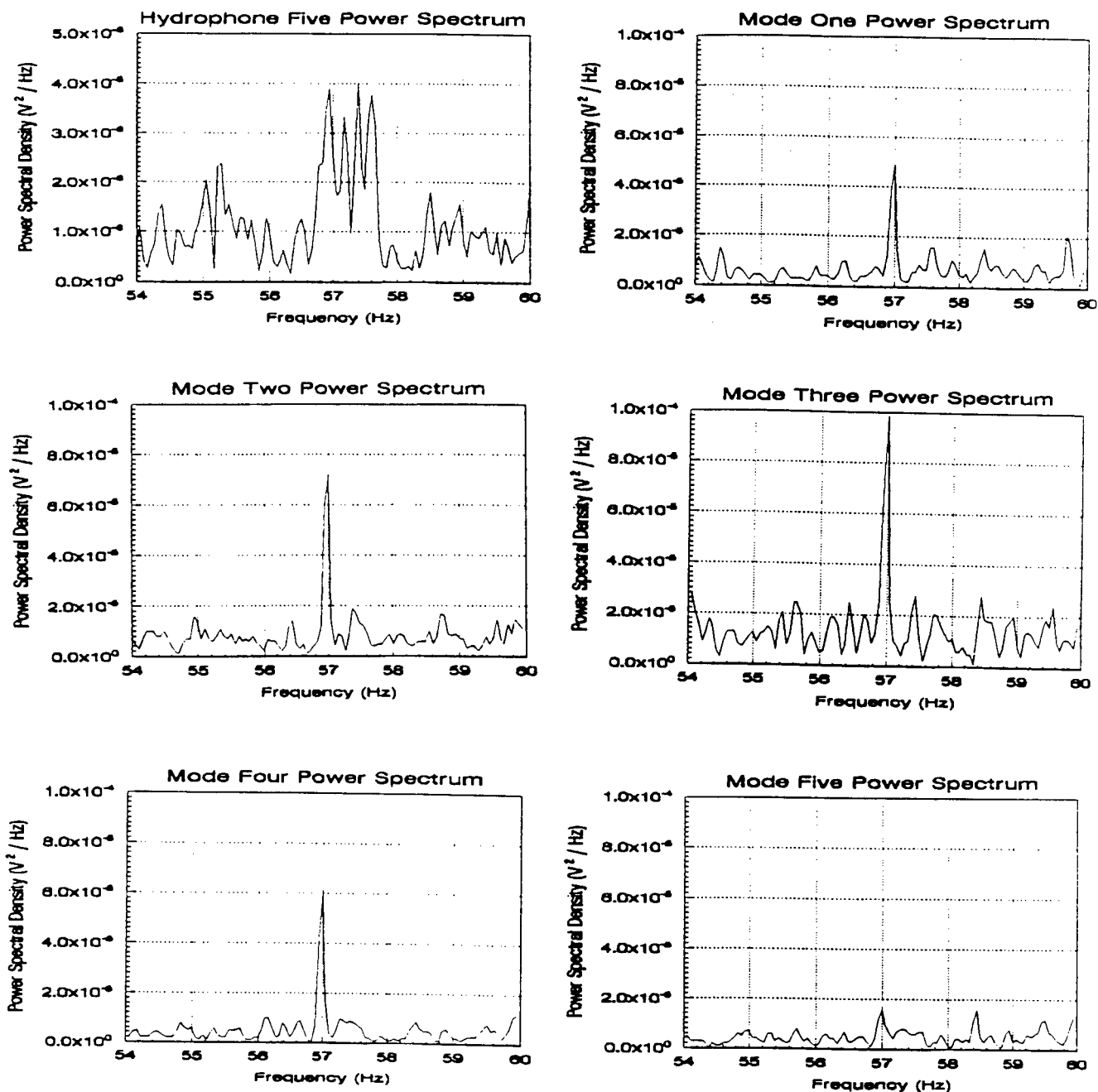


FIG. 10. Comparison of the spectral estimate of a single hydrophone with the spectra of modes 1-5 after modal beamforming.

gain is clearly evident. More importantly, the spectra for mode 3 has a peak level almost 3-dB higher than all the others. This is remarkably consistent with the sonogram and frequency-vertical wave-number analyses.

The aperture of the array was constrained so modal beamforming leads to crosstalk in the estimates for higher-order modes; consequently, beamforming above mode 5 was not attempted.

F. Modal fitting

Modal beamforming is equivalent to matched mode methods in matched-field processing.²⁰ If the array spanned the entire column with a dense sensor spacing, the orthogonality of the modes leads to an ideal separation of the modes.

In practice it does not, so there is cross talk among the modes by what can be considered the modal equivalent of sidelobes.

One way of reducing this is to perform a least-mean fit to the data using the mode shapes as the basis functions. This is done by finding the coefficients $a_i(t)$ which minimize the mean-square error over an interval around t , or minimize $\mathcal{E}(t)$ vs $a_i(t)$ where

$$\mathcal{E}(t) = \frac{1}{\Delta T} \int_{t-\Delta T/2}^{t+\Delta T/2} \sum_{i=1}^M \left| \tilde{r}_i(\tau) - \sum_{j=1}^N a_j(t) \phi_j(Z_i) \right|^2 d\tau, \quad (9)$$

where $\tilde{r}_i(t)$ is the Doppler shifted and tilt corrected complex envelope of the signal at channel i . For a given tilt angle this is a straightforward problem in linear least-squares estima-

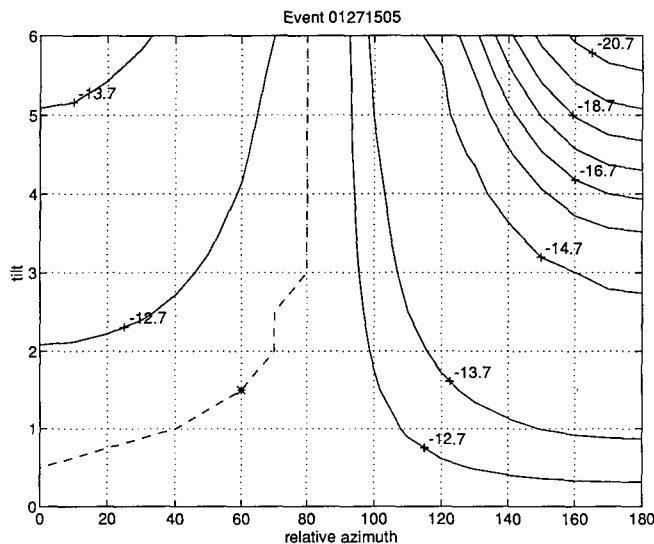


FIG. 11. Fitting error versus array tilt and azimuth. The dotted line is the locus of the best fit on a very broad plateau. The asterisk indicates the nominal tilt from the top tiltmeter.

tion and the solution can be found in many references.²¹ Alternatively, one can view it as a system identification or inverse theory problem and again many references are available.²² The problem as formulated above leads to an unstable solution because the array has a finite number of sensors and does not span the space of the propagating modes. The approach used is to limit the number of modes and add a penalty function on the coefficients $a_i(t)$. This leads to an additional term for $\mathcal{E}(t)$, or

$$\mathcal{E}(t) \rightarrow \mathcal{E}(t) + \epsilon \sum_{j=1}^N |a_j(t)|^2. \quad (10)$$

In estimation theory this is a standard approach which goes under several guises including stabilization, desensitizing and diagonal loading to name a few. The solution for the $a_i(t)$ is given by

$$\mathbf{a}(t) = [\Phi + \epsilon \mathbf{I}]^{-1} \mathbf{R}(t), \quad (11)$$

where the elements of Φ and $\mathbf{R}(t)$ are given by

$$\Phi_{k,l} = \sum_{i=1}^M \phi_k(Z_i) \phi_l(Z_i),$$

$$\mathbf{R}_k(t) = \sum_{i=1}^M \int_{t-\Delta T/2}^{t+\Delta T/2} \tilde{r}(\tau) d\tau \phi_k(Z_i).$$

The solution can be determined using the matrix inverse directly or using a singular value decomposition. Intuitively, Φ represents the cross coupling among the modes and $\mathbf{R}(t)$ the projection of the average value of the complex envelope within the fitting interval on the modes. The factor ϵ mitigates the effects of small eigenvalues in the inversion. For the final fit we actually performed a search over tilt angles to minimize an average of \mathcal{E} .

The tradeoffs for the VLA data concerned the choice of the averaging interval, ΔT , and the number modes, N , in the

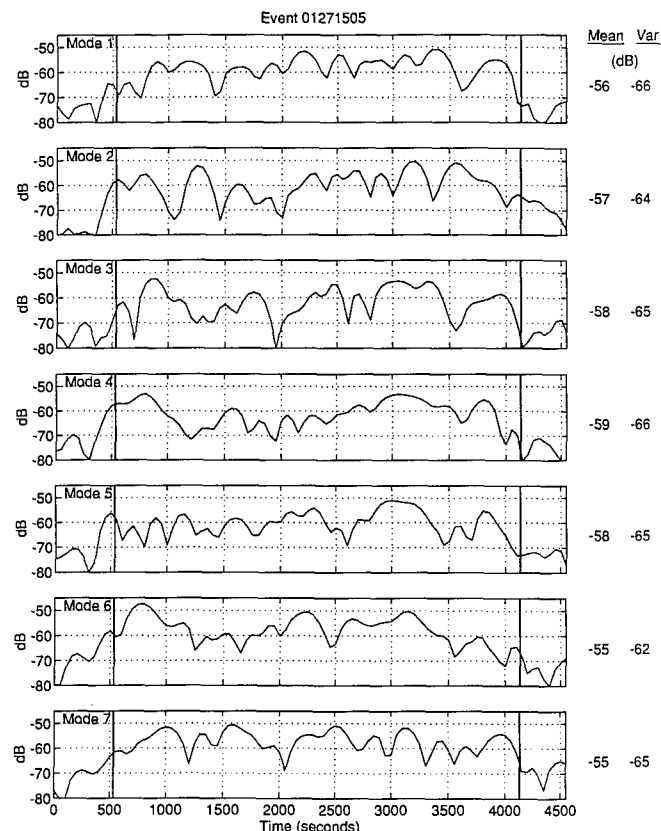


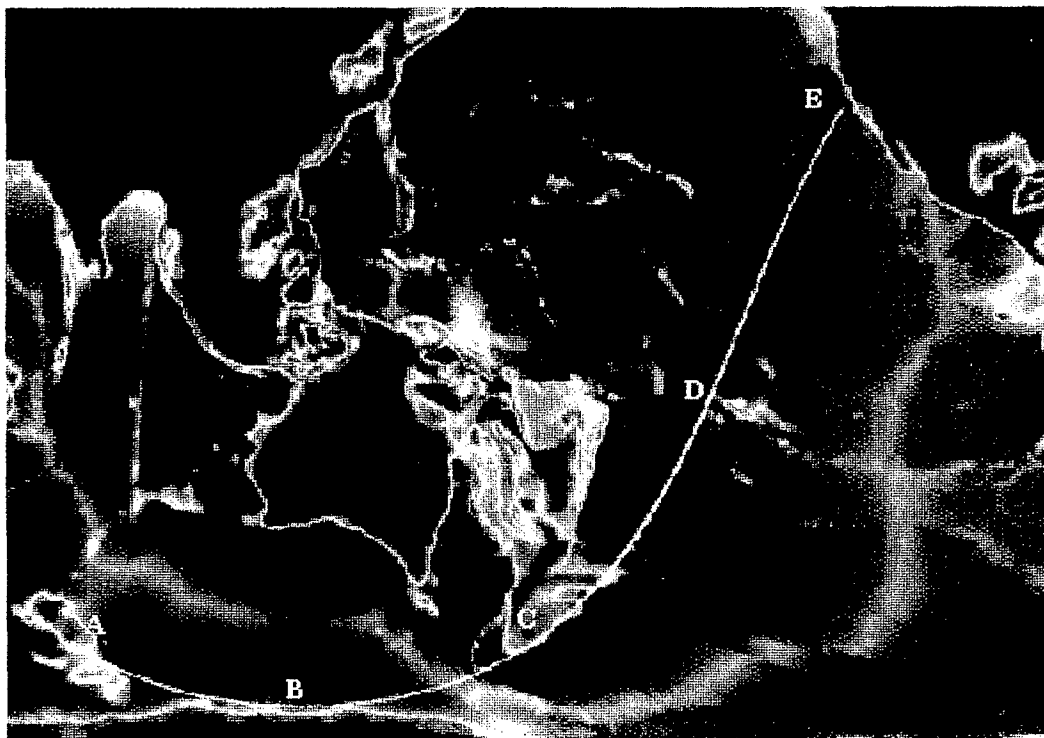
FIG. 12. Modal amplitude coefficients for a time varying least-squares fit of the data from the three cw events. The vertical lines indicate the data reception level; the numbers on the left side are $20 \log_{10}$ (mean) and $10 \log_{10}$ (variance of the envelope expressed). (Processing gains need to be included to convert to dB re: 1 V.)

fitting. The time varying character of the complex envelope permitted just a short averaging time. The mode fitting depends upon both amplitude and phase so the amplitude fluctuations were problematic. We used a 200-s averaging time which was consistent with the bandwidths of the FIR filters in the signal conditioning. The number of modes is largely determined by the number channels. The number of degrees of freedom in the fitting must be constrained, otherwise any data set can be represented with nonphysical results. We felt very confident about the top 14 channels and used 7 modes to keep the number of degrees of freedom in the fit constrained. This reduced the mode shape orthogonality to the point where crosstalk above modes 6 and 7 precluded estimating any signal there and a relatively large value of 25% diagonal loading was used to keep nearly singular eigenvalues from dominating the estimate.

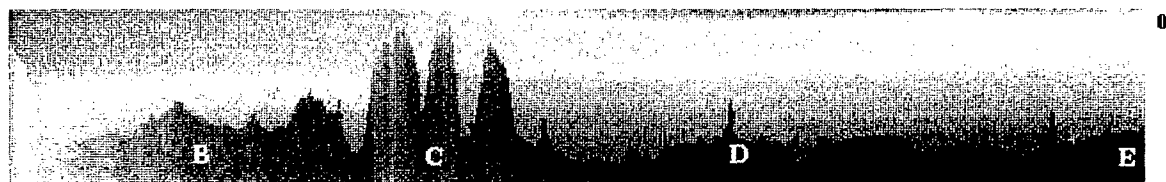
Since the adjusted mode shapes, $\phi_i(Z_i)$, reflect the array orientation, the mean fit could be scanned over a range of tilts and azimuths. The inference is that the best fit yields an estimate of the actual array orientation. An example of such a sweep is shown in Fig. 11 for event 01271505. The dashed line indicates the best fit for each tilt angle; the array azimuth was estimated to be $\approx 60^\circ$ which is consistent with the ship's drift.

Figure 12 illustrates the modal fit amplitudes, $a_i(t)$, for the same event. Vertical lines indicate the predicted arrival

Mode 1 Path



Mode 1 Path PE TL



Modal Excitation vs Range

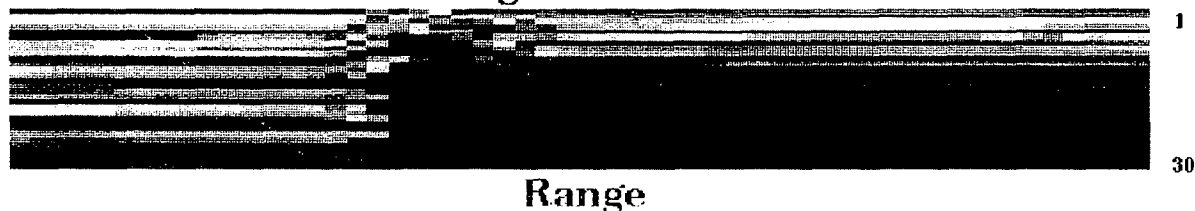


FIG. 13. Parabolic equation solution for the path from Heard Island to the VLA [from McDonald, *et al.* (Ref. 14)]. The geodesic is at the top, the magnitude of the PE solution in the middle and the projection on the local modes at the bottom. Note that the Antarctic Convergence Zone and the bathymetry near "C" cuts out the very high order modes and repopulates them into a distribution consistent with the modes observed at the VLA.

time based on the modeling by Chiu *et al.*¹¹ An increase in the modal amplitudes is apparent at the onset of the signal, but the highly fluctuating levels makes it difficult to assign a definite ranking. Averages and standard deviations over the arrival duration are noted at the right. Modes 6 and 7 show the highest energy and are consistent with the frequency-wave-number and sonogram analysis that higher-order mode energy is present. If the 1.5° up arrival in the $\omega-k$ is interpreted to be energy from modes 1 and 2, which it could using an effective tilt of 1° , this would also agree with the least squares fitting. Such comparisons should not be taken too far given the uncertainties in array geometries and low SNRs.

Event 01261525 indicated a strong mode 3 presence as well as energy in higher order modes. Event 01270322 was less clear, possibly due to the higher level of array motion as recorded on the depth sensors.

VI. DATA INTERPRETATION AND SUMMARY

We have performed four analyses of the VLA receptions of the Heard Island signals. All four suggest the presence of higher order modes. The frequency-vertical wave-number analysis and the modal beamforming indicate that mode 3 has the highest amplitude while the modal fitting suggests

that modes 5 and 6 are largest. It is difficult to resolve the differences since the SNR at the VLA, nearly 18 000 km away with a transmission loss of approximately 140 dB, is quite low. Individual arrivals could not be distinguished because of the long integration time necessitated by the low SNR.

The results are, nevertheless, consistent with the modeling done by McDonald *et al.*,² for the propagation from Heard Island to the VLA site. Figure 13 indicates this. The top of Fig. 13 is the refracted geodesic for mode 1 from Heard Island to Monterey. (The geodesics for the higher modes do not differ by much.) The middle illustrates the solution of a wide angle parabolic equation (PE) starting at the source depth and location near Heard Island. One can see the solution appears to be nearly adiabatic except near the point designated "C." The bottom part of the figure is the result of projecting the PE solution on range dependent modes 1–30 along the geodesic. The projections suggest a large number of modes present up to "C"; then there is significant attenuation by the blockage and nonadiabatic conversion of the surface modes to ducted modes. From "C" to "E" the signal propagates adiabatically. While it is difficult to discern, the model suggests that modes 5 and 6 are most energetic. Nevertheless, the PE solution incorporated only very long wavelength environmental changes, so it does not incorporate modal scattering due to shorter scales of environmental variability such as internal waves.

The engineering of the VLA was also instructive. The failure of the sensors for monitoring array shape and heading complicated the signal processing. While we knew a tethered deployment would be tricky, it was not as much of a problem as anticipated once we developed the procedure for prepositioning the array, carefully backing down on it when it came under tension and monitoring its response via the depth sensor. We certainly were favored by calm seas for most of the experiment.

The most important conclusion is that the vertical distribution of energy for signals which propagated nearly antipodal distances around the Earth is more complicated than predicted and much needs to be learned for future efforts involving such long range propagation.

ACKNOWLEDGMENTS

The Vertical Line Array effort for the Heard Island Feasibility Test was supported by the Monterey Bay Aquarium Research Institute (MBARI), the Department of Energy (DOE, Grant DE-FG0291ER61100), the Naval Postgraduate School (NPS) and Science Applications International Corporation (SAIC). The authors wish to thank the officers and

crew of the R/V POINT SUR for their help with a complicated deployment of the VLA. We also want to thank E. Scheer (WHOI), D. Gever (SAIC), L. Ehret (NPS), G. Frogner (NPS) and S. Crocker (NPS) for their assistance in the data analysis. This is contribution number 8326 of the WHOI.

- ¹W. H. Munk, W. C. O'Reilly, and J. L. Reid, "Australia-Bermuda sound transmission experiment (1960) revisited," *J. Phys. Oceanogr.* **18**(12), 1876–1898 (1988).
- ²B. E. McDonald, W. A. Kuperman, and K. D. Heaney, "Horizontal multipath in transoceanic propagation: Model results and data," *J. Acoust. Soc. Am.* **96**, 2357–2370 (1994).
- ³W. H. Munk, R. C. Spindel, A. B. Baggeroer, and T. G. Birdsall, "The Heard Island Feasibility Test," *J. Acoust. Soc. Am.* **96**, 2330–2342 (1994).
- ⁴L. Brekovskikh and Y. Lysansov, *Fundamental of Ocean Acoustics* (Springer-Verlag, New York, 1982).
- ⁵Y. Desaubies, C. S. Chiu, and J. H. Miller, "Acoustic mode propagation in a range dependent ocean," *J. Acoust. Soc. Am.* **80**, 1148–1160 (1986).
- ⁶R. Evans, "The decoupling of stepwise coupled modes," *J. Acoust. Soc. Am.* **80**, 1414–1419 (1986).
- ⁷T. R. Cummings, "Strumming: keeping cable quiet," *Sea Technol.* **32**(7), 29–31 (July 1991).
- ⁸K. von der Heydt, "An optical disk based data acquisition system (ODAS)," Woods Hole Oceanographic Institution Technical Report Number 91-14 (June 1991).
- ⁹"Bermuda Global Warming Array Recovery Report," SAIC Report No. R92-92 (February 1992).
- ¹⁰T. G. Birdsall, K. Metzger, and M. A. Dzieciuch, "HIFT signals, signal processing, and general results," *J. Acoust. Soc. Am.* **96**, 2343–2352 (1994).
- ¹¹C.-S. Chiu, A. J. Semtner, C. M. Ort, J. H. Miller, and L. L. Ehret, "A ray variability analysis of sound transmission from Heard Island to California," *J. Acoust. Soc. Am.* **96**, 2380–2388 (1994).
- ¹²R. M. Jones, J. P. Riley, and T. M. Georges, "Harpo—A versatile three-dimensional Hamiltonian ray tracing program for acoustic waves in an ocean with irregular bottom," NOAA Wave Propagation Laboratory Report (October 1986).
- ¹³A. J. Semtner and R. M. Chervin, "A simulation of the global ocean circulation with resolved eddies," *J. Geophys. Res.* **93**(C12), 15,502–15,522 and 15,767–15,775 (1988).
- ¹⁴S. Levitus, "Climatological atlas of the world ocean," NOAA Prof. Paper 13, pp. 173, U.S. Government Printing Office, Washington, DC (1982).
- ¹⁵S. E. Crocker, "Time domain modal beamforming for a near vertical acoustic array," M.S. thesis, Naval Postgraduate School (December 1991).
- ¹⁶J. H. Miller, Naval Postgraduate School, personal communication on DANES noise predictions (July 1990).
- ¹⁷W. Renner (personal communication, July 1990).
- ¹⁸J. H. Miller, Naval Postgraduate School, Report on noise trials of the R/V Point Sur (August 1990).
- ¹⁹G. J. Heard and N. R. Chapman, "The Heard Island Feasibility trial: Analysis of Pacific path data obtained with a horizontal line array," *J. Acoust. Soc. Am.* **96**, 2389–2394 (1994).
- ²⁰A. B. Baggeroer and W. A. Kuperman, "Matched field processing in ocean acoustics," in *Acoustic Signal Processing for Ocean Exploration*, edited by J. M. F. Moura and I. M. G. Loutrie (Kluwer, Dordrecht, The Netherlands, 1993).
- ²¹C. L. Lawson and R. J. Hanson, *Solving Least Squares Problems* (Prentice-Hall, New York, 1974).
- ²²W. Menke, *Geophysical Data Analysis: Discrete Inverse Theory* (2nd edition) (Academic, New York, 1984).

Differential Doppler as a Diagnostic

Matthew Dzieciuch and Walter Munk

Scripps Institute of Oceanography, University of California, San Diego, La Jolla, California 92093

(Received 19 August 1992; accepted for publication 7 June 1994)

Differential Doppler compression and travel time of individual peaks in the arrival sequence (relative to an overall average) are measured for the 5500-km acoustic transmissions from a moving source at Heard Island to Christmas (Crab) Island. The differentials cannot be explained by simple adiabatic propagation models. A hybrid theory, coupling polar and temperate models at the Antarctic Front, can account for some of the qualitative features. Differential Doppler could be a useful tool for identifying ray arrivals.

PACS numbers: 43.30.Qd, 43.30.Es, 43.60.Rw

INTRODUCTION

We have measured the travel time and Doppler frequency shift of acoustic transmissions from a moving source at Heard Island to a receiver at Christmas (Crab) Island. At any one time, different ray arrivals have different Dopplers, and different rates of change of travel time with clock time. This paper is an attempt to exploit these measured differentials as an aid to sort out the rather complex arrival pattern.

This paper develops as follows. First we look at the transmission path. There are two essential features: (i) a plunge of the sound channel axis at a range of about 1000 km, separating a polar sound channel (with RSR ray propagation, the lower turning point is refracted and the upper turning point is surface reflected) from a temperate sound channel (RR, upper and lower turning points refracted), and (ii) a bottom ridge extending upward to the axis at about 3000 km range. A detailed look at the receiver records shows rather surprising variations in differential Doppler and travel time. Some simple short-range Arctic data are then examined for illustration of the phenomenon of interest. Next we compute the expected pattern for a polar sound channel only, and for a temperate sound channel only. These two simple propagation models are inadequate to account for the observed pattern. It is found that by combining the two models with the novel use of a ray angle-depth diagram drawn at the location of the Antarctic Circumpolar Front, some qualitative agreement can be achieved. Finally we consider the effect of a "knife-edge" bottom ridge.

This is one of three papers dealing with Heard Island Dopplers. Dzieciuch *et al.*¹ are concerned with slight fluctuations of *overall* Doppler during the transmission hour. These Doppler fluctuations are the result of the source ship not traveling with precisely uniform velocity, and are in close agreement with GPS derived fluctuations in source velocity. We believe that most of this fluctuation has to do with medium variability, such as surface currents associated with internal waves. A paper by Forbes and Munk² uses the *overall* Doppler, averaged over the transmission hour for each of 16 transmissions, to estimate the launch azimuth of the ray path from Heard Island to Ascension Island. Good agreement is obtained with the geodetically computed azimuth. The vertical tilt of the ray paths is ignored. Both of these papers are concerned only with overall Doppler, which is an average

over the entire arrival pattern. In the present paper, we are concerned only with the difference between this overall average and the Doppler of individual arrivals.

I. THE RECORD AT CHRISTMAS (CRAB) ISLAND

The source ship CORY CHOUEST was located about 5500 km from the sonobuoy receiver. Figure 1 shows the bathymetry of the transmission path and a plan view of the experiment. An M-sequence was transmitted with a carrier frequency $f_c = 57$ Hz and a period $T = 44 + 47/57$ s exactly. (See Birdsall *et al.*³ for a detailed description.) For the data under discussion, the source ship was moving away from the receiver at a range-rate $V = 1.733$ m/s. The Doppler shift of the carrier was estimated using spectral analysis. The 1-h reception was then processed using a constant overall Doppler compression

$$\alpha^* = 1 + \Delta f/f_c = 1 - V/C, \quad (1)$$

where Δf is the estimated Doppler shift, $V = dr/dt$ is the ship's mean opening velocity (the component along the path in the direction away from the receiver), and $C = 1453.0$ m/s is the speed of sound at the source. The location of the moving source differed by 6.5 km between start and end of the hour-long transmission. This introduces some added complexities into the analysis, but it also provides some Doppler information that may be useful. The purpose of this paper is to exploit this information.

The germane data are summarized in Table I. The CORY CHOUEST speed and course were taken from GPS measurements aboard the vessel. The azimuth to the receiver at the source is obtained from constructing refracted geodesics (Heaney *et al.*⁴). The sound speed C , at the depth of the source was measured daily. All these values are believed to be accurate to three significant figures. The expected Doppler based on the navigational and geodetic measurement is then $\alpha^* - 1 = -V/C = -0.00119$. The overall Doppler, measured acoustically at the receiver is $\Delta f/f_c = -0.00120$. The difference is not significant; it could, for example, be the result of a 1-cm/s drift of the receiver away from the source. We interpret this result to mean that we cannot distinguish the reference ray tilt from 0° , but it can be anywhere between ± 0.1 radians. What *can* be measured is the *differential* Doppler between individual rays and the reference ray.

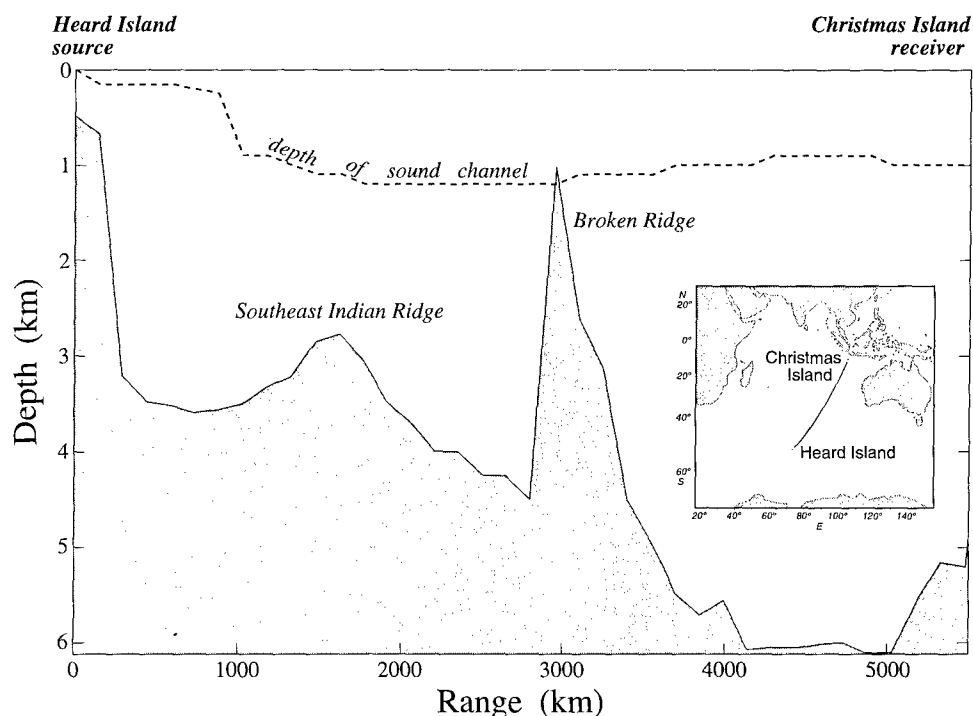


FIG. 1. Plan view and bathymetry of the Heard-Christmas transmission path. The depth of the sound channel minimum is shown as dotted line. Inset map shows locations of Heard and Christmas Islands.

Figure 2 (bottom) shows the amplitude pattern (the square root of the incoherent sum of energy) for each of the 80 periods³ during a 1-h transmission. This is one of our best records. It shows a series of ridges, some lasting as long as 20 min (27 sequence periods). The pattern is well above the ambient noise level as shown by comparison with the 10 min preceding and following the signal. The record shows an arrival pattern lasting for about 6 s. There is a traditional SOFAR crescendo and sharp final cutoff typical of deep-water sound propagation.

The top of Fig. 2 shows the same data plotted in a different manner. The lower presentation ignores the phase information of the complex demodulation. At the top we have plotted the relative phase (referred to an overall phase) along the amplitude ridges using a "color wheel." Relative phase of ridge n is determined for each period of 44.82 s; its time rate of change is given by

$$\delta\dot{\phi}_n(t) = 2\pi f_c(\alpha_n - \alpha^*), \quad (2)$$

TABLE I. Transmission parameters.

| | |
|---------------------------------|------------------------|
| Receiver location | Christmas Island |
| Heard Island transmission start | 1991 January 27:0900 |
| Geodetic range r | 5497 km |
| Travel time t | 3716 s |
| Speed of CORY CHOUET | 1.81 m/s |
| Course of CORY CHOUET | 238.66° true |
| Azimuth of receiver at source | 41.92° true |
| Range rate $V = dr/dt$ | 1.733 m/s |
| Sound speed at source | 1.453 km/s |
| V/C (from GPS) | 1.19×10^{-3} |
| $\Delta f/f$ (from Doppler) | -1.20×10^{-3} |

where the $\delta\dot{\phi}_n \equiv d(\delta\phi)/dt$ signifies the phase rate along ridge n relative to the overall phase rate $2\pi f_c \alpha^*$. When the exact Doppler compression is used, the phase is constant. Thus the variations of phase can be used as a measure of differential Doppler.

We note from Fig. 2 that phase and travel time rates have no simple dependence on the arrival sequence, and that tracks start and stop during the hour. We shall try to account for these observed features. It is helpful, for illustration purposes, to first discuss these differential quantities for some Arctic measurements taken under the simplest possible conditions.

II. A SIMPLE DEMONSTRATION

For orientation we first take an isovelocity sound channel with rays bouncing between surface and bottom (Fig. 3). Let $n=0,1,2,\dots$ be the number of cycles ($n=2$ for the example in Fig. 3). Thus

$$r = 2nR \quad \tau = 2nL/C \quad (3)$$

are range and travel time, respectively, where

$$L = \sqrt{R^2 + H^2}. \quad (4)$$

Multiplying both sides of Eq. (4) by $2n/C$

$$\tau_n(t) = (1/C)[r(t)^2 + (2nH)^2]^{1/2} \quad (5)$$

and

$$\dot{\tau}_n(t) = \frac{d\tau_n}{dr} \frac{dr}{dt} = \frac{V}{C} \left[1 + \left(\frac{2nH}{r(t)} \right)^2 \right]^{-1/2}, \quad (6)$$

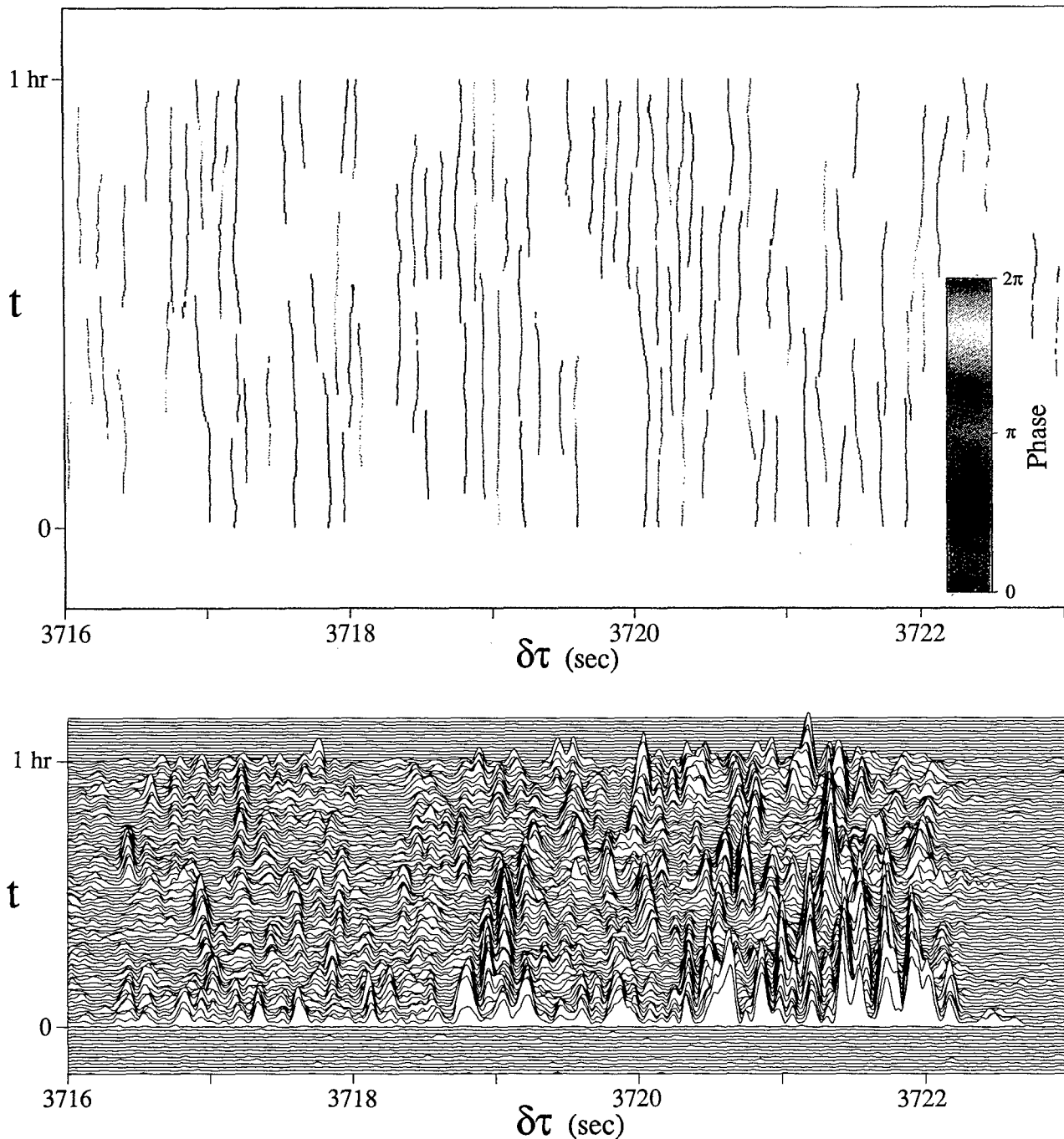


FIG. 2. Adjusted travel time $\delta\tau$ vs clock time t at Christmas Island. Top shows magnitude squared, complex demodulated pressure. Bottom shows phase of tracked peaks.

where $V = dr/dt$ is the ship's speed projected along the ray path away from the receiver, and C is the (uniform) sound speed. Thus if

$$r(t) = r_0 + Vt \quad (7)$$

it follows that

$$\dot{\tau}_n(t) = (V/C) \cos \theta_n, \quad (8)$$

where $\theta_n(t) = \arctan[H/R_n(t)]$ is the glancing angle of ray n . Accordingly, θ_n increases and $\dot{\tau}_n(t)$ decreases with increasing n .

We select some prominent reference ray n^* with travel time $\tau^*(t)$ and make a transformation such that $\dot{\tau}^*(0) = 0$. The adjusted quantities are

$$\delta\tau_n(t) = \tau_n(t) - \dot{\tau}^*(0)t \quad (9)$$

and

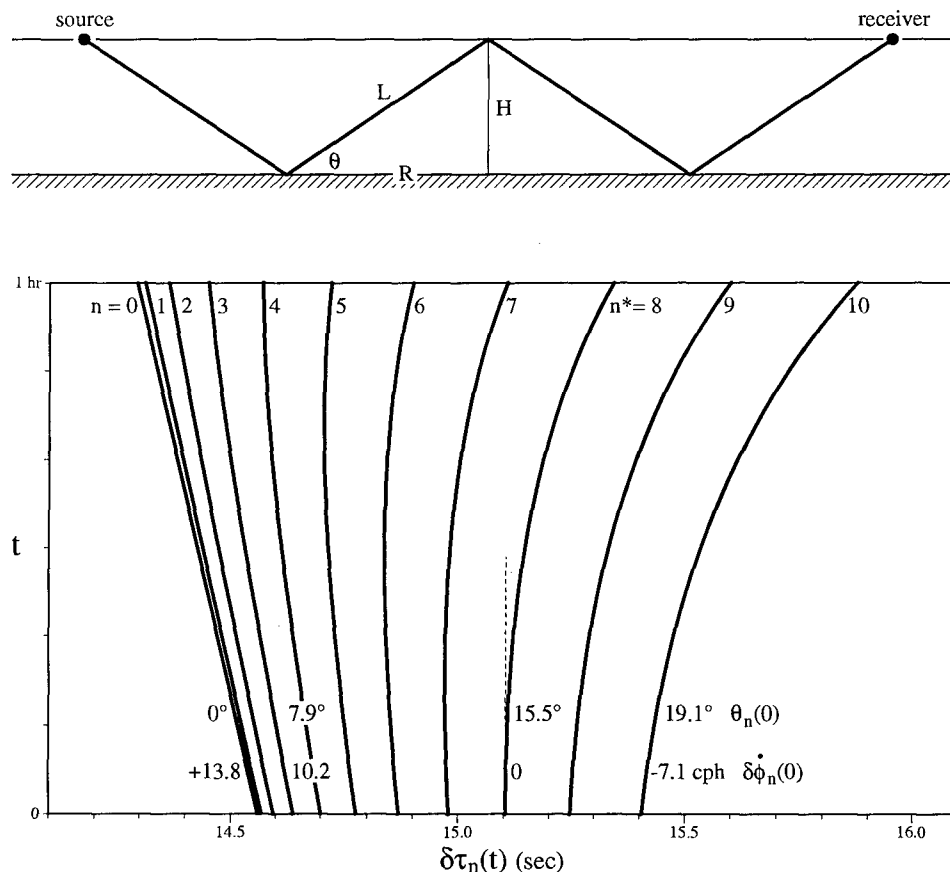


FIG. 3. Arctic transmission: computed adjusted travel times $\delta\tau_n(t)$ as a function of clock time t for rays $n=0, 1, \dots, 10$ relative to $n^*=8$. Initial range $r_0=21.4$ km, $H=0.37$ km, $C=1.47$ km/s, ship speed $V=-3$ m/s (towards receiver), $f_c=52$ Hz. $\theta_n(0)$ are the initial ray inclinations, and $\delta\phi_n(0)$ are the relative initial phase rates in cycles per hour (cph). Note that $\delta\tau_8(t)$ is stationary as $t \rightarrow 0$. The parameters are chosen to correspond roughly to the measurements shown in Fig. 4.

$$\delta\dot{\tau}_n(t) = \dot{\tau}_n(t) - \dot{\tau}^*(0). \quad (10)$$

The signal is complex demodulated so that each peak has an associated phase $\phi_n(t)$, so defined that $\phi_n(t) = 2\pi f_c \alpha_n(t)$, and

$$\begin{aligned} \delta\dot{\phi}_n(t) &= 2\pi f_c [\alpha_n(t) - \alpha^*] \\ &= -2\pi f_c (V/C) [\cos \theta_n(t) - \cos \theta^*]. \end{aligned} \quad (11)$$

where θ^* is the reference ray angle at the source. The phase rate thus depends only on the ray angle at the source. Comparing Eqs. (8), (10), and (11), a consistency check

$$\delta\dot{\phi}(c/h) = -f_c(\text{Hz}) \delta\dot{\tau}(s/h), \quad (12)$$

can be used with this simple model. Here $\dot{\phi}$ is in cycles per hour (c/h) and $\dot{\tau}$ in seconds per hour (s/h). For a full discussion we refer to Chap. IX of Morse and Ingard.⁵

We can test these formulas against some Arctic short-range measurements (not Heard Island) in shallow water under essentially constant C conditions. A bottom-based receiver recorded transmissions from a towed low-frequency source.⁶ During 1 h of transmission the range changed appreciably from $r_0=21.4$ km to $r=10.6$ km and this accounts for the strongly curved $\delta\tau_n(t)$ lines. The comparison between measured and computed $\delta\tau_n(t)$ is generally favorable (Figs. 3 and 4, and Table II). Measured $\delta\tau_n(t)$ are split into pairs corresponding to up- and down-going ray paths from a sub-

merged source at 60-m depth. An M-sequence signal as in the Heard Island Feasibility Test (HIFT) was used to resolve ray paths (frequency was 52 Hz compared to HIFT 57 Hz). All results are referred to $n^*=8$ and accordingly $\tau_8(t)$ approaches a constant as $t \rightarrow 0$. For the model, $\delta\phi_n = -52 \delta\tau_n$ as required by Eq. (12). The measured values are in rough accord with model values. We have the following general rule:

For a *closing* course (negative V) flat rays have the largest *positive* Doppler Δf , and the largest *positive* phase rate $\dot{\phi}_n$, hence the largest *negative* rate of change of arrival time $\dot{\tau}_n$. For an *opening* course, replace *positive* by *negative*, and *vice-versa*.

III. A DIFFERENTIAL PLOT FOR THE HEARD ISLAND TRANSMISSION

It was hoped that the relatively simple results for the Arctic transmission could serve as a guide for interpreting the Heard Island results. A comparison of Figs. 2 and 4 shows that the two cases are very different. There are many more arrivals for the Heard Island transmission. The fractional change in range is very small (5000-km versus 20-km ranges), hence the inclination of the arrivals is too small to be easily measured.

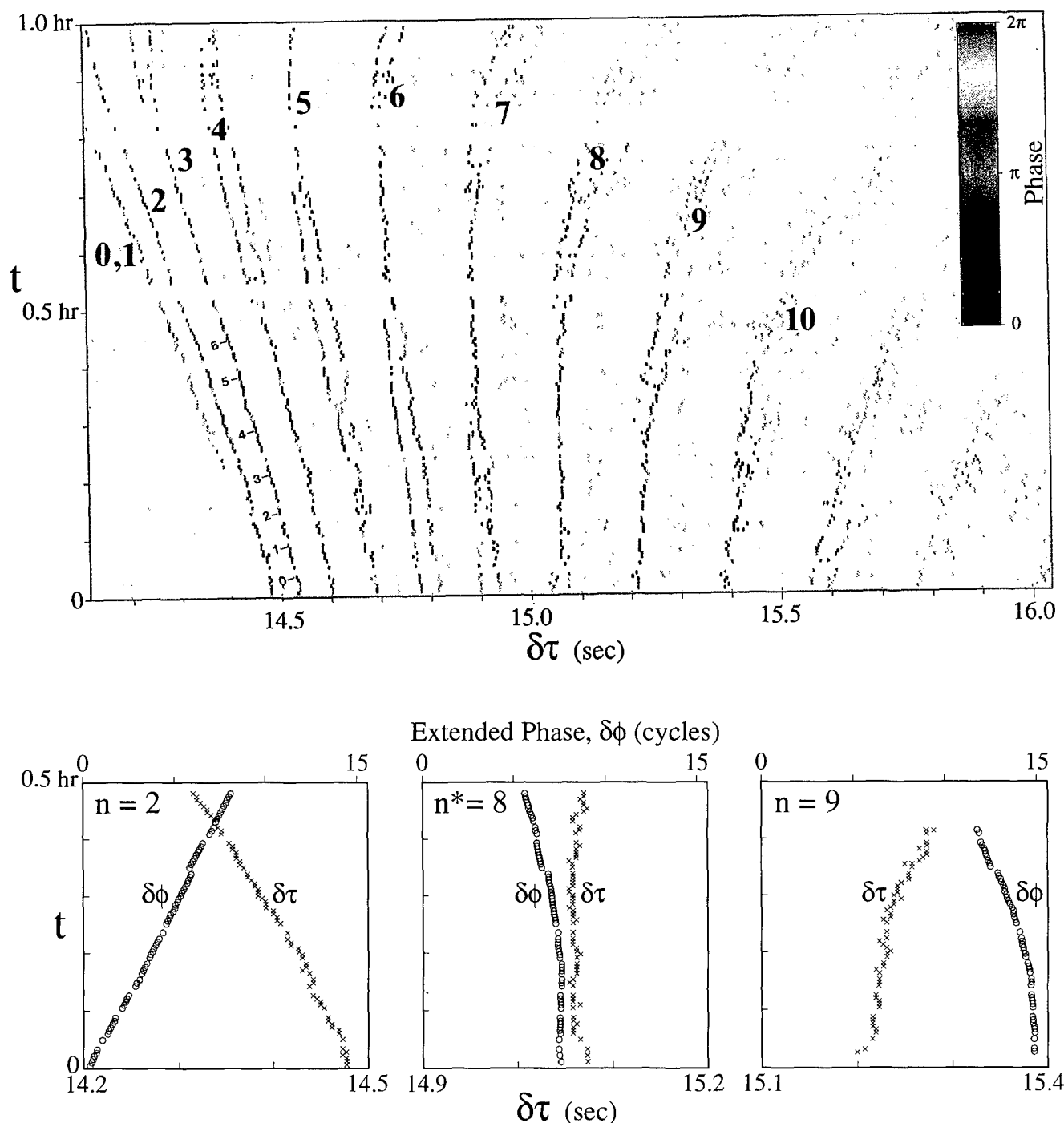


FIG. 4. Measured arrivals for Arctic transmission. All arrival peaks lying 8 dB above median intensity are plotted as a function of clock time. The attempted ray identification is shown (rays 0 and 1 are not resolved). The relative phase is color coded. For ray 3 the change in phase $\phi(t)$ is indicated (0, 1, 2 corresponding to $0, 2\pi, 4\pi$ radians). $\delta\phi_n$ is positive for $n < 8$ and negative for $n > 8$, as expected.

For comparison we have plotted the measured Heard Island differentials for some selected arrivals on a magnified scale (Fig. 5). There is no longer a simple relation between $\delta\tau(t)$ and $\delta\phi(t)$, the magnitudes are different and the changes are not monotonic with arrival time (note the opposite signs of $\delta\phi$ for two successive arrivals 41.1 and 41.6 s). In the following, we interpret some of these features in terms of propagation models.

IV. DISPERSION IN A SOUND CHANNEL

In the preceding Arctic example, sound speed was taken as constant, and the dispersal was entirely the result of reflection of rays from the boundaries. This may be a good model for shallow water propagation at high latitudes. We now consider the case of deep water, with the vertical sound-speed gradient playing the vital role.

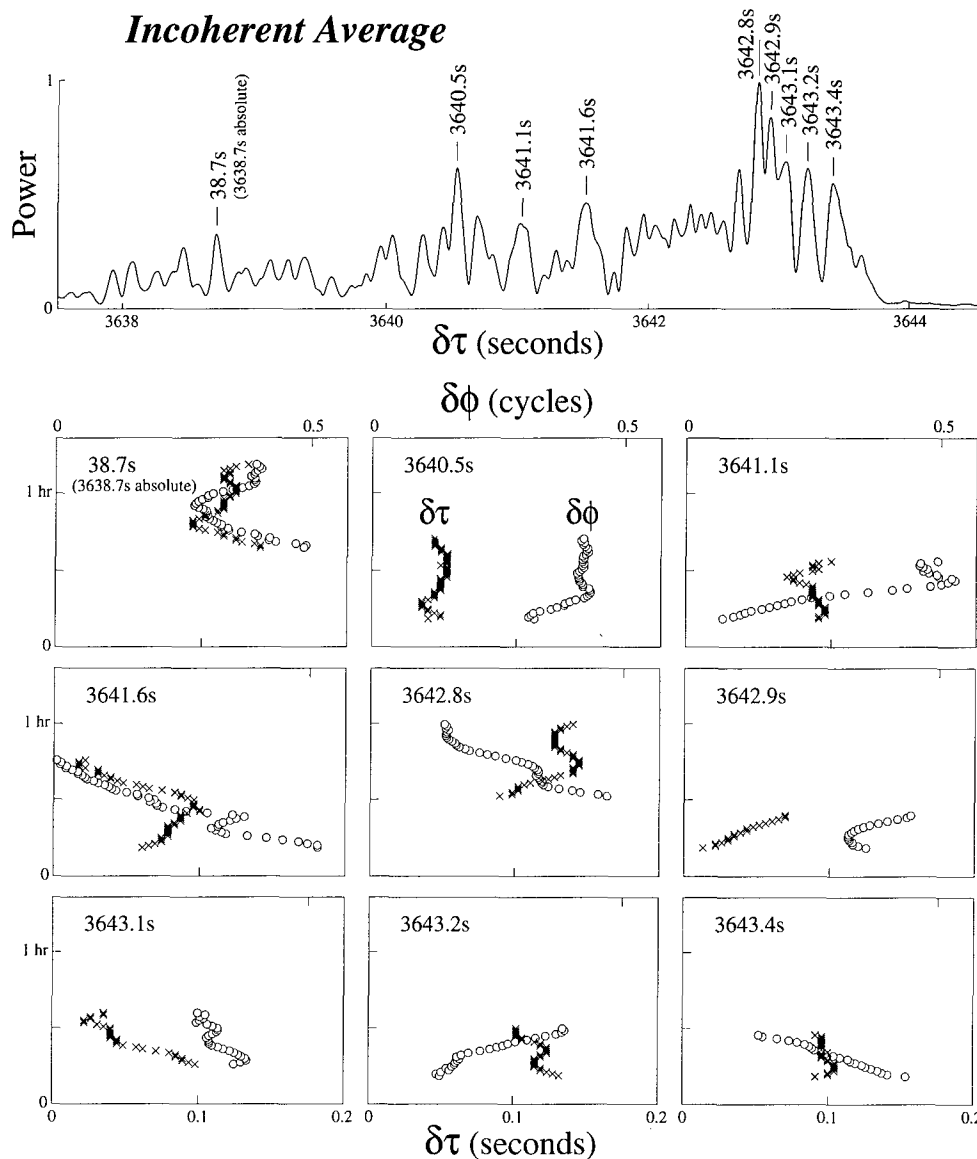


FIG. 5. Christmas Island reception. The measured $\delta\tau(t)$, (x), and $\delta\phi(t)$, (O), are shown for nine selected peaks in the arrival pattern.

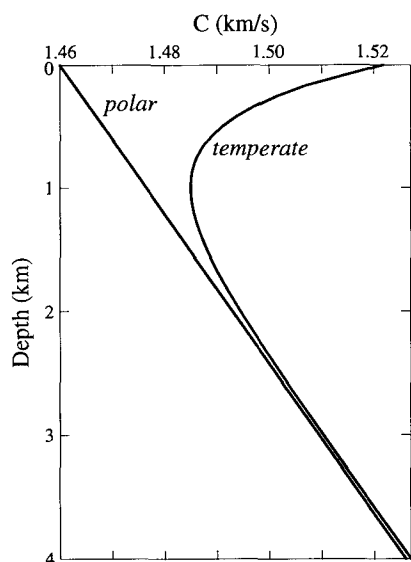


FIG. 6. Models for a polar and a temperate sound-speed profile. Model parameters are $C_0=1.46$ km/s, $C^{-1}dC/dz=\gamma_{\text{adiabatic}}=0.0113$ km $^{-1}$ for the polar ocean, $C_{\text{axial}}=1.485$ km/s for the temperate ocean.

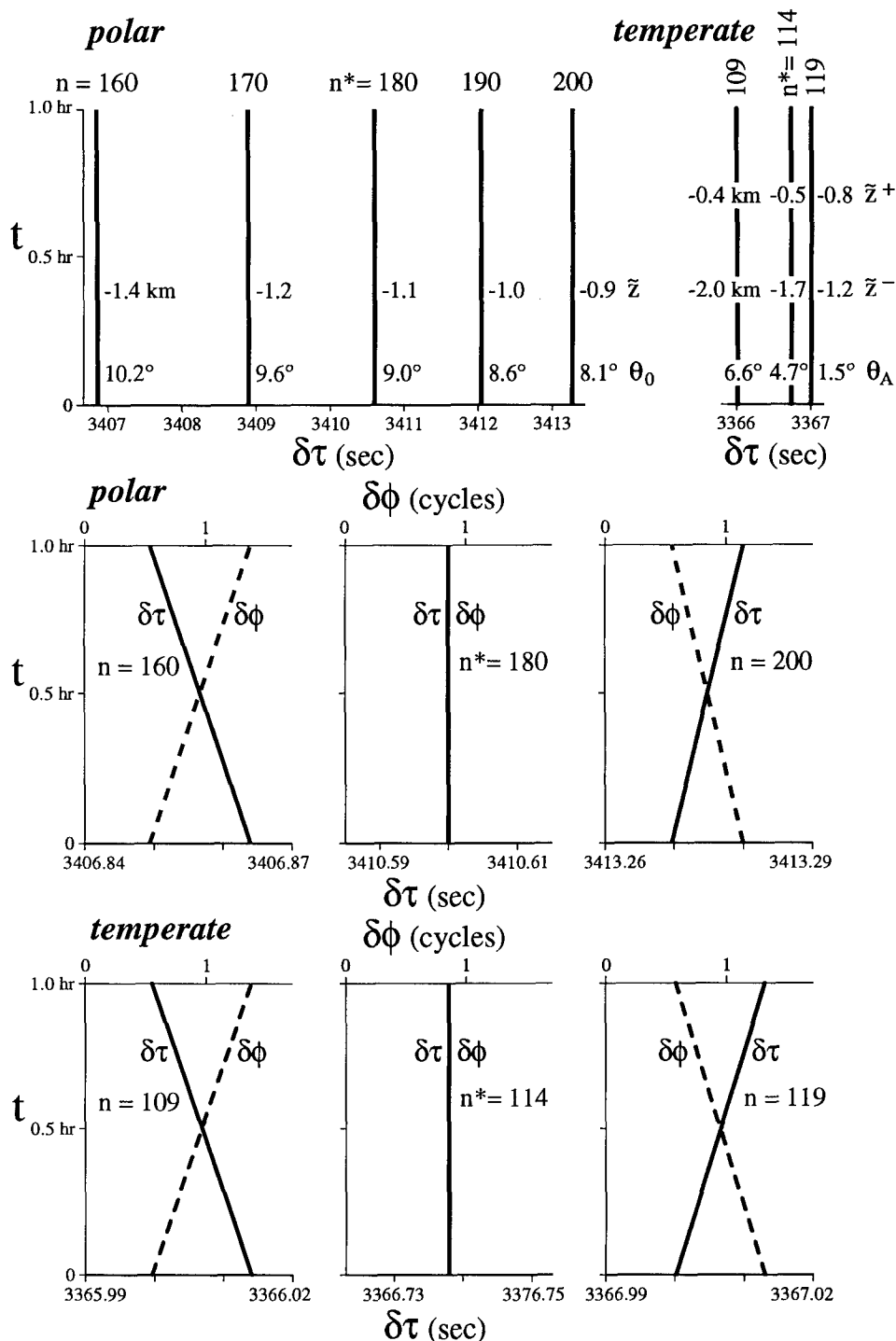


FIG. 7. Adjusted travel times $\delta\tau_n(t)$, for the polar and temperate sound-speed profiles, respectively. For both cases, $r_0=5000$ km, $f=57$ Hz, and $V=1.798$ m/s (opening course). Arrivals are dispersed over 6 s for the polar profile, and over only 1 s for the temperate profile. Upper and lower turning depths and ray tilts are indicated for selected ray numbers n . Lower plots show $\delta\tau_n(t)$ and $\delta\phi_n(t)$ on an expanded scale.

In HIFT, the propagation was complicated by the presence of the Antarctic convergence, marking the transition from a polar ocean to a temperate ocean across a localized front (Fig. 1). First we consider two separate models of sound-speed profiles (Fig. 6): (i) a “polar duct” with upward ray refraction and surface reflection (RSR) and (ii) a “temperate” sound channel with upward ray refraction beneath the sound axis and downward ray refraction above (RR). In both cases the flat rays (axial rays) come in *last*, which is

typical in SOFAR propagation. (The dispersal is opposite to that of the previous case where the flat rays come in first.)

It follows from ray theory that

$$\tau_n = r s_{g,n}(r) \quad \frac{d\tau_n}{dr} = s_{p,n}(r), \quad (13)$$

where s_g and s_p are the group and phase slowness, respectively. Hence

TABLE II. Adjusted Doppler parameters at $t=0$ for Arctic transmission (closing course).

| n | 0 | 2 | 3 | 4 | 6 | $n^*=8$ | 9 | 10 |
|---------------------|-------|-------|-------|-------|-------|---------|-------|-------|
| From model | | | | | | | | |
| $\tau_n(s)$ | 14.56 | 14.59 | 14.64 | 14.70 | 14.87 | 15.10 | 15.25 | 15.40 |
| θ_n | 0.0° | 4.0° | 5.9° | 7.9° | 11.7° | 15.5° | 17.3° | 19.1° |
| $\delta\phi_n(c/h)$ | 13.8 | 12.9 | 11.8 | 10.2 | 5.9 | 0.0 | -3.4 | -7.1 |
| $\delta\tau_n(s/h)$ | -0.27 | -0.25 | -0.23 | -0.20 | -0.11 | 0.0 | 0.07 | 0.14 |
| From measurements | | | | | | | | |
| $\delta\phi_n(c/h)$ | | 14.0 | 13.0 | 12.0 | 6.4 | 0.0 | -8.6 | |
| $\delta\tau_n(s/h)$ | | -0.35 | -0.34 | -0.28 | -0.16 | 0.0 | 0.18 | |

$$\dot{\tau}_n = \frac{d\tau_n}{dt} = V s_{g,n}, \quad (14)$$

where $V=dr/dt$. (For the case under consideration we consider such large ranges r that $\delta r/r$ is negligible for a 1-h transmission, and hence $\dot{\tau}_n(t)$ is sensibly constant with time.) In general $s_{p,n}=\tilde{S}_n$, where $S(\tilde{z})\equiv\tilde{S}$ is the sound slowness at the ray turning depth \tilde{z} : the phase slowness equals the sound slowness at the turning point. There is no corresponding simple expression for s_g , and we need to go to specific sound-speed models.

V. MODELS OF POLAR AND TEMPERATE SOUND CHANNELS

As a model of a high latitude sound channel we take the case of sound speed increasing adiabatically downward (slowness increasing upward):

$$S=S_0(1+\gamma_a z), \quad \gamma_a=0.013 \text{ km}^{-1}, \quad (15)$$

(z is positive upward). Let n be the number of loops. For this model of constant dC/dz , rays are arcs of a circle⁷ and

$$\tilde{z}_n = -r^2 \gamma_a / 8n^2 \quad (16)$$

is the lower turning depth. The ray inclination θ_n at the surface boundary is given by

$$\sin \theta_n \equiv \tilde{\sigma}_n = r \gamma_a / 2n, \quad \tilde{\sigma}^2 = (S_0^2 - \tilde{S}^2) / S_0^2 \quad (17)$$

under oceanic conditions $\tilde{\sigma} \ll 1$. From Eq. (15)

$$s_{p,n} = \tilde{S}_n = S_0(1 + \gamma_a \tilde{z}_n) = S_0(1 - \frac{1}{2} \tilde{\sigma}_n^2) \quad (18)$$

it can be shown that

$$s_{g,n} \approx S_0(1 - \frac{1}{6} \tilde{\sigma}_n^2) \quad (19)$$

and accordingly

TABLE III. Heard Island to Christmas Island, $r_0=5000$ km, $f_c=57$ Hz, $C_0=1.46$ km/s, $C_A=1.485$ km/s. Range is opening at $V=1.798$ m/s.

| n | Polar sound channel | | | Temperate sound channel | | |
|--------------------|---------------------|-----------|--------|-------------------------|-----------|--------|
| | 160 | $n^*=180$ | 200 | 109 | $n^*=114$ | 119 |
| $\tilde{z}^+(km)$ | | | | -0.38 | -0.54 | -0.83 |
| $\tilde{z}^-(km)$ | -1.38 | -1.09 | -0.88 | -2.01 | -1.66 | -1.19 |
| θ | 10.1° | 9.8° | 8.1° | 6.6° | 4.7° | 1.5° |
| $\tau(s)$ | 3406.9 | 3410.6 | 3413.3 | 3366.0 | 3366.7 | 3367.0 |
| $\delta\phi(c/h)$ | 0.83 | 0.0 | -0.59 | 0.81 | 0.0 | -0.74 |
| $\delta\tau(ms/h)$ | -14.0 | 0.0 | 10.0 | -14.0 | 0.0 | 13.0 |

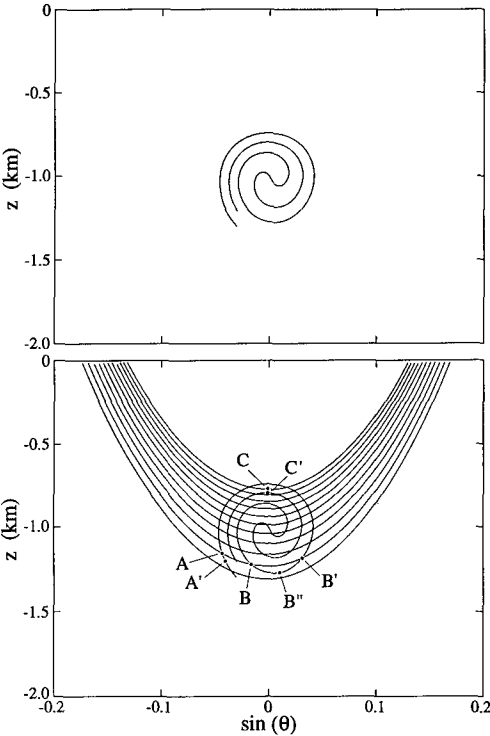


FIG. 8. The upper panel shows a ray angle-depth diagram for an axial source in a temperate ocean at a range of 4500 km. The lower panel shows the temperate diagram refracted across a temperate-polar front, with the ray angle-depth diagram for a surface source in a polar ocean at a range of 1000 km superimposed. Turning depths were limited to the depth range 0.7-1.3 km. Intersecting points are eigenrays.

$$\tau_n(t) = r(t) S_0(1 - \frac{1}{6} \tilde{\sigma}_n^2), \quad \dot{\tau}_n(t) = V S_0(1 - \frac{1}{2} \tilde{\sigma}_n^2). \quad (20)$$

Large n rays arrive last (large τ_n), as in the isotropic case. But now large n is associated with flat axial (surface) rays, whereas previously large n was associated with steep rays.

Figure 7 (top left) shows the computed arrivals from $n=160$ to $n=200$, relative to $n^*=180$. The n values were chosen to resemble measured arrivals at Christmas Island. The divergent $\delta\tau(t)$ tilt and phase drift $\delta\phi(t)$ are shown below. The scales are chosen in accordance with Eq. (12), so that $\delta\tau(t)$ and $\delta\phi(t)$ have equal but opposite slopes. The inferred relative Doppler is 0.83 c/h for the early arrivals and

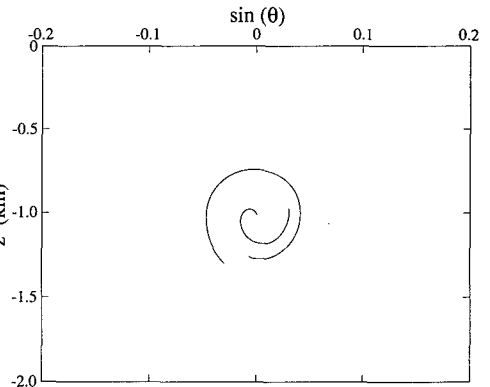


FIG. 9. As in Fig. 8, upper panel, with a "knife-edge" ridge 2500 km from the front which stops all intersecting rays deeper than 0.9 km.

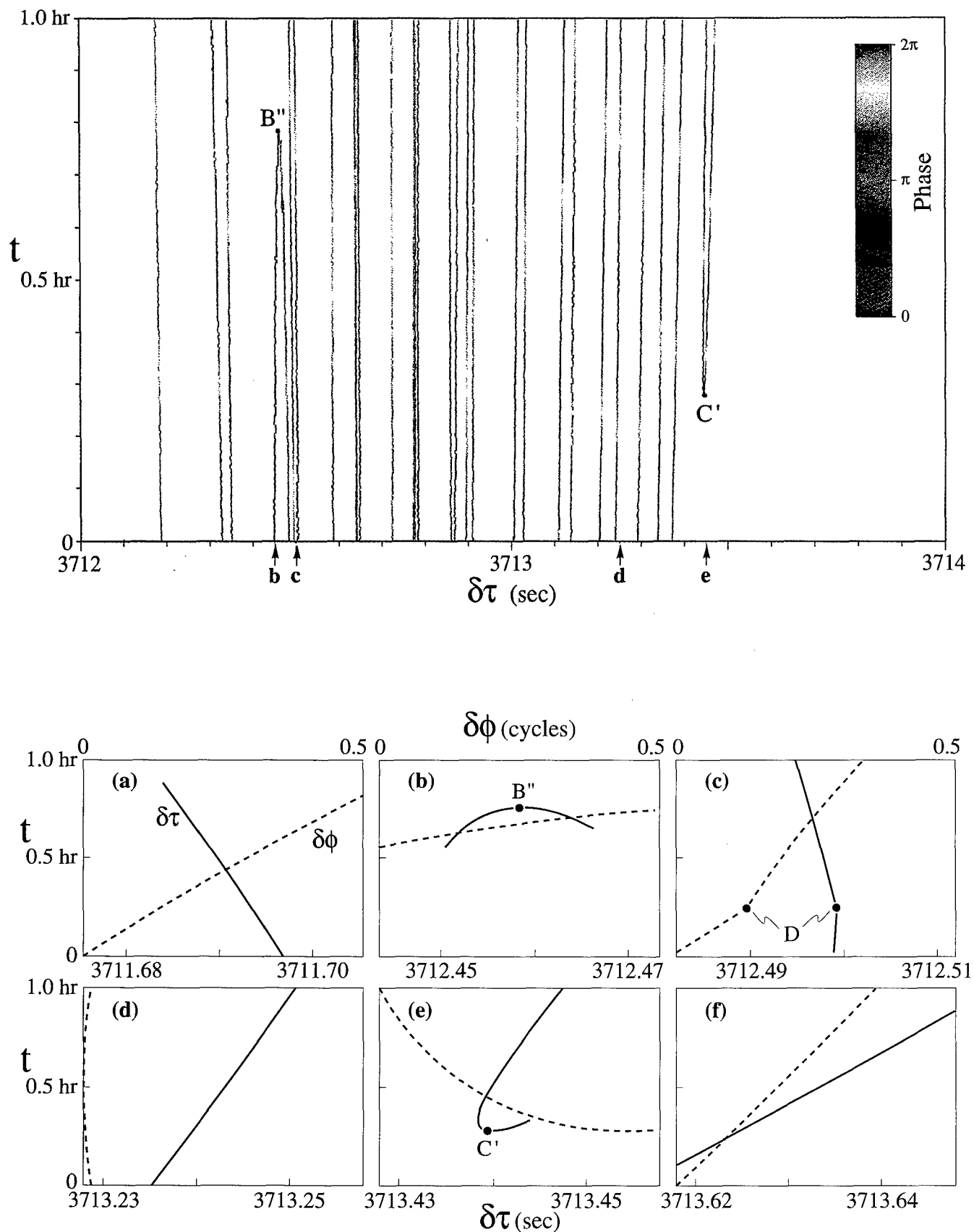


FIG. 10. Travel time $\delta\tau$ and phase $\delta\phi$ vs clock time t for 1000-km propagation in a polar ocean and 4500-km propagation in a temperate ocean, with a “knife-edge” ridge 2500 km beyond the front. Top panel shows arrival structure. Bottom panels show six individual paths in order of increasing travel time τ . Eigenrays B'' and C'' correspond to those in Fig. 8.

-0.59 c/h for late arrivals. The computed differentials (Table III) are monotonic functions of travel time related according to Eq. (12), and do not resemble the measured Heard Island differentials.

Most of the transmission takes place north of the Antarctic Front in a temperate sound channel, which we represent by the canonical sound channel⁸ with the axis at 1.0 km. The results are shown in Fig. 7 and Table III. (For the time being the effect of the Broken Ridge is ignored.) The channel is much less dispersive, with a spread of 1 s as compared to 6 s for the polar profile. But again, the differentials behave in a simple monotonic manner and cannot account for the observed complexity.

VI. HYBRID SOUND CHANNEL

Next, we consider a hybrid model, with the polar and temperate profiles patched at the Antarctic Circumpolar Front. For the adiabatic case, i.e., a diffuse front with thickness larger than a ray loop (50 km), north-traveling rays follow the deepening axis (see Fig. 6 of Dashen and Munk⁹) and the combination of the two provinces does not differ qualitatively from the results obtained for either case alone. We now take the other extreme of an infinitely sharp front.

Let z_P and z_T designate the ray elevation at the polar and temperate sides of the front, respectively, and similarly for the inclinations θ_P and θ_T . The conditions across the front are that the rays are continuous and that their change in slope follows Snell's law

$$z_P = z_T, \quad \frac{\sin \theta_P}{\sin \theta_T} = \frac{S_T(z)}{S_P(z)}. \quad (21)$$

Figure 8 shows the situation in ray angle-depth space at the front. Curves are generated by varying the launch or receiver angle θ_0 and computing $z(\theta_0)$ and $\theta(\theta_0)$ at some specified distance r . The upper panel shows the angle-depth diagram on the temperate side of the front from an axial source in a temperate ocean 4500 km from the front; the lower panel shows the same diagram on the poleward side of the front using Eq. (21) (differences are negligible) superimposed on a ray angle-depth plot from a polar surface source at a distance of 1000 km. The oceanic parameters are the same as in Sec. V. Intersections of the temperate and polar curves correspond to the eigenrays of the combined systems. The construction assures that eigenrays go through source and receiver. For the sake of clarity, we have limited construction to rays having turning points no shallower than 0.7 km and no deeper than 1.3 km.

The sound-speed profiles of the polar and temperate oceans (Fig. 6) have different effects as the ray turning point changes, and this produces an extremum in ray travel time. Referring to Fig. 8 beneath the depth of the sound axis, group velocity in both the polar and temperate oceans increases with increasing depth and the earliest arrival is presumably associated with the deepest rays bypassing the ridge. Moving above the axis, polar group velocity decreases, and temperate group velocity increases, leading to a maximum in travel time for ray turning at 0.55-km depth (not shown).

So far we have ignored the Broken Ridge which actually juts into the sound channel axis (Fig. 1). The ridge is very narrow and has been modeled as a "knife-edge" which stops all intersecting rays deeper than 0.9 km. This effect is shown in ray angle-depth space in Fig. 9.

Next we consider the effect of the source motion, taking an opening velocity of 1.8 m/s (6.5 km/h). As the source moves away from the receiver, the polar curves change shape: the loops lengthen and become steeper and deeper. An eigenray A , shown in the lower panel of Fig. 8, moves to A' over the course of 1 h. In the same time frame, eigenrays B and B' converge at B'' and then disappear. New eigenrays appear when C moves to C'' . The presence of the ridge reduces the number of eigenrays, but increases the percentage of appearing and disappearing arrivals. This mechanism for the appearance and disappearance of arrivals is completely deterministic as opposed to a stochastic fading mechanism.

The same events are viewed in $\delta\tau$ - t space in Fig. 10. Here travel time τ is the sum of polar and temperate travel times. Phase $\delta\phi(t)$ is found from the ray angle at the source $\theta_0(t)$ using Eq. (11). The upper figure is drawn for turning points between 0.7 and 1.3-km depths (as in Fig. 9), whereas the lower panels include some shallower and deeper turning points. Only the paths that pass the "knife edge" are shown. The panels are arranged in order of increasing travel time τ . We note the following new features in the $\delta\tau(t)$ and $\delta\phi(t)$ tracks:

- (i) $\delta\tau$ and $\delta\phi$ do not change monotonically with travel time τ .
- (ii) The slopes of $\delta\tau$ and $\delta\phi$ are no longer simply related in accordance with Eq. (12). In fact, the slopes are sometimes of opposite sign (panel *a*) and sometimes of the same sign (panel *f*).
- (iii) Both tracks may be sharply curved.
- (iv) Tracks may end (B'') or start (C'), as already shown in Fig. 8.
- (v) Two unrelated (in ray angle-depth space) eigenray tracks may coincidentally have nearly the same travel time and cross each other (D in panel *c*). The tracking algorithm can follow only one eigenray at a time and locks onto one eigenray, then the other, switching at point D . The result is a sharp change in slope at the crossing point.

The important result is the loss of the one-to-one relation between phase and travel time. As the source moves, the dynamics of the eigenray in angle-depth space at the front are illustrated in the tracks. The phase rate is just a measure of the launch angle of the eigenray as given in Eq. (11), while the travel time is a more complicated function based on the angle and depths of the coupling at the front.

VII. CLIMATE MONITORING

This paper has dealt with transmissions from a moving source through a fixed front to a fixed receiver. We briefly consider the situation where a source and receiver are at fixed positions on opposite sides of a seasonally moving front. This would be the worst case geometry for an acoustic climate monitoring experiment.

Computations of $\delta\tau$ vs t show, not unexpectedly, that the results are similar to the moving source situation considered

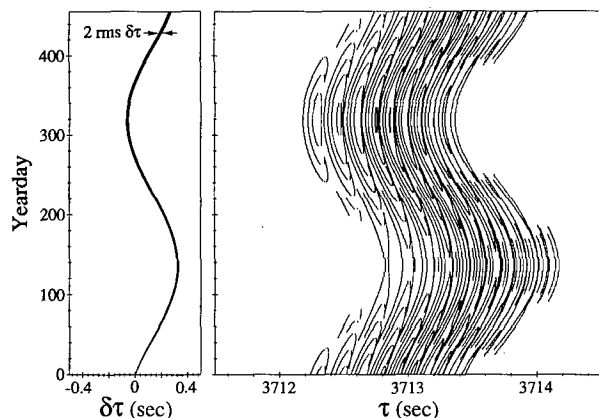


FIG. 11. Seasonal travel time variation caused by frontal movement. Right panel shows travel times of individual paths. Left panel shows the sum of daily average slopes. The standard deviation of the sum is depicted by the width of the line.

in the previous sections. The displacement of the polar front in a month is of the same order as the movement of the CORY CHOUEST in 1 h and so we interpret Figs. 2 and 10 as one month records for a transmissions across the moving polar front. Thus we can expect a typical ray path to be stable for something less than one month.

How would one extract a time series to monitor climatic trends in such a data set, given the path instability? Consider a seasonal frontal migration, the ocean remaining otherwise stationary (Fig. 11). The most favorable situation is one where, after one year, the arrival pattern closely resembles the original pattern so that one can infer the yearly travel time change to the usual tomographic precision of a few ms. The most unfavorable situation is where a centroid estimate of the 1.5-s broad arrival pattern is needed. Here, we consider an intermediary situation. For any one month we draw a line with a slope equal to the average slope of the neighboring ray paths. This corresponds to a monthly change in travel time τ with some standard deviation σ_τ . From our calculations we estimate $\sigma_\tau = 5.5$ ms. This is an example of a random walk, so that after one year the expected cumulative error is $5.5\sqrt{12} = 19$ ms. This value is about one-tenth the presently expected greenhouse signal of 200 ms from anthropogenic CO_2 (Munk *et al.*¹⁰).

VIII. DISCUSSION

The Christmas Island record (Fig. 2) is complicated in both travel time and phase. Four important features of the

measured tracks are: the nonlinear relationship of $\delta\phi$ and $\delta\tau$, the nonmonotonic variation of $\delta\phi$ and $\delta\tau$ with travel time, the frequent starting and stopping of the tracks, and the large number of arrivals. These features can be accounted for in the hybrid model whereas the adiabatic models included none of these effects. Quantitatively, the fluctuation in the data tracks and the model tracks have the right order of magnitude, although the data tracks display even more variability. The spread and the density of the arrivals are also within the correct limits. We do not, however, consider the evidence as a proof for the reality of the hybrid model.

In summary, neither the polar or temperate models alone can account for the observed record. A hybrid model can provide some qualitative basis for understanding and shows how a deterministic model of the Antarctic Circumpolar front can produce nonlinear, perhaps chaotic, features. Finally, and perhaps most importantly, observations of travel time and differential Doppler are not simply related and might be used to identify arrivals.

ACKNOWLEDGMENTS

We would like to thank K. Metzger and P. Sutton for their thoughtful comments. The experiment was supported by the Office of Naval Research, the National Oceanic and Atmospheric Administration, the Department of Energy, and the National Science Foundation. W. M. is Secretary of the Navy Professor of Oceanography.

- ¹ M. A. Dzieciuch, W. Munk, and A. Forbes, "Interpretation of GPS Offsets from a Steady Course," *J. Atmos. Oceanic Tech.* **9**, 862–866 (1992).
- ² A. Forbes and W. Munk, "Doppler-inferred launch angles of acoustic ray paths," *J. Acoust. Soc. Am.* **96**, 2425–2427 (1994).
- ³ T. G. Birdsall, K. Metzger, and M. A. Dzieciuch, "Signals, signal processing, and general results," *J. Acoust. Soc. Am.* **96**, 2343–2352 (1994).
- ⁴ K. D. Heaney, W. A. Kuperman, and B. E. McDonald, "Perth-Bermuda sound propagation 1960: Adiabatic mode interpretation," *J. Acoust. Soc. Am.* **90**, 2586–2594 (1991).
- ⁵ P. M. Morse and K. W. Ingard, *Theoretical Acoustics* (McGraw-Hill, New York, 1968).
- ⁶ W. Jobst (personal communication).
- ⁷ C. B. Officer, *Introduction to the Theory of Sound Transmission* (McGraw-Hill, New York, 1958).
- ⁸ W. H. Munk, "Sound Channel in an exponentially stratified ocean, with application to SOFAR," *J. Acoust. Soc. Am.* **55**, 220–226 (1974).
- ⁹ R. Dashen and W. Munk, "Three models of global ocean noise," *J. Acoust. Soc. Am.* **76**, 540–554 (1984).
- ¹⁰ W. H. Munk, R. C. Spindel, A. B. Baggeroer, and T. G. Birdsall, "The Heard Island Feasibility Test," *J. Acoust. Soc. Am.* **96**, 2330–2342 (1994).

Doppler-inferred launch angles of global acoustic ray paths

Andrew Forbes

Commonwealth Scientific and Industrial Research Organisation, Marine Laboratories, Hobart, Tasmania
7000, Australia

Walter Munk

Scripps Institution of Oceanography, University of California, San Diego, La Jolla, California 92093

(Received 20 August 1992; accepted for publication 7 June 1994)

Doppler measured at Ascension Island from a moving acoustic source at Heard Island is used to compute the azimuth of the acoustic path at the source. This method yields a launch angle of $268.06 \pm 0.1^\circ$ as compared to the geodesically derived launch angle (allowing for Earth flattening and horizontal refraction) of 268.05° . Although the Doppler-derived launch azimuths should theoretically be able to resolve the small angular differences between acoustic paths to hydrophones to the West and East of Ascension, this proved not to be the case.

PACS numbers: 43.30.Qd, 43.30.Es, 43.30.Cq

INTRODUCTION

In January 1991, the Heard Island Feasibility Test (HIFT) broadcast 57-Hz acoustic signals from a ship located 70 km southeast of Heard Island. The primary aim of the experiment was to test the feasibility of using long-range acoustics to deduce long-term temperature changes in the interior of the ocean. A secondary aim was to investigate the nature of refraction, attenuation, and dispersion of acoustic signals over ranges of order 10 megameters.

The acoustic sources were suspended from the CORY CHOUET in the local sound channel at a depth of 175 m. The source ship was steered as closely as possible to a straight and steady course necessarily directed into the prevailing wind and sea during each hour-long transmission. For the main purposes of HIFT the Doppler-induced shift in the carrier frequency was considered a nuisance and careful processing was carried out to remove it. Here we shall take advantage of the Doppler shift to compute the azimuth of the acoustic path at the source, for comparison with the geodesically derived launch angles.

For the Heard to Ascension transmission the agreement between Doppler-estimated and geodesically derived launches is excellent, as will be shown. But this is not always the case. As shown elsewhere in this issue (Forbes, 1994), the expected path to the American west coast through the Tasman Sea appears to be blocked, and the recorded signal arrived along a quite different route.

I. PROCEDURE

Positive Doppler is due to the component of ship's motion in the direction of the launch azimuth of a ray that eventually intersects the receiver. Negative Doppler indicates ship's motion away from the receiver and zero Doppler indicates ship's motion precisely at right angles to the launch azimuth. The course differed from one transmission to the next, so that a number of independent calculations of Doppler-derived launch azimuths were obtained.

The basic relation is

$$\frac{f-f_0}{f_0} = \frac{U}{C} \cos(\alpha_s - \alpha), \quad (1)$$

where f is the received and $f_0=57$ Hz is the transmitted frequency, $C=2822$ kn is the sound speed at the source (which determines the Doppler, ignoring any temporal changes during transmission), U and α_s are the ship's speed in knots and heading measured by GPS, and α is the direction at the source of the acoustic path from source to receiver. (All directions are clockwise from north.) The Doppler-derived azimuth α_d is therefore

$$\alpha_d = \alpha_s \pm \arccos\left(\frac{f-f_0}{f_0} \frac{C}{U}\right). \quad (2)$$

The \pm ambiguity is not a problem; one of the two values usually gives a totally false direction. Values of α_d are plotted in Fig. 1. We note that on average α_d is consistent with the geodesic angle $\alpha_g=268.1^\circ$, which was computed by Heaney *et al.* (1991) for individual vertical modes. The Doppler correction associated with the vertical ray tilt (Dzieciuch and Munk, 1994) can be ignored since it is generally small compared to $\alpha_s - \alpha$.

We expect a more precise determination for the "broad-side" runs $\alpha_s - \alpha \rightarrow \pm 90^\circ$, than for the "endfire" runs $\alpha_s - \alpha \rightarrow 0^\circ$. To investigate this we have plotted, in Fig. 1, α_d vs $\alpha_s - \alpha_g$, neglecting for the moment the difference between the true ray azimuth α and the geodesic azimuth α_g . Indeed the data are widely scattered for $\alpha_s - \alpha_g < 20^\circ$.

To make this quantitative, we write (2) in the form

$$\beta \equiv \frac{f-f_0}{f_0} \frac{C}{U} = \cos(\alpha_s - \alpha_d). \quad (3)$$

Then any error in β (for whatever reason) produces an error in the Doppler-inferred azimuth of

$$\delta\alpha_d = \delta\beta / \sin(\alpha_s - \alpha_d) \quad (4)$$

and this is greatly amplified for small $\alpha_s - \alpha_d$. For the present purpose we can replace α_d by α_g in (4), and write

$$\delta\alpha_d = \delta\beta / \sin(\alpha_s - \alpha_g). \quad (5)$$

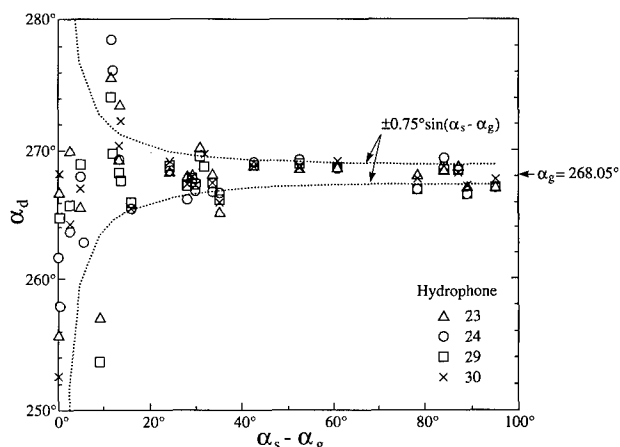


FIG. 1. The Doppler-inferred azimuth α_d for Ascension hydrophones as a function of the angle between the ship's course α_s and the geodesic launch azimuth α_g . The dotted curves are the estimated error limits.

Anticipating the result, the dotted curves in Fig. 1 are drawn for $\delta\beta = 1.32 \times 10^{-2} = 0.75^\circ$.

The data scatter can arise in different ways, such as the inaccuracy of the ship coordinates, or in the measured Doppler. To test the latter assumption, we compute the Doppler from the measured ship speed and direction,

$$f_{\text{comp}} - f_0 = f_0 (U/C) \cos(\alpha_s - \alpha_g), \quad (6)$$

and plot $f_{\text{meas}} - f_{\text{comp}}$ again SNR (Fig. 2). There is no obvious correlation, for the following reason. The expected error for a record of length $T = 1$ h is

$$\delta f = \frac{1}{T} \frac{1}{\sqrt{\text{SNR}}} = 3 \times 10^{-6} \text{ Hz},$$

for 40 dB SNR, and thus vastly smaller than the measured 10^{-3} Hz. We do not know the source of the error.

There are two conclusions to be drawn. One is that with a special future effort the error in α_d might be reduced by yet another order of magnitude over the rather satisfying results already obtained for HIFT. Second, for the present purpose we might as well assume a constant error (independent of SNR). For the data in Fig. 2, $\text{rms } f = 0.75 \times 10^{-3}$ Hz.

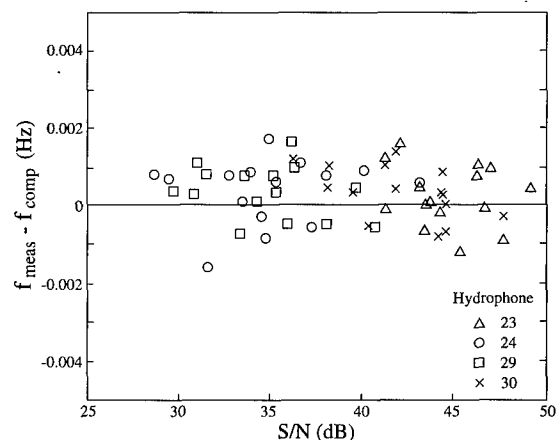


FIG. 2. Scatter in Doppler frequency for $\alpha_s - \alpha_g > 20^\circ$.

TABLE I. Weighted mean Doppler-derived launch azimuths towards fixed receivers, compared with estimated geodesics. N is the number of transmissions.

| N | Ascension receiver | α_d | α_g |
|-----|--------------------|------------------------------|----------------|
| 16 | #23 | $268.16^\circ \pm 0.2^\circ$ | 268.0° |
| 16 | #24 | $267.98^\circ \pm 0.2^\circ$ | 268.0° |
| 16 | #29 | $267.90^\circ \pm 0.2^\circ$ | 268.1° |
| 16 | #30 | $268.19^\circ \pm 0.2^\circ$ | 268.1° |
| | | $268.06^\circ \pm 0.1^\circ$ | 268.05° |

II. AZIMUTH ESTIMATES

The remaining problem is to combine measurements of different quality to form an estimate of the mean and of the variance of the mean. The quality of the k th transmission is represented by its variance. The variance ν_k is given by

$$\sqrt{\nu_k} = \frac{\text{rms } \delta f}{f_0} \frac{C}{U_k} \frac{1}{\sin[(\alpha_s)_k - \alpha_g]}. \quad (7)$$

The value of the k th measurement is

$$(\alpha_d)_k = (\alpha_s)_k \pm \arccos\left(\frac{f_k - f_0}{f_0} \frac{U_k}{C}\right). \quad (8)$$

The final estimate is given by

$$\alpha_d = \langle \alpha_d \rangle \pm \sqrt{V},$$

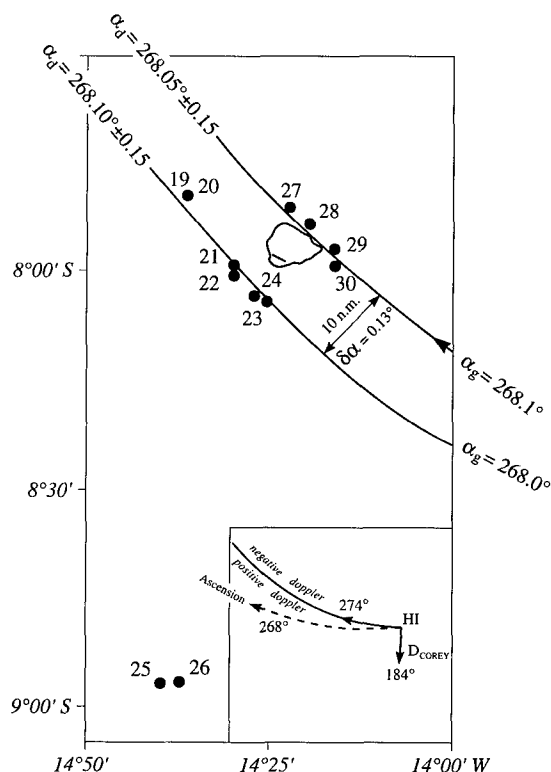


FIG. 3. Locations of the Ascension hydrophones. Geodesic launch angles are given for the two sides of the island. Inset shows the situation at the Heard island source for transmission 29:1800. Cory headed towards $\alpha_s = 184^\circ$ at $U = 3.38$ kn. The 274° azimuth, perpendicular to ship's heading, separates positive from negative Doppler.

where

$$\langle \alpha_d \rangle = \frac{\sum_{k=1}^M (\alpha_d)_k / \nu_k}{1/V}, \quad \frac{1}{V} = \sum_{k=1}^M \frac{1}{\nu_k}. \quad (9)$$

The results are shown in Table I and in Fig. 3. The overall mean for Ascension is $\alpha_d = 268.06^\circ \pm 0.1^\circ$ and $\alpha_g = 268.05^\circ$, which demonstrates good agreement.

We cannot resolve the left stations (23,24) from the right stations (29,30); in fact the relative magnitudes of α_d are in the reverse order of α_g . Metzger (1992) computed Doppler differences between receivers (to cancel clock errors) but the result was not significantly changed. Dzieciuch (1992) investigated the bathymetric refraction of the geodesics over the local topographies at Heard and Ascension Islands. In principle it is possible for geodesics to cross, but this was found not to be the case.

The present application of Doppler-derived azimuths is a special case of synthetic-aperture sonar. It was not anticipated prior to HIFT. By optimizing the procedure, the precision of the Doppler-derived path directions should be greatly

improved. We now plan to augment future transmissions between fixed sources and fixed receivers by occasional measurements using towed sources and towed receivers. These will serve as controls of the geodesic calculations, but might conceivably be useful as an indicator of changed ocean conditions.

ACKNOWLEDGMENTS

We are indebted to Prof. T. Birdsall for the statistical discussion of azimuthal estimates (Sec. II). W. Munk acknowledges support from the Office of Naval Research, Grant No. N00014-91-J-1149.

- Dzieciuch, M., and Munk, W. (1994). "Differential Doppler as a diagnostic," *J. Acoust. Soc. Am.* **96**, 2414–2424.
 Dzieciuch, M., (1992). Personal communication.
 Forbes, A. M. G. (1994). "The Tasman Blockage—An Acoustic Sink for the Heard Island Feasibility Test," *J. Acoust. Soc. Am.* **96**, 2428–2431.
 Heaney, K. D., Kuperman, W. A., and McDonald, B. E. (1991). "Perth-Bermuda sound propagation 1960: Adiabatic mode interpretation," *J. Acoust. Soc. Am.* **90**, 2586–2594.
 Metzger, K. (1992). Personal communication.

The Tasman blockage—An acoustic sink for the Heard Island feasibility test?

A. M. G. Forbes

CSIRO Division of Oceanography, Hobart, Tasmania 7000, Australia

(Received 20 August 1992; accepted for publication 7 June 1994)

Low-frequency (57-Hz) signals from the Heard Island Feasibility Test, conducted in January 1991 were received on many hydrophones around the globe. The Atlantic and Indian Ocean paths were relatively clear and unimpeded, so received signal-to-noise ratios (after some averaging) were generally high. The Pacific paths were not as clear and considerable interaction with bathymetric features attenuated the signals received off the west coast of the U.S. A New Zealand-manned receiver in the Tasman Sea received the transmissions strongly, but a Japanese ship, placed strategically northeast of the south Fiji (Lau) Ridge did not detect any signals. There is good evidence from U.S. west coast receivers with beam forming capability, that the signals arrived from 20 deg further south (i.e., south of New Zealand, then through the Polynesian window) than if they had passed through the Tasman Sea window. Doppler-derived matching of transmitted and received azimuths further indicates that all U.S. west coast signals traveled south of New Zealand. A series of transverse ridges lying between northern New Zealand and New Caledonia and Fiji appears to have effectively blocked the transmissions from exiting the Tasman Sea. An adiabatic modal model of refracted geodesic raypaths sheds some light on the reasons for such effective blockage.

PACS numbers: 43.30.Qd, 43.30.Re

INTRODUCTION

Signals from the Heard Island Feasibility Test (HIFT) were received at a number of hydrophones around the world, see Fig. 1. The quality of some of these receptions was exceptional (Christmas Island), average (Ascension Island), marginal (Los Angeles), or absent (Samoa). Prior to the 1991 Heard Island Feasibility Test, Munk and Forbes (1989) stated that there was "possibly" an acoustic path through the Tasman Sea from Heard Island to Oregon. However, a series of submarine ridges, seamounts, and islands which lie to the north of New Zealand give grounds for caution in treating the Tasman as an acoustic window to the North Pacific. Nevertheless, our axial-ray, refracted geodesic propagation model showed that there was a narrow region amongst those physical barriers which could allow HIFT signals to pass through to Oregon. Despite our cautious optimism, the Tasman did not cooperate and there is now very strong evidence that the "window" was not sufficiently transparent for acoustic energy to traverse that narrow region.

By using the Doppler technique of Forbes and Munk (1994) we can determine which paths the energy took to reach the U.S. west coast. Once we have determined the path that the energy took, we can address more fundamental questions of energy loss in the Tasman Sea and how to refine our propagation model.

I. PREDICTION

The method of Munk *et al.* (1988) was used to predict the refracted geodesic paths in Fig. 1. The global distribution of sound velocity at the sound channel axis was calculated from 8000 oceanographic stations world-wide and through this field, acoustic ray paths could be computed from Heard Island, given any initial launch azimuth. Rays along paths

where the axis of the sound channel did not intersect the bottom were considered successful. Two of these paths were predicted and are shown in Table I. Both the Tasman and Polynesian windows appeared to exist because the model's simple criterion of bottom interaction (i.e., no sound channel intersection by the bottom) was satisfied.

II. OBSERVATION

A New Zealand ship east of Sydney in the Tasman Sea did receive eastward signals (apparently *en route* to the U.S. west coast), but along the U.S. western seaboard, the story was quite different. At Whidbey Island, where multiple hydrophones could be accessed, horizontal beam forming was used to identify the arrival azimuth of the 57-Hz HIFT signals. Instead of arriving at the predicted azimuth of 235° (through the Tasman Sea), the energy arrived at 215°. And, further down the coast, towards Los Angeles, the arrival azimuth was 213°. Both of these arrival angles strongly suggest that the acoustic energy came from south of New Zealand as shown in Fig. 2.

The Doppler method of Forbes and Munk (1994) was applied to the observed Doppler at Whidbey Island yielding a launch azimuth of 130°, and for the observed Doppler off Los Angeles, a launch azimuth of 134°. Thus we can now be certain, as is depicted in Fig. 2, that the successful receptions were via the Polynesian window, not the Tasman window.

The question then is—what became of the acoustic energy with launch azimuths of 112°–115° that tried to pass through the Tasman Sea?

III. LOSSES

The trans-Pacific paths experienced greater energy losses than the Atlantic paths. While signal-to-noise ratios

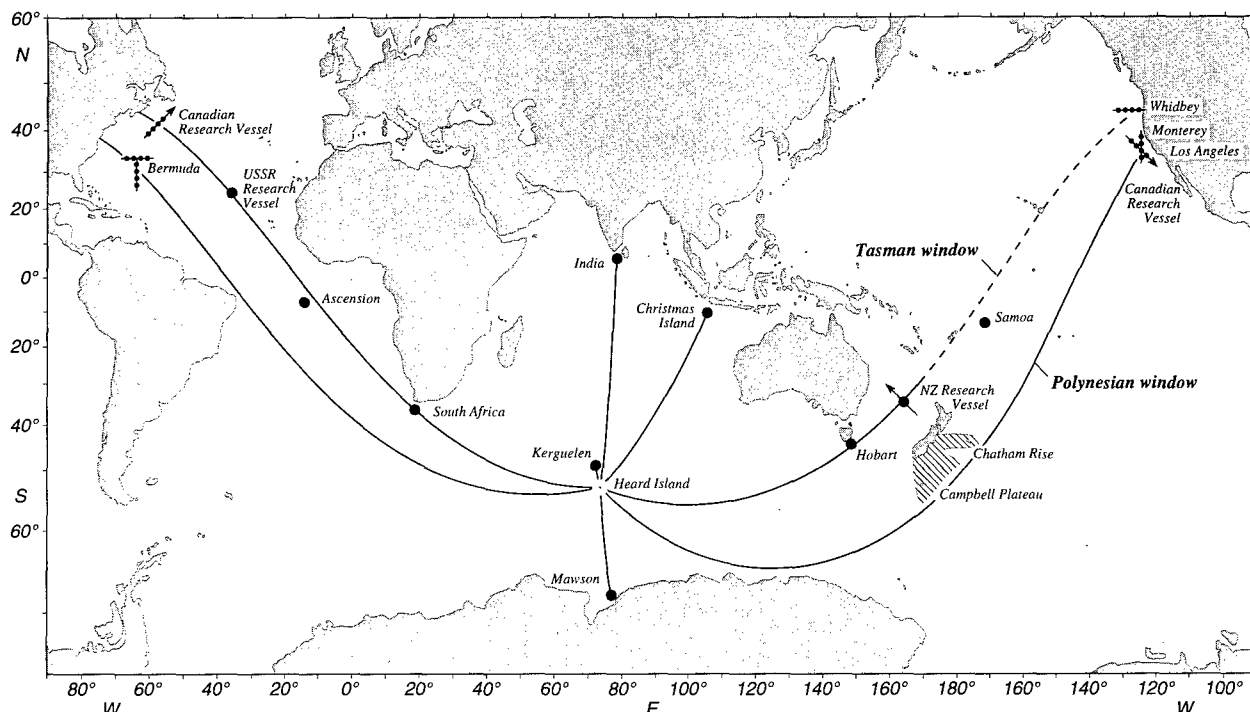


FIG. 1. Acoustic ray paths from Heard Island to receivers during the 1991 Heard Island Feasibility Test. The dashed portion of the Heard–Whidbey path is doubtful.

(SNR) at Ascension Island, Krylov Seamount, and Bermuda were in the range 15–40 dB, SNR from Monterey to Los Angeles were 5 to 10 dB (after 10- to 15-dB array gain). Figure 1 illustrates that eastward raypaths from Heard Island spend twice as long south of the Antarctic convergence ($\sim 50^\circ$ S) in the Southern Ocean, than do westward rays. As the sound channel is shallow in the Southern Ocean, this leads to greater surface losses for eastward rays than for westward, which may account for part of the difference in received energy, but the more likely zone of loss is the bottom.

In the simple lowest mode axial propagation model which Munk and Forbes (1989) used to predict possible paths through the Tasman Sea, they assumed that the flat, limiting ray contained all the energy at precisely the depth of minimum sound speed. This is an oversimplification which does not represent bottom losses well. Heaney *et al.* (1991) suggested that an adiabatic modal representation is more realistic and applied their adiabatic modal propagation model to the Perth–Bermuda acoustic paths which both Shockely *et al.* (1982) and Munk *et al.* (1988) had previously treated. Heaney *et al.* were successful in explaining both the first and second arrivals (in time and amplitude). We applied Heaney *et al.*'s method at the HIFT center frequency of 57 Hz to enable us to compute the paths of a large number of rays. We

chose to use the Levitus (1982) oceanographic data base to calculate the sound-speed field at all standard depths for the entire global ocean.

The feature of the Heaney *et al.* model that we will concentrate on here is the modal representation of bottom loss, since it generally exceeds surface loss, especially after rays have left the Southern Ocean. For the first (lowest) mode, the

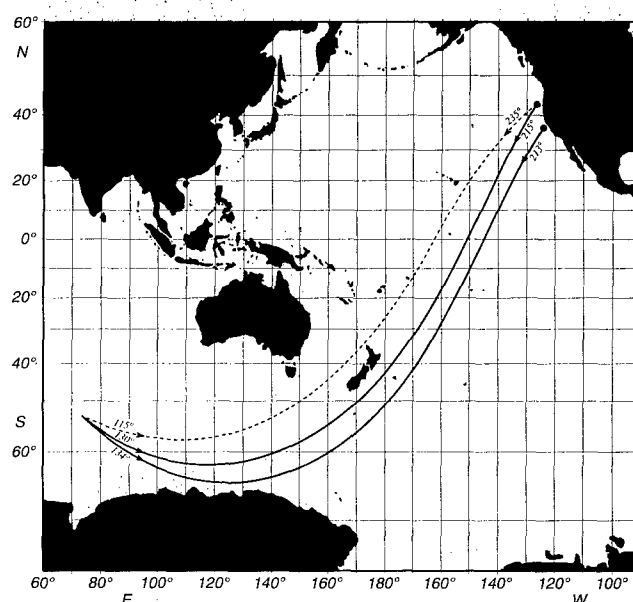


FIG. 2. Refracted geodesic acoustic ray paths from Heard Island to the U.S. west coast. The dashed path was apparently not successful. The path with a launch angle of 130° and a received azimuth of 215° was drawn with some artistic license.

TABLE I. Launch angles of refracted geodesic paths from Heard Island through the Pacific to two receiver locations.

| Path | Via | Predicted launch azimuth |
|-------------------------|-------------------|--------------------------|
| Heard–Coos Bay (Oregon) | Tasman window | 112° |
| Heard–San Francisco | Polynesian window | 133° |

TASMAN SEA PATHS - SAMOAN REGION, MODE 1

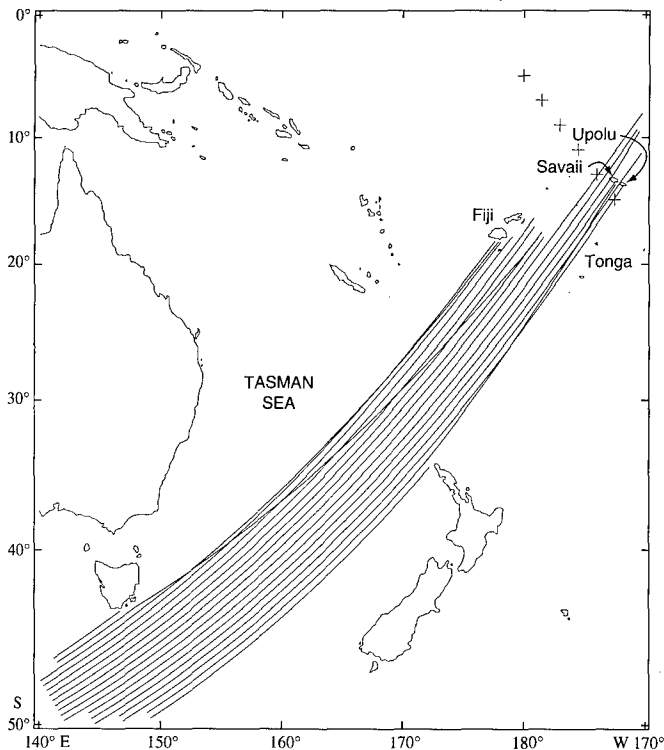


FIG. 3. Bundle of refracted geodesic acoustic ray paths for mode 1 propagation through the Tasman Sea. Most are stopped by bottom interaction (i.e., when integrated bottom attenuation >50 dB).

total bottom attenuation along a ray is, from Heaney *et al.*,

$$\text{dB loss} = \frac{\beta_0}{\lambda_0} \int ds \int_{-\infty}^{-h} \rho^{-1} \psi_n^2 dz, \quad (1)$$

where h is ocean depth, λ_0 is acoustic wavelength, ρ is density, ψ_n is the local vertical eigenmode, and β_0 is the attenuation coefficient.

Bottom attenuation coefficients may vary by an order of magnitude (Ingenito, 1973), but we chose a conservative value of 0.1 dB per wavelength.

IV. MODAL PREDICTION OF RAY PATHS

We computed the paths of an azimuthal fan of rays emanating from the source at Heard Island towards Whidbey Island on the U.S. west coast. A group of rays with launch azimuths from 108° to 115.5° pass south of Tasmania through the Tasman Sea and just clear northern New Zealand. A ray is considered stopped when its integrated bottom attenuation [calculated from Eq. (2)] exceeds 50 dB. Figure 3 shows this fan of rays, only four of which apparently pass successfully through the Tasman Sea past the ridges and islands of the southwestern Pacific and through to deep water somewhere off Whidbey Island. Table II lists the characteristics of the four rays.

The 113.5° ray is refracted strongly off Savaii (Western Samoa) and the 114.5° ray refracts weakly off Upolu (Western Samoa). Both of these interactions with the bottom result in large, but not "fatal" attenuation. The other two rays are

TABLE II. Mode 1 rays, Heard Island to Whidbey Island.

| Launch azimuth | Arrival azimuth | Attenuation (dB) |
|----------------|-----------------|------------------|
| 112.5° | 230.2° | 26.14 |
| 113.0° | 229.0° | 10.95 |
| 113.5° | 225.8° | 47.00 |
| 114.5° | 229.0° | 32.52 |

more robust as they appear to pass well clear of Savaii. All rays with launch azimuths between 108° and 110° are stopped by Viti Levu (Fiji) and from 110.5° to 112° , the rays pass to the south of Fiji but are stopped very soon afterwards by the Lau Ridge. It is interesting to note that up to the point at which the four successful rays pass south of Fiji, their range of integrated bottom attenuation is only 4.15 to 6.87 dB so they all appear to experience significant further losses in the short distance between Fiji and Samoa as they too cross the Lau Ridge and pass through the Samoan group.

If we chose β_0 to be 0.5 (still reasonable according to Ingenito, 1973) instead of 0.1 dB/wavelength, then all four of the apparently successful rays would be stopped (i.e., their integrated attenuation exceeds 50 dB). This may well explain why nothing was heard at Whidbey with the appropriate arrival azimuth of 230° . There remains the question of why the Japanese ship heard nothing at their six stations off Samoa. The simple (Munk and Forbes, 1989) axial model of refracted geodesic rays was used to define the six station positions which were occupied on successive days from North to South, as marked in Fig. 4. The first three were intentionally placed to determine where the edge of the shadow zone cast by New Caledonia and Fiji might be. The last three should have been "illuminated" according to that model. However, if we now examine the station positions relative to the rays traced by the adiabatic modal model, we see in Fig. 4 that only the southernmost two of these stations appear to have had any chance of receiving the HIFT signals. By chance, these two stations neatly straddle the limiting rays of the bundle that could conceivably pass Samoa, which makes their potential for reception marginal, and on those final two days the source (array) which started life at 222 dB was operating at reduced power, 212 dB on 30 January and finally 205 dB on 31 January. This combination of marginal position, low power, and large bottom attenuation (as the new model reveals) could well have conspired to make single hydrophone reception unviable.

V. CONCLUSIONS

With the benefit of hindsight, we see that it is not surprising that HIFT signals were not received at Whidbey Island from paths through the Tasman Sea. (Our new model shows that if we were to repeat the experiment, more careful placement of receivers, perhaps in the Lau Basin between Fiji and Samoa, might determine where the greatest bottom attenuation losses occurred.) It has been clearly demonstrated that to reach the west coast of the U.S. from Heard Island, the acoustic energy must pass south of New Zealand. Information of this type must be used when planning the long-

TASMAN SEA PATHS, MODE 1

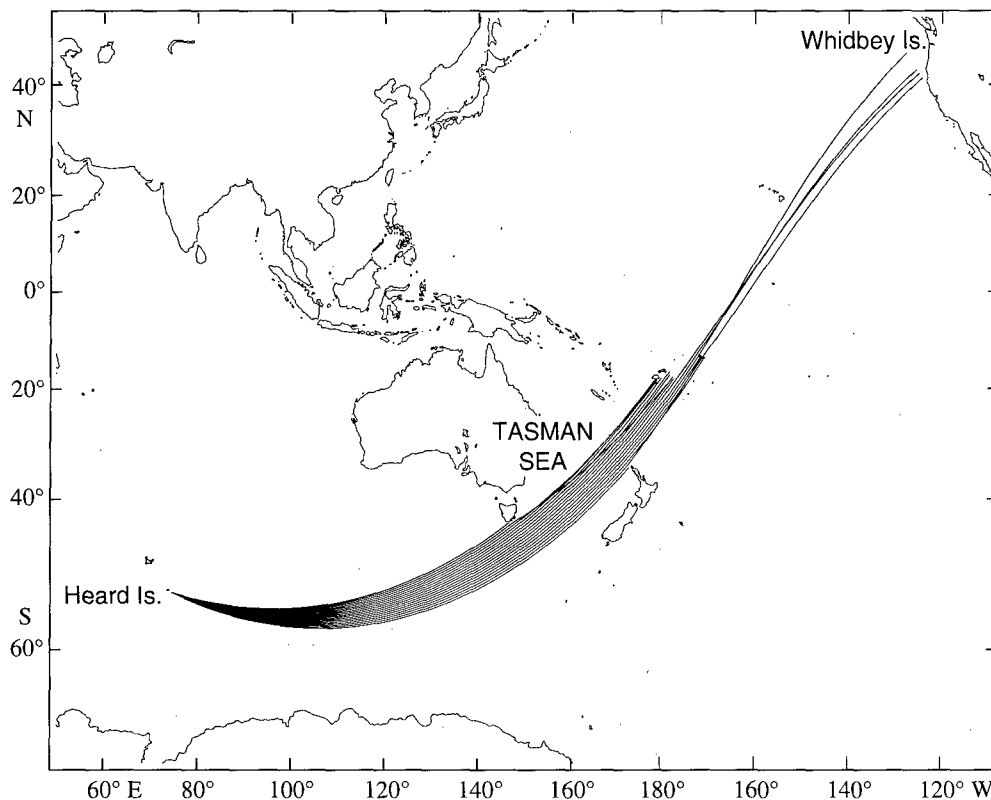


FIG. 4. Tasman Sea refracted geodesic ray paths with some detail in the Samoan region. The crosses near Samoa indicate receiver positions occupied by the Japanese ship, NATSUSHIMA, on six successive days during HIFT.

term global network of sources and receivers for monitoring ocean climate change. One or more Pacific sources will certainly be required to illuminate the acoustic shadows cast by the Southwest Pacific island groups and their associated ridges.

Forbes, A., and Munk, W. (1994). "Doppler-inferred launch angles of global acoustic ray paths," *J. Acoust. Soc. Am.* **96**, 2425–2427.

Heaney, K. D., Kuperman, W. A., and McDonald, B. E. (1991). "Perth–Bermuda sound propagation (1960): Adiabatic mode interpretation," *J. Acoust. Soc. Am.* **90**, 2586–2594.

Ingenito, F. (1973). "Measurement of mode attenuation coefficients in shallow water," *J. Acoust. Soc. Am.* **53**, 858–863.

Levitus, S. (1982). "Climatological atlas of the world ocean," National Oceanic and Atmospheric Administration Professional Paper **13**, 173 pp.

Munk, W. H., and Forbes, A. M. G. (1989). "Global ocean warming: an acoustic measure?," *J. Phys. Oceanogr.* **19**, 1765–1778.

Munk, W. H., O'Reilly, W. C., and Reid, J. L. (1988). "Australia–Bermuda sound transmission experiment (1960) revisited," *J. Phys. Oceanogr.* **18**, 1876–1898.

Shockley, R. C., Northrup, J., Hansen, P. G., and Hartdegen, C. (1982). "SOFAR propagation paths from Australia to Bermuda: Comparison of signal speed algorithms and experiments," *J. Acoust. Soc. Am.* **71**, 51–60.

Reception at Ascension of the Heard Island Feasibility Test transmissions

D. R. Palmer

NOAA/Atlantic Oceanographic and Meteorological Laboratory, 4301 Rickenbacker Causeway, Miami, Florida 33149

T. M. Georges and J. J. Wilson

NOAA/Wave Propagation Laboratory, 325 Broadway, Boulder, Colorado 80303

L. D. Weiner and J. A. Paisley

NOAA/Atlantic Oceanographic and Meteorological Laboratory, 4301 Rickenbacker Causeway, Miami, Florida 33149

R. Mathiesen, R. R. Pleshek, and R. R. Mabe

Computer Science Raytheon Co., Patrick Air Force Base, Florida 32925

(Received 24 March 1992; accepted for publication 7 June 1994)

At Ascension, about 9200 km from the source ship, all transmissions from the Heard Island Feasibility Test were recorded on at least eight hydrophones and, for many transmissions, on 11 hydrophones. The depths of most of these hydrophones are near the depth of the sound channel axis but some are considerably deeper. All are bottom mounted. Signal-to-noise ratios were found to be surprisingly high. Averaged over the continuous wave (cw) transmissions and in a 1-Hz band, signal-to-noise ratios for the axial hydrophones south of the island range from about 19 to 30 decibels (dB), adjusted to a source level of 220 dB (referenced to $1 \mu\text{Pa}$ at 1 m). The average signal-to-noise ratio for a hydrophone at a depth approximately 0.8 km below the axis is about 16 dB, suggesting acoustic energy was not restricted to a narrow interval in depth centered about the sound channel axis as had been anticipated. The travel time of the earliest arrival was found to be about 1 h, 44 min, 17 s. A late, scattered signal was observed for at least 23 min after termination of the direct signal. An unexpected combination of phase stability and amplitude variability was observed in the received signals. Continuing analysis of the Ascension data set is likely to provide considerable information about the characteristics of acoustic signals that have propagated global distances.

PACS numbers: 43.30.Qd, 43.30.Pc, 43.30.Wi

INTRODUCTION

From 26 January through 31 January 1991, underwater acoustic signals were transmitted from a string of large hydraulic sources suspended from the research ship R/V CORY CHOUEST while underway near Heard Island in the southern Indian Ocean. Remarkably, from this location acoustic energy can travel through portions of all five major ocean basins. These signals were monitored at listening stations throughout the world. The objective of the Heard Island Feasibility Test (HIFT) was to ensonify the global oceans from a single source site to determine the feasibility of measuring the extent of ocean warming due to the greenhouse effect.¹⁻³

At Ascension (Fig. 1) the HIFT acoustic transmissions were recorded using U.S. Air Force Missile Impact Locating System (MILS) hydrophones. Ascension was chosen as a listening station because of its location at an intermediate global range from the source ship and the availability there of bottom-mounted hydrophones positioned at depths near the depth of the sound channel axis.

All HIFT transmissions were recorded on at least eight hydrophones, and many were recorded on 11 hydrophones using both digital and analog data acquisition systems. Signal-to-noise ratios were surprisingly high. The signals

were easily detected throughout the course of the test. The data set seems to be generally of high quality.

In this paper, we describe the observational effort undertaken at Ascension and discuss general features of the data set collected there. Emphasis is on the spectral characteristics of the received signals and their temporal characteristics before demodulation. Reference 4 contains a more detailed description of the monitoring effort at Ascension and the data collected there.

I. GEOPHYSICAL SETTING

Ascension is located in the Atlantic Ocean approximately 890 km south of the equator on the western edge of the Mid-Atlantic Ridge. Figure 1 shows the geodesic from the nominal position of the source ship ($53^{\circ}22'S$, $74^{\circ}30'E$) to Ascension ($7^{\circ}57'S$, $14^{\circ}24'W$) and beyond. The angles of the geodesic at the source ship and at Ascension are approximately 268° and 142° , respectively, measured relative to true North. The distance along the geodesic is approximately 9200 km, or about one quarter of the distance around the Earth.

The ocean region along the geodesic from the source ship to Ascension was arbitrarily partitioned into ten overlap-

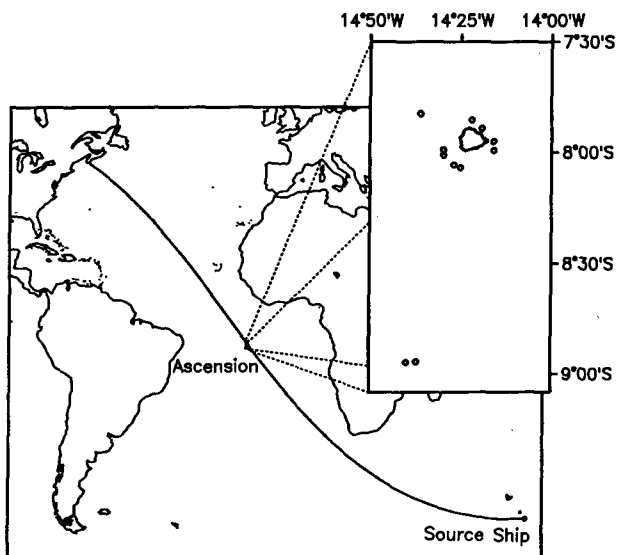


FIG. 1. Geodesic from the nominal position of the source ship ($53^{\circ}22'S$, $74^{\circ}30'E$) to Ascension ($7^{\circ}57'S$, $14^{\circ}24'W$) and beyond. The insert shows the location of the MILS BOA hydrophones (small circles) relative to the triangular-shaped island.

ping rectangular regions as indicated in the top panel of Fig. 2. National Oceanographic Data Center (NODC) archival sound-speed data from hydrographic stations within the ten regions were obtained for the seasonal period December

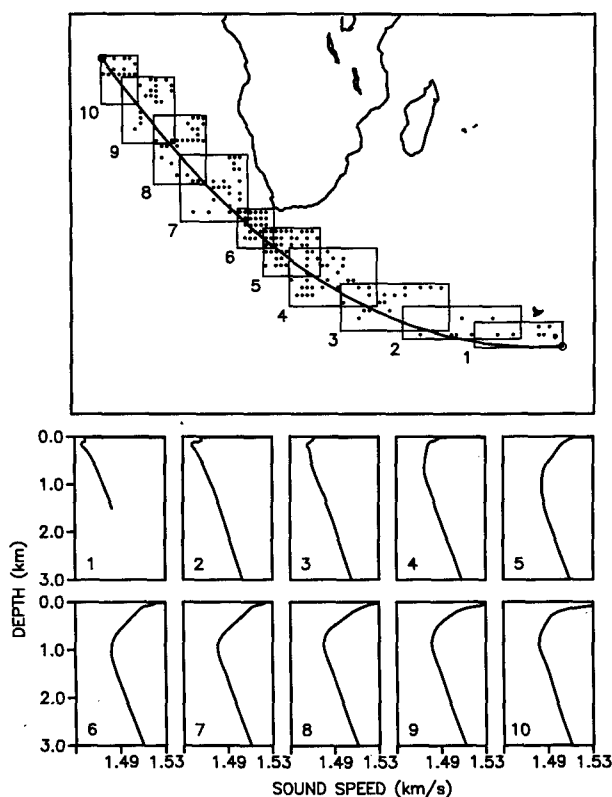


FIG. 2. Top: Locations (dots) along the geodesic of hydrographic stations. Bottom: Sound-speed profiles obtained by averaging archival data from the hydrographic stations within the rectangular regions indicated in the top panel.

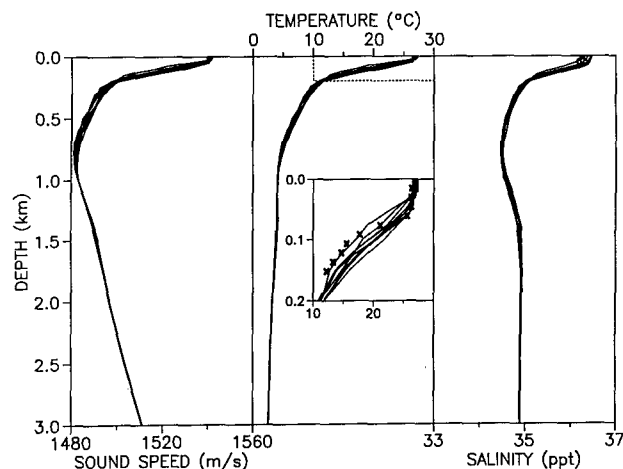


FIG. 3. Composite plots of seasonal, archival sound speed, temperature, and salinity profiles for the Ascension region ($7^{\circ}30'-9^{\circ}30'S$, $12^{\circ}30'-15^{\circ}30'W$). The insert shows a comparison of AXBT temperature data (crosses) with the upper-ocean archival temperature data (plotted on a reduced vertical scale within the area outlined by the dashed line). The AXBT data were collected at 0945Z, 26 January at $8^{\circ}2.5'S$, $14^{\circ}22.5'W$.

through March. The sound-speed profiles for each region were averaged to obtain those plotted in the bottom panel of Fig. 2. These average profiles are intended to show the evolution of the sound speed along the geodesic. Average profiles 1–3 indicate the sound-speed field before the circumpolar front was encountered and profiles 4–10 the conditions beyond it. Beyond the front, the profiles are typical of the deep ocean.

Figure 3 shows composite plots of seasonal (December–April) NODC archival sound speed, temperature, and salinity profiles for the immediate vicinity of Ascension. They indicate the average sea-surface temperature is approximately $27^{\circ}C$. The mixed layer extends to 35–45 m below the sea surface. A sharp thermocline exists from the bottom of the mixed layer to about 200 m. Below 200 m the temperature gradient is not as severe and is more characteristic of the gradients that exist at midlatitudes. The sound-channel axis is between 800 and 900 m.

Airborne expendable bathythermograph (AXBT) data do not indicate that any anomalous hydrographic conditions existed during the test. A U.S. Navy maritime patrol aircraft launched an AXBT south of Ascension ($8^{\circ}2.5'S$, $14^{\circ}22.5'W$) at 0945Z, 26 January to provide us with upper-ocean temperature data. These data are compared with the archival temperature data in the insert of Fig. 3. The temperature and the depth of the mixed layer are estimated to have been $26^{\circ}C$ and 49 m, respectively, consistent with the archival data.

The bathymetry between the source ship and Ascension is shown in Fig. 4 together with the sound channel axis (dotted line).⁵ There are no bathymetric features that extend up to the depth of the sound channel axis. This figure indicates the abrupt change in axis depth at the circumpolar front.

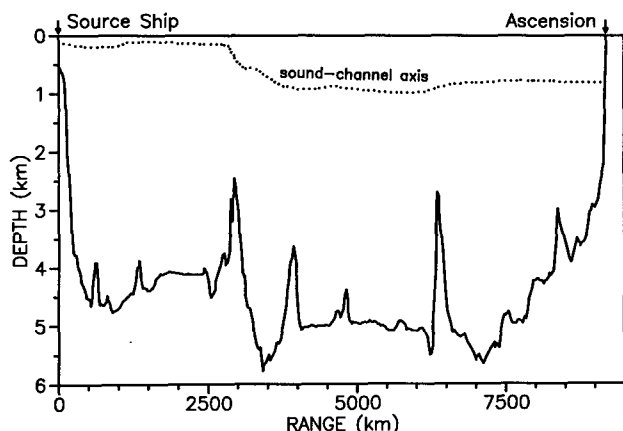


FIG. 4. Bathymetry along the refracted geodesic from the HIFT source ship to Ascension. The dotted line indicates the depth of the sound channel axis. Note the source ship location near Heard Island is on the left, with Ascension on the right.

II. INSTRUMENTATION AND DATA RECORDING PROCEDURES

The Missile Impact Locating System (MILS) at Ascension consists, in part, of a set of 12 Broad Ocean Area (BOA) hydrophones cabled to a shore site. Their approximate locations are indicated in the left panel of Fig. 5. The depths of the BOA hydrophones are shown in the right panel of Fig. 5, together with the average sound speed for the region. Most hydrophones are at depths near the depth of the sound channel axis. The exceptions are the pair far to the south (25,26) and the pair to the northwest (19,20).

Figure 6 shows a block diagram of the recording system. Data were recorded on both the MILS analog system and a PC-controlled digital system designed and built at the University of Michigan and the Applied Physics Laboratory of the University of Washington.³ Similar digital systems were used at the Christmas Island, Goa, Mawson Station, Ker-

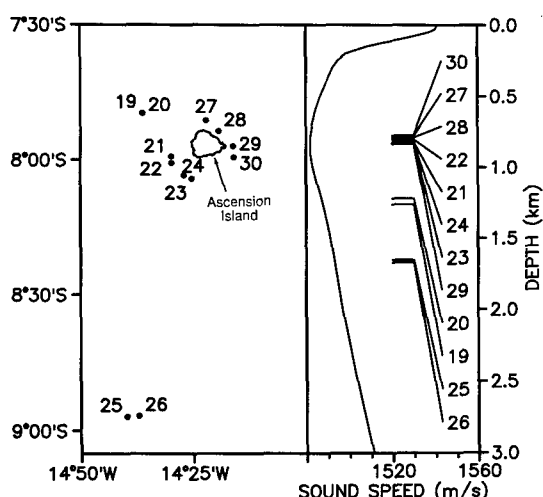


FIG. 5. Left-hand side: Locations (dots) of the Ascension MILS BOA hydrophones. The dots indicating the locations of hydrophones 19 and 20 overlap. Right-hand side: Hydrophone depths and the average sound speed for the region. Most hydrophone depths are near the depth of the sound channel axis.

guelen, and South African listening stations. Two complete digital systems were used at Ascension and recorded data from a total of eight hydrophones during the test. The signals were filtered and digitized in the same manner as those recorded on the systems used at the other stations.

Table I shows the data recorded by the BOA hydrophones according to transmission signal type. All 35 transmissions were recorded using the two digital data acquisition systems and 20 transmissions were recorded on 10 hydrophones using the MILS analog system. Some data were collected on all BOA hydrophones with the exception of hydrophone 27.

III. CHARACTERISTICS OF THE RECEIVED SIGNALS

A. cw transmissions and signal-to-noise ratios

An indication of the strength of the signals received at Ascension is shown in Fig. 7. Shown are 5 s of a strip chart recording of the reception of the initial transmission on hydrophone 23 (located south of the island at $8^{\circ}4.2'S$, $14^{\circ}25.2'W$ and at a depth of 832 m). The recording was made without logarithmic compression and without filtering. The 57-Hz cw transmission is quite apparent in the recording.

At 0145:06Z, indicated in the figure, 1 h, 44 min, 15 s had passed since the source ship began transmitting.⁶ From the recording, the time of travel of the first arrival is estimated to be between 1 h, 44 min, 15 s and 1 h, 44 min, 18 s. Spectral analysis indicates the best single estimate of the travel time of the earliest arrival at hydrophone 23 is 1 h, 44 min, 17 s. Processed M-sequence receptions indicate the direct, multipath arrivals are spread over 8–10 s.^{3,7}

Representative power spectral displays for the cw transmissions during the first day of the test are shown in Fig. 8. Each spectrum shown represents an incoherent average of 30 individual spectra, each of which was obtained by integration for 35.93 s giving a total averaging time of about 18 min. A complex 1024-pt fast Fourier transform (FFT) was used and each complex demodulated sample was determined from eight samples (two cycles) of the carrier for a sampling frequency of the demodulated signal of 28.5 Hz giving a Nyquist co-interval from -14.25 Hz to $+14.25$ Hz. The resolution of the individual lines is 0.0278 Hz. Convolution with a triangular window was used to reduce spectral sidelobes. In each case, the scale is linear and spectra are normalized so that the maximum rms value is unity.

Also shown are the signal-to-noise ratios for a 1-Hz band calculated from these power spectra. Measured signal-to-noise ratios in this paper have been adjusted to a hypothetical source level of 220 dB. This was done to account for the variations in source level that occurred during the test. No attempt was made to further adjust the signal-to-noise ratios for changes in noise level which may have occurred between transmissions.

Average signal-to-noise ratios for the nine cw transmissions are listed in Table II. They are again in a 1-Hz band. The ratios for the axial hydrophones south of the island range from about 19 to 30 dB. It is on these hydrophones that one would expect the reception to be strongest. Hydrophone

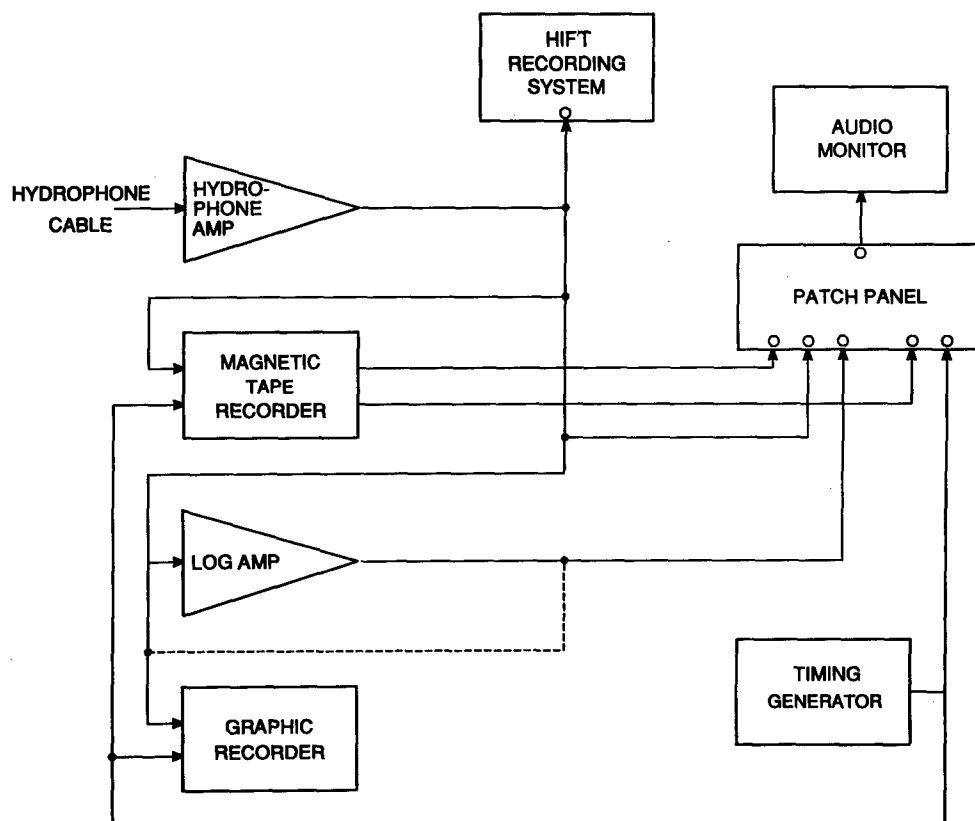


FIG. 6. Block diagram of the Ascension recording system.

25 (114 km from Ascension at a depth of 1650 m) is about 0.8 km below the axis. Its average signal-to-noise ratio of about 16 dB suggests acoustic energy was not restricted to a narrow depth interval centered about the sound channel axis. An examination of the normal-mode profiles⁸ calculated for the region about Ascension, indicates that mode 4 and higher are not attenuated at 0.8 km below the axis. It was anticipated that over global propagation distances the signal would consist only of the late SOFAR (sound fixing and ranging) arrivals that correspond to the lowest-order modes and that propagate along the axis.² The early SOFAR arrivals that have greater vertical extent and correspond to higher-order modes would be attenuated by interaction with the ocean's boundaries. The Ascension data, as well as the data obtained from the vertical array deployed off Monterey,⁹ indicate that some of the early SOFAR arrivals persisted.

The signals recorded on hydrophones 20 and 28 were clearly attenuated by propagation along or across the rising bathymetry associated with the island. None of the direct, horizontal ray paths from the source ship to the monitored hydrophones intersected the island, however.¹⁰

B. Phase stability and amplitude variability

The pentaline receptions illustrate the remarkable combination of phase stability and amplitude variability observed in the Ascension receptions. Figure 9 shows chart recordings of three periods of two pentaline signals. The top recording is of a signal made from an analog tape of a pentaline simulation.¹¹ It corresponds to an arrival without any multi-

path structure. The amplitude variability results only from the rapid 45° phase shifts of the coded signal.¹²

The top recording is compared with a chart recording of a portion of the pentaline signal of 1500Z, 29 January recorded at about 1644:33Z on hydrophone 22. The clearly evident pentaline period is an indication of the remarkable phase stability of the signal. For a hypothetical ocean frozen in time and a stationary source, each of the multipaths would have the pentaline period and an amplitude variability resulting from phase coding. The received signal, consisting of the coherent sum of the multipaths, would also have the period of the pentaline but an amplitude variability bearing no simple relationship to the amplitude variability of any one of the multipaths.

In the actual ocean, with a source in motion, the period of each multipath is not precisely defined because of phase variability. Figure 9 indicates that the individual multipaths have sufficient phase stability for the pentaline period to be evident in the received signal.

The experimental power spectrum for the 1500Z 29 January transmission is shown in the lower portion of the figure. It was obtained using a real 1024-pt FFT of the digitized signal (no demodulation) giving a frequency resolution of 0.223 Hz and an integration time of 4.49 s. An average of 500 individual spectra resulted in a total averaging time of 37.4 min.

Simultaneous strip chart recordings of three periods of a pentaline signal received on axial hydrophones 23, 29, and 30 are shown in Fig. 10. The pentaline period is again evi-

TABLE I. Data collected by BOA hydrophones 19–30, according to transmission signal type.

| No. | Transmission | | Hydrophone No. | | | | | | | | | | | |
|-------------------|--------------|------------|----------------|----------------|-----|----|----|----|----|-----|-----|----|----|----|
| | time | Julian Day | 19 | 20 | 21 | 22 | 23 | 24 | 25 | 26 | 27 | 28 | 29 | 30 |
| cw | | | | | | | | | | | | | | |
| 1 | 0000Z | 26 | A ^a | D ^a | A | DA | DA | DA | DA | A | ... | DA | DA | DA |
| 2 | 1200Z | 26 | A | D | A | DA | DA | DA | DA | A | ... | DA | DA | DA |
| 3 | 0000Z | 27 | A | D | A | DA | DA | DA | DA | A | ... | DA | DA | DA |
| 4 | 1200Z | 27 | A | D | A | DA | DA | DA | DA | A | ... | DA | DA | DA |
| 5 | 1200Z | 29 | A | D | A | DA | DA | DA | DA | A | ... | DA | DA | DA |
| 6 | 0000Z | 30 | ... | D | ... | D | D | D | D | ... | ... | D | D | D |
| 7 | 1200Z | 30 | ... | D | ... | D | D | D | D | ... | ... | D | D | D |
| 8 | 0000Z | 31 | ... | D | ... | D | D | D | D | ... | ... | D | D | D |
| 9 | 1200Z | 31 | ... | D | ... | D | D | D | D | ... | ... | D | D | D |
| Pentaline | | | | | | | | | | | | | | |
| 1 | 0300Z | 26 | A | D | A | DA | DA | DA | DA | A | ... | DA | DA | DA |
| 2 | 1500Z | 26 | A | D | A | DA | DA | DA | DA | A | ... | DA | DA | DA |
| 3 | 0300Z | 27 | A | D | A | DA | DA | DA | DA | A | ... | DA | DA | DA |
| 4 | 1500Z | 27 | A | D | A | DA | DA | DA | DA | A | ... | DA | DA | DA |
| 5 | 1500Z | 29 | A | D | A | DA | DA | DA | DA | A | ... | DA | DA | DA |
| 6 | 0300Z | 30 | ... | D | ... | D | D | D | D | ... | ... | D | D | D |
| 7 | 1500Z | 30 | A | D | A | DA | DA | DA | DA | A | ... | DA | DA | DA |
| 8 | 0300Z | 31 | ... | D | ... | D | D | D | D | ... | ... | D | D | D |
| 9 | 1500Z | 31 | ... | D | ... | D | D | D | D | ... | ... | D | D | D |
| 255/5 M-sequence | | | | | | | | | | | | | | |
| 1 | 0600Z | 26 | A | D | A | DA | DA | DA | DA | A | ... | DA | DA | DA |
| 2 | 1800Z | 26 | A | D | A | DA | DA | DA | DA | A | ... | DA | DA | DA |
| 3 | 0600Z | 27 | A | D | A | DA | DA | DA | DA | A | ... | DA | DA | DA |
| 4 | 1800Z | 29 | A | D | A | DA | DA | DA | DA | A | ... | DA | DA | DA |
| 5 | 0600Z | 30 | ... | D | ... | D | D | D | D | ... | ... | D | D | D |
| 6 | 1800Z | 30 | ... | D | ... | D | D | D | D | ... | ... | D | D | D |
| 7 | 0600Z | 31 | ... | D | ... | D | D | D | D | ... | ... | D | D | D |
| 8 | 1800Z | 31 | ... | D | ... | D | D | D | D | ... | ... | D | D | D |
| 511/5 M-sequence | | | | | | | | | | | | | | |
| 1 | 0900Z | 27 | A | ... | A | A | DA | DA | A | A | ... | A | DA | DA |
| 2 | 0900Z | 30 | ... | D | ... | D | D | D | D | ... | ... | D | D | D |
| 3 | 2100Z | 31 | ... | D | ... | D | D | D | D | ... | ... | D | D | D |
| 1023/5 M-sequence | | | | | | | | | | | | | | |
| 1 | 0900Z | 26 | A | D | A | DA | DA | DA | DA | A | ... | DA | DA | DA |
| 2 | 0900Z | 29 | A | D | A | DA | DA | DA | DA | A | ... | DA | DA | DA |
| 3 | 2100Z | 30 | ... | D | ... | D | D | D | D | ... | ... | D | D | D |
| 2047/5 M-sequence | | | | | | | | | | | | | | |
| 1 | 2100Z | 26 | A | D | A | DA | DA | DA | DA | A | ... | DA | DA | DA |
| 2 | 2100Z | 29 | A | D | A | DA | DA | DA | DA | A | ... | DA | DA | DA |
| 3 | 0900Z | 31 | ... | D | ... | D | D | D | D | ... | ... | D | D | D |

^aA "D" indicates the transmission was recorded using one of the two digital systems; an "A" indicates the transmission was recorded using the MILS analog system.

dent in each chart recording, but the amplitude variability has a pattern that varies from one hydrophone to the next.¹³ While it is likely the temporal variability of the signals is due primarily to source motion, the spatial variability illustrated in Fig. 10 may be due to a combination of source motion and changes in propagation conditions along the paths to the individual hydrophones.

On the right-hand side of Fig. 10 are power spectra for the three signals. They were obtained using a complex 1024-pt FFT where each complex demodulated sample was determined from two cycles of the carrier for an integration time of 35.93 s. Fifteen spectra were then incoherently averaged for a total averaging time of 8.98 min. (The three periods of the pentaline time series shown on the left-hand side

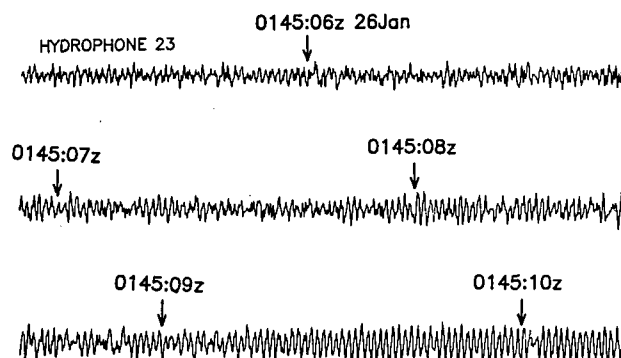


FIG. 7. Strip chart recording of the initial HIFT transmission on BOA hydrophone 23. Five seconds of the cw signal are shown. At 0145:06Z, 1 h, 44 min, and 15 s had passed since the source ship began transmitting.

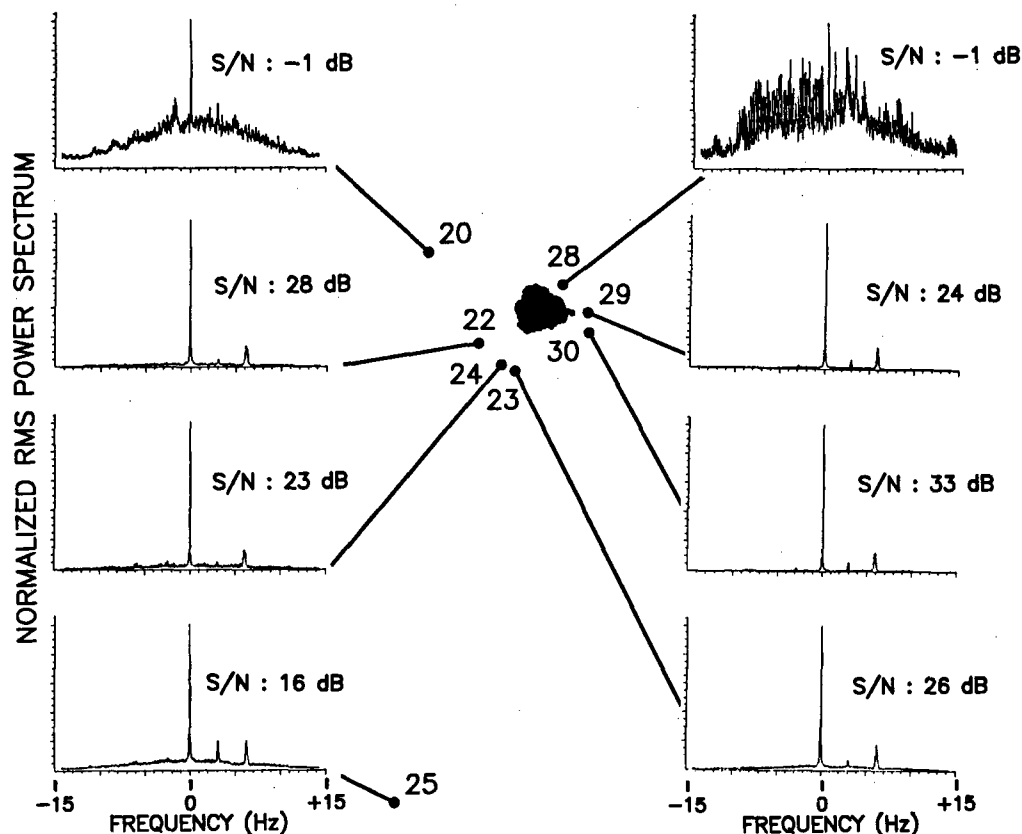


FIG. 8. Spectral displays for the cw transmissions during the first day of the test. The frequency range is from 15 Hz below to 15 Hz above the carrier frequency (57 Hz). As with all power spectra displayed in this paper, the peak values have been normalized to unity. The secondary peaks represent 60-Hz noise and the interference at 63 Hz between the signal and the 60 Hz line. The signal-to-noise ratios calculated from each power spectrum are for a 1 Hz band and have been adjusted to a source level of 220 dB.

of Fig. 10 are only 1.59-s samples of the time series analyzed to obtain the spectra on the right-hand side.) The differences in the spectral levels of the lines on either side of the carrier and for the three hydrophones illustrate the selective fading at the individual frequencies that constitute the signal. In the

TABLE II. Transmission-averaged signal-to-noise ratios for the nine cw transmissions.

| Hydrophone No. | Signal-to-noise ratio ^a | |
|----------------|------------------------------------|----------------------|
| | Average (dB) | Range of values (dB) |
| 20 | 2.1 | -4.9-6.5 |
| 22 | 25.2 | 19.7-28.1 |
| 23 | 30.0 | 25.8-35.1 |
| 24 | 18.7 | 15.2-22.0 |
| 25 | 15.8 | 8.3-19.3 |
| 28 | 3.2 | -3.9-7.7 |
| 29 | 25.7 | 22.2-27.3 |
| 30 | 25.7 | 22.2-27.3 |

^aFor a 1-Hz band and adjusted to a hypothetical source level of 220 dB (referenced to 1 μ Pa at 1 m). Average values listed were obtained using

$$\text{SNR}_{\text{average}} = 10 \log_{10} \left[\left(\frac{1}{9} \right) \sum_{i=1}^9 \left(\frac{S}{N} \right)_i \right],$$

where $\text{SNR}_i = 10 \log_{10}(S/N)$, is the signal-to-noise power ratio in decibels adjusted for variations in transmitted power by adding the difference between 220 dB and the actual source level to the measured signal-to-noise ratio for the i th transmission. The smallest and largest values of SNR_i are listed in the last column.

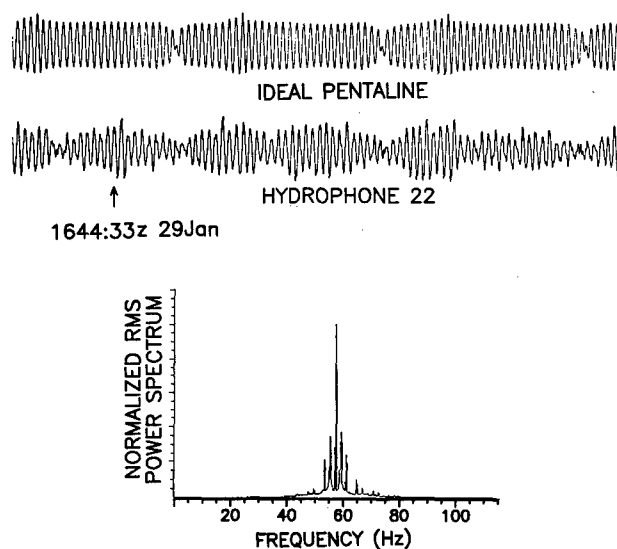


FIG. 9. Top: Strip chart recording of three periods of the pentaline signal of 1500Z, 29 January, recorded at about 1644:33Z on hydrophone 22 compared with a chart recording made from an analog tape of a pentaline simulation (ideal pentaline). The pentaline period consists of 30 cycles of the carrier partitioned into three digits of 10 cycles each. The period is 30/57 or about 0.53 s. Bottom: experimental power spectrum made by incoherently averaging 500 individual spectra, each of which was constructed by coherent integration for 4.49 s. Only a very small portion of the data record used to calculate the spectrum is displayed in the strip chart recording.

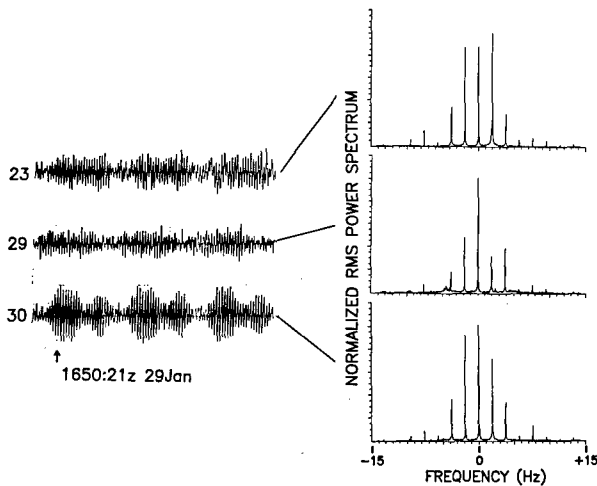


FIG. 10. Examples of spatial variability in the signal amplitude. Left-hand side: Strip chart recordings of three periods of the pentaline signal of 1500Z, 29 January recorded simultaneously at 1650:21Z on hydrophones 23, 29, and 30. Right-hand side: Spectra for the signals on the left-hand side calculated by Fourier transforming 35.9 s of the demodulated signal. Fifteen spectra were then incoherently averaged to obtain the power spectra shown.

top spectral display the carrier is not even the strongest line. The amplitude and phase of these lines produce the observed amplitude variability in the pentaline signals. One must average over a sufficiently long time period to reduce the influence of the fading and obtain symmetric spectra similar to the ideal pentaline spectrum. The power spectrum in Fig. 9 is an example. It was created by (coherently and incoherently) averaging for 37.4 min, while the spectra in Fig. 10 were obtained by averaging for 9.0 min.

The amplitude variability of the individual frequencies that constitute the main lobe of the pentaline signal can be seen in the time series of Fig. 11. The four arrows indicate examples of amplitude fades of individual spectral lines. Because the fading does not persist over the 1.9-Hz frequency interval between lines, the fading band width is less than this interval. Figure 11 was adapted from a plot contained in Ref. 14.

C. Late, scattered arrivals

There is anecdotal evidence that the signal that arrives at Ascension from a source in the South Atlantic or the Indian Ocean consists not only of the direct arrivals, i.e., the arrivals that propagate along the refracted geodesics, but also of arrivals scattered from the continental margins of South America, Africa, and Antarctica. Munk and Zachariasen¹⁵ recently suggested that scattered arrivals will be present in the recordings of basin- and global-scale transmissions and might provide additional information about the horizontal structure of the ocean. They computed relative intensities for scattering from simplified models of islands and seamounts and concluded that scattered arrivals can be a significant (–10 dB) component of the received signal.

During the test, a signal was routinely observed by real-time spectral analysis for at least 23 min after the direct signal ended. The spectrograms in Fig. 12 show this late signal. They both were produced by using a 16384-pt

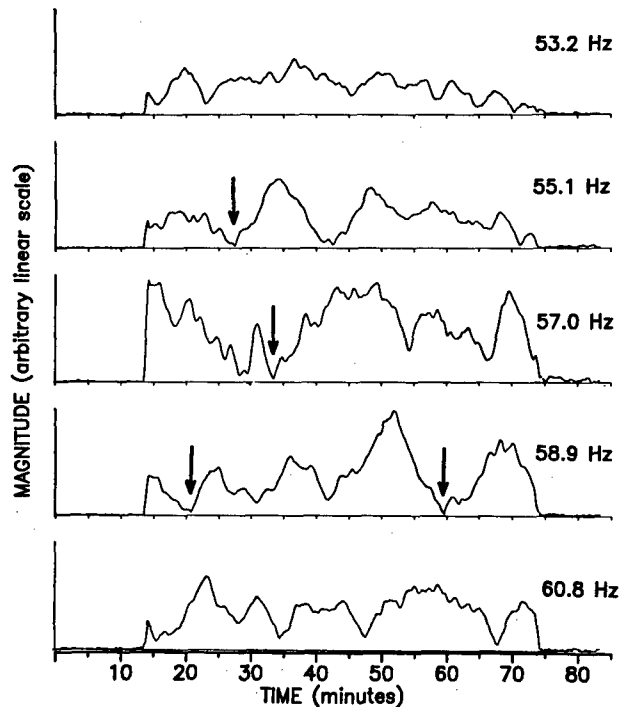


FIG. 11. Time series of the magnitude of the five spectral lines in the main lobe of the pentaline signal transmitted at 1500Z, 27 January, and recorded on hydrophone 23. The arrows indicate four examples of amplitude fading.

(71.9-s) real FFT of the digitized signal (no demodulation) with a 62.9-s overlap between consecutive transforms. The spectrogram consists of dots placed at the time of a particular FFT and at the frequencies for which the magnitudes are 3.0 times greater than the median magnitude for the transform. Only frequencies between 47 and 67 Hz are considered. The top spectrogram is for a pentaline transmission and the bottom one for a 255/5 M-sequence transmission, both recorded on hydrophone 23. The length of the pentaline spectrogram is 84 min, the nominal recording time for HIFT transmis-

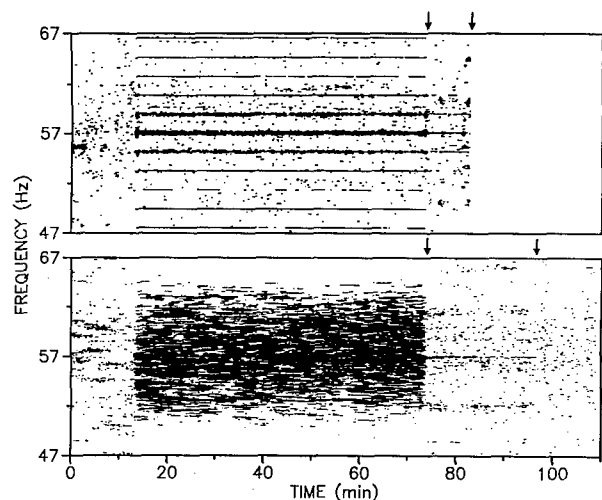


FIG. 12. Spectrograms showing a late, scattered signal. Top: Spectrogram for the 1500Z, 27 January, pentaline transmission. Bottom: Spectrogram for the 1800Z, 29 January, 255/5 M-sequence transmission. Both transmissions were recorded on hydrophone 23.

sions. The recording time for the M-sequence was extended to obtain additional data.

The direct signal began at about 12 min after recording started and lasted for 60 min. For each spectrogram the arrow at 72 min indicates its end. At any instant it consisted of the order of 10 identifiable arrivals.^{3,7,14} They all arrived within about 10 s of one another after having traveled for about 1 h, 44 min (to hydrophone 23) along distinct but closely spaced refracted geodesics.²

The identification of the direct signal has been based on travel-time and Doppler-shift considerations. For an average axial sound speed of 1.48 km/s, a travel time of 1 h, 44 min gives a propagation distance of 9240 km, consistent with the length of the refracted geodesics from the source ship to Ascension. The launch angles inferred from the overall Doppler shift of the direct signal agree with the angle of the refracted geodesics at the source ship.¹⁶ Deviations of the ship from a steady course have been correlated with variations in the overall Doppler shift of the direct signal but only if it is assumed the direct signal propagated along the refracted geodesics.¹⁷

The signal persisted beyond the time when the direct signal ended. The pentaline spectrogram in Fig. 12 indicates a weak signal was still present when data recording was terminated (arrow at 84 min). The M-sequence spectrogram shows the presence of a signal for about 23 min after termination of the direct signal (arrow at 97 min). Not all Fourier components are present in the spectrograms of the late signal; the weaker ones are lost in the noise. This late signal consists of arrivals having travel times up to 23 min longer than those of the direct arrivals or travel times of up to about 2 h, 7 min. For an average sound speed of 1.48 km/s, the corresponding propagation distance is up to 2040 km greater than the propagation distance of the direct signal. This late signal must have arrived at Ascension after having been scattered or diffracted from topographic features far removed from the geodesic. It is being investigated further by us using correlation techniques and Doppler-shift analyses.

IV. CONCLUDING REMARKS

The Ascension data set is of interest not only because it contributes to the objectives of the Heard Island Feasibility Test but also because the observed high signal-to-noise ratios provide an opportunity to study the characteristics of acoustic signals that have propagated over global distances. The survey of signal characteristics presented here and the analyses of the Ascension data set contained in several papers of this issue represent a first step in exploiting this opportunity. We expect that analysis of the data set will be a fruitful area of research for some time to come.

One area of investigation is likely to be the statistical study of signal variability. The signals recorded at Ascension are characterized by a combination of phase stability and amplitude variability. As an acoustic signal propagates in range, one expects that ocean variability would first result in phase fluctuations. Then, at greater ranges, these fluctuations would generate amplitude fluctuations (scintillations) through diffractive mechanisms. Subjectively, at least, the amplitude fluctuations of the Ascension signals are much

more significant than phase fluctuations and one wonders if these amplitude fluctuations can arise from such a stable phase.¹⁸

The time of travel of the earliest arrival from the source ship to hydrophone 23 (an axial hydrophone immediately south of Ascension) was approximately 1 h, 44 min, 17 s. However, some of the acoustic energy took considerably longer to reach Ascension. A late, scattered signal was observed for longer than 23 min after the end of the direct signal. It may be the result of reflections off the margins of southern-hemisphere continents and from islands and seamounts. The study of this signal may yield new techniques for acoustic remote sensing of the ocean over basin- and global-scale distances.

ACKNOWLEDGMENTS

We are grateful to the U.S. Air Force Systems Command, Eastern Space and Missile Center, and Computer Sciences Raytheon Company for supporting our data collection effort at Ascension. We thank the Office of the Assistant Secretary of Defense, Production and Logistics, for allowing space-required transportation to Ascension. Environmental data in the vicinity of Ascension were obtained with the assistance of officers and crew from U.S. Navy Patrol Squadron 26. We thank the participants in the HIFT at the APL/University of Washington and the University of Michigan for technical support. Much of the discussion of the spectral characteristics of the Ascension data is based on plots produced by Theodore Birdsall, Kurt Metzger, and Matthew Dzieciuch. We are particularly thankful to Walter Munk for his leadership in organizing the test. We gratefully acknowledge research support from the Assistant Administrator of NOAA's Office of Oceanic and Atmospheric Research, the Director of NOAA's Environmental Research Laboratories, and the Measurement Technique Development Element of NOAA's Climate and Global Change Program.

¹W. H. Munk and A. M. G. Forbes, "Global ocean warming: an acoustic measure?," *J. Phys. Oceanogr.* **19**, 1765-1778 (1989).

²W. H. Munk, R. C. Spindel, A. B. Baggeroer, and T. G. Birdsall, "The Heard Island Feasibility Test," *J. Acoust. Soc. Am.* **96**, 2330-2342 (1994).

³T. G. Birdsall, K. Metzger, and M. A. Dzieciuch, "Signals, signal processing, and general results," *J. Acoust. Soc. Am.* **96**, 2343-2352 (1994).

⁴D. R. Palmer, T. M. Georges, J. J. Wilson, L. D. Weiner, J. A. Paisley, R. Mathiesen, R. R. Pleshek, and R. R. Mabe, "Reception at Ascension Island, South Atlantic, of the Transmissions from the Heard Island Feasibility Test," NOAA Technical Memorandum ERL AOML-73 (February 1993).

⁵Adapted from J. G. Dworski, unpublished figure, Applied Physics Laboratory, University of Washington (1991).

⁶In this paper all times are Greenwich Mean Time and are indicated by the letter "Z" for Zulu.

⁷T. M. Georges, L. R. Boden, and D. R. Palmer, "Features of the Heard Island signals received at Ascension," *J. Acoust. Soc. Am.* **96**, 2441-2447 (1994).

⁸Provided courtesy of B. E. McDonald.

⁹A. Baggeroer, K. Lashkari, J. H. Miller, C. S. Chiu, P. N. Mikhalevsky, and K. von der Heydt, "Vertical array receptions off Monterey for the Heard Island Feasibility Test signals," *J. Acoust. Soc. Am.* **96**, 2395-2413 (1994).

¹⁰Hydrophone 27, the only BOA hydrophone not used during the test, definitely was in the shadow of the island.

¹¹This analog tape was provided courtesy of T. Birdsall, K. Metzger, and M. Dzieciuch, University of Michigan.

¹²The synthetic signal was produced by band-pass filtering the phase-coded signal to simulate the frequency response of a realistic source. Since not all the Fourier components resulting from the rapid 45° phase shifts were passed by the filter, amplitude variations occur at the times of the phase shifts.

¹³The maximum difference in arrival times between hydrophones 23, 29, and 30 for the direct signal from the source ship is about 3.5 s. The amplitude variability between hydrophones illustrated in Fig. 10 would not have been reduced had the strip chart recordings been aligned by arrival time.

¹⁴T. G. Birdsall, M. A. Dzieciuch, and K. Metzger, "Herald Island Feasibility Test: Signal processing, first results," University of Michigan Report, May 8, 1991 (unpublished).

¹⁵W. H. Munk and F. Zachariasen, "Refraction of Sound by Islands and Seamounts," *J. Atmos. Oceanic Technol.* **8**, 554–574 (1991).

¹⁶A. M. G. Forbes and W. Munk, "Doppler-inferred launch angles of global acoustic ray paths," *J. Acoust. Soc. Am.* **96**, 2425–2427 (1994).

¹⁷M. Dzieciuch, W. Munk, and A. Forbes, "Interpretation of GPS offsets from a steady course," *J. Acoust. Soc. Am.* **96**, 2414–2424 (1994).

¹⁸Reference 7 argues that the observed amplitude and phase variations are not inconsistent with those expected from mid-latitude internal waves in a range-independent ocean.

Features of the Heard Island signals received at Ascension

T. M. Georges

NOAA Environmental Technology Laboratory, Boulder, Colorado 80303

Linda R. Boden

CIRES, University of Colorado, Boulder, Colorado 80309

David R. Palmer

NOAA Atlantic Oceanographic and Meteorological Laboratory, Miami, Florida 33149

(Received 20 August 1992; accepted for publication 7 June 1994)

The Heard Island transmissions were received 9140 km away at Ascension Island by an irregular array of bottom-mounted hydrophones. The single-hydrophone signal-to-noise ratio sometimes exceeded 30 dB in a 1-Hz band, confirming the detectability of 57-Hz underwater sound at global distances. The arrival-time pattern consists of a single broad pulse about 10 s long, whose fine structure decorrelates in about 12 min, in sharp contrast with the stable, discrete sequences observed over shorter, midlatitude paths. The amplitude fluctuations of both the fine arrival structure and the unmodulated receptions are uncorrelated between hydrophones as little as 3.4 km apart. Phase varies less than one cycle during a 1-h transmission after correcting for source motion, and the rms phase difference between hydrophones is about 3 rad averaged over the array. Phasor diagrams suggest that the effects of both source motion and ocean dynamics vary over the array. The probability density functions of the real and imaginary parts of a downshifted cw transmission are nearly Gaussian.

PACS numbers: 43.30.Qd, 43.30.Pc, 43.30.Re

INTRODUCTION

The Heard Island Feasibility Test (HIFT) proposed by Munk and Forbes (1989) was conducted on 26–31 January 1991 (Munk *et al.*, 1994). Its purpose was to measure globally the strength and short-term stability of 57-Hz underwater sound transmitted from Heard Island in the southern Indian Ocean. If successful, the experiment would be a prelude to a global network of “acoustic thermometers” to monitor the effects of climate change on the deep ocean. Of the 14 worldwide receiving stations, the highest signal-to-noise ratios (S/N) were recorded at Ascension Island in the South Atlantic Ocean by a team of NOAA scientists and engineers using facilities provided by the U. S. Air Force (Palmer *et al.*, 1994).

Although coherently generated sound (in contrast with explosions) has never been observed at such distances (9140 km from Heard Island), signal-to-noise ratios were unexpectedly high, with single-hydrophone S/N sometimes exceeding 30 dB in a 1-Hz band. The strength of the receptions has not been completely explained, but it is believed to be due to a combination of three factors: A lack of obstructing bathymetry along the Heard–Ascension path, a relatively short path through the Antarctic surface duct, and low background (shipping) noise at Ascension. The variability of signal strength with time and over the Ascension hydrophone array is discussed by Palmer *et al.* (1994). Here, we briefly examine the pulse-arrival patterns of two coded transmissions and the phase and amplitude stability and spatial coherence of one unmodulated transmission.

I. SINGLE-HYDROPHONE ARRIVAL PATTERNS

Figure 1 shows the geometry of the eight bottom-mounted hydrophones at Ascension from which data were digitally recorded. Circles with an X indicate the locations of the four hydrophones whose signals were recorded on the primary data-acquisition system, and which were used to analyze the coded transmissions for arrival time. The circles with a dot indicate the two additional hydrophones that are used to analyze the unmodulated (cw) signals. All the hydrophones shown are located near the nominal depth of the sound-channel axis, about 800 m, with the exception of hydrophone 25, about 100 km south of the island, which lies at a depth of 1650 m. The orientation of a plane wavefront arriving from the nominal direction of Heard Island from Ascension (142 deg) is also shown.

We used the moving-ship tomography analysis program developed by the University of Michigan Communications and Signal Processing Laboratory to remove the pseudorandom (or M-sequence) coded phase modulation and reveal the pulse-arrival pattern. The demodulated time sequence is a cross correlation, versus time lag, between the downshifted received signal and a replica of the transmitted modulation code. The magnitude of the cross correlation shows, in effect, the pulse-arrival sequence every 22.4 s for a 255-digit M-sequence (Birdsall *et al.*, 1994). We smoothed the complex demodulates in time, as described by Spiesberger *et al.* (1989a), to improve the S/N by about 12 dB, at the expense of unneeded time resolution.

Figure 2 shows the pulse-arrival sequence versus relative arrival time for the 255-digit M-sequence transmission that began at 0600 UTC 26 January. The four panels show the receptions 104 min later at the four primary hydrophones

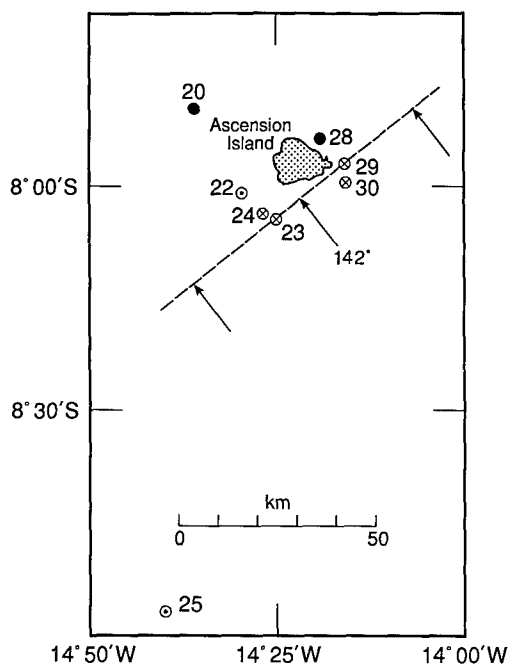


FIG. 1. Map of the vicinity of Ascension Island showing the geometry of the eight bottom-mounted hydrophones from which signals are digitally recorded during the Heard Island Feasibility Test. Circles with an X indicate the four primary hydrophones located near the sound channel axis, whose coded receptions are analyzed. The circles with a dot indicate two additional hydrophones whose cw receptions are studied. All the hydrophones shown are near the depth of the sound-channel axis, about 800 m, except that hydrophone 25 lies at a depth of about 1650 m. The signals at hydrophones 20 and 28 were significantly weaker than at the rest. A plane phase front from 142 deg, the nominal azimuth of Heard Island, is also shown.

near the sound-channel axis. The length of each record is the 84-min recording time, and the start and stop of the 1-h signal received at each hydrophone are clearly visible. Darkness is proportional to the signal magnitude, and the Doppler

shift caused by the average radial speed of the source ship has been removed. If it was not removed, the traces would have a nearly constant slope corresponding to the source's radial motion. Figure 3 shows the pulse-arrival patterns for another 255-digit M-sequence transmission beginning at 0600 UTC 27 January.

The main feature of all the coded arrivals is a "clump" of what appear to be dozens of pulses, the main part of which lasts about 10 s. Given the array geometry, a 142-deg angle of arrival, and an axial sound speed of 1480 m s^{-1} , a plane wavefront would arrive first at hydrophone 30, then (by coincidence) simultaneously 2.46 s later at hydrophones 23 and 29, then 1.99 s after that at hydrophone 24. The observed clumps do arrive at the four hydrophones in the correct order and roughly correct delay times, but because the detailed pulse structure within the clumps is almost uncorrelated among the hydrophones, relative clump arrival time can be estimated within only about 1 s, as is evident in Fig. 4.

The most persistent discrete pulses within the clumps appear to last 40 to 50 min, and many features are identifiable for about 20 min. To quantify this persistence, we computed the autocorrelation of the pulse-arrival pattern versus time for the eight panels of the two figures. The average $1/e$ decorrelation time is about 12 min, and the standard deviation is 4.5 min. Birdsall *et al.* (1994) computed the autocorrelation width of a single pulse to be about 0.1 s (compared with 0.088 s at the source).

In the patterns of Figs. 2 and 3, the arrival times of the identifiable and persistent features exhibit uncorrelated slope changes and "wiggles" with time. If these features correspond to energy arriving over many slightly different ocean paths, their travel-time (phase) fluctuations may be a measure of slightly different ocean-induced Doppler shift over those paths.

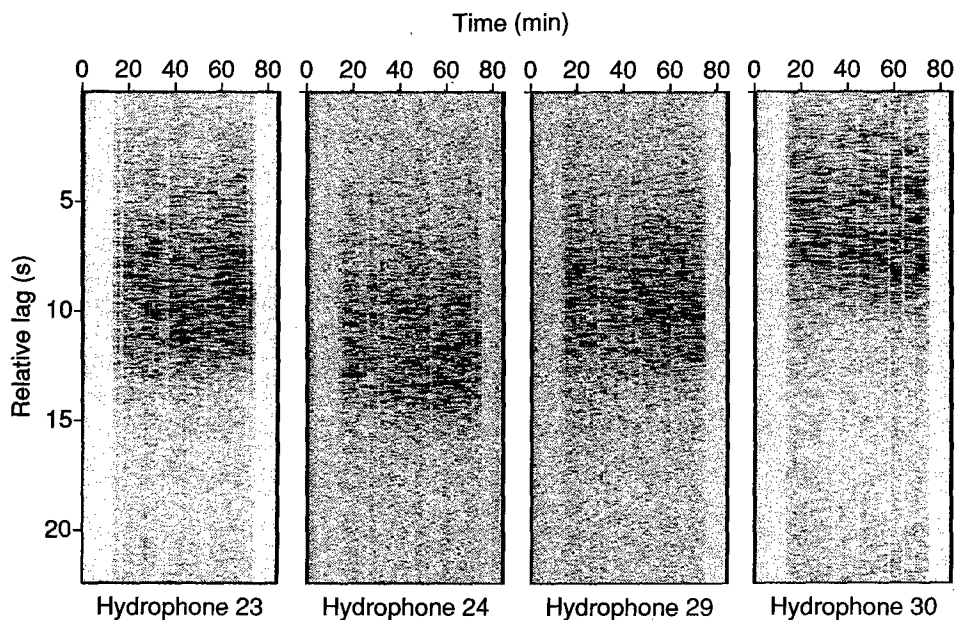


FIG. 2. Pulse-arrival amplitude sequences versus relative arrival time for the four primary hydrophones during the 255-digit M-sequence transmission beginning at 0600 UTC 26 January 1991. Darkness is proportional to signal magnitude, and the Doppler shift due to the average radial motion of the source ship has been removed.

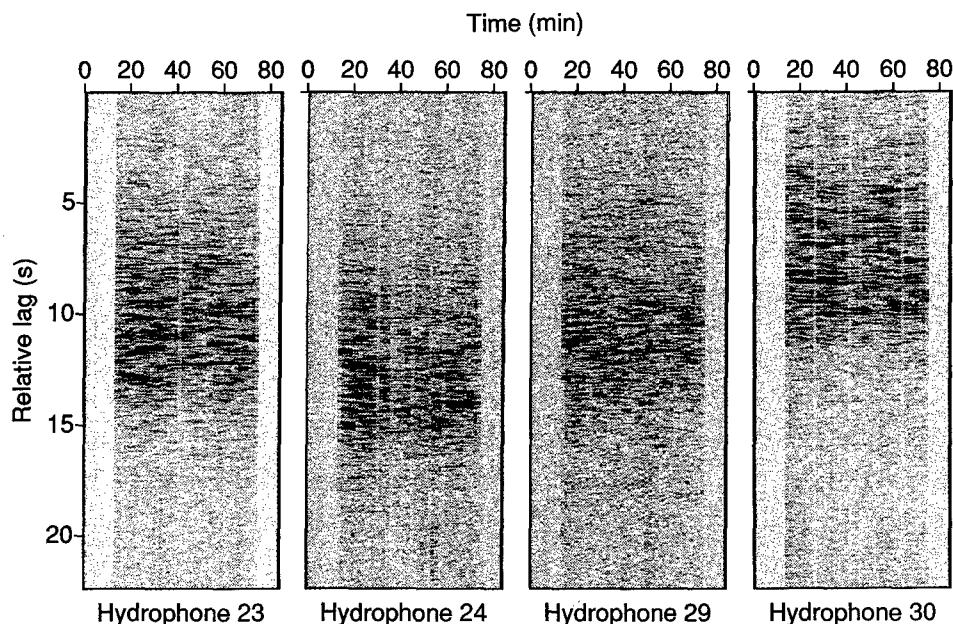


FIG. 3. Same as Fig. 2, except for the transmission beginning at 0600 UTC 27 January 1991.

A. Time-averaged arrival patterns

Because persistent arrival features or correlations among hydrophones might escape attention in the plots of Figs. 2

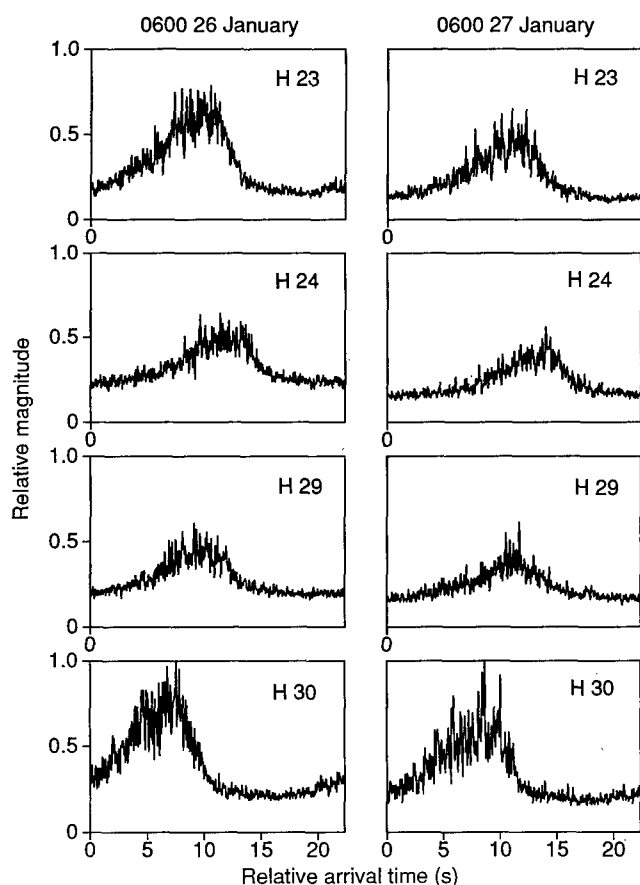


FIG. 4. Eight 1-h incoherent-average arrival patterns corresponding to the eight receptions shown in Figs. 2 and 3. No absolute intensity calibrations were performed; instead, hydrophone gains were adjusted to produce approximately the same background noise levels.

and 3, we show in Fig. 4 the 1-h incoherent average arrival pattern for each of the four hydrophones and the two M-sequence transmissions. The minimal correlation of average arrival patterns among hydrophones and transmissions is an unexpected result, in light of other experiences with 1000-km tomography paths and 3000–4000 km North Pacific paths (Spiesberger *et al.*, 1989a,b). The arrival pattern for pulse propagation in a sound channel usually consists of discrete and persistent pulses that can be identified with different resolvable ray paths (numbers of loops) between the source and receiver or, alternatively, with, resolvable normal modes (Munk and Wunsch, 1983). No such persistence is evident in the Heard–Ascension receptions.

B. Phase stability

In view of the instability of the observed amplitudes, we turn our attention to phase stability. Spiesberger *et al.* (1989a) showed how to interpret phase in terms of travel-time variability. Two kinds of phase measurement are possible, in principle. One uses cw transmissions (or coded transmissions, summing over multipaths), in effect merging the phase of multipath arrivals. Spiesberger *et al.* interpreted this integrated phase as responding to path-averaged barotropic (depth-independent) fluctuations in ocean temperature.

The second kind of phase measurement separates the multipath arrivals of coded transmissions. Different phase variability of different multipaths would reveal path-averaged, baroclinic (depth-dependent), ocean-temperature variability. Unfortunately, following the phase of a specific arrival feature requires continuously tracking that feature. Birdsall *et al.* (1994) did so for one Ascension reception and showed that phase remained stable for the 20 min or so that individual pulses could be tracked. For the Heard–Ascension path, therefore, only the integrated or barotropic phase appears to be of use for long-term tracking. We therefore examine the phase stability of a representative cw transmission.

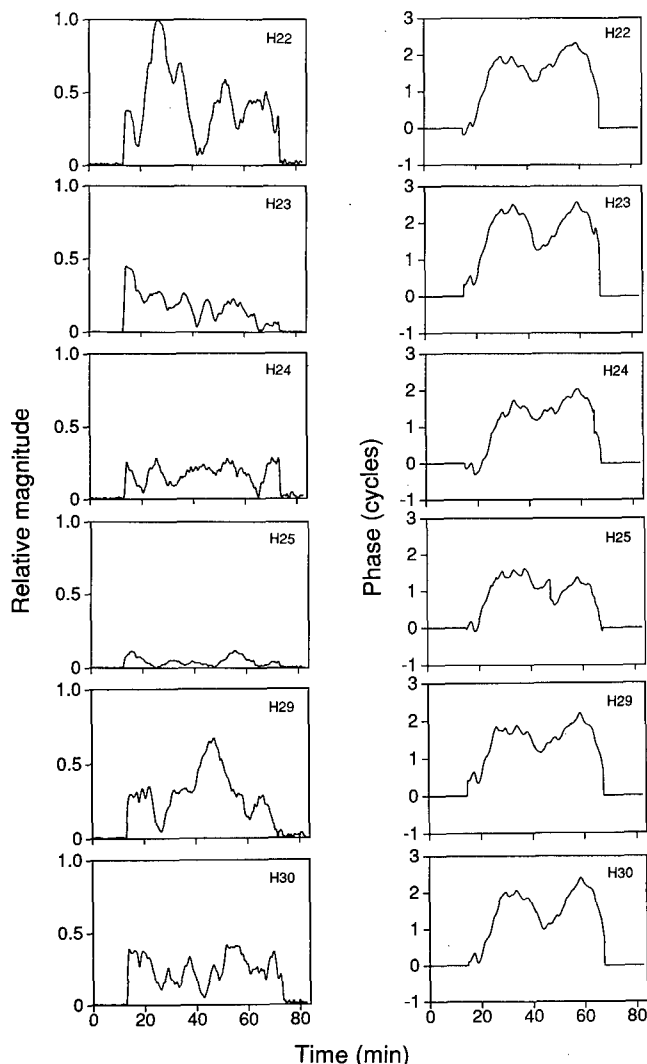


FIG. 5. The histories of amplitude and phase (with linear trend removed) at six hydrophones for the cw transmission beginning 1200 UTC 30 January 1991. The signals have been coherently averaged over 71-s intervals. Most of the phase variability is believed to be caused by nonuniform source motion.

Figure 5 shows the time histories of phase and amplitude of the cw transmission that began at 1200 UTC 30 January and was received at 1344 UTC at six Ascension hydrophones (Fig. 1). A linear trend has been removed from the phase plots to compensate for the uniform part of the radial source motion. The remaining phase fluctuations shown are caused by a combination of ocean variability and departures of the source ship from uniform radial motion. To extract the part of the phase due to ocean variability, it is necessary to estimate and remove the part of the phase (Doppler) attributable to nonuniform source motion. Birdsall *et al.* (1994) analyzed the ship motions derived from the Global Positioning System (GPS) during the 1200 UTC 27 January transmission and showed that most of the phase variability at a single hydrophone is due to nonuniform ship motion, such as ship surge. The residual phase, presumably due to ocean variability, varied by less than one cycle during the transmission. (Longer transmissions from a stationary source are required to determine longer-term phase stability.) A similar result would be

obtained by subtracting the average phase variation over several hydrophones, assuming that most of the average phase variability is due to nonuniform source motion.

II. CROSS CORRELATIONS BETWEEN HYDROPHONES

The coherence of the receptions over the irregular hydrophone array is of interest for the design of horizontal receiving arrays, for interferometric studies of arrival-angle stability, and for the use of scintillations over the array to measure cross-path transport by waves and ocean currents (Farmer and Clifford, 1986). The negligible degree of spatial coherence of the pulse-intensity arrival pattern is evident from Figs. 2, 3, and 4. The computed time-lagged intensity covariance between hydrophones thus exhibits only a broad maximum at about the correct clump lag and reveals no fine structure that can be attributed to the correlation of individual arrivals. For the two coded transmissions studied, the average cross-correlation coefficients of the amplitude pattern at the expected time lag for the hydrophone 23–24 pair are 0.30 and 0.29. For the 23–30 pair, they are 0.37 and 0.38. (Strangely, the higher correlation is for the more widely separated hydrophone pair: 23 and 24 are 3.4 km apart with a transverse separation of 1.57 km, and 23 and 30 are 19.2 km apart with a transverse separation of 18.9 km.)

A. Mutual coherence, phase structure function, and coherence length

Flatté *et al.* (1979, Eq. 8.5.1) show that, for a wide range of propagation conditions, the mutual coherence function (MCF) is

$$\text{MCF} = \langle \psi_1 \psi_2^* \rangle = \exp(-D/2),$$

where D is the phase structure function, and ψ_1 and ψ_2 are appropriately normalized complex demodulates at two separated receivers. The coherence length is the separation where $\text{MCF} = 1/e$. We therefore computed the average MCF for six 10-min pieces (estimated coherence time) of the cw transmission and hydrophone pairs 23–24 (3.4-km separation) and 23–30 (19.2-km separation). Both normalized MCFs were less than 0.1. We conclude that the transverse coherence length is less than the smallest transverse hydrophone separation (1.57 km).

B. Directional stability

Because the Ascension hydrophones are deployed in an irregular array and are spaced many acoustic wavelengths apart (about 113 for the closest pair, 23–24), coarse direction of arrival can (in principle) be computed from relative pulse-arrival times, and fine directional stability within a grating lobe can be estimated from phase differences, provided phase is coherent between hydrophones. As Figs. 2, 3, and 4 show, only crude pulse-arrival delays can be obtained because of the low amplitude coherence for the hydrophone spacings used. However, real-time phase observations made at Ascension using the unfiltered analog signals from hydrophones 23 and 24 to form a stable oscilloscope Lissajous

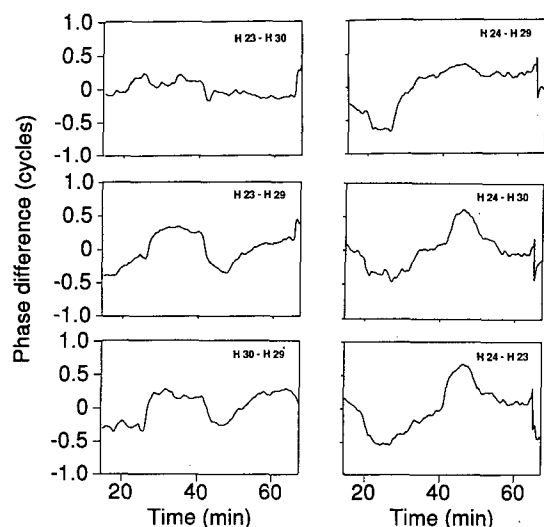


FIG. 6. Zero-lag phase differences between six hydrophone pairs, using the cw transmission of 1200 UTC 30 January. The mean phase difference (many cycles) has been removed, and the signs of the differences have been chosen by ordering the hydrophones along the unperturbed plane wavefront direction (Fig. 1).

pattern suggested phase coherence (little change in phase difference) for at least 10 min between these two hydrophones during cw receptions.

To examine phase coherence (that is, arrival-angle wander) over the array more closely, we computed phase differences among six hydrophone pairs. To compare phase differences consistently, that is, so that the sign of a given phase change corresponds to the same sign of arrival-angle change, we ordered the hydrophones progressing northeastward along the arriving phase front (Fig. 1). Figure 6 shows representative (zero-lag) phase differences between all pairs of the four primary hydrophones, 23, 24, 29, and 30.

First, we see that the phase differences vary by less than one cycle during the 1-h transmission. A rough translation from phase to arrival direction gives a sensitivity of about 0.08 angular degrees for 1 rad of phase change between hydrophones 23 and 24.

Next, we see correlations of the phase-difference variations between some hydrophone pairs, but not others. For example, the phase difference between H30 and H29 appears to be correlated with the difference between H23 and H29. Similarly, the H24-H30 difference appears to be correlated with the H24-H23 difference, and to a lesser degree with the H24-H29 difference. However, these correlations do not depend in a simple way on the transverse separations of the hydrophones. We conclude that the shape of the arriving wavefront is complex and that many more measurements would be required to obtain a statistically significant estimate of phase coherence length.

III. PHASOR PATTERNS

Another aid to understanding propagation mechanisms lies in the time variability of the downshifted acoustic phasor. Flatté *et al.* (1979), for example, used phasor patterns

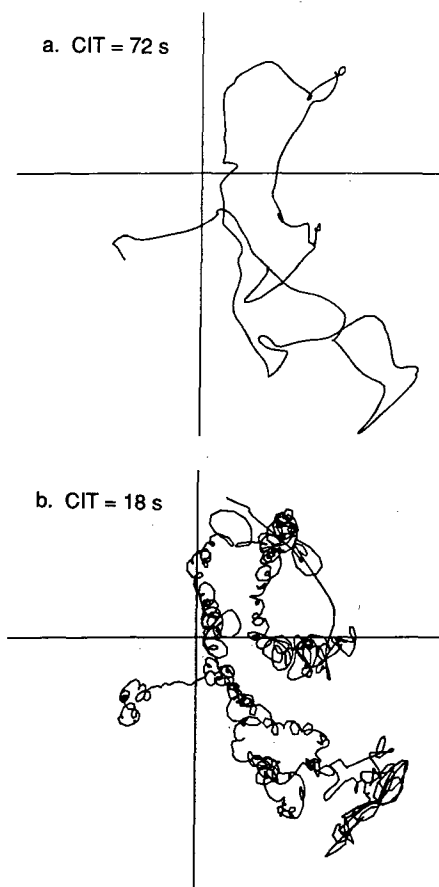


FIG. 7. Phasor diagrams showing the downshifted cw signal received at hydrophone 22 for the transmission at 1200 UTC 30 January 1991. In the top diagram, each point represents a coherent average over 72 s ($\frac{7}{8}$ overlap), whereas for the lower diagram, it is 18 s. A four-hydrophone-mean phase has been removed. CIT is the coherent integration time.

and amplitude statistics to identify the scattering regime in the theory of propagation through random media.

Figure 7(a) shows a representative phasor diagram for the 1-h cw transmission made by sampling the complex downshifted time series at hydrophone 22 using a running coherent average 72-s long with $\frac{7}{8}$ overlap (9-s time steps). The residual phase used to construct this diagram is computed by removing the mean phase over the four hydrophones with the strongest signals (22, 23, 29, and 30) rather than the GPS-derived ship motion. The residual phase is therefore a mixture of the (high-pass spatially filtered) parts of the ship-surge and ocean-dynamics effects that vary over the array. The pattern resembles a short sample of a random walk with a few deterministic phase fluctuations superimposed.

If we quadruple the time resolution by using a running 18-s coherent average (2-s time steps), we get Fig. 7(b), which resolves a small-scale quasiperiodic looping pattern that is smoothed out by the longer average. The pattern persists, though with more high-frequency noise, when even greater time resolution is used. It may be the signature of the source ship surging through ocean swell (and the response of the source string), but this is only conjecture. If true, the effects of source motion vary over the receiving array, since

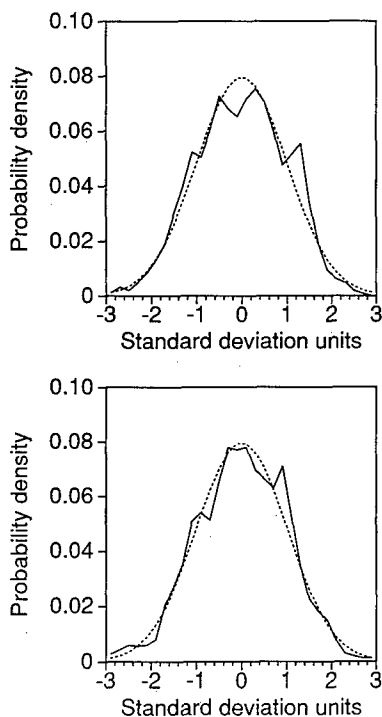


FIG. 8. Probability density functions for the real (top) and imaginary (bottom) parts of the downshifted signal received at six hydrophones from the cw transmission at 1200 UTC 30 January 1991. Samples are smoothed over 18 s with $\frac{7}{8}$ overlap, and signals from the six hydrophones are normalized to their rms values. The dotted line shows a Gaussian distribution for comparison.

we have removed the four-hydrophone mean phase.

IV. SIGNAL STATISTICS

Using the complex downshifted cw time series from six hydrophones and normalizing to their respective rms values to remove unknown hydrophone-gain factors, we computed the probability density functions (PDFs) of their real and imaginary parts. As in the phase diagrams, the statistics appear to be a mixture of source-motion and ocean-dynamics effects, so that the fine structure of the PDFs depends on the amount of smoothing applied to the time series. For 18-s smoothing with $\frac{7}{8}$ overlap, the PDFs (Fig. 8) are close to a Gaussian shape, shown as the dotted line (rms errors of 0.005 and 0.006 for the real and imaginary parts). The largest rms error encountered was 0.018 for 36-s smoothing. Gaussian statistics may result from a number of causes (such as deterministic multipath) and do not necessarily prove that the propagation is fully saturated, in the sense defined by Flatté *et al.* (1979).

V. INTERPRETATION

Monitoring climate change using acoustic thermometry requires tracking the travel-time changes of stable, identifiable arrival features over a period of years. The expected ocean-temperature increase is about 12 millidegrees C per year, an average of the expected 20 millidegrees at the surface and the 4 millidegrees at 1-km (Munk, 1991). This translates into an acoustic travel-time change of about 246

ms for a 9.14-Mm path, or a phase change of about 14 cycles per year at a 57 Hz frequency. Such changes are easily measurable with the instruments of ocean acoustic tomography (Worcester *et al.*, 1991).

The limits on detecting such a long-term temperature trend are imposed by the much larger “noise” of shorter-term ocean variability and by acoustic dispersion that spreads the arrival pattern in time. Ocean variability is believed to be dominated by two scales of motion: mesoscale eddies, with time scales of months, and internal waves, with time scales of minutes and hours. The effects of mesoscale eddies on acoustic thermometry have been modeled deterministically by Semtner and Chervin (1990) using an eddy-resolving ocean model.

Of more direct concern in this short experiment is the variability caused by internal waves, which is usually modeled statistically. According to figure 8.6 of Flatté *et al.* (1979), internal-wave-dominated propagation is expected to lie in the fully saturated regime (many uncorrelated micromultipaths), with a strength parameter Φ of about 5, for the frequency and range of the Heard–Ascension path. For full saturation, the cw wavefunction phasor should follow a random walk with an rms phase rate (Eqs. 7.5.16–17) of about 3.4 rad h^{-1} for a flat ray, and about 9 rad h^{-1} for a steep ray. Estimating amplitude coherence time using their Eq. (8.4.12) gives about 12 min for the Heard-to-Ascension path. Using $l_H=3.7 \text{ km}$ (p. 119) in their Eq. (8.5.2) to estimate the transverse coherence length of the acoustic field gives about 1.8 km. None of these estimates differs greatly from our Ascension observations. We should note, however, that Flatté *et al.* based their model on a large number of micromultipaths surrounding a single geometric ray and not the superposition of many geometric rays.

The failure of the arrival time sequence to separate into stable, identifiable pulses may be caused by the nonuniformity of the path, which traverses Antarctic and tropical waters. Shang *et al.* (1994) have shown that mode coupling is significant near the Circumpolar Front, where the sound channel changes from a surface duct to a deep sound channel and in this transition actually splits into two ducts. Strong mode coupling multiplies the number of paths in mode space; that is, different arrival times are expected for a pulse propagating as mode m up to the coupling region, then as mode n to the receiver, for all values of m and n for which coupling is significant. If pulses arriving by different paths in mode space overlap in time, the fine structure of the observed arrival pattern may be at least partly due to mode interference, and its time variability can be caused by ocean dynamics, source motion, or both.

We have not yet interpreted the arrival patterns in terms of propagation mechanisms; indeed, this may not be possible in detail. The multiplicity and instability of the Ascension pulse-arrival patterns could represent (a) discrete but unstable rays or modes, (b) a single dominant ray or mode dispersed by micromultipath, or (c) the interference of unresolved or overlapping rays and/or modes unique to this non-

uniform path. The instability of the pattern with time suggests great sensitivity to source position, ocean dynamics, or both. Probably the best that can be done is to combine deterministic and stochastic representations of the paths to reproduce the qualitative features of the receptions.

With regard to the detectability of the travel-time increase caused by the expected greenhouse warming, (a) we cannot infer anything from the short-term stability of the Heard-Ascension pulse-intensity arrival pattern, because the pattern decorrelates in 12 min; and (b) the rms phase change of the Heard-Ascension transmissions appears to be about a few radians per hour in the part of the spectrum dominated by internal waves. These fluctuations can be filtered out by space-time averaging. With 2-h gaps between transmissions, the experiment is unlikely to yield any information about phase stability for periods longer than the 1-h transmissions. The detectability of greenhouse warming will depend not on short-term phase stability but on longer-term phase fluctuations caused by mesoscale eddies and by interannual variability. The best available information about long-term phase and travel-time stability for basin- and global-scale paths still appears to come from the simulations of Semtner and Chervin (1990) and from the North-Pacific acoustic measurements of Spiesberger *et al.* (1989a,b).

ACKNOWLEDGMENTS

We thank K. D. Heaney, R. M. Jones, R. J. Lataitis, B. E. McDonald, and E. C. Shang for helpful discussions and K. Metzger for providing the moving-ship tomography analysis software. We are also grateful to the Center for Wave Phenomena, Colorado School of Mines, for the use of its computing facilities and seismic display programs.

- Birdsall, T. G., Metzger, K., and Dzieciuch, M. A. (1994). "Signals, signal processing, and general results," *J. Acoust. Soc. Am.* **96**, 2343-2352.
- Farmer, D. M., and Clifford, S. F. (1986). "Space-time acoustic scintillation analysis: a new technique for probing ocean flows," *IEEE J. Oceanic Engr.* **OE-11**, 42-50.
- Flatté, S. L. (1983). "Wave propagation through random media: contributions from ocean acoustics," *Proc. IEEE* **71**, 1267-1294.
- Flatté, S. L. (Ed.), Dashen, R., Munk, W. H., Watson, K. H., and Zachariasen, F. (1979). *Sound Transmission Through a Fluctuating Ocean* (Cambridge U.P., Cambridge).
- Munk, W. H., Spindel, R. C., Baggeroer, A. B., and Birdsall, T. G. (1994). "The Heard Island Feasibility Test," *J. Acoust. Soc. Am.* **96**, 2330-2342.
- Munk, W. H., and Forbes, A. M. G. (1989). "Global ocean warming: an acoustic measure?" *J. Phys. Oceanogr.* **19**, 1765-1778.
- Munk, W. H., and Wunsch, C. (1983). "Ocean acoustic tomography: rays and modes" *Rev. Geophys. Space Phys.* **21**, 777-793.
- Munk, W. H. (1991). "The Heard Island Experiment" *Inaugural Lecture, International Science Lecture Series* (National Academy, Washington, DC).
- Palmer, D. R., Georges, T. M., Wilson, J. J., Weiner, L. D., Paisley, J. A., Mathiesen, R., Pleshek, R. R., and Mabe, R. R. (1994). "Reception at Ascension Island, South Atlantic, of the transmissions from the Heard Island Feasibility Test" *J. Acoust. Soc. Am.* **96**, 2432-2440.
- Semtner, A. J., and Chervin, R. M. (1990). "Environmental effects on acoustic measures of global warming," *J. Geophys. Res.* **95**, p. 12,973-12,982.
- Shang, E. C., Wang, Y. Y., and Georges, T. M. (1994). "Dispersion and repopulation of Heard-Ascension modes" *J. Acoust. Soc. Am.* **96**, 2371-2379.
- Spiesberger, J. L., Bushong, P. J., Metzger, K., and Birdsall, T. G. (1989a). "Ocean acoustic tomography: estimating the acoustic travel time with phase" *IEEE J. Oceanic Eng.* **OE-14**, 108-119.
- Spiesberger, J. L., Bushong, P. J., Metzger, K., and Birdsall, T. G. (1989b). "Basin-scale tomography: synoptic measurements of a 4000-km length section in the Pacific," *J. Phys. Oceanogr.* **19**, 1073-1090.
- Worcester, P. F., Cornuelle, B. D., and Spindel, R. D. (1991). "A review of ocean acoustic tomography: 1987-1990," *Rev. Geophys. Suppl., U. S. National Report to IUGG 1987-1990*, 557-570.

Observation of the Heard Island signals near the Gulf Stream

Ian A. Fraser and Peter D. Morash

Defence Research Establishment Atlantic, P.O. Box 1012, Dartmouth, Nova Scotia B2Y 3Z7, Canada

(Received 20 August 1992; accepted for publication 7 June 1994)

Transmission-loss and spatial-coherence data were obtained for acoustic signals of center frequency 57 Hz projected from the vicinity of Heard Island in the southern Indian Ocean during the 1991 Heard Island Feasibility Test. The acoustic signals were monitored nearly 17 000 km away from the source by a 1.8-wavelength-long array of hydrophones towed from warm water south of the Gulf Stream to the much colder water north of the Stream. An adiabatic normal mode model predicted acoustic transmission losses in good agreement with those measured in cold water near the Gulf Stream. In warmer water, the measured signal level was generally higher than predicted, possibly because of signal energy scattered from lower to higher modes by boundary scattering. At the most southerly measurement sites, no signal was detected, probably because of bathymetric blockage. The spatial coherence of the signal was limited only by incoherent background noise and occasional interfering signals from discrete directions.

PACS numbers: 43.30.Qd, 43.30.Bp

INTRODUCTION

Transmission-loss and spatial-coherence data were obtained by Defence Research Establishment Atlantic (DREA) for the 57 Hz center-frequency acoustic signals projected from the vicinity of Heard Island in the southern Indian Ocean during the Heard Island Feasibility Test (HIFT). The HIFT signals were expected to travel between Africa and South America into the North Atlantic Ocean, eventually reaching the continental shelf off the northeastern United States.^{1,2} Fortunately, the DREA research vessel CFAV QUEST was scheduled to tow a research array of hydrophones across the Gulf Stream during a portion of the signal-transmission period, while engaged in other experimental activities. Although the received signals were relatively weak, the unusual opportunity to measure properties of an acoustic signal propagating nearly 17 Mm (17 000 km) in the ocean renders the results worth reporting.

As QUEST transited northeastward from the vicinity of the Bahamas, the signal from Heard Island was expected to become detectable only after the ship moved out of an acoustical shadow cast by South America. A substantial increase in signal level at the array tow depth of 100–200 m was expected after passage out of the warm Sargasso Sea and Gulf Stream into the cooler water of the continental slope, where the sound-channel axis, and hence the major concentration of acoustic energy, moves to shallower depths.^{3,4}

Digital recordings were made of signals from a 48-m-long segment of the array at intermittent times on 29 and 30 January 1991. Approximately 8 h of acoustic data were recorded on occasions when the projector signal was expected to be present (taking into account the 3.15-h transit time of the signals from Heard Island). To date, spectral analysis has been conducted on the signals from four hydrophone groups in the array in a first pass through the data. The spectral data have been processed further to obtain (1) absolute values of transmission loss at times when the HIFT signal was resolvable from background noise and interfering signals, and (2) coherence magnitude and phase information during two pe-

riods when the signal was strongest relative to the background interference.

In Sec. I we briefly describe the experimental equipment, the locations and environment in which it was operated, and the signal analysis parameters. Model results obtained using an adiabatic normal mode model are presented in Sec. II and are compared with experimental transmission losses in Sec. III. Section III also includes a description and interpretation of the spatial coherence results, and data on the signal arrival direction. Finally, the conclusions drawn from the experiment are presented in Sec. IV.

I. EXPERIMENTAL DETAILS

The locations of the research vessel as it moved northeastward during the times of data collection on 29 and 30 January 1991 are depicted as filled circles in the portion of the western North Atlantic Ocean displayed in Fig. 1. The lightest grey shading represents continental-shelf water less than 200 m deep. The darkest shading represents the deep basin with depths greater than 4 km. The intermediate shade includes the continental slope, part of the continental rise, and sea mounts. The dashed curves define the estimated boundaries of the Gulf Stream during the experimental period. Two of the expected paths of signals from Heard Island,⁵ annotated by their azimuthal direction of emission from the source, are also included in the figure. These paths define approximate shadow boundaries imposed on the left by South America and Bermuda, and on the right by southern Africa. The two southeast-pointing arrows indicate the arrival directions of the HIFT signal inferred from interhydrophone coherence phase measurements at two of the recording locations.

The measurement array consisted of 24 groups of eight equispaced hydrophones, with 2 m spacing between adjacent groups. Each hydrophone and its associated electronics was amplitude calibrated to better than 1 dB. (Henceforth each group of eight hydrophones will be referred to as a "sensor" to simplify the discussion.) Tow depths ranged between 165

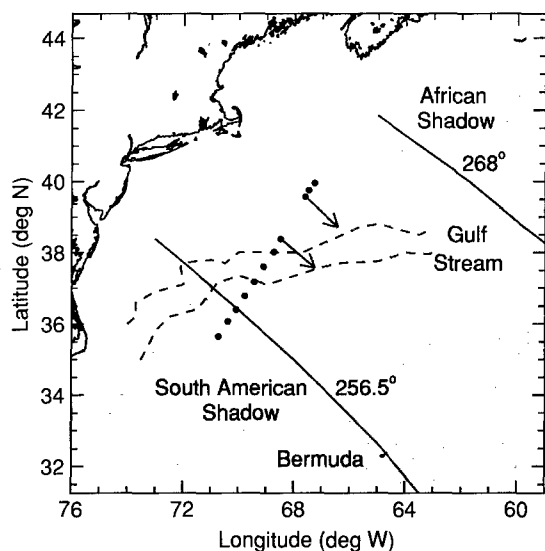


FIG. 1. Map of western North Atlantic Ocean showing data collection locations (●) and the estimated position of the Gulf Stream during the experiment; solid lines refer to the northern and southern limits of unobstructed signal paths from Heard Island; arrows indicate measured arrival directions of signals.

and 208 m during the observation periods. The digitally recorded data from four of the sensors were subsequently played back through an analog-reconstruction system and re-sampled at 250 Hz to allow a "quick-look" spectral analysis to be performed at a maximum frequency resolution of 0.031 Hz using 8192-point FFTs. As other experiments were being conducted near the receiving array during the HIFT, only two of the 1-h data collection periods were relatively free of interruptions. During the remaining periods, the data stream was interrupted for a few seconds at intervals of 1.0, 3.5, or 5.0 min. Because of the weak signal and frequent interruptions, it repeatedly proved necessary to alter the spectral analysis parameter values to obtain the best compromise among conflicting requirements on frequency resolution, sample-collection time, and number of averaged samples.

The measurement system operated during ten of the 1-h signal projection periods (allowing for the 3.15 h propagation time to the receiver location). The actual projection times and estimated source levels⁶ are listed in Table I. No effort was made to investigate the information provided by the various sidebands of the 57 Hz carrier signal during the first pass through the data. Examples of the spectra obtained during the period when the average transmission loss was smallest are provided in Fig. 2. On this occasion, the source was emitting a "pentatone" signal consisting essentially of the carrier and four dominant sidebands equispaced in frequency at intervals of 1.9 Hz.⁵ Signals arriving in phase at four array sensors were summed to produce the displayed spectra (as described in Sec. III B) in order to increase the signal-to-noise ratio (SNR). The four spectra are consecutive, starting at the bottom of the figure, with successive spectra offset vertically by values shown at the right-hand side of the figure. The frequency resolution was 0.031 Hz and the averaging time for each spectrum was 65.5 s. An examination of the amplitudes of the signals in these and 14

TABLE I. Projector operating times and source levels (Ref. 6) during DREA recording periods.

| Date (Jan. 1991) | Time on (UTC) ^a | Time off (UTC) | Effective source level (dB/1 μ Pa@1 m) |
|------------------------------|-------------------------------|-------------------|--|
| 29 | 12:00 | 13:00 | 220.8 |
| | 15:00 | 16:00 | 217.8 |
| | 18:00 | 18:37 | 217.8 |
| | 18:37 | 19:00 | 215.7 |
| | 21:00 | 22:00 | 215.7 |
| 30 | 00:00 | 01:00 | 218.7 |
| | 03:00 | 04:00 | 215.7 |
| | 06:00 | 07:00 | 215.7 |
| Measurement system inboard | | | |
| | 15:00 | 16:00 | 210.0 |
| | 18:00 | 19:00 | 210.0 |
| | 21:00 | 21:17 | 213.2 |
| Measurement system shut down | | | |

^aUniversal Coordinated Time (essentially equivalent to the former standard, Greenwich Mean Time).

other successive spectra (not illustrated) suggests that there was little correlation among the amplitudes of the five signals.

Transmission losses were determined experimentally by subtracting the signal-level estimates obtained with the calibrated sensors from the effective source levels listed in Table I for the appropriate time period, allowing for the propagation time. Each of the signal-level estimates includes an ambient-noise correction based on the median of background-noise estimates in frequency bands surrounding the signal frequency. The transmission-loss data are presented and discussed in Sec. III A.

In addition to the autospectral analysis performed on all of the data, cross-spectral analysis was performed on two data segments that were relatively free of interruptions. The results are presented in Sec. III in terms of coherence magnitude and signal arrival direction.

To supplement the acoustic data, expendable bathyther-

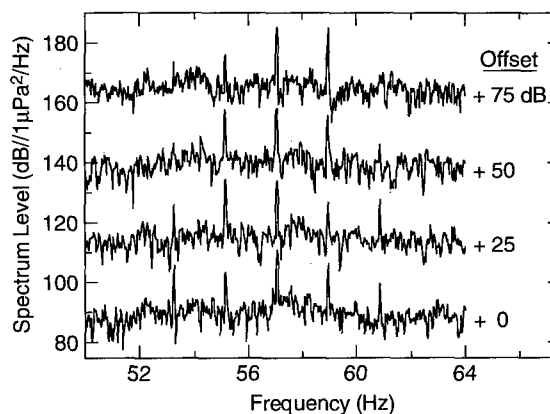


FIG. 2. Successive power spectra (starting at the bottom of the figure) of the "pentatone" Heard Island signals, as measured at a range of nearly 17 Mm with a frequency resolution of 0.031 Hz.

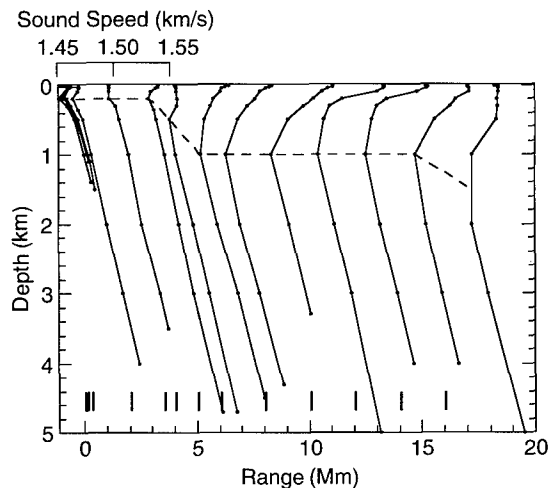


FIG. 3. Sound-speed profiles used in modeling the sound transmission from Heard Island to the vicinity of Bermuda; the sound-speed scale refers to the leftmost profile; for each profile the sound speed of 1.48 km/s is located directly above a vertical bar which, in turn, is located at the measurement range of the profile; (---) depth of sound-channel axis.

mographs (XBTs) were deployed at irregular intervals, and the array location, depth, and heading were monitored continuously.

II. TRANSMISSION-LOSS MODELING

A. Environmental inputs

1. Sound speed

For model comparisons with the experimental data, a single sound path was chosen that lay approximately midway between the two shown in Fig. 1, since it would have been impractical to calculate the transmission along a succession of 17-Mm-long paths as the receiver moved towards larger source-emission bearings. Vertical profiles of sound speed at intervals of 1–2 Mm along the track were deduced from contour maps of temperature and salinity in Ref. 7 and of sound speed in Ref. 8 at a number of depths; these profiles, illustrated in Fig. 3 for ranges of up to 16 Mm, extend to the estimated ocean depth at the range of the profile. The scale drawn above the main body of the diagram refers to each of the sound-speed profiles, but is aligned with the left-most profile. Vertical bars appear at the bottom of the figure at the range of each profile. Each profile is arranged so that its sound speed of 1.48 km/s appears directly above the corresponding vertical bar. The sound-channel axis is indicated by the dashed line. At cold latitudes near Antarctica the sound channel is observed to remain near the ocean surface. At ranges closer to the equator (crossed at a range between 11 and 12 Mm) the sound channel moves to somewhat deeper depths. At these intermediate ranges there is expected to be little or no interaction of the sound with either the surface or the bottom of the ocean since the most-strongly populated normal modes are confined to a relatively small range of depths near the sound-channel axis.

Historical sound-speed contour maps were considered to provide sufficient accuracy for input to an adiabatic-mode model at ranges well removed from both the source and re-

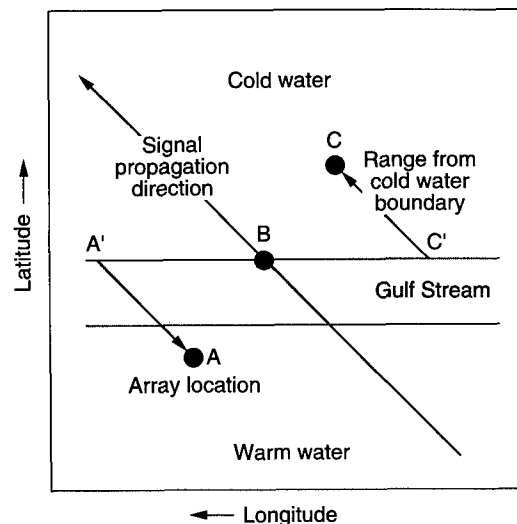


FIG. 4. Simplified view of the area traversed by the receiving array.

ceiver. Near the source and receiver, however, it was necessary to determine the sound speed with more care since the modal structure (and hence the transmission loss) depended strongly upon the sound-speed structure at these locations. Therefore, the sound-speed environment shown in Fig. 3 includes profiles measured at the time of the experiment near the source.⁹ (Sound speeds near the receiver are considered in more detail in the following paragraphs.)

It proved difficult to define a satisfactory independent variable for the model-experimental comparisons near the Gulf Stream because of the nonideal geometry of the experiment. As indicated in Fig. 1, the receiver was towed along a relatively straight track at an angle nearly perpendicular to the direction of the sound source. To complicate the geometry, the major environmental feature, the Gulf Stream, maintained an average course oblique to both the tow track and the source direction. The independent variable finally chosen can be visualized with assistance from the idealized map of the experimental area shown in Fig. 4. A new coordinate system is defined whose origin (labeled B in Fig. 4) is taken to be the intersection of the tow track and the acoustically important northern boundary of the Gulf Stream at a nominal range of 16.77 Mm from the source. When the sensor array is not located at B, its range is measured relative to this water-mass boundary along the appropriate acoustic path extending outward from Heard Island. For example, at location A in warm water, the range (A'-A) would be negative since the receiver is located closer to the sound source than is the coordinate origin at point B. At location C in the colder water, the range (C'-C) would be positive by a roughly equal amount. For modeling purposes the new ranges are simply subtracted from or added to the reference range of 16.77 Mm since the differences in distances to points A', B, and C' from the sound source are negligible in comparison to the exceptionally large total distance.

Several of the sound-speed profiles deduced from XBTs deployed from QUEST are plotted in Fig. 5 in accordance with the new coordinate scheme defined above. Vertical bars appear at the bottom of the figure at the range of each profile.

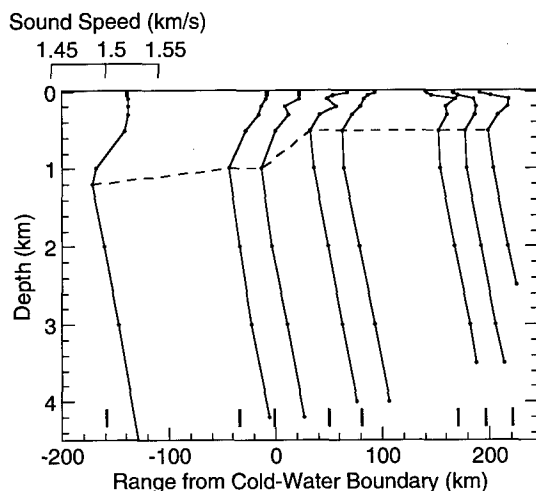


FIG. 5. Sound speed profiles used in modeling the sound transmission in the vicinity of the Gulf Stream; the sound-speed scale refers to the leftmost profile; for each profile the sound speed of 1.50 km/s is located directly above a vertical bar which, in turn, is located at the measurement range of the profile; (---) depth of sound-channel axis; ranges northwest of the Gulf Stream are positive.

Each profile is arranged so that its sound speed of 1.50 km/s appears directly above the corresponding vertical bar. The sound-channel axis, indicated by a dashed line in the diagram, rises from 1.2 km in depth to 0.5 km as the northern boundary of the Gulf Stream is crossed. Still further north, an overlying layer of cold continental shelf water creates an additional sound channel at the surface that is expected to influence transmission to the shallow receiving array.

A more dramatic indication of the change in sound speed at the northern boundary of the Gulf Stream is provided by Fig. 6, which shows the measured dependence of sound speed on range at the sensor array depth.

2. Bathymetry

The seabed was expected to have an important influence on sound transmission near Heard Island since the water depth was as little as 1000 m along the propagation path in this area. A rough estimate of water depth for the first 50–60

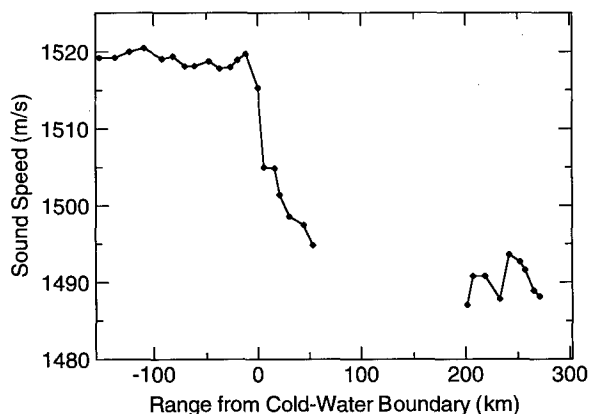


FIG. 6. Sound speed at the measurement-system depth as a function of distance northwestward from the Gulf Stream.

km distance from the source was obtained from Fig. 24 of Ref. 1. At several intermediate ranges, islands and undersea ridges or seamounts extend upwards into the sound channel along the anticipated acoustic path. The sound path skirts to the west of Ascension Island at a range of 9.2 Mm from Heard Island and to the east of Bermuda at a range of 16.0 Mm, and is bisected by St. Peter and St. Paul Rocks near the Equator at 11 Mm. Since several nearly parallel paths are expected to contribute to the received signal,^{10,11} isolated obstacles such as seamounts or islands should not have strongly affected the total acoustic signal level at the receiver. Therefore a rough median of the water depth over a distance of several tens of kilometers to either side of the nominal path of the signal was used as the water depth for modeling purposes at each range. As the sensor track approached the continental slope southeast of New England, the water depth decreased rapidly from 3300 m to approximately 1800 m before the experiment was terminated.

3. Boundary properties

The seabed along the entire signal path was modeled as a semi-infinite fluid layer in the absence of detailed information on either the bottom depth or sub-bottom composition. Typical values for bottom parameters^{12,13} were used: ratio of sound speed in the bottom to that in the adjoining water = 1.01, density of the bottom relative to that of water = 1.5, bottom attenuation at 57 Hz = 5.7×10^{-4} dB/m (= 0.01 dB/m at 1 kHz).

Refinements such as bottom roughness and shear-wave conversion in the seabed were not included in the environmental model because of a lack of relevant input data.

B. Model calculations

In order to provide insight into the evolution of the modal structure of the HIFT signal, the transmission-loss results were interpreted with the assistance of the adiabatic normal mode model PROLOS¹⁴ (in the absence of a readily available coupled-mode model). Such models rapidly estimate the modal structure and transmission loss as a function of depth and range in weakly range-dependent environments.¹⁵ A recent example of the use of such models for calculations involving long transmission distances is provided by Heaney *et al.*¹⁰ Except for one sound-speed profile at the source and several along the towed-array track, only historical sound-speed information was available, as noted earlier. Historical data tend to attenuate the steep horizontal gradients of sound speed that would promote mode coupling. Detailed bathymetric information was also not available, and may not have been of great use since the actual sound paths to the moving receiver were uncertain and variable. The preceding factors, together with the emphasis in this paper upon experimental results, led us towards the use of an adiabatic-mode representation of sound transmission. The probable effects of mode coupling will be elaborated upon at appropriate points in the following discussion.

PROLOS was employed to calculate the mode (eigen-) functions and eigenvalues at each range for which a sound-speed profile was specified. (Twenty modes were retained

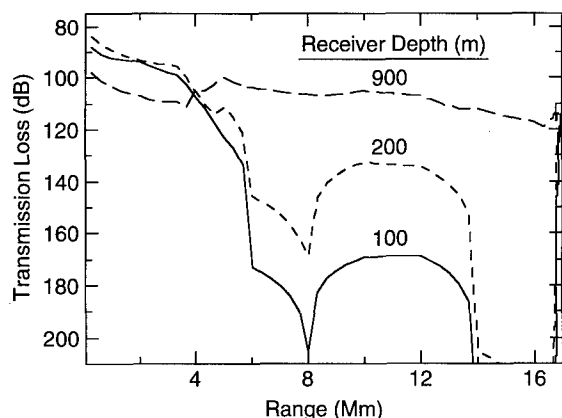


FIG. 7. PROLOS model estimates of transmission loss for the environments shown in Figs. 3 and 5; source depth is 175 m and frequency is 57 Hz.

out to a range of 17.0 Mm; higher-order modes were found to be too highly attenuated by bottom interaction over the first 50–60 km of the signal path to be worth considering at longer ranges.) Transmission losses were then calculated at much smaller range intervals, with the required estimates of the mode-function shapes and eigenvalues obtained by linear interpolation between the nearest ranges at which a full modal calculation was performed. Only incoherent transmission losses are considered since the coherent-loss predictions of PROLOS were found to be unreliable at the ranges of primary interest (16–17 Mm).

Estimates of transmission loss obtained with PROLOS are presented in Fig. 7 for the mean depth of the source array, 175 m, and for sensor-array depths of 100, 200, and 900 m at ranges out to 17 Mm from the source. The dependence of transmission loss upon both range and depth in Fig. 7 is seen to be quite significant. At a depth of 900 m the receiver is accessible to all of the modes at all ranges, so the transmission loss does not deviate strongly from cylindrical-spreading range dependence. Transmission to a receiver at 100- or 200-m depth is better than at 900 m depth for the first 4 Mm of range from the source since the shallow receiver depths are closer to the sound-channel axis in this range interval. At longer ranges, the populated normal modes move with the sound channel to somewhat greater depths. As an extreme consequence, in the range interval of 14.0–16.77 Mm, the model calculates that effectively no signal at all reaches the 100 and 200 m receiver depths. (In other words, all of the populated modes have zero amplitude at these receiver depths.) In the colder water beyond the Gulf Stream, a large decrease in transmission loss to the shallow receivers is observed at the extreme right-hand side of Fig. 7 as the modes begin to populate shallow depths again. If mode coupling was permitted, it is likely that the deep nulls in Fig. 7 would be much shallower, since sound-speed gradients and boundary scattering would spread the available signal power over modes that extend to the shallower depths.

The range interval in Fig. 7 covered by the array during the experiment is plotted again on a finer range scale in Fig. 8. In this case, the range variable has been transformed in accordance with Fig. 4 so that the cold-water boundary of the

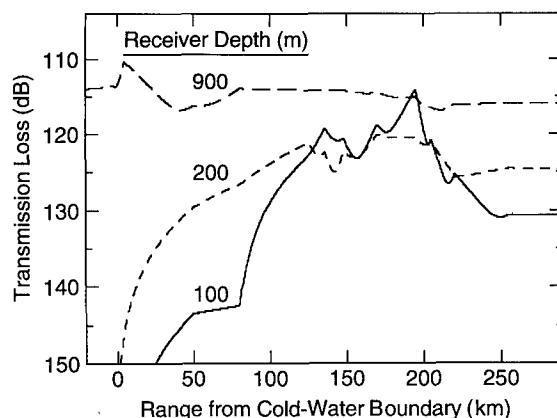


FIG. 8. PROLOS model estimates of transmission loss at ranges near the Gulf Stream (positive ranges are northwestward) for the environments shown in Figs. 3 and 5; source depth is 175 m and frequency is 57 Hz.

Gulf Stream is at zero range. Again the estimates for a receiver depth of 900 m exhibit relatively little structure. In contrast, receivers at the two shallow depths experience a large decrease in transmission loss as they move from the Gulf Stream into colder water.

The effect of surface scattering loss upon modeled sound transmission was examined by assuming a surface-wave field with a root-mean-square (rms) height of 1 m in one set of model calculations. This degree of surface roughness, approximating sea state 3, resulted in an overall increase in transmission loss at the longer ranges shown in Figs. 7 and 8 of approximately 3 dB for sensor depths of 100 and 200 m.

An estimate of the relative importance of each normal mode to the total sound field at a given range from the source and a given receiver depth can be obtained by multiplying (1) the amplitude of the mode function calculated at zero range for the source depth by (2) the amplitude at the receiver depth of the mode function that applies at the receiver range. This product is plotted in Fig. 9(a)–(c) at receiver ranges of, respectively, 50, 170, and 220 km from the Gulf Stream boundary for each of the 20 modes that were estimated by the adiabatic-mode model to be only modestly attenuated at significant distances from the source. (These ranges were chosen to be representative of three distinctly different transmission-loss regimes in Fig. 8.) Both 100-m (black column) and 200-m (white column) receiver depths are represented, although the sensor array depth was close to 200 m at the ranges under consideration. Modes 11–20 incorporate an estimate of bottom loss incurred during the first 300 km of travel in relatively shallow water. This attenuation was found to decrease from 5 dB for mode 20 to 0.1 dB for mode 11.

With two exceptions, the principal contributions to sound transmission in Fig. 9 are seen to be spread broadly over modes 9–19, suggesting that the total signal field at these ranges and depths will have a complicated multipath arrival structure. The exceptions involve the 100-m-depth data in Fig. 9(b) and (c). In Fig. 9(c), the modal structure peaks at mode 14. At 175 km range [Fig. 9(b)] modes 5 and

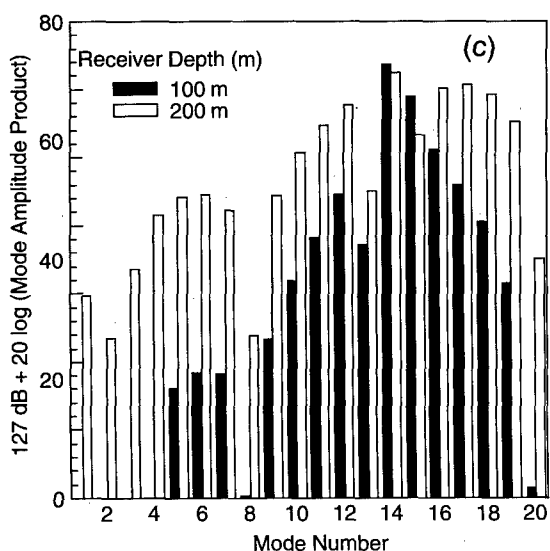
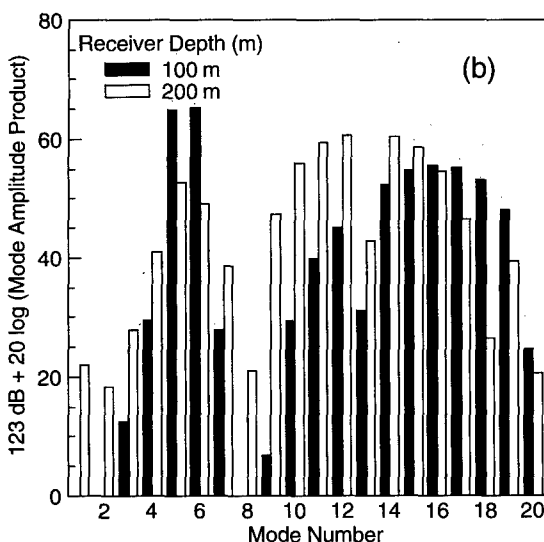
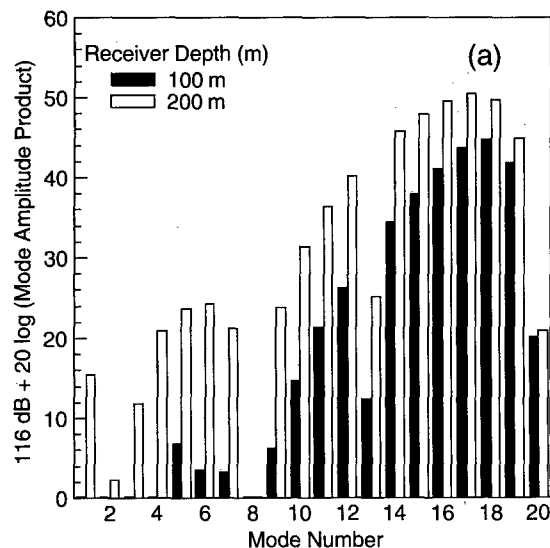


FIG. 9. PROLOS model estimates of the relative importance of each modal order to transmission loss; receiver ranges are (a) 50 km, (b) 170 km, and (c) 220 km northwest of the Gulf Stream cold-water boundary.

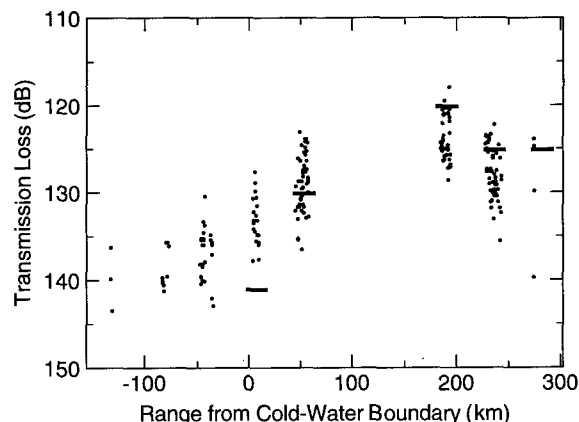


FIG. 10. Experimental transmission loss (dots) and PROLOS model predictions (horizontal bars) for 57-Hz signals from Heard Island; positive ranges are northwestward from the Gulf Stream northern boundary.

6 stand out above the others. The model also predicted that strong low-order modes would occur at the shallowest depths at several other ranges between +50 and +220 km, with only a single mode dominating in some cases (not shown). The addition of mode coupling would likely have redistributed the available acoustic energy among a larger number of modes, resulting in relatively little change in the predicted transmission loss at the ranges examined in Fig. 9.

For convenience in modeling, we assumed in the preceding discussion that only one signal path in the horizontal plane was present at a given range. More likely, over such long distances and complicated environments, several nearly parallel paths will contribute significantly to the received signal at any time.^{10,11} Potential causes of multiple arrival directions at a given sensor location are scattering from the upper and lower ocean boundaries, including seabed protuberances such as seamounts and continents, and refraction by turbulence, internal waves, mesoscale eddies, and thermal fronts. One can visualize a "swath" of signal paths in the horizontal dimension dominated by those that are most direct and least attenuated by bottom and surface interaction. Under such conditions, the interception of a few of the possible paths by seamounts or islands should not strongly affect the signal level at the receiver. The relative contribution of each path probably changed rapidly with time in the case of interest here since the tow track of the sensor array was nearly orthogonal to the signal paths.

III. DISCUSSION

A. Transmission loss

The principal DREA experimental results, to date, from the Heard Island Feasibility test are transmission-loss data at sensor array depths of between 100 and 200 m near and in the Gulf Stream. These data are presented in Fig. 10 as a function of range from the Gulf Stream northern boundary. Also included are adiabatic-mode transmission-loss estimates for the sound-speed environments shown in Figs. 3 and 5. These estimates are indicated by horizontal bars in Fig. 10. No bars are shown for the first three time intervals, as losses in excess of 200 dB were predicted by the model at

the corresponding ranges (see Figs. 7 and 8). The data in Fig. 10 are discontinuous because of the 1 h on, 2 h off duty cycle of the projector source array. A longer gap appears between 60 and 180 km, during a period when the measurement system was not deployed. The first two data-collection sites of the experiment, represented by the two southernmost dots in Fig. 1, do not appear in Fig. 10 because the HIFT signal was not detected at these locations.

Of the six groups of transmission-loss values in Fig. 10 containing a significant number of data points, the agreement between the experimental mean values and the predictions of the PROLOS model is within 3 dB in the three cases for which the average transmission loss was smallest. This quality of agreement is perhaps better than should be expected, considering the simplified environmental inputs and the exclusion of mode coupling in the model. The sensitivity of the transmission-loss predictions at these three ranges to bottom characteristics near the source was evaluated by varying key geoacoustic parameters. An increase in the attenuation coefficient by a factor of 10 increased the transmission losses by 0–6 dB; an increase in the sound-speed ratio from 1.01 to 1.02 decreased the losses by 0–4 dB, and a change in the density ratio from 1.5 to 1.3 had little noticeable effect. (It was noted earlier that an assumed surface roughness of 1 m rms caused the estimated transmission loss to increase by approximately 3 dB.) No attempt was made to refine the agreement between model predictions and experimental values by varying the bottom-parameter values since (1) it is unlikely that a unique fit would have been found, (2) only a single, homogeneous bottom layer was included, (3) the effect of shear was not taken into account, and (4) mode coupling was not taken into account.

According to the model, the transmission loss at +5-km distance from the Gulf Stream boundary in Fig. 10 should have been approximately 8 dB greater than that observed experimentally. The model transmission loss at the tow depth of 200 m has a very steep slope at this range (see Fig. 8). Hence any uncertainty in the relative locations of the Gulf Stream boundary, the sensors, and the nearest XBT locations can cause a large discrepancy between modeled and measured loss. The model also implies that the HIFT signals received at –50 and –80 km range relative to the Gulf Stream boundary should have been submerged in ambient noise. Indeed, the discrepancy between model and experiment south of the northern boundary of the Gulf Stream is shown by comparison of Figs. 7 and 10 to be at least 60 dB at a sensor depth of 200 m. A likely explanation for the presence of a detectable signal at these ranges is that a small proportion of the acoustic power that populated the 20 propagating modes at the source was eventually scattered into higher-order modes, a move that is specifically excluded in the adiabatic-mode approximation. Such transitions could have occurred because of mode coupling at fronts such as the Antarctic Convergence¹⁶ or because of low-angle scattering from the water surface and seabed, especially near Heard Island.

The modal structure applicable to warm water and shallow receiver depths was investigated by running the PROLOS model using only the sound-speed profile dis-

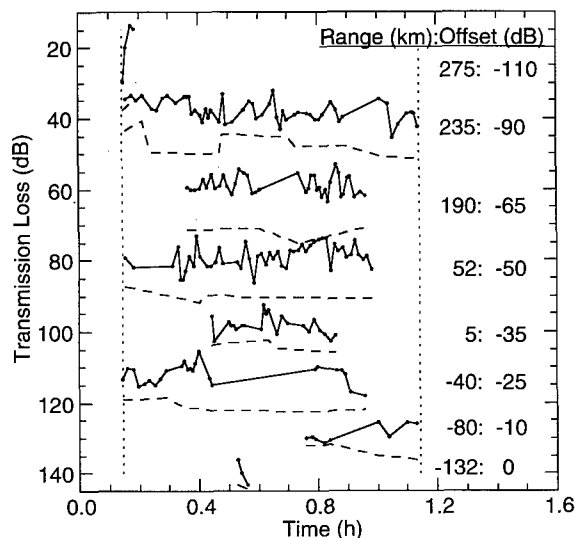


FIG. 11. Experimental transmission loss (connected dots) and noise-floor estimates (dashed curves) for 57-Hz signals from Heard Island, as a function of time from commencement of the nearest preceding hour; vertical offsets and nominal ranges northwest of the cold-water boundary are listed on the right-hand side of the figure; vertical dotted lines represent estimated start and finish times of signal.

played in Fig. 5 for a range of –35 km relative to the cold-water boundary. The lowest-order mode in this environment that peaked in amplitude at the receiver depth was No. 35, with a phase speed of 1521.9 m/s. In contrast, the highest-order mode propagating strongly from Heard Island was expected to be No. 20 with a phase speed of 1510.7 m/s and minimum depth of 600 m at the range of interest.

If no factors, other than scattering to higher-order modes, are involved in the detection of sound south of the Gulf Stream, then the transmission loss should remain nearly constant as one moves towards greater negative ranges from the Gulf Stream. However, the transmission loss is observed in Fig. 10 to increase gradually as the range becomes more negative, until the signals are no longer detectable (ranges beyond –130 km). The gradual onset of bathymetric blockage by Bermuda and South America are likely responsible for this data trend.

The transmission-loss data of Fig. 10 are redrawn in Fig. 11 in a format that provides a better indication of their time variability. The eight data sets of Fig. 10 are stacked vertically in Fig. 11 with the time axis denoting the absolute time of arrival after the nearest preceding hour. Since the HIFT signal started on the hour each time, and since the actual range between the source and receiver changed very little during the experiment, the signal appears to start at nearly the same time (denoted by the vertical dotted line at 0.145 h) in each of the four groups for which data are available at the appropriate time. (Note that the nominal range of each data set, listed at the right of the figure is the distance from the cold-water boundary of the Gulf Stream. Since this distance changes much more rapidly from one data set to the next than the actual acoustic path distance from source to receiver, it is not surprising that the signals appear to start and stop at the same times after the hour, independently of the

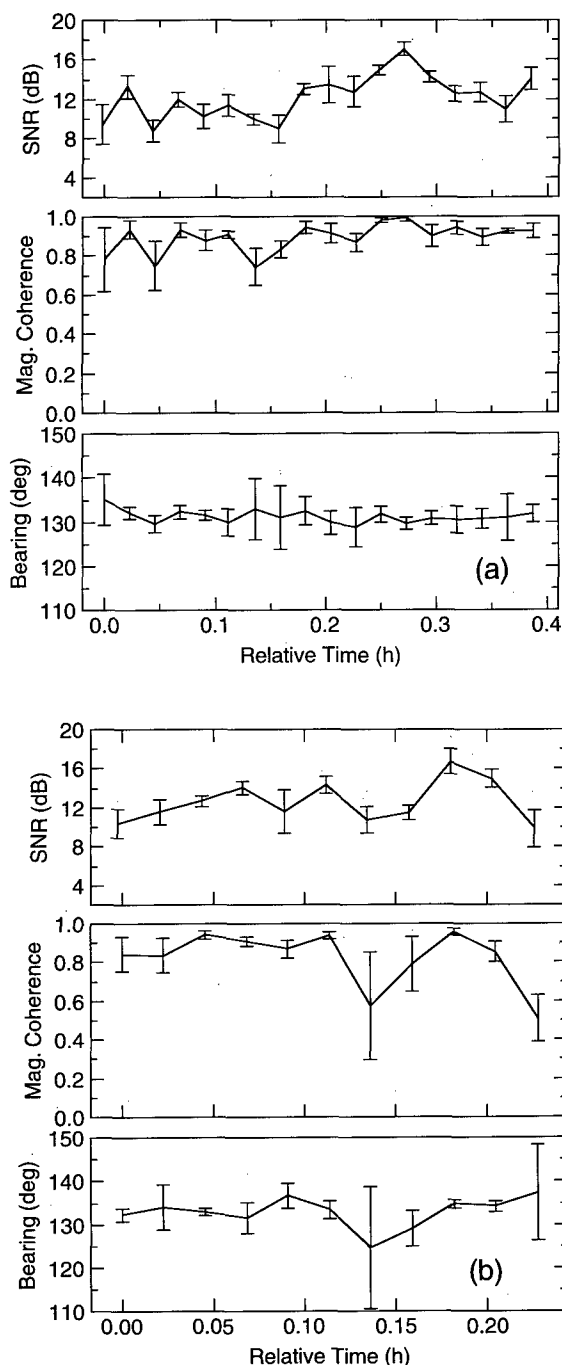


FIG. 12. Data series of signal-to-noise ratio (SNR) (top curve), coherence magnitude (middle curve), and signal arrival bearing (bottom curve) for 57 Hz Heard Island data during two data-collection periods; error bar lengths represent $2\times$ standard deviation; nominal ranges northwest of the Gulf Stream are (a) 50 km and (b) 190 km.

range shown in the figure.) One would expect the signals to end almost exactly 1 h later. Two of the data sets indeed persist to this limit (denoted by the second dotted line at 1.145 h). The signal arrival times obtained from the spectral analysis are uncertain by at least the averaging times of the data points in Fig. 11, which range from 30 to 60 s. Improving the time resolution of the analysis is not practical in view of the need for high resolution in frequency to discriminate against the noise background.

The upper limits on measured transmission loss that are imposed by the noise background are represented in Fig. 11

by dashed curves. (The separation between a data point and the underlying dashed curve at any time is equal to the SNR observed in the associated spectral peak, measured at the frequency resolution of the analysis.) On a few occasions, the signal faded below the level of the background; since these data points are not included in Fig. 11, the transmission loss, as displayed, has a slightly negative bias. A statistical analysis of the transmission-loss fluctuations was not performed because (1) many gaps of one or more data points were interspersed in the time-series data, (2) frequent changes in the time-bandwidth product were required during the spectral analysis, and (3) the SNR was often too small to yield useful statistical information.

B. Array coherence

Since the measurement array had a maximum aperture of only 1.8 wavelengths at 57 Hz, beamforming was attempted on only a few isolated time intervals during the first pass through the experimental data. (With this aperture, and conventional processing, the beamformed signals should have a beamwidth of approximately 30° near broadside.) To learn more about the spatial properties of the acoustic field, cross-power spectral analysis was performed on the data obtained from four sensors during the two longest periods of uninterrupted reception. The three intersensor spacings were, consecutively, 12, 16, and 14 m—amounting to a total aperture of 42 m.

Coherence magnitude and phase were calculated for all possible combinations of the four sampled sensors at a frequency resolution of 0.031 Hz. Each estimate was obtained by averaging five spectral samples with 50% overlap.

The signal arrival angle θ (relative to the array broadside direction) of a single plane wave of wave number k can be easily deduced from the cross power or coherence phase

$$\theta = \sin^{-1}(\phi/kd), \quad (1)$$

where ϕ is the coherence phase and d is the intersensor spacing. (Side lobe ambiguity was not expected to present a problem since d was approximately one-half wavelength and the HIFT signal arrivals were near broadside.) The arrival direction of the signal can be determined, aside from the usual line array left-right ambiguity, by adding the signal arrival angle θ to the true bearing of the array broadside direction. Since there appeared to be little dependence of the coherence magnitudes or deduced arrival angles upon intersensor spacing, the mean values of coherence magnitude and the signal arrival bearing (relative to true north), calculated using Eq. (1), were obtained for each time sample. The mean values of these variables are plotted against time in Fig. 12(a) and (b) for data segments at nominal ranges of +50 and +190 km, respectively, from the northern (or cold-water) boundary of the Gulf Stream. Each data point represents an average over the six possible intersensor combinations. The standard deviation of each sample is represented by half the length of each error bar. Also plotted (topmost curve) is the time dependence of the decibel-averaged SNR for the four sensors.

In the first data set [Fig. 12(a)] there appears to be relatively little variation in coherence magnitude and signal bear-

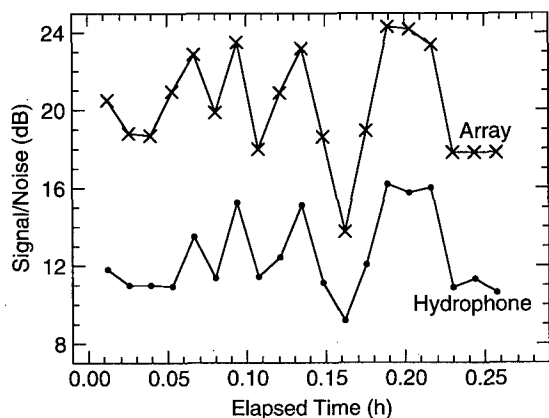


FIG. 13. Comparison of experimental signal-to-noise ratios for single-sensor reception and for four sensor signals coherently summed; successive sensor spacings were 12, 16, and 14 m in a horizontal line; direction of 57-Hz signal was close to broadside; nominal range was 190 km north of cold-water boundary.

ing with time. The coherence-magnitude values imply that the SNR is approximately 10 dB in most of the samples, in agreement with the measured mean SNR values, assuming that the noise background is spatially incoherent.

Although the range of mean SNR values during the second period [Fig. 12(b), upper graph] was very similar to that of the first, both the coherence magnitudes (middle graph) and signal bearings (lower graph) are seen to be more variable than in Fig. 12(a). In particular, the coherence magnitudes at 0.135 and 0.230 h are unusually low, and the signal bearing is seen to deviate from the trend at these times. In both cases, the standard deviations are also unusually large. These symptoms are consistent with the presence of two unrelated signals that have different arrival angles, and incompletely resolved frequencies. Indeed, at both times a signal of slightly lower frequency was observed to contaminate the HIFT signal at 57 Hz. Since the four strong sideband signals that were projected from Heard Island during this time interval did not exhibit similar evidence of frequency broadening, we can conclude that the interfering signal was unrelated to HIFT. A beamformed data sample obtained near 0.135 h [with reference to the horizontal axis of Fig. 12(b)] also exhibited the presence of two signals near 57 Hz: in addition to the HIFT signal, arriving near broadside, there was an almost equally strong signal with an arrival angle 65° from broadside.

The mean values of the signal bearing calculated from each of the time series displayed at the bottom of Fig. 12(a) and (b) are indicated by arrows in Fig. 1, for comparison with the expected arrival directions of the HIFT signals. The 256.5° and 268° limiting paths displayed in Fig. 1 have reverse bearings of, respectively, 130° and 125° (relative to true north) at their intersections with the array track. The reverse bearings of the signals at track locations between these two intersections are therefore expected to lie between 125° and 130° . It is not clear whether the discrepancy between these values and the slightly larger experimental values of 130.5° and 133° results from experimental error or from unanticipated horizontal refraction of the signal.

Since the HIFT signals were observed to arrive from a direction near broadside during the period depicted in Fig. 12(b), the four sensor signals were summed in one case before spectral analysis was performed, thereby effectively steering a beam in the direction of the signal of interest. This was done to provide an indication of the magnitude of SNR gains that might be achieved if beamforming was attempted on the entire data set. The results are displayed in Fig. 13, where the top curve shows the SNR derived from spectral analysis of the summed data, and the bottom curve represents the SNR for a single sensor. Since adjacent sensors were separated very approximately by one-half wavelength, one would expect a SNR (array) gain for the four-sensor sum of $10 \log 4 = 6$ dB if the noise field is isotropic in three dimensions. In fact the array gain averaged closer to 7 dB, suggesting that discrimination was being provided against a discrete interfering source. Evidently, it would be worthwhile to beamform all of the data before subjecting them to more sophisticated signal processing analysis in the future.

IV. SUMMARY AND CONCLUSIONS

Signals centered at 57 Hz that were generated during the Heard Island Feasibility test on 29 and 30 January 1991 were recorded by a measurement system including a 48-m-long hydrophone array towed across the Gulf Stream at depths between 100 and 200 m. In this paper, the effect of underwater transmission over a distance of 17 Mm is examined experimentally and with the assistance of the adiabatic-mode model PROLOS. The emphasis is on a "quick look" assessment of signal level relative to the noise background, the modal structure of the signal, and the spatial coherence across a sensor-array baseline of 42 m; no attempt is made to examine the timing capabilities of the complicated signals.

The experimental transmission loss was observed to decrease by at least 20 dB as the hydrophone array was towed from the warmer Sargasso Sea water through the Gulf Stream into the cooler water to the north. South of the Gulf Stream, the signal level gradually decreased until it became undetectable, probably because of bathymetric blockage by Bermuda and South America. A much more rapid change in transmission loss (approximately 60 dB) was predicted by the propagation model for shallow sensors moving southward out of the Gulf Stream than was observed experimentally. Scattering from modes 20 and below into higher modes is the suspected source of the signal strength in the acoustic shadow zone.

Relatively good agreement (approximately 3 dB) was obtained between experiment and model transmission losses north of the Gulf Stream assuming typical values of seabed geoacoustical properties in the vicinity of Heard Island.

Sound-speed inhomogeneities in the horizontal plane were expected to lead to a diversity of sound paths between source and receiver. The statistical nature of such inhomogeneities should limit both the need and ability to accurately model seabed properties, since (1) isolated obstacles such as seamounts would not obstruct all of the contributing paths and (2) it would be virtually impossible to determine the exact course of the most significant signal paths.

Intersensor coherence was measured during two periods when the signal was strongest relative to the noise backgrounds. Four sensors with a maximum aperture of 42 m were chosen for the measurements. The mean coherence magnitude of the six possible sensor pairs was found to be nearly independent of time or sensor separation. The coherence magnitude was consistent with observed SNR values, except in two cases when unrelated signals from different directions contaminated the signal of interest.

The mean acoustic bearing of the HIFT signals, obtained from coherence phase data, was found to be slightly biased, possibly because of unanticipated horizontal refraction of the arriving signal.

During a period when the HIFT signals were expected to arrive near broadside to the hydrophone array, beamforming by performing a simple summation of four sensor signals (over a total aperture of 42 m) yielded a mean array gain slightly greater than $10 \log 4$. In view of the marginal SNR, the good coherence properties of the signals, and the possibility of interfering signals from different directions, the use of a beamformer is recommended in future passes through the data.

Most of the signal data were contaminated by interruptions occurring at intervals as short as 1 min. Although spectra encompassing such interruptions were excluded from the data shown in this paper, it may be possible to process through the interruptions in future passes through the data, depending upon the objective and the sophistication of the processing algorithms.

ACKNOWLEDGMENTS

The beamformed sample was provided by D. V. Crowe. The Canadian Forces METOC Centre supplied information on the Gulf Stream location. Data on projector operations were provided by W. H. Munk, M. A. Dzieciuch, and K.

Metzger. Our appreciation is extended to W. H. Munk for inviting DREA to participate in the Heard Island Feasibility Test.

- ¹W. H. Munk, "The Heard Island Experiment," *Naval Research Reviews* **43**, No. 1, 2-22 (1991).
- ²W. H. Munk and A. M. G. Forbes, "Global ocean warming: An acoustic measure?," *J. Phys. Oceanogr.* **19**, 1765-1778 (1989).
- ³C. Levenson and R. A. Doblar, "Long-range acoustic propagation through the Gulf Stream," *J. Acoust. Soc. Am.* **59**, 1135-41 (1976).
- ⁴F. D. Tappert, "The Parabolic Approximation Method," in *Wave Propagation and Underwater Acoustics*, edited by J. B. Keller and J. S. Papadakis (Springer-Verlag, New York, 1977), Chap. V, Fig. 5.
- ⁵T. G. Birdsall, M. A. Dzieciuch, and K. Metzger, "Heard Island Feasibility Test signal processing first results," EECS Department, The University of Michigan, Ann Arbor, MI Informal Report, 8 May 1991 (unpublished).
- ⁶W. H. Munk (private communication, 1991).
- ⁷A. L. Gordon, E. J. Molinelli, and T. N. Baker, *Southern Ocean Atlas* (Columbia U.P., New York, 1982).
- ⁸*World Ocean Atlas: Atlas of the Atlantic and Indian Oceans*, edited by S. G. Gorshkov (Pergamon, New York, 1985), Vol. 2.
- ⁹M. A. Dzieciuch (private communication, 1992).
- ¹⁰K. D. Heaney, W. A. Kuperman, and B. E. McDonald, "Perth-Bermuda sound propagation (1960); Adiabatic mode interpretation," *J. Acoust. Soc. Am.* **90**, 2586-2594 (1991).
- ¹¹B. E. McDonald, W. A. Kuperman, and K. D. Heaney, "Horizontal multipath in transoceanic propagation: Model results and data," *J. Acoust. Soc. Am.* **96**, 2353-2356 (1994).
- ¹²E. L. Hamilton, "Acoustic properties of sediments," in *Acoustics and the Ocean Bottom*, edited by A. Lara-Sáenz, C. Ranz-Guerra, and C. Carbó-Fité (Consejo Superior de Investigaciones Científicas, Madrid, 1987), pp. 3-58.
- ¹³A. C. Kibblewhite, "Attenuation of sound in marine sediments: A review with emphasis on new low-frequency data," *J. Acoust. Soc. Am.* **86**, 716-738 (1989).
- ¹⁴D. D. Ellis, "A two-ended shooting technique for calculating normal modes in underwater acoustic propagation," Defence Research Establishment Atlantic, Dartmouth, NS, Canada, Report No. 85/105, Sept. 1985 (unpublished).
- ¹⁵A. D. Pierce, "Extension of the method of normal modes to sound propagation in an almost-stratified medium," *J. Acoust. Soc. Am.* **37**, 19-27 (1965).
- ¹⁶E. C. Shang, Y. Y. Wang, and T. M. Georges, *J. Acoust. Soc. Am.* **96**, 2371-2379 (1994).

Heard Island Feasibility Test: Long-range sound transmission from Heard Island to Krylov underwater mountain

S. V. Burenkov, A. N. Gavrilov, A. Y. Uporin, and A. V. Furduev
N. N. Andreyev's Acoustics Institute, Shvernik St., 4, 117036 Moscow, Russia

(Received 19 August 1992; accepted for publication 7 June 1994)

The Russian research vessel *AKADEMIK NIKOLAI ANDREYEV* participated in the HIFT experiment while anchored above the Krylov Seamount (17.5° N, 30° W). The propagation path length from Heard Island to Krylov was 12.5 Mm, and was located just between the Ascension station (9 Mm) and the more distant American and Canadian stations (16 to 17 Mm). All 35 successful transmissions were received by two omnidirectional hydrophones and a 30-m-long array. Reception was sampled at 228 Hz and processed in both time and frequency domains. The main result of the processing was quite unexpected: the signal exhibited strong amplitude variability (fading as deep as 20 dB in less than 5 min) and simultaneously exhibited an incredible phase stability. All the phase variance up to the accuracy of positioning was due to the mutual motion of the transmit and receive ships. The minimal propagation loss for cw transmissions was 120 dB. *M*-sequence processing indicated an 18- to 20-s arrival spread estimate. However, the arrivals were very unstable with a lifetime of about 5 min.

PACS numbers: 43.30.Qd, 43.30.Pc, 43.60.Rw

I. EXPERIMENTAL SETUP

In order to participate in the HIFT experiment the Soviet research vessel *AKADEMIK NIKOLAI ANDREYEV* was anchored above the Krylov seamount where the depth was 1760 m. Mooring of the 10 000-ton displacement ship was a serious task and it demanded high qualifications of the crew. There were two principal goals of the mooring: (a) to fix the ship position during the experiment and (b) to reduce flow noise at the receivers. Both goals were achieved only partially. With a 3-km mooring line and the unstable weather the ship experienced a complicated motion with a total displacement of 3.5 km and speeds of 0.1 to 0.8 knots (0.05 to 0.41 m/s). GPS tracks of this motion illustrated a tangled pattern. In the morning of 28 January the mooring system failed and subsequent measurements were made while drifting.

During the experiment the vessel was in "silence" mode using a special damped generator to provide power to the systems. This allowed elimination of the signal spectrum harmonics caused by the ship's machinery gears. The noise level in a 1-Hz band near the 57-Hz carrier ranged from 82 to 88 dB/ μ Pa without a significant difference between the drift and anchored periods.

Signals were received using two omnidirectional hydrophones and a flexible 100-m array. Unfortunately, the array was damaged and we were able to use only the sum of three elements with 10-m spacing. The depths of the receivers were 200 and 800 m for the individual hydrophones and 750 m for the array center.

The data acquisition system was PC-based, having a 13-bit analog-to-digital (A/D) capability and precision clocked by a 5-MHz rubidium oscillator. One to three channels were sampled simultaneously at 228 Hz, i.e., four times per one period of the 57-Hz carrier frequency. All of the 35 successful transmissions were recorded, providing a total data con-

tribution of 240 megabytes. A separate PC recorded the GPS track. Spectrum analyzers were used for reception control and real time analysis.

II. PROPAGATION PATH AND TRAVEL TIME

For the deep ocean conditions, adiabatic mode theory is the simplest method to solve long-range propagation problems at low frequency.¹ This theory assumes that there is no modal energy exchange and that each mode adjusts its vertical shape slowly during propagation. Propagation of each mode on the Earth's surface is represented by a "horizontal" ray trajectory. Excluding harmonic time dependence and spreading factors the acoustic pressure is taken to be

$$p(x, y, z) = \sum_n P_n(x, y) Z_n(z, x, y). \quad (1)$$
$$P_n(x, y) = \exp\left(i \int_{S_n} k_n(x, y) ds\right),$$

where $Z_n(z, x, y)$ is the local eigenfunction of the n th mode, $k_n(x, y)$ is the local eigenvalue of the n th mode, and the integration is carried out along the ray trajectory S_n which connects the source and receiver.

In choosing the position of the receiver ship for the experiment, we were very much concerned about the shadowing caused by the South of Africa and the Prince Edward Islands. Calculations showed that the ellipticity of the Earth has a significant influence on the shape of the mode rays with the deviation of the ray trajectory from the great circle being as large as hundreds of kilometers.

To treat this problem properly one must solve the ray equation in the elliptical coordinates u, θ, ϕ that are related to the geographic longitude and latitude ϕ_g, θ_g , respectively, as

HEARD ISLAND EXPERIMENT

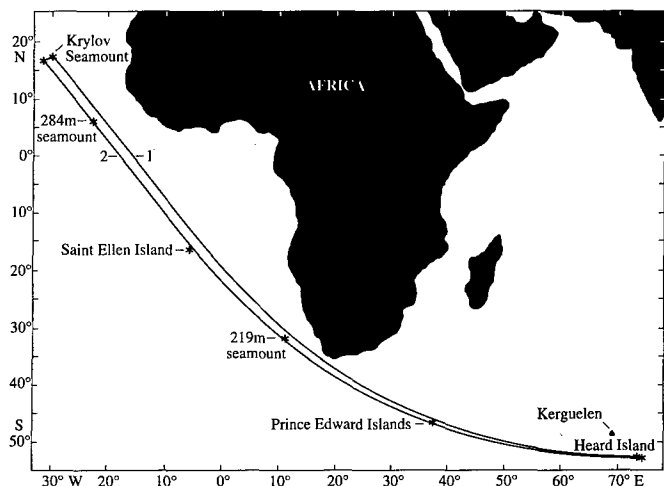


FIG. 1. Calculated ray paths: 1—Heard Island—Krylov seamount; 2—Heard Island—the end point of R/V AKADEMIK NIKOLAI ANDREYEV drift.

$$\begin{aligned}\phi &= \phi_g, \quad \gamma = b/a, \\ \tan \theta &= (1/\gamma) \tan^{-1} \theta_g, \\ \sinh(u) &= b/\sqrt{a^2 - b^2} = \text{const},\end{aligned}\tag{2}$$

where we take ϕ_g top be negative in the western hemisphere and θ_g to be negative in the southern hemisphere, with $a = 6378.245$ km and $b = 6356.863$ km being the ellipsoidal radii.²

By using Fermat's principle (in a fashion similar to Ref. 1) and assuming only latitude dependence of the sound-speed profile one can obtain a simplified ray equation,

$$\frac{d\theta}{d\phi} = \pm \sqrt{\frac{|\{ [k_n(\theta) \sin \theta] / [k_n(\theta_0) \sin \theta_0 \sin \alpha_0] \}^2 - 1|}{\tan^{-2}(\theta) + \gamma^2}}.\tag{3}$$

where θ_0 and ϕ_0 are the source coordinates, α_0 is the launch angle measured clockwise from north, and the sign (+ or -) depends on both launch angle and the sign of terms within modulus bars. The useful feature of Eq. (3), in comparison to more general equations of Munk³ and Heaney,¹ is that it does not contain the derivatives of k_n . As the hydrographic data for such paths are coarsely spaced and are often inaccurate, then in the numerical solution of the equation these derivatives will be very sensitive to such errors and to the method of data interpolation.

We used a January average distribution of sound speed in the Indian and Atlantic Oceans⁴ to calculate the ray path from the location of transmitting ship (53.4° S, 74.5° E) to the Krylov seamount (Fig. 1). The launch angle of this ray was 271.5°. The ray path to the last point on the receiving ship drift path cross the Prince Edward Islands and some underwater mountains that penetrate into the SOFAR axis (i.e., the second ray in Fig. 1).

The ray length from the source point θ_0, ϕ_0 to the reception point θ_r, ϕ_r is given by

$$R = \int_{s_n} ds = \int_{\phi_0}^{\phi_r} ds \sqrt{g_\theta \left(\frac{d\theta}{d\phi} \right)^2 + g_\phi},\tag{4}$$

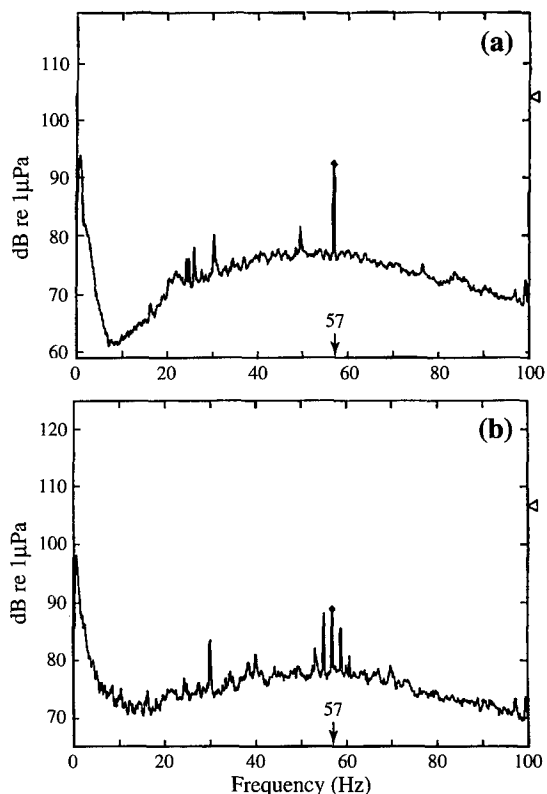


FIG. 2. Spectra of received signals with a 0.125-Hz resolution: (a) 57 Hz; (b) pentaline.

where g_θ, g_ϕ are the components of the metric tensor. In the assumption made above the ray path S_n is frequency independent and therefore the travel time along the ray is equal to

$$t = \int_{s_n} \frac{ds}{V_n(s)},\tag{5}$$

where $V_n(s)$ is the distribution of the n th modal group velocity along the ray. In order to estimate the travel time with the accuracy of the order of the arrival spread we used $c(\theta)$ instead of $V_n(s)$ in Eq. (5). So the calculated ray length from the source location to the Krylov seamount was 12 620 km with a travel time of 8480 s.

III. SPECTRAL ANALYSIS OF SIGNALS

During the experiment we used spectrum analyzers to detect the signal and measure its magnitude in real time. Spectrum analysis was performed over a 100-Hz frequency range with a 0.125-Hz resolution. This analysis band was sufficient to resolve the signal from noise without averaging [Fig. 2(a)]. Besides the 57-Hz carrier, the four sidelines of the pentaline signal were also clearly detected [Fig. 2(b)].

On-line digital spectrum analysis of sampled signals was performed by the fast Fourier transform (FFT). The sampled signal p_n was previously demodulated by shifting down to zero the carrier frequency, i.e., multiplied by $\exp(i\pi n/2)$ with subsequent averaging over two cycles. A 256-point FFT with Hamming weighing and eight-spectrum incoherent averaging was used to obtain the time dependence of signal magnitude and phase.

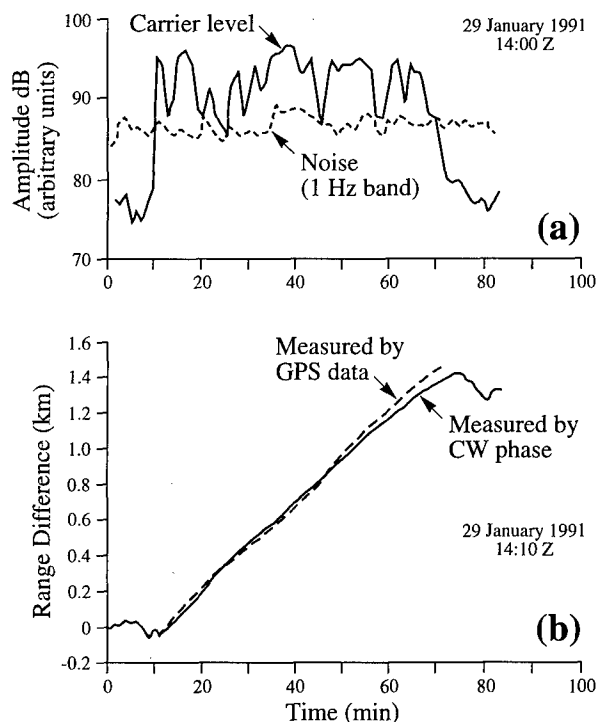


FIG. 3. (a) Amplitude fluctuation of cw signal. (b) Variation of distance between corresponding ships measured by navigational data and by cw phase.

On most of the cw transmissions the signal-to-noise (S/N) ratio was 10 to 15 dB in a 1-Hz band at the carrier frequency, decreasing slowly with the degradation of the source level [Fig. 3(a) and also Fig. 3.4 in Ref. 5]. The signal exhibited severe fading with changes in signal level as large as 20 dB in less than 5 min. The maximum signal level during the best transmission was approximately 100 dB/ μ Pa. Using this value, the propagation loss was estimated as 120 dB. This is nearly the same as for the Ascension station,⁶ but in our case the noise level was sufficiently higher (82 to 88 dB/ μ Pa) resulting in degraded signal quality. Temporal variation of the signal phase was mostly due to the relative motion of the transmitting and receiving ships. The range differences estimated by measuring the variation of cw phase were in accordance with the navigational data of both ships [Fig. 3(b)]. Doppler correction by the navigational data almost excludes the shift of instant frequency histogram (Fig. 4).

A nonuniformity of ship's motion was the main reason of cw spectral line extension by value $\delta f/f_0 \approx 0.3 \times 10^{-3}$. Relative extension of the spectral line due to the internal waves in the ocean can be estimated as $\delta f/f_0 \approx 6 \times 10^{-6} \sqrt{R}$,⁷ where R is the distance from the source in kilometers. If $R = 12.5$ km then $\delta f/f_0 \approx 0.7 \times 10^{-4}$. This value is considerably lower than that measured in the experiment.

The temporal variations of pentaline spectral components were also determined by FFT. The magnitude fluctuations of these components did not correlate with each other (Fig. 5).

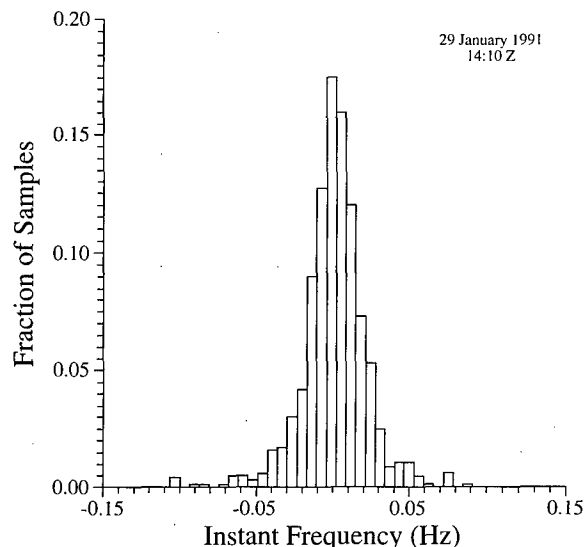


FIG. 4. Distribution of cw instant frequency for one reception session with compensated Doppler shift.

IV. MEASURING THE TRAVEL TIME VARIATIONS

Both the internal waves and the motion through the interference structure of a multimodal sound field can lead to strong fluctuations of cw signals. These fluctuations mask the

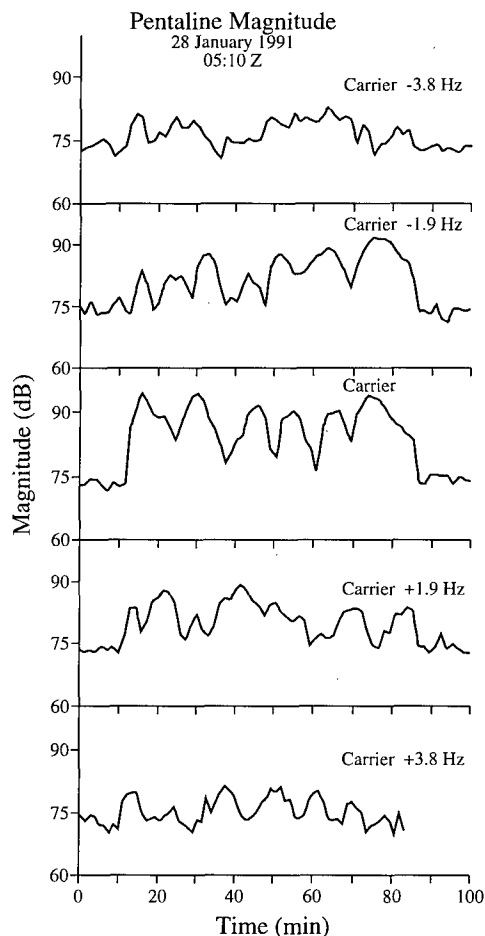


FIG. 5. Amplitude fluctuations of the pentaline spectral components.

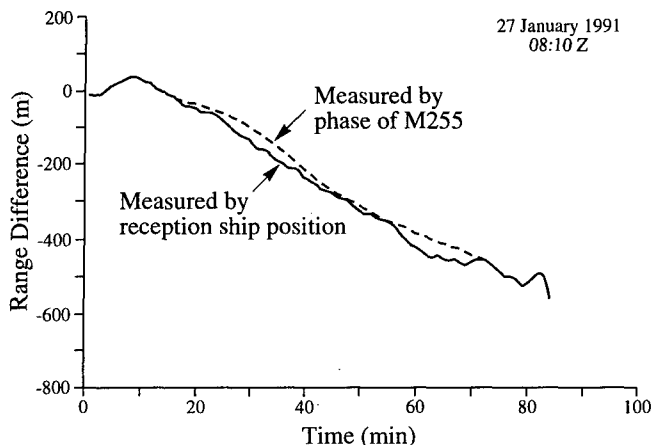


FIG. 6. Motion of the receiving ship along the ray path: dashed line—evaluated from phase variations of M1 signal, solid line—GPS data.

phase differences due to long-term variation of the signal travel time because of the 2π uncertainties of the phase difference measurements. One must extend the frequency band of the signal to minimize the effect of high-speed fluctuations. The phase differences can then be determined using the autocorrelation of the periodic pseudonoise signal.⁸

Phase-coded signals were used to estimate the travel time variation. The period of the shortest M-sequence M1 was equal to 22.4 s. On most of the transmissions the Doppler shift was greater than 0.05 Hz, hence the phase difference over one period of M1 exceeded 2π with high probability. To eliminate the 2π uncertainties the sampled signal p_n was demodulated with a compensation of Doppler shift f_D estimated previously, i.e., $d_n = p_n \exp[i\pi n(57 + f_D)/(2 \times 57)]$. The value f_D was determined from the projection of the average speed of the source ship to the calculated propagation path. It was taken to be a constant for each transmission. The demodulated signal was then decimated by a factor of 5 after filtering by the low-pass 30-order FIR filter with an 11.4-Hz cutoff frequency. Then the data set were divided into fractions of the same length as the period of the M-sequence. The phase difference of two adjacent fractions is the phase of correlation,

$$A(m) \exp[i\Delta\phi(m)] = \sum_{n=1}^N d_n(m-1) d_n^*(m), \quad (6)$$

where $\Delta\phi(m)$ is phase difference, $A(m)$ is correlation magnitude, m is fraction number, and $N=2M$. If the phase variation is due to the ship motion then the range difference per one measurement of phase difference $\Delta\phi$ is $\Delta R = c\Delta\phi/2\pi f_0$, where c is the axial sound speed at the transmitter. Assuming a uniform motion of the transmit ship, the acoustic measurement of the receiving ship motion along the propagation path is in accordance with the GPS data of receiving ship (Fig. 6).

For one session of M1 signal reception, the temporal variation of travel time was compensated by the variation of the receiving ship motion obtained from its GPS track. The corrected travel time variations represented by the distance differences during transmission were compared with the GPS

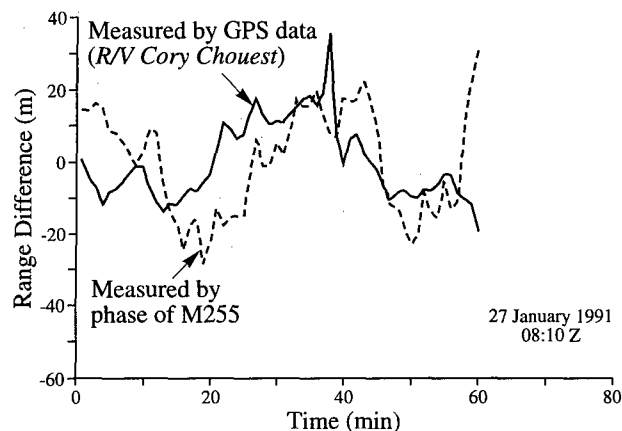


FIG. 7. Deviation of transmission ship motion from uniform along the ray path: dashed line—evaluated from phase variations of M1 signal, solid line—source ship R/V CORY CHOUSET GPS data.

data of the transmitting ship represented as the deviations of its motion from uniform, along the propagation path (Fig. 7). The rms difference of acoustic and navigational measurements was about 10 m. Such accuracy is really astonishing, taking into account that the receiver was suspended 800 m below a ship driven by waves and winds. The phase M-sequence analysis together with the cw processing, indicated an outstanding stability of the multipath phase, similar to that mentioned at the Ascension and Christmas stations.⁶

V. INVESTIGATION OF ARRIVAL STRUCTURE

An investigation of the arrival structure of the multipath signal was performed using the factor inverse filtering technique,⁹ i.e., calculating the correlation function of the received signal with the replica. One of the main problems arising in the implementation of this method is that the Doppler frequency shift can decrease the correlation and destroy the information about arrival structure. As the modulation angle was $\pi/4$ one can neglect effects of the Doppler shift f_D only if $2\pi f_D T < \pi/4$, where T is integration time, which is no less than one cycle of M-sequence. For the shortest sequence M1 ($T=22.4$ s) it means that the value f_D must be no more than 6 mHz while measured values were usually greater by an order.

Three various methods were used to eliminate the Doppler distortions based on the assumption that carrier frequency can be detected and measured in the received signal. In a multimode waveguide the carrier frequency can coincide with the interference minimum and disappear, but during HIFT it was usually strong enough for detection. The first method implies a time scale changing via appropriate (time-dependent) interpolation of the input data set. Another (simplified) approach is to use the corrected frequency, $f_0 + f_D$, for demodulation. This procedure does not eliminate spectrum extension of wideband signals but it is not important when $f_D/f_0 < 1/\Delta f T$, where Δf is the frequency range of analysis. In our processing, T was not more than four cycles of the M1 sequence. Therefore, in the 10-Hz frequency range the value $f_D < 0.06$ Hz was not critical. The third way is to

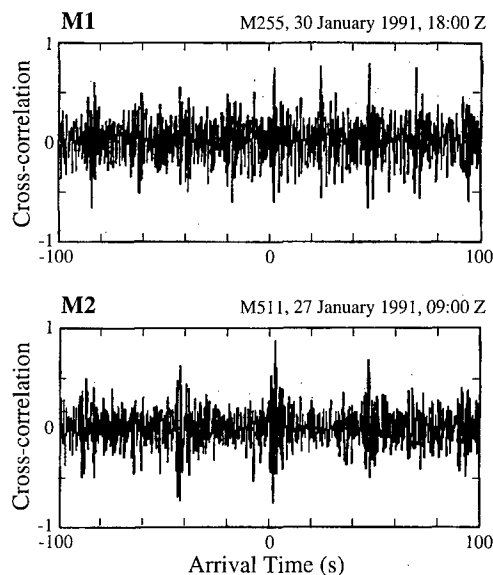


FIG. 8. Cross correlation of demodulated signal with replica in the 2-Hz band.

change the time scale of the replica that is essentially shorter than the input data set. This method is only valid for records with stable Doppler shift.

Two dual-channel spectrum analyzers were used for on-line processing. With the help of the first one the value f_D was estimated and used to set the correct demodulating frequency. The correlation of the demodulated signal and the output from the M-sequence generator was determined by the second analyzer. It was found that the correlation was weak and unstable in an analysis band of 10 Hz. The visible impulse response with clear correlation peaks was obtained only for a 2-Hz analysis band as shown in Fig. 8 for the respective M1- and M2 sequences.

The objective of post-processing was to resolve separate arrivals and investigate the behavior of the arrival structure. The data stored were demodulated with a Doppler shift correction, low-pass filtered, and decimated to obtain frequency spans of ± 11.4 , ± 5.7 and ± 2.85 Hz. The time dependence of the Doppler shift during transmission was determined previously by FFT. The demodulated set was correlated with the replica in the same frequency band. First, we tried to study the arrival structure in general. A modulus of the correlation function of the M1 signal incoherently averaged during 1 h is shown in Fig. 9. The arrival spread is approximately 18 to 20 s, but there is no clear structure that can be treated as modal or ray arrivals.

To obtain more detailed information on arrivals behavior, we calculated the time dependence of the correlation function (Fig. 10). This correlation analysis was performed in the ± 2.85 -Hz frequency range with averaging over four periods of the M1 sequence. Then the modulus of the correlation function was averaged incoherently over five periods. The function obtained is periodic along the x axis with the period of M1. Its behavior along the y axis is less clear. There are some peaks, but their lifetime is no more than 5 min. It is impossible to trace the transformation of correlation peaks into each other. At the present moment we have

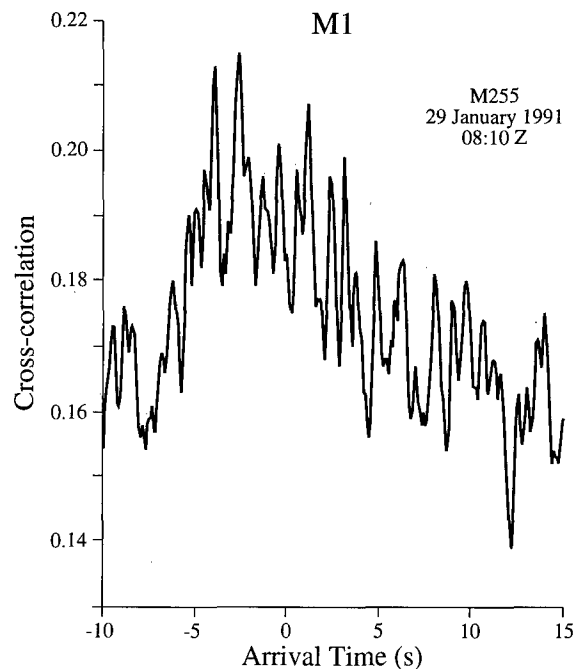


FIG. 9. Cross correlation in the ± 5.7 -Hz band averaged incoherently over reception session.

no evidence for which factor is responsible for this instability—ship motion, variability of ocean waveguide and mode dispersion, horizontal multipath, or any other.

VI. CONCLUSIONS

The results obtained on a 12.5-Mm path from Heard Island to the Krylov seamount provided important information on the reality of global ocean monitoring. A source level of 220 dB *re*: 1 μ Pa/1 m was sufficient for the reliable reception of Heard Island signals to the receiver ship. The region near the west corner of the Cape Verde Islands is situated in an area of good reception of the Heard Island transmission. This fact enables the possible installation of a stationary reception station for future experiments on global ocean monitoring.

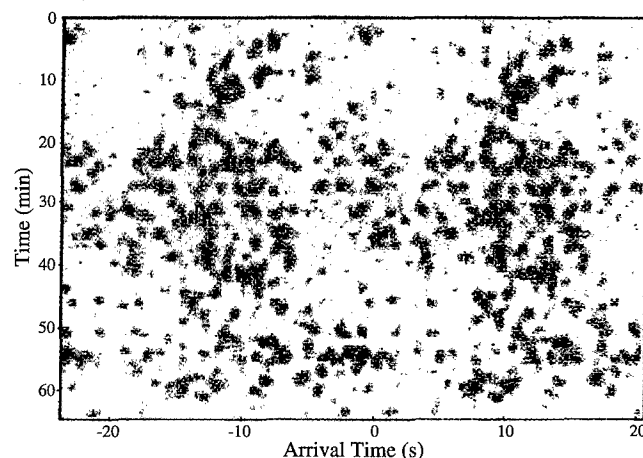


FIG. 10. Variability of the arrival structure during one reception session for M1 sequence in the ± 2.85 -Hz band.

On one hand, the signal exhibited an amazing phase stability that promises the possibility of the precise measurement of the propagation time between the future fixed transmitters/receivers. On the other hand, the arrival structure appeared to be much more complicated and variable than expected. This fact can hamper the elaboration of future ocean acoustic thermometry projects. But no matter which tendency will dominate, the results of the HIFT experiment provide an important positive results to hydroacoustics, and lead us to deeper insight into the physics of sound propagation through and across the global oceans.

ACKNOWLEDGMENTS

We are glad to thank Dr. W. Munk and Dr. R. Spindel for the invitation to take part in the Heard Island Feasibility Test. We thank Dr. T. Birdsall for complete information about the transmitted signals, and also with him Dr. K. Metzger and Dr. M. Dzieciuch for consultation on signal processing. We extend our thanks to Dr. K. Sabinin from the

Acoustics Institute who provided all the necessary oceanological information and invaluable moral support.

- ¹K. D. Heaney, W. A. Kuperman, and B. E. McDonald, "Perth-Bermuda sound propagation (1960): Adiabatic mode interpretation," *J. Acoust. Soc. Am.* **90**, 2586-2594 (1991).
- ²H. I. Fine, *Navigation, Loci and Marine Astronomy* (Transport, Moscow, 1977).
- ³W. H. Munk, W. C. O'Reilly, and J. L. Reid, "Australia-Bermuda Sound Transmission experiment (1960) Revisited," *J. Phys. Oceanol.* **18**, 1876 (1988).
- ⁴S. Gorshkov (Ed.), *World Ocean Atlas* (Pergamon, New York, 1979).
- ⁵W. H. Munk, R. C. Spindel, A. Baggeroer, and T. G. Birdsall, "The Heard Island Feasibility Test," *J. Acoust. Soc. Am.* **96**, 2330-2342 (1994).
- ⁶T. G. Birdsall, K. Metzger, and M. A. Dzieciuch, "Signals, signal processing, and general results," *J. Acoust. Soc. Am.* **96**, 2343-2352 (1994).
- ⁷S. M. Flatté (Ed.), *Sound Propagation in the Fluctuating Ocean* (Cambridge U. P., Cambridge, 1979).
- ⁸J. L. Spiesberger, P. J. Bushong, T. G. Birdsall, and K. Metzger, "Ocean acoustic tomography: Estimating the acoustic travel time with phase," *IEEE J. Ocean. Eng.* **14**, 108-119 (1989).
- ⁹T. G. Birdsall and J. Metzger, "Factor inverse matched filtering," *J. Acoust. Soc. Am.* **79**, 91-99 (1986).

Heard Island signals through the Agulhas retroflection region

G. B. Brundrit

Department of Oceanography, University of Cape Town, Rondebosch 7700, South Africa

L. Krige

Institute for Maritime Technology, P.O. Box 181, Simon's Town 7995, South Africa

(Received 20 August 1992; accepted for publication 7 June 1994)

Heard Island Feasibility Test sound transmissions were received at sea some 300 km southwest of the Cape of Good Hope on a four-hydrophone vertical array deployed from the vessel SAS UMZIMKULU. This area, 53-min travel time along the Atlantic path from Heard Island, lay immediately down path from strong regional variability in the acoustic properties of the SOFAR channel, associated with the retroflection of the Agulhas current. Many transmissions were not received at all whilst the four successful recordings exhibited a relatively high transmission loss. It appears that interaction between a warm water Agulhas ring and the local seamount bathymetry may have been responsible for the deterioration in the HIFT signal received off Cape Town and at other sites further along the Atlantic path. Nevertheless, the overall quality of these received signals with respect to phase stability and intensity was sufficient for the standard HIFT signal processing to be carried out.

PACS numbers: 43.30.Qd, 43.30.Pc, 43.30.Re

INTRODUCTION

In January 1991 the Heard Island Feasibility Test (HIFT) was carried out to establish the limits of usable long-range underwater acoustic transmissions. Acoustic ray paths heading west from Heard Island and turning northwestwards into the Atlantic Ocean on the African side pass through the retroflection region of the Agulhas Current. Thus such paths pass twice in rapid succession through the extension of a powerful western boundary current with its strongly perturbed acoustic environment. The question arises as to whether or not this varying environment would result in any deterioration in the quality of the HIFT signals. A joint effort from the Department of Oceanography at the University of Cape Town (UCT) and from the Institute for Maritime Technology (IMT) successfully intercepted the HIFT signals at sea some 300 km southwest of the Cape of Good Hope in an endeavour to answer this question.

I. THE ENVIRONMENTAL SETTING

The oceanographic region south of Africa is dominated by the Agulhas Current and the various elements of its retroflection back into the Indian Ocean (Lutjeharms and van Ballegooyen, 1988). The narrow, energetic, warm water, western boundary current leaves the tip of the continental shelf of Africa and re-curves back on itself, exhibiting considerable spatial variability in its chosen path on time scales of one month. Warm Agulhas rings are intermittently cut off the main current and can drift slowly into the South Atlantic Ocean. Although these rings rapidly lose their surface temperature expression, they retain their deep thermal and acoustic characteristics as they move up the Atlantic ocean. The Agulhas Return Current meanders eastward and forms the boundary of the subtropical convergence of the South East Indian Ocean.

The acoustic ray paths from Heard Island travel in the surface duct of polar waters until they reach the Antarctic Convergence Zone where they cross into the internal sound fixing and ranging (SOFAR) channel of temperate waters. South of Africa the penetration of the Agulhas Current interposes subtropical SOFAR channel features into this temperate background. The SOFAR channel is depressed by the overlying warm water and broadened through the dynamic mixing beneath the current. Sound focused on the axis of the sound channel and entering the Atlantic Ocean (Fig. 1) will deepen temporarily from approximately 700 to 1200 m as it moves first beneath the Agulhas Return Current and then beneath the Agulhas Current. The minimum sound speed will increase by almost 10 m s^{-1} during these deep excursions.

Similar changes to the SOFAR channel are found beneath any warm Agulhas rings that are encountered and lead to considerable variability in the acoustic environment along their preferred routes into the South Atlantic (Gordon and Haxby, 1990). The presence of the warm water features associated with the Agulhas Current and the consequent perturbations to the acoustic environment may lead to unexpected spreading and transfer of acoustic energy in the same way as occurs at the Antarctic Convergence (Munk *et al.*, 1994).

The actual configuration of these variable elements of the Agulhas Current at the time of, and immediately prior to, the HIFT transmissions is shown in Fig. 2. In late 1990, the Agulhas Current flowed well to the west of South Africa before retroflection. The current cut off at 20° E in December 1990 and shifted to a southward extension and retroflection in January 1991. This was the configuration at the time of the HIFT transmissions. The remnant Agulhas ring moved slowly northward into the area where the receptions were to be made. Its presence was confirmed by warm water, with a sound speed of minimum at 1200 m, found at (37° S , 17° E) at the time of recordings. An effort was made to avoid the vicinity of the Agulhas ring and record in the temperate wa-

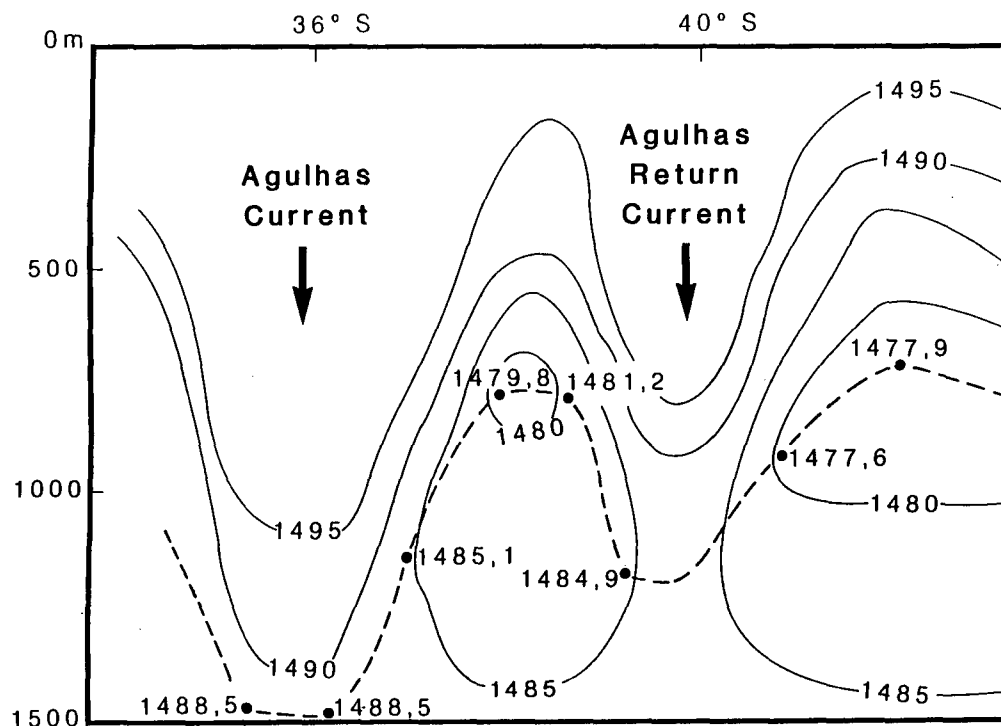


FIG. 1. A vertical section of sound-speed contours through the Agulhas Return current and Agulhas current south of Africa. The depth of the sound-speed minimum is shown by the dashed line joining spot minimum values from data taken from the RV KNORR (Gordon *et al.*, 1987) along 25° S.

ter closer to the continent. However, this could only be achieved at the expense of possible interference from bathymetric features associated with seamounts and the continental shelf south of Africa.

II. CHARACTERISTICS OF RECEIVED SIGNALS

A double four-element array, used for flexibility and redundancy, was towed behind the SAS UMZIMKULU. Whilst

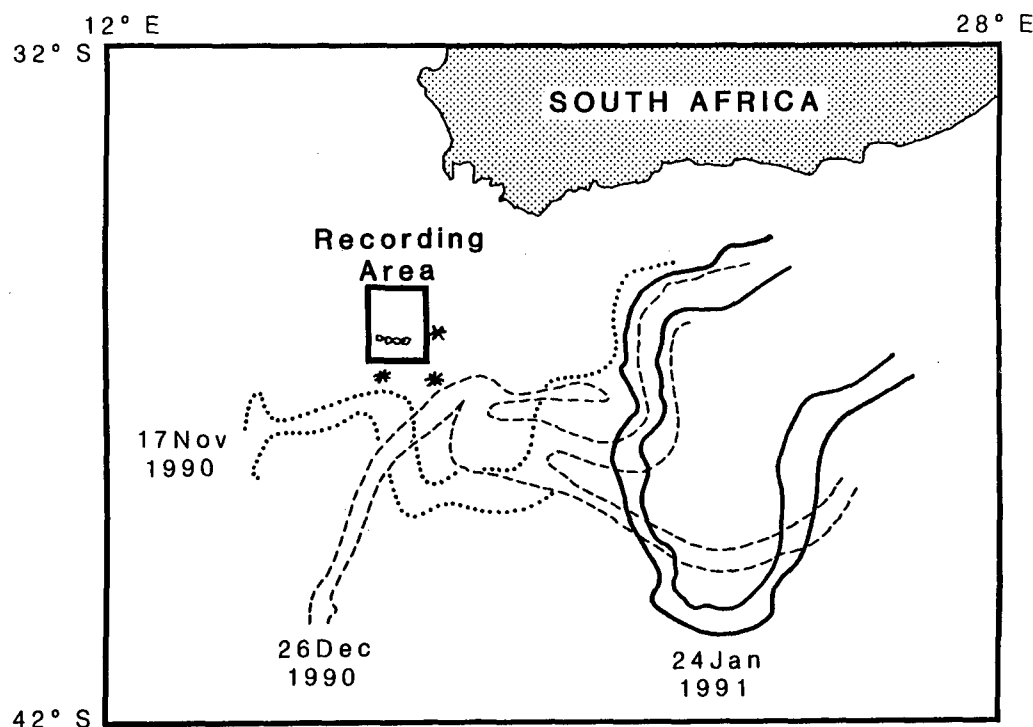


FIG. 2. Evolving configuration of the Agulhas current retroflexion before and during HIFT; line drawing from NOAA 11 thermal band imagery. The recording area is shown with its surrounding seamounts and the positions of the line of successful recordings.

both halves were recorded with a view to possible post processing analysis, only one half was fed into the standard HIFT supplied data acquisition equipment. These recordings were analyzed at the University of Michigan using the methods described in Birdsall *et al.* (1994).

Recordings were taken during 23 transmission periods but only 4 of these contained received signals of analysis quality. The continuous wave (cw) transmission 33 and the pentaline (P) transmission 34 provided good quality recordings and their amplitude and phase curves are shown in Fig. 3. The two M-sequence transmissions 31 and 39 only provided recordings of a quality to warrant carrier (C) analysis.

Pertinent details of these transmissions and received signals are given in Table I, as are transmission losses estimated from a processing gain of 16.5 dB (Birdsall *et al.*, 1994).

III. DISCUSSION

The original objective in recording HIFT signals off the Cape of Good Hope was to establish whether or not the passage through the Agulhas Retroflexion region had led to a deterioration in the quality of the signals. The general character of the received signals in respect of amplitude fluctuation and phase stability was similar to those received at other

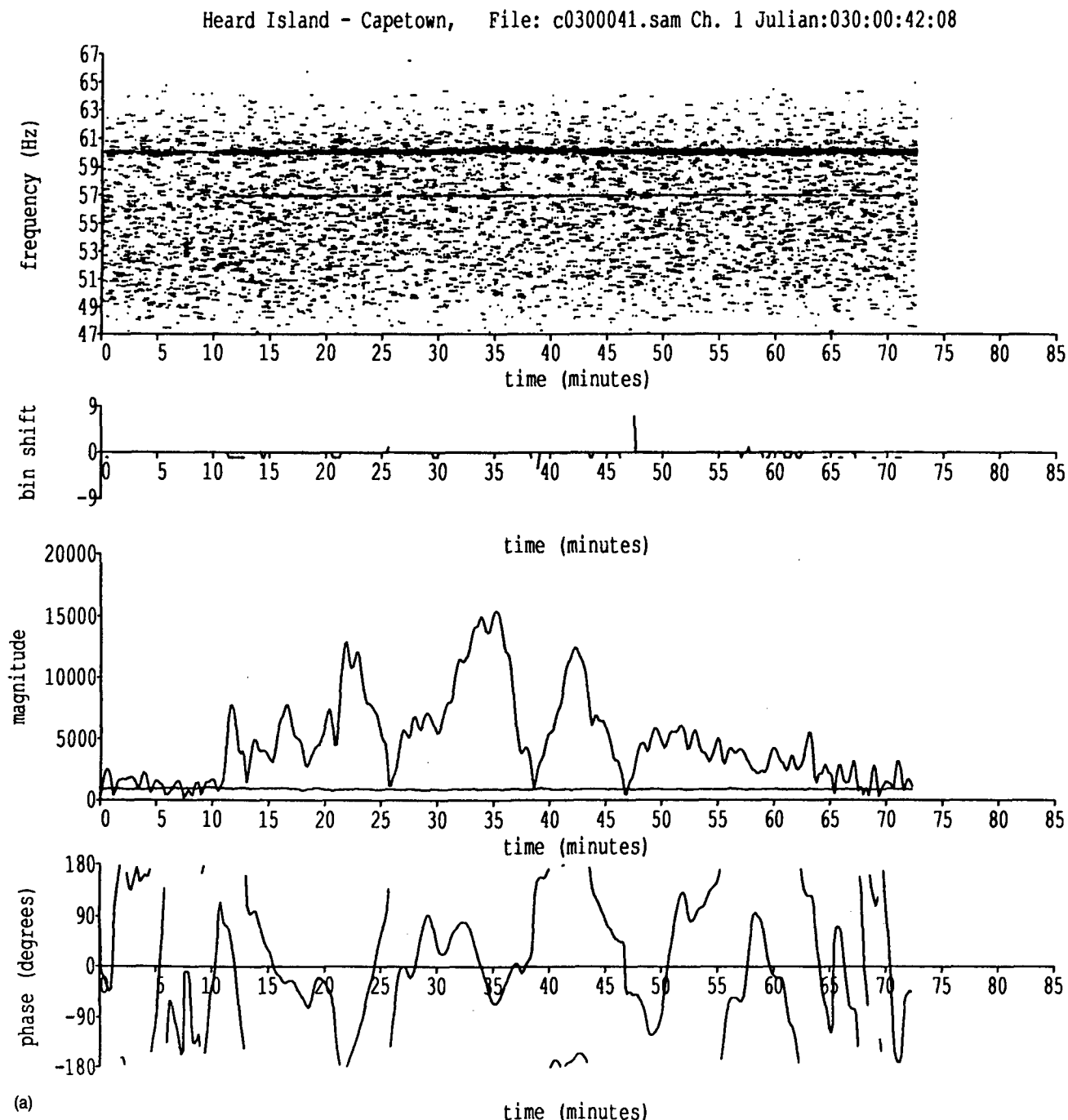


FIG. 3. A continuous wave transmission (a) and a pentaline transmission (b) received by a ship-suspended hydrophone off Cape Town, South Africa. The ubiquitous 60-Hz ship's power is evident but caused no difficulties.

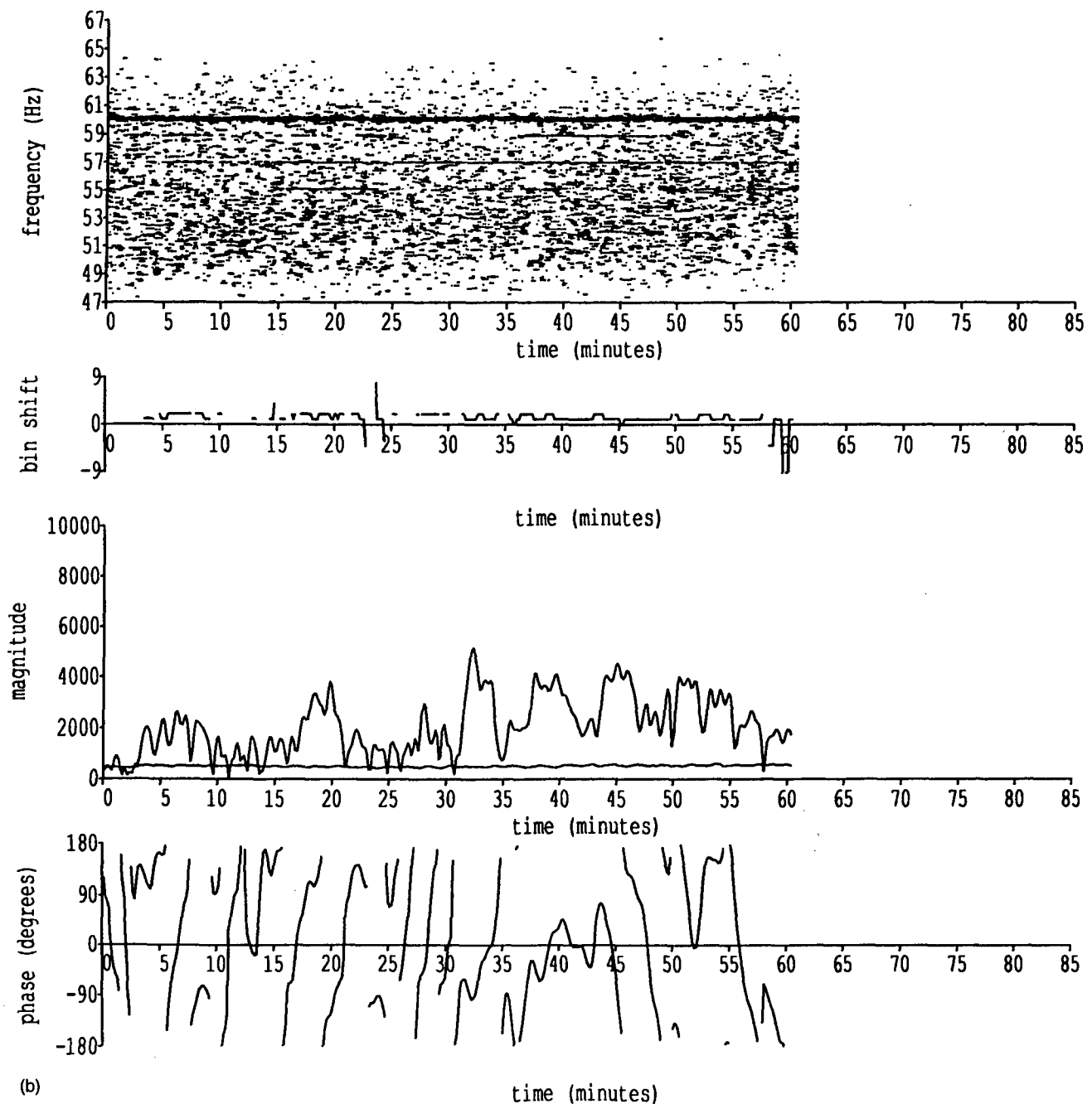


FIG. 3. (Continued.)

TABLE I. Successful recordings made by the SAS UMZIMKULU. Transmission index (a), commencing at day/time (b), of type (c), at source level (d), was recorded at background noise level (e), and after analysis of type (f), has a mean signal-to-noise ratio (g), and a calculated transmission loss (h); source levels in dB re: $1 \mu\text{Pa}$ at 1 m, and signal levels in dB re: $1 \mu\text{Pa}$.

| a | b | c | d | e | f | g | h |
|-----|----------|----|-------|----|---|------|-------|
| T31 | 029/1800 | M | 220.8 | 70 | C | 14.8 | 152.5 |
| T33 | 030/0000 | cw | 218.7 | 74 | C | 17.5 | 143.7 |
| T34 | 030/0300 | P | 218.7 | 70 | P | 14.5 | 150.7 |
| T39 | 030/1800 | M | 213.0 | 75 | C | 10.0 | 144.5 |

HIFT receiving sites. Thus these Cape Town signals could also be subjected to the same remarkable signal processing as the other HIFT signals received elsewhere.

The principal differences from other sites were in the few signals received and their relative weakness. The transmission loss in the four signals approaches 150 dB, a loss which is much higher than that experienced at Ascension but is comparable to that at distant sites, Krylov seamount and the Canadian towed array off Newfoundland (Birdsall *et al.*, 1994). This suggests that the cause of the higher transmission

loss should be a feature or process confined to a more easterly path into the Atlantic, possibly within the Agulhas retroflexion region. Rather than being due to a single cause such as sound spreading by an Agulhas ring or interference from bathymetry, the explanation may be a combination of these effects.

The four successful recordings off Cape Town were all taken whilst the SAS UMZIMKULU was steaming west along latitude $36^{\circ} 26' S$ close to $17^{\circ} E$. Recordings taken both north and south of this line showed little evidence of any received signal at all. Thus it appears as if the successful, though weak, receptions came through a gap in some substantial blockage. This is consistent with the positions of the Protea and Argentina seamounts off the continental shelf of South Africa on either side of the upstream sound path. However, these seamounts reach only 1400 m below the surface and it is somewhat surprising that they should have such a profound effect. The crucial factor may be the presence of the Agulhas ring with its deepened SOFAR channel temporarily located astride the seamount chain. It is possible that the seamounts intrude sufficiently into the SOFAR channel beneath the Agulhas ring to significantly interfere with sound transmission, both immediately downtrack off the Cape of Good Hope and further into the Atlantic Ocean.

In conclusion it appears that interactions between oceanographic features of the Agulhas retroflexion region

and the local bathymetry adversely affected the strength of the HIFT signal. Nevertheless, the overall quality of the HIFT signal was unimpaired so that standard analysis of the Cape Town recordings could still be carried out and they could form a part of the usable HIFT data set.

ACKNOWLEDGMENTS

The authors are indebted to their colleagues, E. Potgieter, M. P. Stander, R. C. van Ballegooyen, P. B. Runciman, D. Sale, A. C. Hardisty, and H. R. Valentine from IMT and UCT for the preparatory work and for recording the signals at sea under difficult circumstances. Support and assistance were provided by the South African Department of Environment Affairs, the South African Naval Hydrographer, and the South African Navy.

- Birdsall, T. G., Metzger, K., and Dzieciuch, M. A. (1994). "Signals, signal processing and general results," *J. Acoust. Soc. Am.* **96**, 2343–2352.
- Gordon, A. L., and Haxby, W. F. (1990). "Agulhas eddies invade the South Atlantic: Evidence from Geosat altimeter and shipboard conductivity-temperature-depth survey," *J. Geophys. Res.* **95**, 3117–3125.
- Gordon, A. L., Lutjeharms, J. R. E., and Gründlingh, M. L. (1987). "Stratification and circulation at the Agulhas retroflexion," *Deep Sea Res.* **34**, 565–599.
- Lutjeharms, J. R. E., and van Ballegooyen, R. C. (1988). "The Agulhas Current retroflexion," *J. Phys. Oceanogr.* **18**, 1570–1583.
- Munk, W. H., Spindel, R. C., Baggeroer, A. B., and Birdsall, T. G. (1994). "The Heard Island Feasibility Test," *J. Acoust. Soc. Am.* **96**, 2330–2342.

Relative abundance and behavior of marine mammals exposed to transmissions from the Heard Island Feasibility Test

Ann E. Bowles

Hubbs-Sea World Research Institute, 1700 South Shores Road, San Diego, California 92109

Mari Smultea and Bernd Würsig

Marine Mammal Research Program, P.O. Box 1675, Galveston, Texas 77553

Douglas P. DeMaster and Debra Palka

Southwest Fisheries Science Center, P.O. Box 271, La Jolla, California 92038

(Received 20 August 1992; accepted for publication 7 June 1994)

The Heard Island Feasibility Test source transmitted a hum at 209–220 dB *re*: 1 μ Pa at 175-m depth, centered on 57 Hz with a maximum bandwidth of 30 Hz for 1 h of every 3. Experienced marine mammal observers conducted line-transect surveys and monitored marine mammal behavior visually and acoustically in a 70 \times 70 km square centered on the transmission site. Thirty-nine groups of cetaceans and 19 of pinnipeds were sighted from both vessels before the start of transmissions. Thirty-nine groups of cetaceans and 23 of pinnipeds were sighted during transmissions. Blue (*Balaenoptera musculus*), fin (*B. physalus*), and sperm (*Physeter macrocephalus*) whales were sighted during the base line period; blue, sperm, and possibly sei (*B. borealis*) whales were sighted during the transmission period. More schools of hourglass dolphins (*Lagenorhynchus cruciger*) were sighted during transmissions, but fewer groups of pilot whales (*Globicephala melas*), southern bottlenose whales (*Hyperoodon planifrons*), and minke whales (*B. acutorostrata*). The density of all cetaceans was 0.0157 groups/km² before the transmissions and 0.0166 groups/km² during. Antarctic fur seals (*Arctocephalus gazella*) and southern elephant seals (*Mirounga leonina*) were seen, but not in sufficient numbers to estimate abundance. One blue whale tracked before, during and after a transmission changed respiration and reorientation rates, but did not avoid the source detectably. Sperm whales and pilot whales were heard in 23% of 1181 min of baseline acoustic surveys; but in none of 1939 min during the transmission period. Both species were heard within 48 h after the end of the test.

PACS numbers: 43.30.Qd, 43.80.Nd

INTRODUCTION

The biological portion of the Heard Island Feasibility Test (HIFT; Munk and Forbes, 1989; Munk and Baggeroer, 1992) was conducted in a 70 \times 70 km square centered on the site of the test, at 53° 25' S \times 74° 30' E, from 19 January to 3 February 1991 (Fig. 1). The area lies south of the Antarctic convergence (at about 50° S) and within the summer feeding range of many species of marine mammals, including endangered balaenopterids and sperm whales (*Physeter macrocephalus*). The study had a dual goal, to monitor the impact of HIFT transmissions on marine mammals and to provide mitigation in the event that mammals were observed close to the sound source immediately prior to transmissions.

The number of pinnipeds and cetaceans likely to be affected by HIFT was difficult to estimate because few surveys for marine mammals have been conducted in the vicinity of Heard Island. Surveys by Ensor and Shaughnessy (1989) found large concentrations of fur seals (*Arctocephalus gazella*) at sea near the island and over the Kerguelen Plateau to the north and east, about 110 km from the study site. About 4000 fur seals breed along the north shore of the island during the austral summer, including a large colony on a

spit at the east end. A declining population of 13 000 elephant seals (*Mirounga leonina*) breeds on the island during the austral winter (Burton, 1986), but the number that return to molt in the summer is unknown.

Small odontocetes are common in the area, particularly the hourglass dolphin (*Lagenorhynchus cruciger*). Other small odontocetes known to occur are the Commerson's dolphin (*Cephalorhynchus commersoni*), the dusky dolphin (*Lagenorhynchus obscurus*), and possibly the spectacled porpoise (*Phocoena dioptrica*). Killer whales (*Orcinus orca*) also occur. None of these species are endangered, and there are no good quantitative estimates of their abundance. Mid-to large-sized, deep-diving odontocetes also occur in the area. The most common are the southern long-finned pilot whale (*Globicephala melas*), southern bottlenose whale (*Hyperoodon planifrons*), Arnoux's beaked whale (*Berardius arnouxii*), and adult bulls of the endangered sperm whale (*Physeter macrocephalus*). Stocks of sperm whales are thought to approach 70% of pre-exploitation levels in the Indian Ocean (Gosho *et al.*, 1984), but no estimates are available for the other species. Mysticetes are known to occur in the area in low density, including minke (*Balaenoptera acutorostrata*), blue (*B. musculus*), fin (*B. physalus*), sei (*B. borealis*), hump-

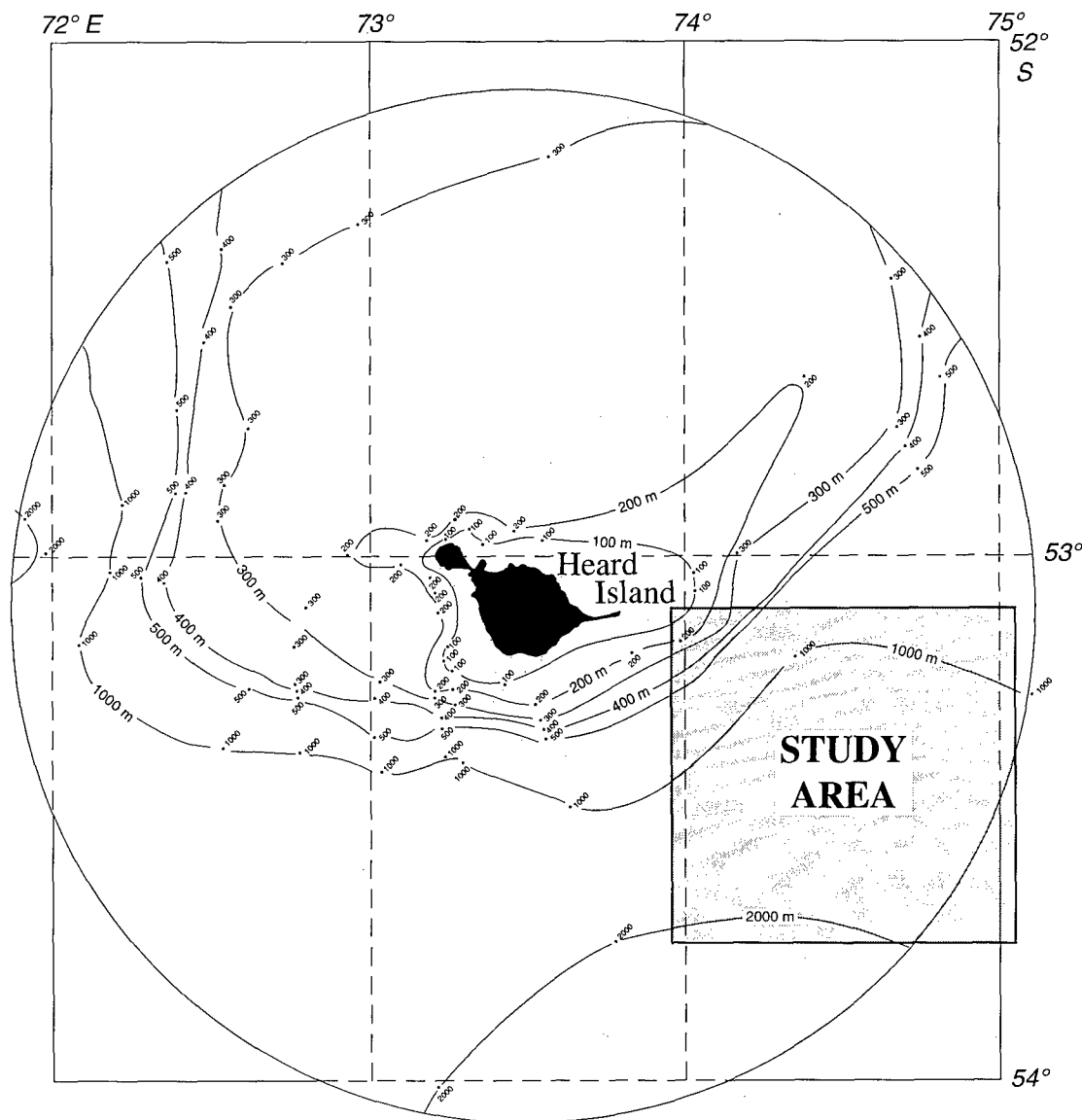


FIG. 1. Map of Heard Island and location of study area.

back (*Megaptera novaeangliae*), and southern right (*Balaena australis*) whales. No density estimates are available for these species in the immediate vicinity of Heard Island, although their abundance near the Antarctic continent has been measured (Mizroch *et al.*, 1984a, b, c).

The potential for impact was also difficult to estimate because the limit of the zone of influence of the transmissions was difficult to define. For the purposes of the Marine Mammal Permit issued to the program, all the marine mammals within International Whaling Commission management sectors III and IV, estimated at a minimum of 349 200 animals, were considered to be exposed, although risks of significant effect were small. The 160-dB isopleth was taken as a limit for possible serious effects in the permit issued for the study (Permit HI-12/7/94 [No. 719] issued to Dr. Walter Munk), including effects on audition. Transmissions were required to be delayed or aborted when any cetaceans were within the zone defined by this limit immediately before a transmission. Transmissions were allowed to continue in the event that pinnipeds and smaller cetaceans approached of

their own volition while the source was active.

Small odontocetes do not hear well at low frequencies and little effort has been expended to measure their low frequency hearing. The bottlenose dolphin has a threshold of 130 dB at 50 Hz (Johnson, 1966) based on measurements of one individual. These species were unlikely to hear the transmissions except at very close range. Mysticetes hear well at low frequencies, based on measurements of cochlear morphology, particularly the large rorquals, with estimated best frequencies ranging from below 500 Hz to 1–2 kHz (Ketten, 1992; Fleischer, 1976; Norris and Leatherwood, 1981). The sperm whale hears best at around 2500 Hz (Carder and Ridgway, 1990), so it probably hears reasonably well at low frequencies, but it is not a low-frequency specialist (Ketten, personal communication).

Short-term behavioral responses of marine mammals, particularly mysticetes, to anthropogenic noise have been measured in detail (Richardson *et al.*, 1991). Short-term behavioral responses have been favored as measures because quantitative estimates of effects on reproduction, survivor-

ship, and distribution have been difficult to obtain. Behavioral responses include deviations in tracks for distances of a few hundred meters, changes in respiration patterns, changes in interindividual distances, and changes in activity (Ljungblad *et al.*, 1985; Richardson *et al.*, 1985; Richardson *et al.*, 1986). Based on short-term experimental exposures to continuous industrial noise, significant proportions of study populations respond at sound pressure levels of 110–120 dB, or 10–30 dB above ambient in the appropriate band. However, such responses can occur at or below ambient (Dalheim and Ljungblad, 1990), that is, at or close to the limits of detection. It is not known whether cetacean responses would eventually decline through habituation. Similar behavioral responses could be expected during HIFT from any cetacean that could hear the transmissions.

Temporary cessation of vocal behavior is common in the sperm whale (Watkins and Schevill, 1975; Watkins *et al.*, 1985) in response to anthropogenic noise. This response is not as well documented in balaenopterids, but it does occur. Therefore, changes in vocal activity of cetaceans in the vicinity of the source site could be expected in addition to changes in surfacing patterns.

The marine mammal monitoring component of HIFT was a short-term study by necessity because the experiment itself was of short term (5 days with eight 1-h transmissions per day). Therefore, only short-term behavioral responses could be monitored. There was little chance that a statistically useful sample of observations could be obtained before, during and after transmissions in such a short period. To provide as sensitive a measure of effects as possible, both changes in density of marine mammals in the immediate vicinity of the transmissions and behavioral responses were collected. While transect surveys over large areas have been used to measure the consequences of exposure to human activity, they have not been used in experimental studies of noise effects previously. The HIFT transmissions were expected to insonify a sufficiently large area that line-transect surveys would provide a useful indication of response.

I. METHODS

The transmission protocol is described in detail elsewhere in this volume. As planned, transmissions of three types were to be emitted by 5 elements of a 10-element phased array of Hydroacoustics HLF-6 sources, with an estimated maximum output level of 220 dB *re*: 1 μ Pa at 1 m. The array was to be centered at 175 m depth, the estimated depth of the sound speed minimum ("sound channel" or "SOFAR channel," see Payne and Webb, 1972) near Heard Island. Transmissions were centered on 57 Hz, and consisted of a continuous tone, a narrow-band pulse-encoded signal (pentatone; 15-Hz bandwidth), and broader-band pulse-encoded signals (M-sequence, 30-Hz bandwidth). The maximum duty cycle for these transmissions was 33%, with transmissions taking place for 1 h out of every three.

The biological portion of the program consisted of three types of measurements, (1) line transect surveys to measure cetacean density and distribution around the source, (2) be-

havioral observations of animals at the surface from the vessel to determine whether there were changes in respiratory profiles during transmissions, and (3) acoustic measurements of calling underwater at a series of listening stations along the survey track. The methods for each type of observation are listed below.

A. Line-transect surveys

Two vessels made the expedition to Heard Island, the transmitting vessel (R/V CORY CHOUEST) and the marine mammal survey vessel (R/V AMY CHOUEST). A line-transect survey was conducted from AMY in the study area (Fig. 1) during a four day baseline period before the start of the transmissions (19–24 January). It was repeated during the transmission period (24 January–3 February). A total of 1120 km (605 nm) of surveys were planned for each period.

From AMY, two teams of observers alternated 2-h watches from 0500 to 2000 h local time, stationed on the flying bridge. During good weather (Beaufort wind condition of 4 or less), one observer searched for animals at long range using 25 \times 150 spotting binoculars, and one monitored closer to the vessel using 7 \times 50 binoculars. The observers stood 15 m from the ocean surface and had an unobstructed view of 90° on either side of the track line. Both sets of binoculars were marked with reticles for estimating sighting distance. The 25 \times 150 binoculars were not useful under poor sighting conditions, e.g., in fog, rain, high glare, and high sea states. In bad weather, one observer searched using the 7 \times 50 binoculars and the other searched with the naked eye. Observations were stopped when the wind condition exceeded Beaufort 8 or when visibility dropped below 0.5 nm.

On the transmitting vessel, CORY, two teams of observers surveyed for marine mammals within 10 km of the transmitting vessel to provide information on marine mammal distribution close to the transmission site and to determine whether marine mammals were present before and during transmissions. They did not survey on randomized lines, and their activities were confined to the 9.25 \times 9.25 km square within which all transmissions took place. Two observers at a time searched 360° around the vessel for at least 15 min before and for the entirety of each transmission, around the clock. One observer was stationed on the flying bridge (15 m) and another on the antenna deck (9 m). During the day, searchers used the 25 \times 150 and 7 \times 50 binoculars as described above. At night, only one observer searched the area within 1.1 km of the vessel using a Dark Invader light-intensifying scope (Meyers).

When groups were sighted, observers recorded date, local time, Beaufort wind condition species, location, distance, and bearing from the survey vessel, sighting cue, estimated speed of travel, estimated direction of travel relative to the vessel, location relative to other marine mammals or birds in the area, group size, age and sex, and notes on activity.

B. Behavioral observations

When weather conditions permitted and cetacean groups remained at the surface for an extended period, behavioral observations of 1 h or more were made from AMY. Observa-

tions were made of mysticete pods preferentially because they were thought to be most vulnerable to the transmissions and because they could be followed reliably from far enough away that the vessel would not mask transmission noise completely, 1–2 km behind the whales. The following data were recorded: general behavior (travel, mill, socialize, feed, and rest); conspicuous surface behaviors; respiration rate; absolute orientation; estimated orientation relative to the vessel; estimated speed (slow: 1–4 km/h, medium: 5–8 km/h, fast: >8 km/h); presence and location of other cetaceans in the area; and estimated interindividual spacing (m). Bearing and distance from the vessel was recorded at or near the first surfacing of each surfacing sequence with the 25×150 binoculars.

From the surfacing sequences, a number of parameters were calculated: number of complete surfacing sequences, defined as a series of blow intervals separated by no more than 1.5 min; total number of blows per surfacing sequence; mean number of blows per minute per individual; mean duration of dives between surfacing sequences; mean duration of surfacing sequences; number of blows per respiration sequence, defined as the surfacing time plus the preceding dive time; and mean number of blows per minute within surfacing. For groups in which individuals could not be distinguished, the mean number of blows per total minutes of observation was divided by the number of whales.

Reorientation rates (a measure of how often the whale changed direction) were calculated by summing the smallest absolute difference between successive orientations and dividing by the total number of minutes of observation. Orientation relative to the survey vessel was measured using a relative orientation score (ROS) whenever animal headings could be determined. This score was calculated from the estimated relative orientation of the group to the vessel, with the vessel's bow defined as 0°, and the bearing of the group relative to the vessel. Distance to the vessel was not considered in this score. The score was obtained using the relation:

$$\text{ROS} = -\cos(\text{group orientation relative to the vessel} \\ - \text{group bearing relative to vessel}). \quad (1)$$

(We are indebted to John Hunter, Commonwealth Scientific and Industrial Research Organization of Australia, for this relation.) Relative orientation scores ranged from -1 (swimming directly away from the vessel) to +1 (swimming directly toward the vessel). They were calculated relative to both the survey vessel (AMY) and the transmitting vessel (CORY). For sightings made on transects, the initial orientation of the group was used to calculate the score. Scores were not calculated for dolphins riding the bow of the vessel.

C. Acoustic surveys

Acoustic monitoring stations were established at night whenever conditions permitted (Beaufort 6 or less), both during the baseline and the transmission period. Magnavox 57A sonobuoys were deployed at four depths (18, 50, 80, and 122 m) from the stern of the vessel. The intermediate depths (50 and 80 m) were set by tying the hydrophone and the bottom

of the transmitter casing to either end of a heavy unbraided natural fiber cord of the correct length. To avoid tangling during deployment, the cord was paid out with a string launcher with the vessel underway slowly. The signal from the sonobuoy was received with an omnidirectional antenna and a Yagi directional antenna mounted on the helicopter deck of the vessel, 12 m above the surface and well away from the ship's radar and satellite antennas. The FM signal was demodulated and amplified with a four-channel Navy sonobuoy receiver (AN/ARR 52A receiving elements). This sonobuoy-receiving system detected the FM carrier from the buoy at adequate levels within 10 km of the vessel when wind conditions were under Beaufort 5–6. The receiving characteristic of the sonobuoy was not linear, de-emphasizing low frequencies. Reverse filtering was used to correct for nonlinearity during analysis. The system saturated at 132 dB at 57 Hz.

Calibrated recordings of the signal from the sonobuoy were made with a four channel TEAC RD101T DAT recorder (0–10 kHz). They were also displayed and recorded with a digital spectrograph to allow detection of infrasonic signals, such as blue whale calls. The recorded signal was corrected for the receiving characteristic of the sonobuoy-receiver system with an analog filter bank, then input to a Spectral Dynamics SD380 digital spectrum analyzer in order to measure absolute sound levels.

Sonobuoys were dropped each night from both vessels. Single buoys were always dropped from CORY, which was kept underway continuously. In marginal weather, AMY steamed slowly into the seas and only one buoy was dropped. Under good conditions, AMY drifted with engines off and buoys were dropped every 2 h to insure coverage for the whole night. Hydrophone depth was set to 80 m by default. If cetaceans were calling, more buoys were deployed, set to 18, 50, or 122 m, based on the target species and sea state. Buoys were also dropped during the daytime during behavioral observations. Surveys were conducted until a group of cetaceans was detected, at which time sonobuoys were deployed. In cases where cetaceans were tracked for a long time, buoys were dropped at half-hour intervals.

The HIFT sources were tested and calibrated on 24 January from 1830–2000 h and on 25 January from 1200–1530 h. before the scheduled start of transmissions on 26 January. The biological survey team assisted this effort by deploying sonobuoys at 80-m depth at ranges of 55–75 km from the source site. During these tests, the AMY's engines were off. The range of the AMY to the sonobuoy was determined with a 9-kHz pinger (provided by the Applied Physics Laboratory, University of Washington).

The acoustic environment below 300 Hz was noisy throughout most of the study due to pulses from a distant French seismic survey vessel, the M/V MARION DUFRESNE, operating along the Kerguelen Plateau, and to noise made by AMY and CORY. Ambient noise measurements included distant noise from these vessels, and could not be estimated in high sea states due to noise generated by sonobuoy motion.

TABLE I. Transmission loss and received source levels from calibration experiments conducted 25 January 1991.

| Source | Sound pressure level at transmission frequency as measured on AMY (dB) | Range at time of measurement (km) | Transmission loss (dB) |
|-------------------------|--|-----------------------------------|------------------------|
| 1 | 129.9 | 57.3 | 73.3 |
| 8 | 131.4 | 57.7 | 72.5 |
| 10 | 128.6 | 61.7 | 72.9 |
| 5 odd-numbered sources | 136.2 | 72.0 | 82.7 |
| 5 even-numbered sources | 137.1 | 72.0 | 83.0 |

D. Measuring changes in concentrations of potential prey species

Marine mammals might have been affected by the source transmissions indirectly as a result of effects on their prey species. Some species of fish could probably have detected source transmissions, as many species of fish are known to be able to detect low frequency sound (Enger *et al.*, 1993). Krill are not known to possess organs that would allow them to detect sound pressure, but they might have been able to detect particle displacement near the source. It therefore seemed desirable to have an index of the effects of the transmissions on potential prey organisms.

The most important prey species in the vicinity of Heard Island are vertically migrating euphausiids, which are common within the first 100 m of depth in the sub-Antarctic. Fish and squid are also important prey species. A fish-finding fathometer (Raytheon V820) was available, and used to detect concentrations of fish and krill, but was not useful for detecting squid. It was deployed 3 m below the surface with a finned stabilizer suspended from a boom along the side of the vessel. It was set to transmit at 220 kHz, to provide maximum resolution in the first 100 m and to be inaudible to cetaceans. Throughout the study, the fathometer was monitored 4–5 times daily for 30 min between 1200 and 2400 local. It was also monitored when balaenopterids were tracked by behavioral observers and when small odontocetes were encountered close to the vessel.

II. RESULTS

A. Analysis of transmission sound pressure level

Source levels for each of the 10 elements in the transmission array ranged from 205.5 to 209.3 dB *re*: 1 μ Pa at 1 m. Transmission losses for individual sources were determined empirically at distances of 57–72 km from the transmitting vessel, with received sound levels from single sources ranging from 129–131 dB at 80-m depth (Table I). The received level of the five-element transmitting array at 80 m was estimated to be 136 dB *re*: 1 μ Pa at 68-km distance. The 160-dB isopleth was estimated to lie 1.1 km from the vessel (Munk and Dworski, personal communication).

TABLE II. Summary of survey effort and sightings from the R/V AMY CHOUEST during baseline and transmission periods.

| Period | Hours surveyed | Hours of effort under good conditions (B 4 or less) | Sightings (groups) |
|---|----------------|---|--|
| Baseline | 70.05 | 25.64 (37%) | 5 unidentified whale 1 sperm whale 5 minke whale 2 fin whale 10 southern bottlenose whale 2 unidentified dolphin 6 hourglass dolphin 1 pilot whale 10 fur seal |
| Transmission (24 January–1 February) | 67.00 | 38.45 (57) | 7 unidentified whale 1 sperm whale 1 unidentified balaenopterid 1 blue whale 4 southern bottlenose whale 1 Arnoux's beaked whale 1 unidentified dolphin 14 hourglass dolphin 8 fur seal 2 elephant seal |
| Post-transmission (1 February–3 February) | 25.70 | 11.47 (45%) | 1 hourglass dolphin 2 pilot whale 1 Arnoux's beaked whale 5 fur seals |

The limit of the zone of influence for behavioral changes was estimated *a priori* to be the 120-dB isopleth. The exact limit of this zone was impossible to characterize due to changes at long range in bottom topography and hydrographic features (principally the Antarctic convergence). However, it is likely to have been at a range of hundreds of kilometers in the top 100 m of water to the west and east of the transmission site.

From 1800 h on 24 January to 0200 h on 1 February, transmissions were made during 33 of 176 available hours (18.8%). The highest daily duty cycle (30%) was transmitted in the first few days of the experiment. A total of 35 transmissions were completed, 16 with the complete five-source array. No transmissions were made on 28 January due to equipment failure. Then, beginning 30 January, a storm disrupted the experiment, progressively damaging the source array and rendering biological observations difficult. The last 18 transmissions were completed with progressively fewer sources. Transmissions after 0500 on 31 January were shortened to half an hour, and the last transmission started at 0200 on 1 February. Thus, marine mammals in the area were exposed to three days of transmissions at full intensity, two days of transmissions with decreasing intensity, during which the background noise rose dramatically due to a storm, and one day of shortened transmissions with a single source, also with high background noise.

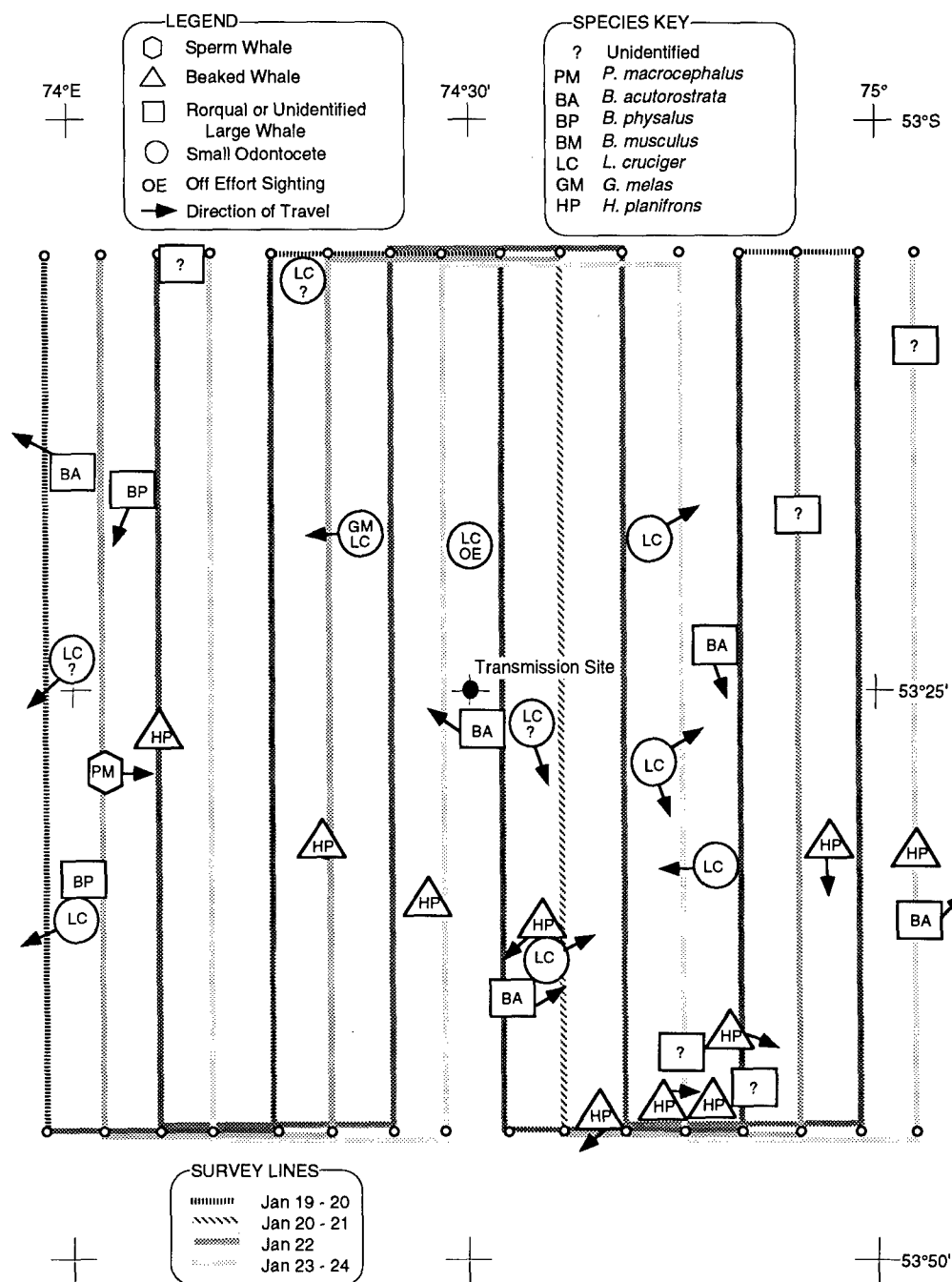


FIG. 2. Map of baseline survey showing locations of cetacean sightings.

B. Results of systematic line-transect surveys from AMY

During the baseline survey, 19 January–24 January AMY completed 1093 km (590 nm) of line-transect surveys in 70.05 h of effort. During the transmission, 25 January–1 February, the AMY repeated these lines; a total of 1010 km (546 nm) of survey lines were completed in 67.0 h of effort. After the transmissions (1–3 February) 309 km (167 nm) were surveyed in 25.7 h.

The weather varied greatly, from Beaufort wind condition 2 to 8. Table II gives a breakdown of the proportion of time spent surveying in good conditions (Beaufort ≤ 5 and visibility > 1 km), which was roughly equal between the baseline and transmission periods.

Figures 2 and 3 show the locations of cetacean sightings during baseline and transmission periods, and Figs. 4 and 5 show the locations of the pinniped sightings. During the baseline period, 31 groups of cetaceans and 10 pinnipeds were sighted. During the transmission period, 30 groups of cetaceans and 15 pinniped groups were sighted. After the transmissions, four groups of cetaceans and five groups of pinnipeds were sighted.

Hourglass dolphins, southern long-finned pilot whales, southern bottlenose whales, Arnoux's beaked whales, sperm whales, fin whales, blue whales, minke whales, fur seals, and southern elephant seals were sighted during these surveys. The predominant cetaceans were the hourglass dolphin,

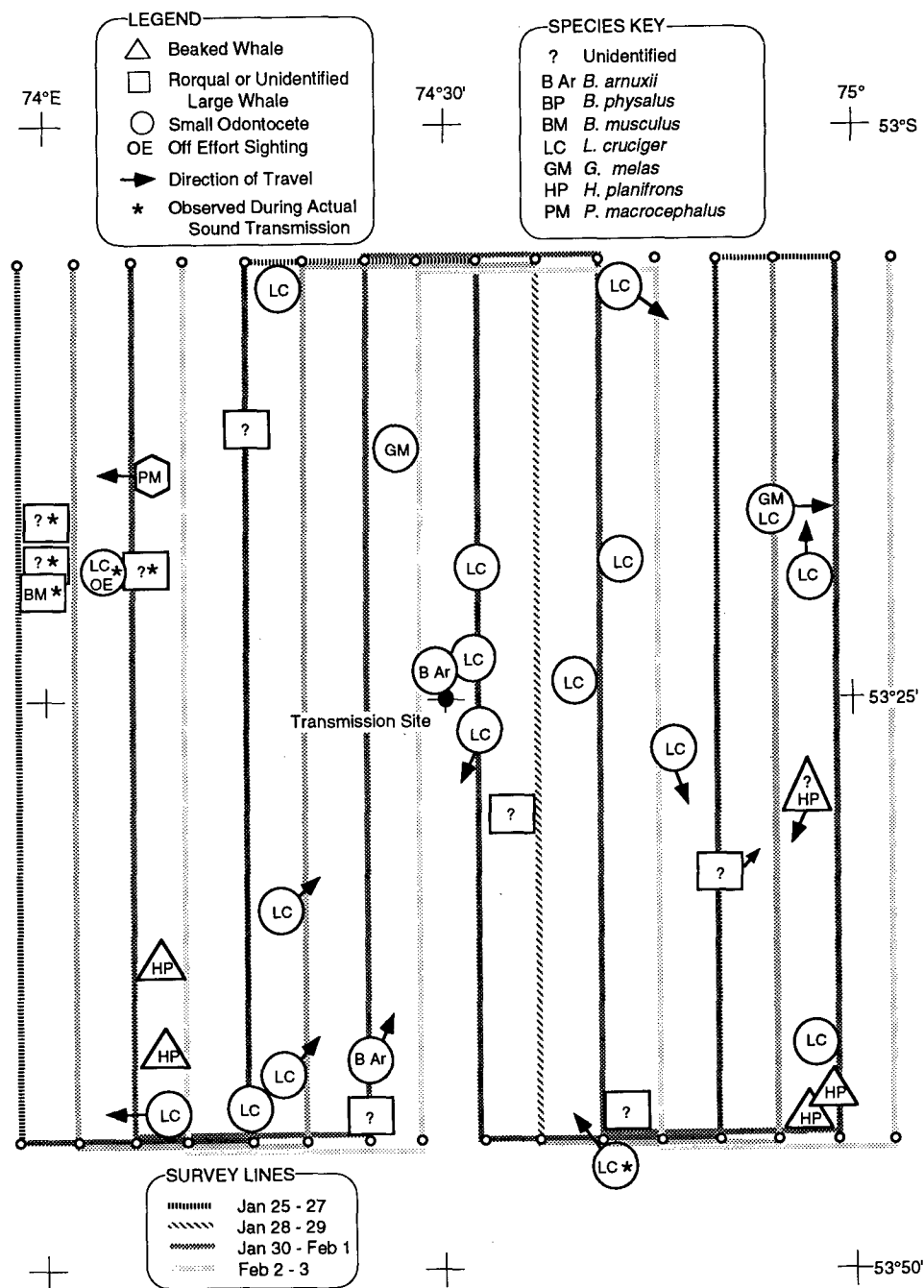


FIG. 3. Map of transmission survey showing locations of cetacean sightings.

southern long-finned pilot whale, southern bottlenose whale, and minke whale (Table II).

Due to one large school of 275 pilot whales and 30 hourglass dolphins sighted during the baseline period, the average group size before and during the transmissions differed greatly (12.16 vs 3.17). The one large school was 5 standard deviations from the mean. Ignoring this extreme value, the average group size dropped to 2.4/group. Because the sample size was small, this school had an undue influence on the estimates of density, and it was removed from further analyses.

The transmission experiment was terminated two days before the line-transect survey was completed for the second time. Therefore, the last two days of this survey were com-

pleted without source noise. Two sets of density estimates were generated, one set for the seven days when transmissions were made (25–31 January), and one for the whole transmission survey (25 January–3 February). The first represents the best estimate possible of the densities of marine mammals during the transmissions. The second allowed a better-matched comparison of distributions in baseline and transmission periods (Table III).

The density of cetacean groups was estimated using the hazard-rate model (Buckland *et al.*, 1993). The 95% confidence intervals were calculated using bootstrap methods. because the sample sizes were small, all abundance estimates have wide confidence intervals and are likely to be unreliable. The only abundance estimates that will be reported are

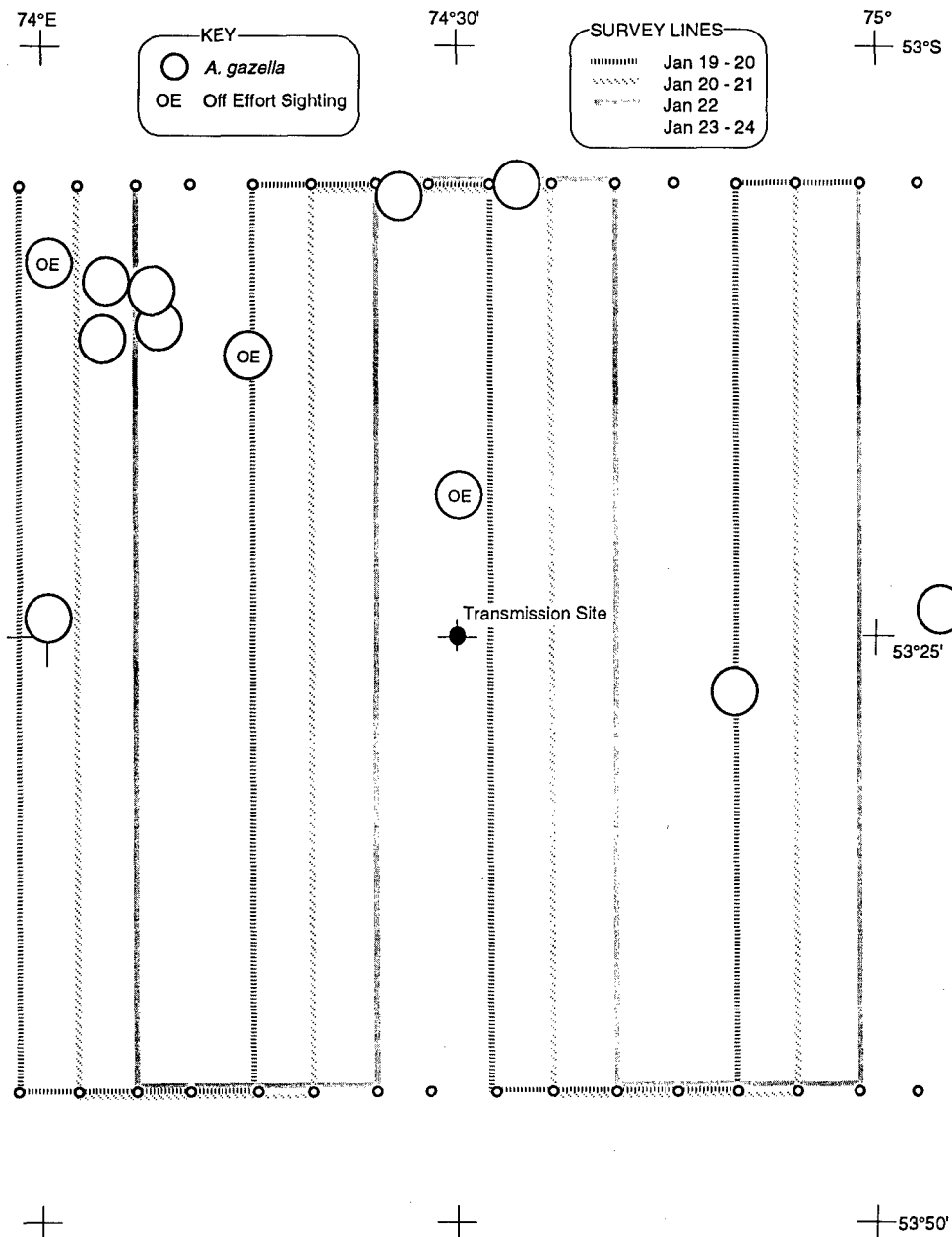


FIG. 4. Map of baseline survey showing locations of pinniped sightings.

overall densities of groups seen from AMY. Before the transmissions, the density of groups was 0.0157 (standard error [se]=0.0076/km²; Table III) and the estimated number of individuals in the area was in the range 65–526. The density of cetacean groups during transmissions was estimated at 0.0166 (se=0.0086/km²) and the estimated number of cetaceans was in the range 64–597. The densities in the base line and transmission periods did not differ.

The number of hourglass dolphin schools sighted during the transmission period was twice that during the base line period (15 vs 6 sightings), rising from 19% to 45% of sightings. Simultaneously, the number of minke whale and southern bottlenose whale sightings declined (from 5 to 0 and from 10 to 4, respectively). These changes could not be explained entirely by biases in sightability.

The sample of pinniped sightings was too small to pro-

duce a reliable density estimate. However, the sighting rates did increase during the transmission period from 0.15 to 0.27 groups/h.

C. Sightings made from the transmission site (CORY)

The CORY traveled within a 9.25 km×9.25 km area around the planned transmission site. During the base line period, CORY searched for 48 h. Observers sighted one hourglass dolphin, one southern bottlenose whale, eight Antarctic fur seals, two unidentified dolphin schools, and three unidentified mid- to large-sized whales (Table IV). Pods were difficult to identify at long range because the CORY could not turn from the track line.

Observations were made for 57.85 h during the transmission period. Nine cetacean schools were sighted (eight

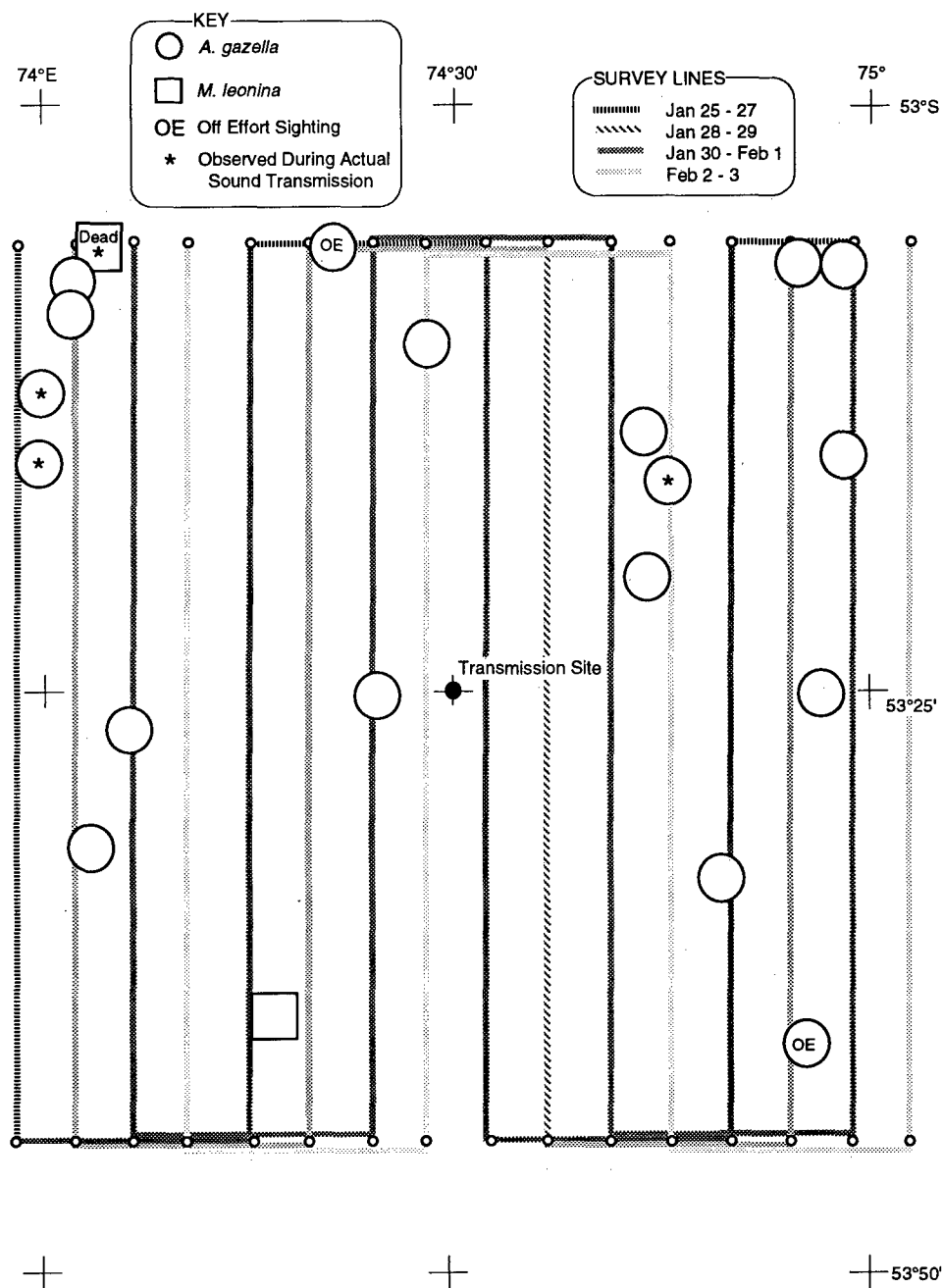


FIG. 5. Map of transmission survey showing locations of pinniped sightings.

hourglass dolphin and one unidentified school) and 13 groups of pinnipeds. The average school size during the baseline period was lower than during the transmission period (1.86/group vs 6.67/group). The number of hourglass dolphin schools seen near the transmitting vessel increased during the transmission period, from 1 school to 8. The number of mid- to large- sized schools dropped from four to none. The number of pinnipeds sighted from the transmitting vessel increased slightly (9 vs 14 sightings).

D. Behavioral observations

Behavioral observations from the transmitting vessel (CORY). There were five sightings of hourglass dolphins and four of pinnipeds during or immediately after a transmission

and five pinniped sightings seen within 15 min of the start of a transmission. Groups were monitored continuously until they left the area to determine their behavioral responses to the transmissions. In no case did the dolphins remain near the vessel long enough to observe their behavior before, during, and after a transmission.

Hourglass dolphins approached the transmitting vessel from 3 to 31 min after the start of a transmission. In one case they appeared to be in transit, that is, they crossed the track-line without approaching the vessel; in three cases they rode the bow for 6, 13, and 19 min, respectively, and in one case they remained for 15 min within 15 m of the vessel's beam without riding the bow. No unusual behaviors were observed. Sighting distance varied between the two periods, from 1875

TABLE III. Results of cetacean sightings from line-transect surveys from the R/V AMY CHQUEST.

| Measure | Baseline period | Baseline period (adjusted) ^a | Transmission period (25 Jan–1 Feb) | Transmission survey (25 Jan–3 Feb) |
|--|----------------------|---|------------------------------------|------------------------------------|
| Distance surveyed in km | 1093 | 1093 | 1010.6 | 1319.2 |
| Schools | 31 | 30 | 30 | 33 |
| Effective strip width in km (standard deviation) | 0.922 (±0.240) | 0.922 (±0.240) | 0.897 (±0.458) | 0.897 (±0.458) |
| Mean group size | 12.16 (±54.5) | 2.40 (±3.74) | 3.17 (±3.40) | 4.79 (±8.38) |
| Density in groups/km ² (standard error) | 0.0154 (±0.0053) | 0.0157 (±0.0076) | 0.0166 (±0.0086) | 0.0111 (±0.0025) |
| Estimated number of groups in study area (95% confidence interval) | 75.4 (37.5–151.6) | 76.89 (30.3–195.3) | 81.13 (30.1–218.6) | 54.6 (30.2–78.9) |

^aOne large school of 275 pilot whales and 30 hourglass dolphins removed from analysis.

m before the transmissions started ($N=4$) to 273 m during transmissions ($N=5$). The schools sighted during transmissions always came close to the transmitting vessel. The sizes of these schools averaged 7.5 individuals during the baseline period and 5.4 individuals during transmissions.

None of the encounters with seals lasted more than a few minutes. Exposed seals (seals seen during transmissions) did not approach the vessel as closely as unexposed seals (mean closest point of approach 174 m during or immediately after transmissions, 57 m at other times). Although this difference was statistically significant (t -test, $N=13$, $p<0.05$), the difference in approach distance was too small to make a substantial difference in the level of exposure to the transmissions.

Behavioral observations of small and mid-sized cetaceans from the survey vessel (AMY): During the baseline period, the large mixed-species school of hourglass dolphins and pilot whales veered away from AMY's course as she approached them closely to count them, but other pods did not obviously avoid AMY. No schools rode the bow during the six sightings and there were no other abrupt changes in behavior. During the transmission period, hourglass dolphins approached initially and then veered away from AMY on 2 of 14 occasions. They rode the bow 3 times for up to 70 min, once when CORY was transmitting at a distance of 31 km.

TABLE IV. Results of transect surveys from R/V CORY CHQUEST, the transmitting vessel.

| Period | Hours surveyed | Distance surveyed (km) | Sightings (schools) |
|--------------|----------------|------------------------|--|
| Base line | 48.00 | 108.9 | 3 unidentified whale 1 southern bottlenose whale 2 unidentified dolphin 1 hourglass dolphin |
| Transmission | 57.85 | 188.31 | 2 unidentified dolphin 8 hourglass dolphin |

Two groups (five and six dolphins, respectively) were observed milling in zig-zag patterns and leaping clear of the water during transmissions. None of these behaviors could be attributed unequivocally to the transmissions, as they are all in the normal repertoire of *Lagenorhynchus* dolphins.

Of the 15 hourglass dolphin sightings for which headings could be recorded, relative orientation scores showed that 6 were traveling toward and 5 away from the AMY. Six of seven schools were oriented away from CORY.

The most frequently sighted mid-sized whale was the southern bottlenose whale (14 sightings). Most sightings were of single individuals. Of the six groups with known headings sighted during the baseline period, half were directed away and half were approaching the AMY. Most were headed away (6 of 7) from the CORY. The number of sightings during the transmission period was too small to characterize typical heading.

Behavioral observations of large whales: Minke whales were observed only before the start of the experiments and only from AMY. On all five occasions, the minke whales were traveling toward AMY. No pattern was apparent with respect to CORY's position.

Detailed observations were made of the few large baleenopterids encountered. Three behavioral observations of 1 h or longer were collected, one during the baseline and two during the transmission period.

Observation of one fin whale, 22 January: During the baseline period, one fin whale was followed for a total of 60 min from 1110 to 1210 h in Beaufort 6 conditions. The whale was initially sighted crossing the bow of AMY to the west, against the prevailing current, heading to W/WNW throughout the observation. The mean blow rate per surfacing was 6.4 blows/min (standard deviation [s]=3.85). The mean dive time was 6.2 min (s =0.605). The whale traveled at a medium speed of 6 km/h throughout the observation, and did not appear to be maneuvering to avoid the AMY, which followed at a range of over 1 km. No unusual behaviors were observed.

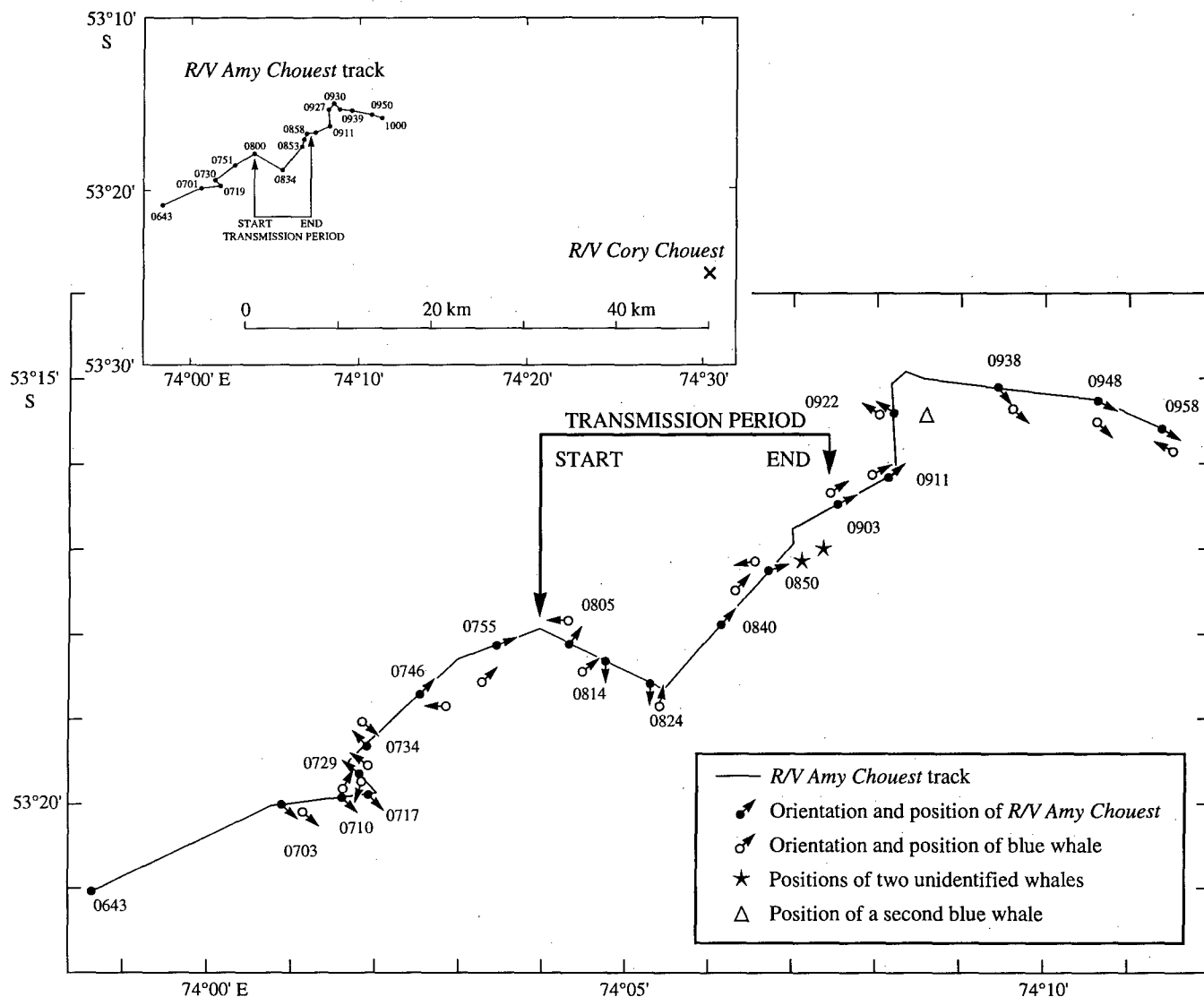


FIG. 6. Track of blue whale on 27 January. Inset shows location of track relative to transmitting vessel. Closed arrows indicate location and orientation of survey vessel. Open arrows indicate location and orientation of whale.

Observation of one blue whale, 27 January: An extended behavioral observation of a blue whale was made on 27 January before, during, and after a transmission. At 0642 h an immature (15–18 m) blue whale was detected by its blow in Beaufort 6 conditions approximately 0.93 km from the AMY and 61 km WNW of the CORY. The animal was followed at a range of 1 km for 194 min, 73 min before, 60 min during, and 61 min after a transmission. No calls were ever detected from this whale.

The track followed by the AMY as it observed the whale is shown in Fig. 6. The detail in this figure indicates the position of the CORY, showing that the whale's track was generally toward and parallel to the transmitting vessel, generally NE. The blue whale traveled at a medium speed (6–8 km/h) for most of the observation. Immediately before the transmission (0745–0748 h), the animal traveled slowly (1.9 km/h) or rested quietly at the surface. At 0805 h, right after the start of the transmission, the whale turned around abruptly (150° directly away from CORY) and increased its rate of travel. It was 52 km from the CORY at the time. After

3 large changes in orientation between 0806 and 0815, which brought it closer to the transmission site, the whale returned to its NE course.

At 0824, two hourglass dolphins joined the blue whale. At this surfacing, the whale changed orientation 150° to the west and increased its speed (estimated at 19 km/h). It lunged forward at the surface for 6 min, after which it slowed to medium speed, stopped lunging for 3 min, and lunged briefly again at high speed until it dove at 0833 after 18 blows. The dolphins appeared to be riding the pressure wave created by the lunging movement. The lunging behavior was similar to that of feeding blue whales (R. Rowlett, NMFS, personal communication). There was no other evidence of feeding (e.g., birds, detritus, swallowing).

The hourglass dolphins were not sighted again after the whale stopped lunging. Through the remainder of the transmission period, the whale traveled at medium speed (6–8 km/h), with overall movement to the NE, generally toward CORY. At 0843, before the end of the transmission, the blue whale dove, and two unidentified rorquals were sighted 4

TABLE V. Results of behavioral observations made during an encounter with a young blue whale 1/27/91 during the 0300Z transmission.

| | Before transmission | During transmission | After transmission |
|--|-------------------------------|-------------------------------|-------------------------------|
| Observation time | 73 min | 60 min | 61 min |
| Number of complete surfacing sequences | 8 | 6 | 6 |
| Number of blows | 67 | 78 | 75 |
| Number of blows per minute | $x=0.92$ | $x=1.30$ | $x=1.23$ |
| Number of blows per surfacing | $x=8.25$ $s=4.33$ $N=8$ | $x=13.0$ $s=3.46$ $N=6$ | $x=12.5$ $s=2.88$ $N=6$ |
| Dive time in minutes | $x=6.72$ $s=1.91$ $N=8$ | $x=5.78$ $s=1.42$ $N=5$ | $x=6.37$ $s=0.77$ $N=5$ |
| Total rate of reorientation (degrees per minute) | 11.10 | 18.3 | 16.22 |
| Rate of reorientation within surfacing sequence (degrees per minute) | 3.28 | 20.8 | 23.8 |
| Time at surface during surfacing sequence (min) | $x=2.04$ $s=1.13$ $N=8$ | $x=3.80$ $s=3.04$ $N=6$ | $x=4.21$ $s=3.71$ $N=6$ |
| Mean distance AMY to whale per surfacing (m) | $x=1008$ $s=518$ $N=8$ | $x=1225$ $s=661$ $N=6$ | $x=973$ $s=378$ $N=6$ |

and 2.5 km NE of it. At the next surfacing, the whale had changed its heading 155° to W, then to the WSW. By the final dive of this surfacing sequence, it was headed E, back in the direction of the CORY. These changes in orientation

TABLE VI. Results of acoustic surveys.

| Period | Recording effort (min) | Time with sperm whales present (min) | Time with pilot whales present (min) |
|---------------------------------------|------------------------|--------------------------------------|--------------------------------------|
| All effort | | | |
| Baseline period | 1137 | 278(24%) | 97 (8%) |
| seismic survey noise present | 380 | 0 (0%) | 0 (0%) |
| seismic survey noise absent | 757 | 278(37%) | 97 (13%) |
| Transmission period | 2202 | 0 (0%) | 0 (0%) |
| Post-transmission period ^a | 587 | 68(12%) | 587(100%) |
| Systematic effort at night | | | |
| Baseline period | 789 | 63 (8%) | 0 (0%) |
| seismic survey noise present | 380 | 0 (0%) | 0 (0%) |
| seismic survey noise absent | 409 | 63(15%) | 0 (0%) |
| Transmission period | 1481 | 0 (0%) | 0 (0%) |
| Post-transmission period ^a | 446 | 0 (0%) | 133 (30%) |

^aThe seismic survey vessel was always audible during the post-transmission period.

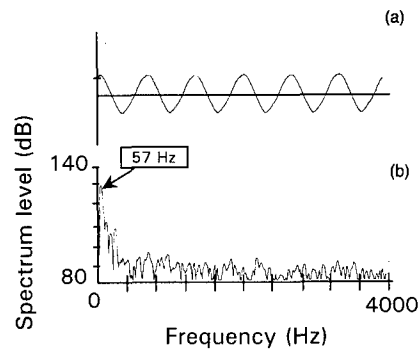


FIG. 7. Waveform (a) and spectrum levels (b) of a continuous-wave (cw) source transmission received at 73 km from the source site.

occurred at the surface, but the whale's track between dives kept it on a NE and then E course (Fig. 6).

The whale's rate of change in orientation was 11°/min before, 18°/min during, and 16°/min after the transmission. The higher reorientation rate during the transmission may have been a response to the AMY, or the presence of hourglass dolphins and prey, or the presence of the other whales in the area. The whale certainly appeared to be avoiding AMY because six of eight relative orientation scores were negative. There was no such pattern with respect to the CORY.

The mean number of blows/min and number of blows per surfacing increased during the transmissions relative to the period before and remained high afterward (Table V). Dive times remained constant, however.

Observation of two unidentified rorquals, 28 January: From 1116 to 1313 h a pod of two 13–14.5 m rorquals was detected and followed. Species identification could not be confirmed due to the immaturity of the whales, but they were either juvenile fin or sei whales (*B. physalus* or *B. borealis*). No transmissions occurred that day due to equipment failure, but the whales had been exposed to two full days of transmissions at the time of the observation.

The observation, which lasted a total of 97 min, included 13 complete surfacing sequences. The whales were sighted initially 38 km WSW of the CORY. The track of the AMY while pursuing them and the position of the CORY are shown

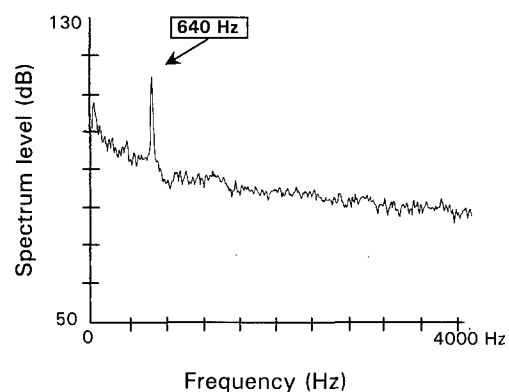


FIG. 8. Spectrum levels of the noise produced by survey vessel, R/V AMY CHOUET.

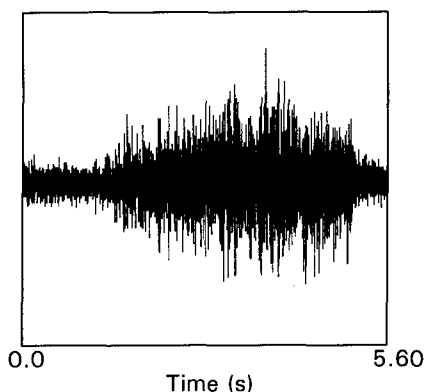


FIG. 9. Waveform of pulses produced by the seismic survey vessel M/V MARION DUFRESNE.

in Fig. 8. They were 58 km W of CORY at the time the observation was terminated.

Throughout the observation, the focal whales appeared to be avoiding the AMY. The mean reorientation rate of $18^\circ/\text{min}$ was high by comparison with the rate of $1^\circ/\text{min}$ recorded for the lone fin whale observed on 22 January and was comparable to that of the blue whale during and after a transmission. The mean number of blows per surfacing per individual for the two whales was half that of the lone fin whale followed during the baseline (3.4 blows vs 6.4 blows). Time at the surface during a surfacing interval was also shorter ($x=2.8$ min, $s=1.01$) compared to the lone fin whale ($x=6.1$, $s=4.18$). No calls were heard at any time during this observation.

E. Acoustic monitoring

1. Source transmissions

The waveform and spectrum of the one transmission type (the continuous sine wave at 57 Hz) are given in Fig. 7(a) and (b). These levels were received at a range of 73 km from the source site during the source tests from a sonobuoy set to deploy its hydrophone at 80-m depth. There was detectable energy in the signal out to approximately 400 Hz, possibly because the source was operated at near-resonance frequencies with consequent nonlinearities in the output. However, the energy in the signal above 100 Hz was 20 dB below the peak level.

2. Background and vessel noise

The noise from the survey vessel AMY was detectable at distances of at least 6 km. Figure 8 shows an example spectrum of this noise collected at 80 m depth on 29 January under Beaufort 4 conditions at a range of 2 km. A major component of this noise was a tonal at 656 Hz and its harmonic at 1318 Hz. This tonal was only present when the vessel was underway and varied considerably with vessel speed and the pitch of the AMY's propellers.

Under typical conditions (Beaufort 6–8), the FM radio signal from the sonobuoys could be received adequately at distances up to 10 km. At this range, the noise levels from the AMY plus the self-noise from the receiving system were probably above the level of the local ambient at low fre-

quency. The combination of noise from all three sources will be called background noise rather than ambient noise. The background noise was lowest when making recordings in low sea states at night, but, of course, this condition did not represent typical conditions in the area. With the ship underway and the sonobuoy hydrophone at 80 m, broadband spectral levels ranged around 97–103 dB *re*: 1 μPa at the limits of good reception. During night observations in calm weather (Beaufort 2–4), with the AMY's engines off, levels ranged from 81–85 dB *re*: 1 μPa at the limits of good reception.

The R/V MARION DUFRESNE, a French seismic survey vessel, conducted surveys along the Kerguelen Plateau 370 km away and to the south throughout the study and during the return trip to Cape Town, South Africa. The low-frequency bursts produced by the vessel were shots from eight synchronized 16 l Bolt air guns, emitted every 100 s (Charvis, personal communication), with an estimated peak overpressure of 263 dB *re*: 1 μPa at the source.

An example waveform of these bursts is given in Fig. 9. The bursts were approximately 3 s in duration and ranged in frequency from 30–500 Hz. The spectrum after subtracting the background noise is given in Fig. 10(b). The levels of noise from the MARION DUFRESNE were measured 6 km from the AMY at night on 29 January, during the transmission period, and while idling on 6 February, shortly before the AMY crossed the Antarctic Convergence. The vessel was 371 nm (687 km) and 578 nm (1070.5 km) from the AMY, respectively. Bursts from the MARION DUFRESNE measured approximately 110 dB *re*: 1 μPa and exceeded the background level by 10–30 dB within the band from 30–500 Hz. They measured 112 dB *re*: 1 μPa on 6 February.

3. Recordings of cetacean vocalizations

Recordings collected during the baseline and transmission periods contained vocalizations of sperm whales, pilot whales, and hourglass dolphins. At no time during the acoustic recordings at nights or during opportunistic behavioral observations were rorqual calls detected by ear or spectrographically. All recordings were monitored below 500 Hz in real time using a digital spectrograph with frequency resolution of 1 Hz, so it is unlikely that rorqual calls were present but undetected.

There were sufficient recordings in the presence of pilot whales and sperm whales to make comparisons between baseline and transmission periods unexposed vocal behavior possible. In particular, sperm whales were detected on many of the recordings made during the baseline period, including the systematic recordings made at night. The effort and results of these surveys are summarized in Table VI.

Echolocation clicks and whistles were recorded from pilot whales during all 4 daytime encounters from 18 January to 3 February. Pilot whales were detected twice at night by their vocalizations. Sperm whale clicks were recorded simultaneously with pilot whale calls on two occasions from hydrophones at 122 m. Pilot whales were never encountered during the transmission surveys and no calls were detected at night.

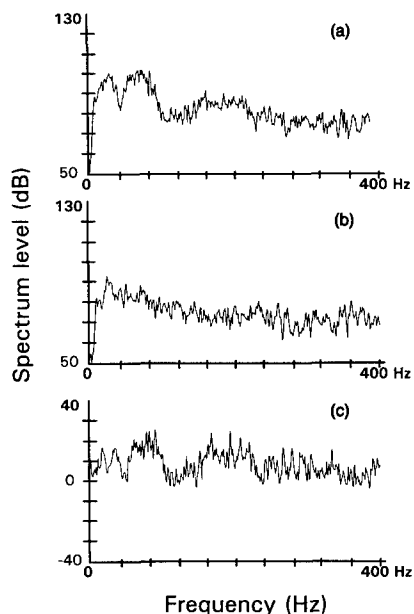


FIG. 10. (a) Power spectrum of noise produced by the seismic survey vessel M/V MARION DUFRESNE at a range of 371 km, (b) same spectrum after subtraction of background noise.

Clicks were recorded in the presence of a single large sperm whale encountered during the baseline period. Sperm whale clicks were also detected often when buoys were dropped during the daytime, although no sperm whales were sighted. Therefore, there were probably more sperm whales in the area than the two observations at the surface suggested. Unfortunately, estimates of the number of sperm whales on each recording could not be made using the methods of Whitehead and Weilgart (1990) because few codas were detected.

Acoustic monitoring was conducted for a total of 1137 min during the baseline period and 2202 min during the transmission experiment. Sperm whale clicks, clangs, and a few codas were detected during 24% of the time in the baseline period and pilot whales were detected during 8% of the time. Systematic night-time recordings were made for 849 min during the baseline period and 1481 min during the transmission period. Sperm whales were present during 8% and pilot whales were present during 0% of this effort. Sperm whales and pilot whales were not detected during the transmission experiments. One silent sperm whale was encountered at great range from the survey vessel during the transmission period. It was sighted in the morning on 25 January, at which time it would have been exposed to the transmissions only briefly. Sperm whale clicks were detected again during the first night-time recording after the storm, or at most 36 h after the end of transmissions.

Sperm whales may also have been silenced by seismic survey impulses, although the sample of recordings in the absence of the MARION DUFRESNE during the baseline period is small. During the systematic night-time recordings in the baseline period, 380 min of recordings were made while the seismic survey vessel was audible and 409 min in its absence. Sperm whales were heard 15% of the time and pilot

whales 5% of the time in the absence of pulses but not in their presence. It is most parsimonious to assume that the small sample of recordings with the vessel present was insufficient to allow pilot whale calls to be detected. However, sperm whale vocalizations were common enough that they could have been expected. The pulses from the MARION DUFRESNE exceeded the background by 10–15 dB during all of these recordings.

4. Results of observations with the fish-finding fathometer

Data collected with the fish-finding fathometer showed the presence of vertically migrating species, most likely krill, throughout the study area. No changes in depth of these concentrations were detected between the baseline and transmission periods from the AMY within the study area (mean depth 57.62 m during base line, $N=24$, vs 59.67 m during the transmission period, $N=21$, $p>0.05$). It is possible that effects on prey close to the CORY went undetected because no fathometer measurements were made.

III. DISCUSSION

As expected, the sample of sightings obtained at Heard Island was too small to estimate changes in densities of individual species during the transmission period. Reliable estimates would have required a sample of 40–80 groups per species (Buckland *et al.*, 1993). Much more survey effort before and in the presence of transmissions would have been required to obtain these data, even for the most common species in the area of Heard Island. Based on the sighting rates during the transmission period, several months of effort in the presence of transmissions would have been required.

Surveys for marine mammals have been used in the past to measure the impact of disturbance associated with mineral exploitation in the Beaufort Sea (Richardson *et al.*, 1985, 1986). In these instances, noise was associated with other sources of disturbance, particularly transiting vessels. Bowhead and gray whales (*Balaena mysticetus* and *Eschrichtius robustus*) appear to avoid areas with heavy vessel traffic (Richardson *et al.*, 1985; Ljungblad *et al.*, 1986; Malme *et al.*, 1984, 1986). The results of these studies are consistent with anecdotal accounts that whales abandon areas with heavy and uncontrolled vessel traffic (Nishiwaki and Sasao, 1977; Swarts and Jones, 1989; Reeves, 1992). However, no previous study has shown that noise, in the absence of vessel traffic, can produce a similar effect over a wide area. The results reported herein suggest that sperm whales, pilot whales, beaked whales, and minke whales could have altered their distribution in the immediate vicinity of the HIFT transmissions, but that they returned or were replaced by new individuals quickly when transmissions stopped. Unfortunately, insufficient samples were collected to detect changes statistically, or to determine whether or not there were long-term effects of the transmissions. For example, in the long run animals might have habituated well to the transmissions.

Even the short-term effects that were observed must be interpreted carefully. The normal distribution and movements of marine mammals in the vicinity of Heard Island

were not known at the start of the experiment, so some of the changes observed could have been caused by natural factors unrelated to the transmissions. In addition, the two survey vessels and the MARION DUFRESNE were confounding disturbances. Finally, if the transmissions caused alterations in behavior, some species might have been seen less or detected acoustically less during the transmissions because they were less detectable rather than less dense. For example, five pods of minke whales were detected during the baseline survey but none were seen during the transmissions. Concurrently, the number of groups of unidentified large whales sighted from AMY increased; some of these could have been minke whales. Antarctic minke whales have been observed avoiding survey vessels (Leatherwood *et al.*, 1982), and they may have been made more wary by the transmissions. However, the lack of sightings of any mid- to large-sized whales from CORY, identified or not, could only suggest effects on distribution within 10 km of the transmission site (within the 150-dB isopleth).

The behavioral changes observed in the few balaenopterids tracked from AMY were consistent with results of playback experiments on other mysticetes (Malme *et al.*, 1984; Richardson *et al.*, 1985). The blow rate, surfacing duration, and reorientation rate appeared to change in the presence of transmissions. The reorientation rate was a particularly dramatic indicator. However, the reorientation rate must be interpreted cautiously because it was based on observer estimates of headings and changes in headings, which are difficult to obtain from a vessel. Also, only one of the observations actually measured the responses of the same whale before, during, and after a transmission (the blue whale on 27 January); the observations on 22 and 28 January could have differed because of species differences or differences in social state. Therefore, while our results are consistent with previous studies, they are not statistically defensible evidence that whales responded to the transmissions.

The young blue actually turned toward the vessel for one surfacing after the start of transmissions, thereafter returning to its original heading. It also increased speed and changed its direction more frequently during this period. It is possible that the whale was trying to localize the transmitting source using the gradient in sound intensity as a cue. In playback experiments with lower-amplitude sources, turning toward or away from a source would have allowed whales to localize a source because the gradient would have been large near the source, i.e., exactly at the range where effects were detected. The sound intensity gradient over the distance that the blue whale traveled in the presence of the HIFT transmission was less than 2 dB, i.e., so small that it would not have been useful to the whale. If the whale attempted to avoid the transmissions, it was unsuccessful—sound levels exceeded the 132-dB upper limit of the sonobuoys throughout the observation. By the end, the focal whale was 38.9 km from CORY, having traveled 20.1 km closer in a generally northeasterly direction, including 6 km of approach during the transmission [Fig. 6(a)].

The biggest changes in the blue whale's orientation occurred during the first surfacing after the transmissions began (150°) and when three other balaenopterids were observed in

the area (155° and 150°). The blue whale was observed to swim away from the CORY (relative orientation score of -1) immediately after the start of transmissions, which could easily have been a startle response. The small deviation of its track that followed was similar to movements observed in the California gray whale after exposure to experimental playback of industrial noise (Malme *et al.*, 1984, 1986). In the case of the gray whale, avoidance was only detectable after statistical examination of the tracks of many individuals, and was never determined to have an important effect on migration.

The changes in distribution and behavior of deep-diving species were somewhat more convincing evidence of disturbance. Sightings of southern bottlenose whales dropped to less than half their baseline value during transmissions and all the sightings during the transmission period were made on January 28 and 29, days when few or no transmissions occurred. All these individuals were observed at the far southern end of the study area and their orientations were generally away from both of the vessels. It is not clear whether the transmissions were aversive by themselves or whether they made southern bottlenose whales avoid the AMY and CORY at greater distances.

Changes in behavior of pilot whales and sperm whales provided unequivocal evidence of behavioral effects of the transmissions. Pilot whales were sighted and heard before and after the experiments, but not during the transmissions; two groups were detected immediately after the storm that shut down the experiment (within 36 h of the end of the experiment). Sperm whales, which were heard frequently in the area during the baseline period, were silent during the transmissions, but their clicks reappeared within 36 h as well. They either left the area or became silent when the transmissions were underway. Such an effect could be expected because sperm whales frequently become silent in the presence of man made noise, including the sound of approaching vessels and sonar noise. It could not be determined whether the individuals that reappeared after the end of the experiment were the same as those in the area earlier.

Small odontocetes and fur seals probably did approach the transmission site, but the reasons for the approach are unclear. Small schools of dolphins were seen more frequently near the transmitting vessel CORY after the start of the experiments (eight sightings versus 1 during the baseline period) and were observed to approach and bow-ride during transmissions. The number of schools seen from the survey vessel AMY more than doubled (from 6 to 15 schools) during the transmissions. Fur seals were more abundant in the study area during the transmissions, based on surveys from both AMY and CORY, but the change was not as dramatic. Changes in density could not be determined in either case due to small sample size. It is quite possible that these species approached the source out of curiosity. Alternatively, the transmissions may have affected prey distribution, availability, or detectability. We found no evidence that prey distribution was a factor, but the surveys with the fish-finding fathometer cannot be considered an adequate study of prey abundance and distribution, particularly not close to the source site.

In summary, changes in distribution, surfacing behavior, and vocalizations were observed in response to the transmission experiment. The long-term effects of the transmissions could not have been ascertained by this short-term experiment. None of the changes observed have been associated with long-term effects in any other species.

- Buckland, S. T., Anderson, D. R., Burnham, K. P., and Laake, J. L. (1993). *Distance Sampling: Estimating Abundance of Biological Populations* (Chapman and Hall, New York).
- Burton, H. R. (1986). "A substantial decline in the numbers of elephant seals at Heard Island," *Tasmanian Naturalist* **86**, 4–8.
- Carder, D. A. and Ridgway, S. H. (1990). "Auditory brainstem response in a neonatal sperm whale, *Physeter spp.*," *J. Acoust. Soc. Am. Suppl.* **1** **88**, S4.
- Dahlheim, M. and Ljungblad, D. K. (1990). "Preliminary hearing study on gray whales (*Eschrichtius robustus*) in the field," in *Sensory Abilities of Cetaceans*, edited by J. Thomas and R. Kastelein (Plenum, New York), pp. 334–346.
- Enger, P. S., Karlsen, H. E., Knudsen, F. R., and Sand, O. (1993). "Detection and reaction of fish to infrasound," *ICES Marine Symp.* **196**, 108–112.
- Ensor, P. H. and Shaughnessy, P. D. (1989). "Fur seals over the Kerguelen plateau and elsewhere in the southern ocean," *Polar Biol.* **10**, 481–483.
- Fleischer, G. (1978). "Hearing in extinct cetaceans as determined by cochlear structure," *J. Paleontology* **50**, 133–152.
- Gosho, M. E., Rice, D. E., and Breiwick, J. M. (1984). "The sperm whale, *Physeter macrocephalus*," *Mar. Fish. Rev.* **46**, 54–64.
- Johnson, C. S. (1966). "Auditory thresholds of the bottlenosed dolphin (*Tursiops truncatus* Montague)," Naval Ordnance Test Laboratory Technical Publication 4178.
- Jones, M. L. and Swartz, S. L. (1984). "Demography and phenology of gray whales and evaluation of whale-watching activities in Laguna San Ignacio, Baja California Sur, Mexico," in *The Gray Whale, Eschrichtius robustus*, edited by M. L. Jones, S. L. Swartz, and J. S. Leatherwood (Academic, New York), pp. 309–374.
- Ketten, D. R. (1992). "The marine mammal: specializations for aquatic audition and echolocation," in *The Evolutionary Biology of Hearing*, edited by D. B. Webster, R. R. Fay, and A. N. Popper (Springer-Verlag, New York).
- Leatherwood, S. L., Awbrey, F. T., and Thomas, J. A. (1982). "Minke whale response to a transiting survey vessel," *Rep. Int. Whal. Comm.* **32**, 795–802.
- Ljungblad, D. K., Wursig, B., Swartz, S. L., and Keene, J. M. (1988). "Observations on the behavioral responses of bowhead whales (*Balaena mysticetus*) to active geophysical vessels in the Alaskan Beaufort Sea," *Arctic* **41**, 183–194.
- Malme, C. I., Miles, P. R., Clark, C. W., Tyack, P., and Bird, J. E. (1984). "Investigations of the potential effects of underwater noise from petroleum industry activities on migrating gray whale behavior, Phase II: January 1984 migration," Report by Bolt Beranek and Newman, Cambridge, MA, U.S. Minerals Management Service, BBN Tech. Rep. No. 5586 (unpublished).
- Malme, C. I., Miles, P. R., Miller, G. W., Richardson, W. J., Roseneau, D. G., Thompson, D. H., and Greene, C. R. (1989). "Analysis and ranking of the acoustic disturbance potential of petroleum industry activities and other sources of noise in the environment of marine mammals in Alaska," Report by BBN Systems and Technologies Corporation, Cambridge, MA, for U.S. Minerals Management Service, Anchorage, August 1989, BBN Tech. Rep. No. 6945 (unpublished).
- Mizroch, S. A., Rice, D. W., and Breiwick, J. M. (1984a). "The blue whale, *Balaenoptera musculus*," *Mar. Fish. Rev.* **46**, 15–19.
- Mizroch, S. A., Rice, D. W., and Breiwick, J. M. (1984b). "The fin whale, *Balaenoptera physalus*," *Mar. Fish. Rev.* **46**, 20–24.
- Mizroch, S. A., Rice, D. W., and Breiwick, J. M. (1984c). "The sei whale, *Balaenoptera borealis*," *Mar. Fish. Rev.* **46**, 25–29.
- Munk, W. H., and Baggeroer, A. (1992). "The Heard Island Feasibility Test," *Phys. Today* **45** (9), 22–31.
- Munk, W. H., and Forbes, M. G. (1989). "Global ocean warming: a acoustic measure?" *J. Phys. Oceanogr.* **19**, 1765–1778.
- Myrberg, A. A., Jr. (1990). "The effects of man-made noise on the behavior of marine animals," *Environ. Int.* **16**, 575–586.
- Nishiwaki, M., and Sasao, A. (1977). "Human activities disturbing natural migration routes of whales," *Sci. Rep. Whal. Res. Inst.* **29**, 113–120.
- Norris, J. C., and Leatherwood, S. (1981). "Hearing in the bowhead whale, *Balaena mysticetus*, as estimated by cochlear morphology," "Tissue structural studies and other investigations on the biology of endangered whales in the Beaufort Sea. Vol. II," edited by T. F. Albert, Report by the Department of Veterinary Science, University of Maryland, College Park, for the U.S. Bureau of Land Management, Anchorage, NTIS PB86-153566, pp. 745–787.
- Payne, R. and Webb, D. (1972). "Orientation by means of long range acoustic signaling in baleen whales," *Ann. NY Acad. Sci.* **188**, 110–140.
- Reeves, R. R. (1992). "Whale responses to anthropogenic sounds: a literature review," *Sci. & Res. Ser.* **47**, N.Z. Dep. Conserv., Wellington, New Zealand.
- Richardson, W. J., Wursig, B., and Wells, R. (1985). "Behavior of bowhead whales, *Balaena mysticetus*, summering in the Beaufort Sea: Reactions to industrial activities," *Biol. Cons.* **32**, 195–230.
- Richardson, W. J., Würsig, B., Miller, G. W., and Silber, G. (1986). "Reaction of bowhead whales, *Balaena mysticetus*, to seismic exploration in the Canadian Beaufort Sea," *J. Acoust. Soc. Am.* **79**, 1117–1128.
- Richardson, W. J., Greene, Jr., C. R., Malme, C. I., and Thomas D. H. (1991). "Effects of noise on marine mammals," Report by LGL Ecological Research Associates, Inc., Bryan, Texas, for U.S. Minerals Management Service, Atlantic OCS Region. February 1991, OCS Study MMS 90-0093.
- Watkins, W. A. and Schevill, W. E. (1975). "Sperm whales (*Physeter catodon*) react to pingers," *Deep-Sea Res. Oceanogr. Abst.* **22**, 123–129.
- Watkins, W. A., Moore, K. E., and Tyack, P. (1985). "Sperm whale acoustic behaviors in the southeast Caribbean," *Cetology* **49**, 1–15.
- Whitehead, H. and Weilgart, L. (1990). "Click rates from sperm whales," *J. Acoust. Soc. Am.* **87**, 1798–1806.